

# **Polymer Crystallization in Ultrathin Films at the Air-Water Interface**

Kumulative Dissertation

zur Erlangung des Doktorgrades der Naturwissenschaften  
(Dr. rer. nat.)

der

Naturwissenschaftlichen Fakultät II  
Chemie, Physik und Mathematik

der Martin-Luther-Universität  
Halle-Wittenberg

vorgelegt von

**Herrn Nazmul Hasan**

geb. am 17.07.1989 in Munshiganj, Bangladesh

Reviewers: Prof. Dr. Jörg Kreßler (Martin-Luther-Universität Halle-Wittenberg)  
Prof. Dr. Christiane Helm (Universität Greifswald)

Public defense: 23.02.2023

## **Preliminary remark**

The present dissertation is written in a cumulative form. The research results that contribute to this work have already been published in peer-reviewed journals. They contain all the experimental details and a detailed discussion of the relevant results.

### **This dissertation is based on the following publications:**

Paper I: Crystallization of poly(ethylene)s with regular phosphoester defects studied at the air-water interface

Nazmul Hasan, Karsten Busse, Tobias Haider, Frederik R. Wurm and Jörg Kressler  
Polymers 2020, 12, 2408, <https://doi.org/10.3390/polym12102408>

Paper II: Crystallization of a polyphosphoester at the air-water interface

Nazmul Hasan, Christian Schwieger, Hisaschi T. Tee, Frederik R. Wurm, Karsten Busse, and Jörg Kressler  
Eur. Polym. J. 2018, 101, 350, <https://doi.org/10.1016/j.eurpolymj.2018.03.001>

Paper III: Crystallization of poly( $\epsilon$ -caprolactone) at the air-water interface studied by IRRAS and GI-WAXS

Nazmul Hasan, Christian Fuchs, Christian Schwieger, Karsten Busse, Oleksandr Dolynchuk, and Jörg Kressler  
Polymer 2020, 196, 122468, <https://doi.org/10.1016/j.polymer.2020.122468>

Paper IV: Formation of surface wrinkles in collapsed Langmuir films of a polyhedral oligomeric silsesquioxane containing diblock copolymer

Nazmul Hasan, Karsten Busse, Asad Ullah, Hazrat Hussain, and Jörg Kressler  
Langmuir 2021, 37, 13399, <https://doi.org/10.1021/acs.langmuir.1c02082>

Paper V: Langmuir film formation of amphiphilic hybrid block copolymers based on poly(ethylene glycol) and poly(methacrylo polyhedral oligomeric silsesquioxane)

Nazmul Hasan, Asad Ullah, Shakir Ullah, Jörg Kressler, and Hazrat Hussain  
Colloid Polym. Sci. 2019, 297, 1149, <https://doi.org/10.1007/s00396-019-04517-2>

# Contents

<b>1 Introduction</b>	<b>1</b>
1.1 Crystallization of polymers	1
1.2 Crystallization of polymers in thin and ultrathin films on solid supports	2
1.3 Fabrication of ultrathin films on aqueous surfaces of the Langmuir trough	4
1.4 Behavior of amphiphilic polymers on the water surface of a Langmuir trough	9
1.5 Crystallization of homopolymers on the water surface of a Langmuir trough	11
1.6 Structure formation of block copolymers on the water surface of a Langmuir trough	14
1.7 Motivation, aim, and outline of the Thesis	16
<b>2 Experimental methods</b>	<b>19</b>
2.1 Langmuir trough and Langmuir-Blodgett (LB) transfer	19
2.2 Brewster angle microscopy (BAM)	24
2.3 Epifluorescence microscopy (EFM)	25
2.4 Infrared reflection absorption spectroscopy (IRRAS)	27
2.5 Atomic force microscopy (AFM)	29
2.6 Grazing incidence wide-angle X-ray scattering (GI-WAXS)	30
<b>3 Results</b>	<b>32</b>
3.1 Paper I: Crystallization of poly(ethylene)s with regular phosphoester defects studied at the air-water interface	32
3.2 Paper II: Crystallization of a polyphosphoester at the air-water interface	50
3.3 Paper III: Crystallization of poly( $\epsilon$ -caprolactone) at the air-water interface studied by IRRAS and GI-WAXS	60
3.4 Paper IV: Formation of surface wrinkles in collapsed Langmuir films of a polyhedral oligomeric silsesquioxane containing diblock copolymer	72
3.5 Paper V: Langmuir film formation of amphiphilic hybrid block copolymers based on poly(ethylene glycol) and poly(methacrylo polyhedral oligomeric silsesquioxane)	84
<b>4 Summary, conclusion, and outlook</b>	<b>97</b>
<b>References</b>	<b>100</b>

<b>Remarks on polymer naming</b>	<b>108</b>
<b>Abbreviations</b>	<b>109</b>
<b>Erklärung</b>	<b>113</b>
<b>Acknowledgments</b>	<b>114</b>
<b>List of publications</b>	<b>115</b>
<b>Curriculum vitae</b>	<b>116</b>



# 1 Introduction

## 1.1 Crystallization of polymers

Crystallization is a process where atoms, molecules, or ions spontaneously organize themselves into a regular, repeated, and 3D periodic pattern called crystal in order to minimize their energetic state.<sup>[1]</sup> Crystallization begins with nucleation, which is followed by crystal growth. Small nuclei form when a melt/solvent cools or a solvent evaporates, growing into a macroscopic crystal with a well-defined shape and facets. Crystallization can be seen in different classes of materials including polymers,<sup>[2,3]</sup> despite being long-chain molecules made of repeating units linked together by covalent bonds.<sup>[4]</sup> Polymers exhibit crystallization during polymerization, under external forces, or even in quiescent conditions.<sup>[5]</sup> Monomers can be joined up into chains leading to the formation of macroscopic single crystals during solid-state polymerization.<sup>[6,7]</sup> Orientation-induced crystallization happens under external forces.<sup>[8]</sup> Extrusion or injection process of polymers partially aligns the chain molecules in the stretch direction and can lead to the development of fibrous crystals.<sup>[8]</sup> Crystallization in a melt or a dilute solution occurs under quiescent conditions during cooling. Usually, polymer chains align by folding or extending and then stacking together to form ordered structures called lamellae.<sup>[9]</sup> The folding process is unique to polymer crystallization and has never been observed in other classes of materials.<sup>[10]</sup> The lamellae in the later stage grow radially in all directions at an almost constant rate, resulting in a spherical region known as spherulite (Figure 1).<sup>[11,12]</sup> Disordered regions denoted as amorphous part are also present between the lamellae of the spherulite.<sup>[13]</sup> 100% crystalline polymers, therefore, do not exist. Secondary crystallization happens in these regions over months or years, forming small crystalline structures and causing lamellae reorganization.<sup>[14]</sup> Flexible polymers like poly(ethylene) (PE) or poly(ethylene oxide) (PEO) exhibit chain folding, lamellae to spherulite formation, and finally, lamellae reorganization in the spherulite.<sup>[9,15-17]</sup> These are the well-accepted characteristic features of crystallization for flexible-chain polymers.<sup>[18,19]</sup> Rigid-chain polymers (e.g., conjugated systems), however, behave differently and their chain folding or non-folding behavior is still one of the major subjects in polymer research.<sup>[18,20,21]</sup> The majority of rigid polymers have an extended chain structure in the crystal.<sup>[18,22]</sup> Some rigid polymers with a high molar mass are capable of chain folding.<sup>[23,24]</sup> The morphology of rigid polymers is layered<sup>[25,26]</sup> or fibrillar<sup>[22]</sup> and rarely spherulitic.<sup>[22]</sup> So far, the ordering process and the resulting morphology are strongly influenced by the polymer molar mass,<sup>[27,28]</sup> presence of side chains/branches at the polymer backbone,<sup>[29]</sup> orientation of pendent groups (e.g., tacticity),<sup>[30]</sup> presence of various chemical compositions in

the backbone chain (e.g., heteropolymers, chain defects),<sup>[31]</sup> different chemical architectures (e.g., star/comb-like),<sup>[32,33]</sup> presence or absence of intracrystalline mobility<sup>[16,34]</sup> and finally, other extrinsic factors (e.g., crystallization temperature/cooling rate)<sup>[10,35]</sup>. For example, PE also shows extended chain lamellae during crystallization of low molar mass polymer, at a slow cooling rate, and under high-pressure recrystallization.<sup>[28,36,37]</sup> Although the crystal morphologies are usually metastable but have a significant impact on the optical, mechanical, thermal, and conductive properties of polymer materials.<sup>[38]</sup>

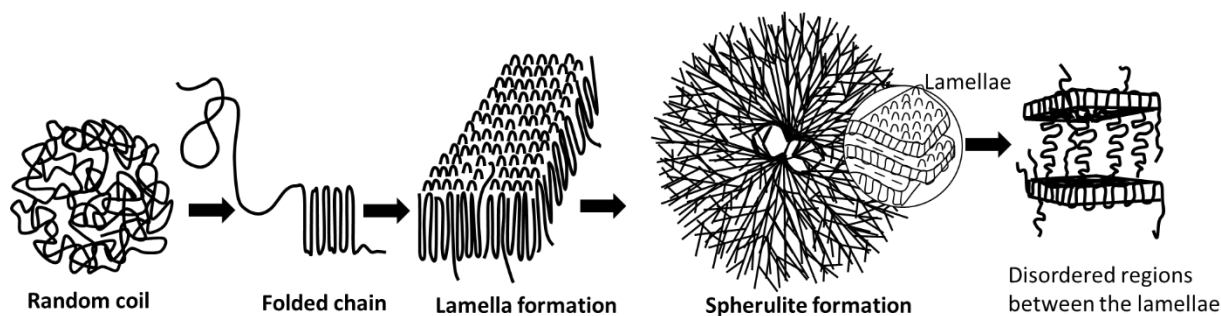


**Figure 1:** Schematic drawing of chain ordering during the crystallization of a flexible-chain polymer from the melt. The figure is reconstructed from several references.<sup>[11–13,39]</sup>

## 1.2 Crystallization of polymers in thin and ultrathin films on solid supports

Crystallization of polymers from random coils to a partially aligned state is one of the most striking phenomena in soft matter science. This is because polymers have to overcome huge entropic barriers originating from the chain connectivity.<sup>[40]</sup> The ordering process, therefore, depends on many factors as already stated earlier. This Thesis however solely deals with the confinement effects on polymer crystallization applied by fabricating ultrathin films. Confinement can also be applied in various ways including polymer blending, synthesizing copolymers, and polymer droplets as summarized in several review articles.<sup>[41–43]</sup> The general definition of a thin film is that the thickness stays within some  $\mu\text{m}$  to a few hundred nm.<sup>[44]</sup> A film thickness of less than one hundred nm is denoted as ultrathin film.<sup>[44]</sup> Crystallization in thin and ultrathin films has been studied over the last few decades dealing with fundamental research and applications.<sup>[45–50]</sup> Several factors that become dominant in thin and ultrathin film crystallization are surface free energy, chain orientation, segmental mobility, and chain diffusion.<sup>[45–50]</sup> Crystallization in confinement, may therefore, demonstrates distinct morphologies, degree of crystallinity, crystallization rates, and melting processes.<sup>[41]</sup> While anisotropic spherulitic development is frequently observed in bulk, crystallization in thin and ultrathin films exhibits unique morphologies with various lamellar orientations and polymorphic crystalline structures.<sup>[51,52]</sup> The two main lamellar orientations are “edge-on”,

where the polymer folded plane (fold surface plane of lamella) is perpendicular to the substrate plane and “flat-on”, where it is parallel to the substrate plane.<sup>[47]</sup> Spherulites, axialites, and lamellar bundles with an edge-on lamellar orientation are most frequently observed during thin film crystallization (Figure 2). The ultrathin films, however, exhibit seaweeds, dendrites, or single-crystallites with mostly flat-on lamellar orientation.<sup>[43,53]</sup> These are large open structures that occur due to less dense molecular packing.<sup>[54]</sup> The direction of the lamellae is further influenced by the substrate types<sup>[50]</sup> and crystallization temperatures.<sup>[47]</sup> It has been observed that edge-on lamellae are found on slippery surfaces, whereas sticky surfaces dominate the flat-on lamellar orientation.<sup>[55]</sup> Substrate interaction also decreases the crystallization rate and crystallinity of thin/ultrathin films compared to the bulk.<sup>[41,51]</sup> This is most likely due to the reduced mobility of polymer chains at the film-substrate interface. However, when polymer and substrate exhibit lattice matching, a phenomenon occurs known as epitaxial crystallization, in which the crystallization rate, melting temperature, and crystallinity of the film increase compared to the bulk.<sup>[41,51]</sup> Unlike morphologies and lamellar orientations, crystallization in thin/ultrathin films can also change crystal plane distances or result in distinct crystal phases, as summarized in several review articles.<sup>[41,51]</sup>

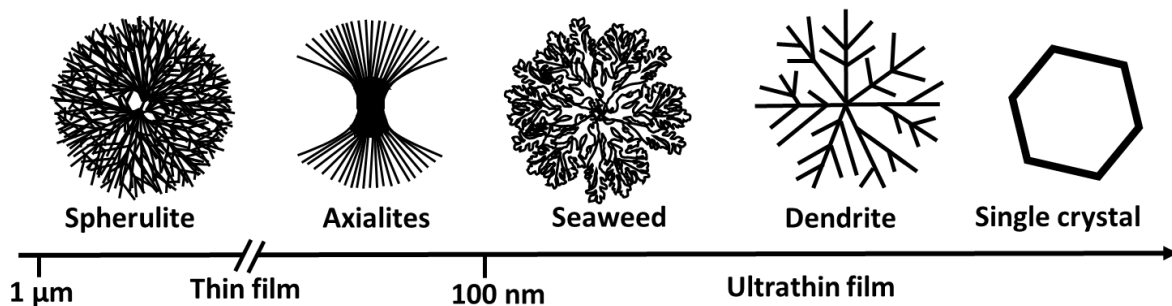


**Figure 2:** Illustration of most prominent morphologies that arise during polymer crystallization as a function of film thickness. The figure is drawn using data from several references.<sup>[41–43]</sup>

The reason for various morphologies is directly related to the lamellar orientations and explained based on both thermodynamics and kinetics models.<sup>[41,47,56,57]</sup> The critical nucleation and lateral surface energies for an edge-on orientation are found to be lower as compared to flat-on lamella in thin films. As a result, edge-on orientation takes precedence initially. However, this becomes unfavorable when the layer thickness decreases to ultrathin films due to many factors such as increased interfacial area of the lamellae on the substrate surface, more heterogeneous nucleation, and limited diffusion of chains.<sup>[43,47,58]</sup> The thermodynamic model cannot alone explain the coexistence of both edge- and flat-on lamellae in thin/ultrathin films, therefore, the kinetic model is taken into consideration. This model state that nucleation of

edge-on orientation occurs at the free surface (polymer/air interface) and quickly propagates to the substrate, meanwhile, flat-on lamellae nucleate at the polymer/substrate interface, then grow to the free surface. As a result, both lamellar orientations are expected.<sup>[57]</sup>

### **1.3 Fabrication of ultrathin films on aqueous surfaces of the Langmuir trough**

Thin/ultrathin films are fabricated using various physical and chemical methods such as sputtering, spin coating, and vapor deposition.<sup>[59]</sup> Some methods possess complex setups (e.g., high voltage and vacuum) and are rigorous to polymers.<sup>[60,61]</sup> The surfaces that support the film may also influence the final film morphology with their roughness,<sup>[62]</sup> causing epitaxial growth<sup>[50,63]</sup> and inducing dewetting.<sup>[45]</sup> The Langmuir technique is a simple alternative approach for resolving these challenges. The self-assembly process of molecules is utilized in this technique to prepare ultrathin films.<sup>[64,65]</sup> The film fabrication starts with dissolving molecules in a volatile solvent such as chloroform, then spreading the solution dropwise by micro syringe over some random points on the aqueous surface of a Langmuir trough up to a desired mean molecular area (*mmA*) value [average area for a single molecule]. After chloroform evaporation, the trough surface is then compressed by moving the barriers, which brings the adsorbed molecules close to each other and facilitates film formation.<sup>[64,65]</sup> Figure 3 shows a Langmuir trough used for ultrathin film fabrication. The setup includes a rectangular trough filled with liquid (e.g., water) that supports the film, a Wilhelmy system as a pressure sensor, and symmetrically moveable two barriers to facilitate compression. The pressure sensor measures the surface pressure ( $\pi$ ) as calculated from the difference between the surface tension of pure water and the water with a monolayer. An electronic control unit is used to adjust the barrier speed and calibrate the Wilhelmy system.<sup>[64]</sup> In comparison to other methods, the Langmuir technique offers precise control over the film thickness in the range of Å- to several nm just by controlling barrier movement, allows to use of hydrophilic or hydrophobic interfaces, offers mimicking cell membrane models, and provides molecular-level information. The method also allows to investigate molecular reorganization and facilitates variation in the crystallization progress of the film by adjusting the subphase temperature or the barrier speed.<sup>[66]</sup> Interfacial viscoelastic characteristics can also be measured using the Langmuir trough.<sup>[67]</sup>

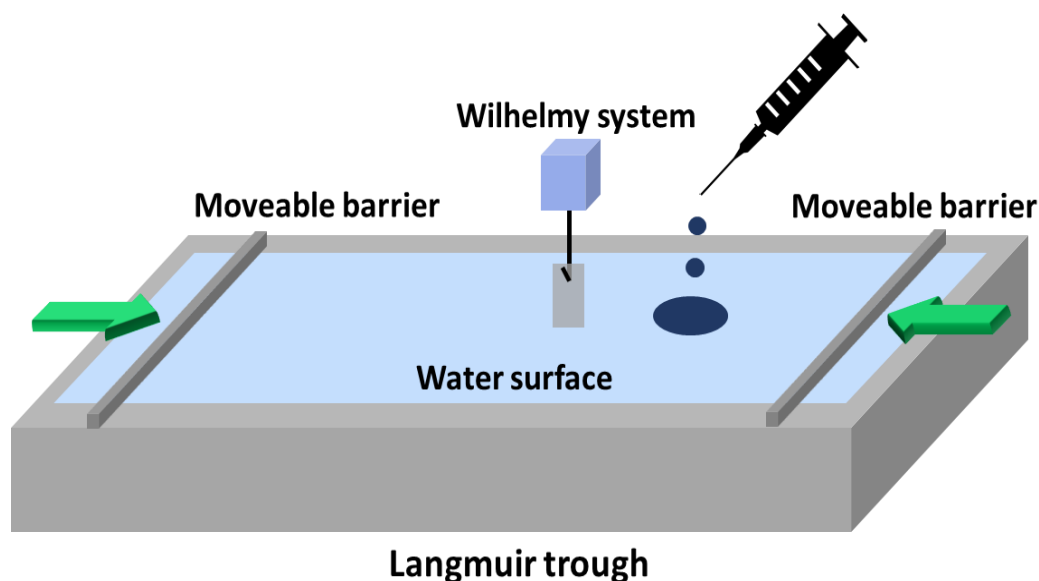


**Figure 3:** Schematic diagram of a Langmuir trough and its components.

The only shortcoming for this method is the need for amphiphilic molecules. These are molecules having hydrophilic and hydrophobic parts in their chemical structure. The hydrophilic part consists of polar groups (e.g., -OH, -NH<sub>2</sub>, -COOH, and -COOR) that help the molecules anchor to the water surface. The hydrophobic part is often a hydrocarbon chain (e.g., C<sub>n</sub>H<sub>2n+1</sub>) or a fluorinated hydrocarbon that keeps the molecules at the air-water interface.<sup>[68,69]</sup> There should also be a balance between these parts to prevent the molecules from dissolving in the water subphase. This means that the hydrophobic part should not be too small and the hydrophilic part should not be too big. Fatty alcohols (Figure 4) and lipids are classical amphiphiles,<sup>[64]</sup> whereas polymers, polypeptides, proteins, polysaccharides, diureasil hybrid compounds, dyes, carbonaceous compounds, macrocyclic molecules, magnetic soft spheres, and fullerenes are non-classical types.<sup>[70-73]</sup> Langmuir film formation from non-classical amphiphiles is briefly discussed elsewhere in several review articles.<sup>[74,75]</sup>

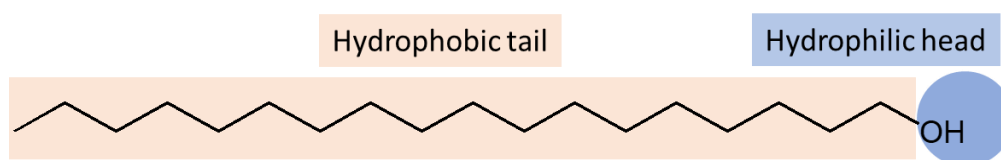


**Figure 4:** Chemical structure of a small amphiphilic molecule (i.e., stearyl alcohol).

Fabrication of ultrathin films on liquid surfaces is a long-standing concept.<sup>[65]</sup> Benjamin Franklin was the first who investigated oil films on the water surface in 1774 through his famous Clapham pond experiment.<sup>[65]</sup> However, he could not estimate the film thickness, which was later done by Lord Rayleigh in 1889.<sup>[76]</sup> Now considering the Langmuir film, the history is around 100 years old. Agnes Pockels showed monolayer preparation on the water surface by

compression using a homemade trough.<sup>[65]</sup> Irving Langmuir adopted the trough used by Pockels and gave the theoretical concepts of monomolecular films.<sup>[77]</sup> Due to his groundbreaking contributions, the film formation of amphiphilic molecules on the water surface is today known as Langmuir film or Langmuir monolayer. The research was later extended by Katherine Blodgett. She developed an instrument to transfer Langmuir film from the water surface to a solid substrate by vertical immersion and withdrawal of the substrate across the air-water interface. This film is known as Langmuir-Blodgett (LB) film.<sup>[78]</sup> Both procedures are required for the creation and characterization of ultrathin films/monolayers on the water surface.<sup>[66]</sup> There are also several methods available for preparing monolayers including self-assembled monolayer method (SAM) and layer-by-layer (LBL) technique.<sup>[79]</sup> They use immersing of solid supports (e.g., gold substrate) in solutions containing molecules with specific end groups (e.g., -SH) or polyions. They also share some common features with a LB technique like the ability to deposit multiple film layers on solid supports as well as deposit the layers in a sequence. However, LBL provides more simplicity in the film manufacturing process, allows to use a variety of materials, and offers robustness in films. Therefore, sometimes LB is replaced by the LBL technique in industrial applications. The Langmuir approach, on the other hand, offers better control over the packing density, orientation, and conformation of the molecules in the layer.<sup>[74]</sup> These are some unique benefits that no other method can offer.<sup>[75]</sup> Now, to understand the film formation, the surface pressure ( $\pi$ ) at a constant temperature is recorded while decreasing the *mmA* of the molecules by barrier movement. This  $\pi$ -*mmA* isotherm gives preliminary hints about the stable film formation along with phase information (e.g., liquid/solid). The molecular orientation information (e.g., vertical/flat/tilted) in the film relative to the water surface can also be extracted.<sup>[80]</sup> The phases that develop during compression depend on the hydrophobic parts and the polarity of the hydrophilic groups of the amphiphiles. The attraction among the molecules rises as the hydrophobic parts increase, resulting in a condensing phase. Ionizable hydrophilic groups, on the other hand, produce repulsive forces among them that impede the phase transitions. The experimental conditions e.g., subphase temperature, composition, and compression speed also strongly influence the film formation.<sup>[64]</sup> In a typical Langmuir film experiment, the trough is filled with ultrapure water or buffer solution, the temperature is kept at  $\approx 20$  °C and a low compression speed is applied.<sup>[64]</sup> Figure 5 depicts  $\pi$ -*mmA* isotherms of two common types of small amphiphilic molecules along with various film phases (e.g., gas, expanded liquid, condensed liquid, and solid) that are formed at different compression states of the molecules.

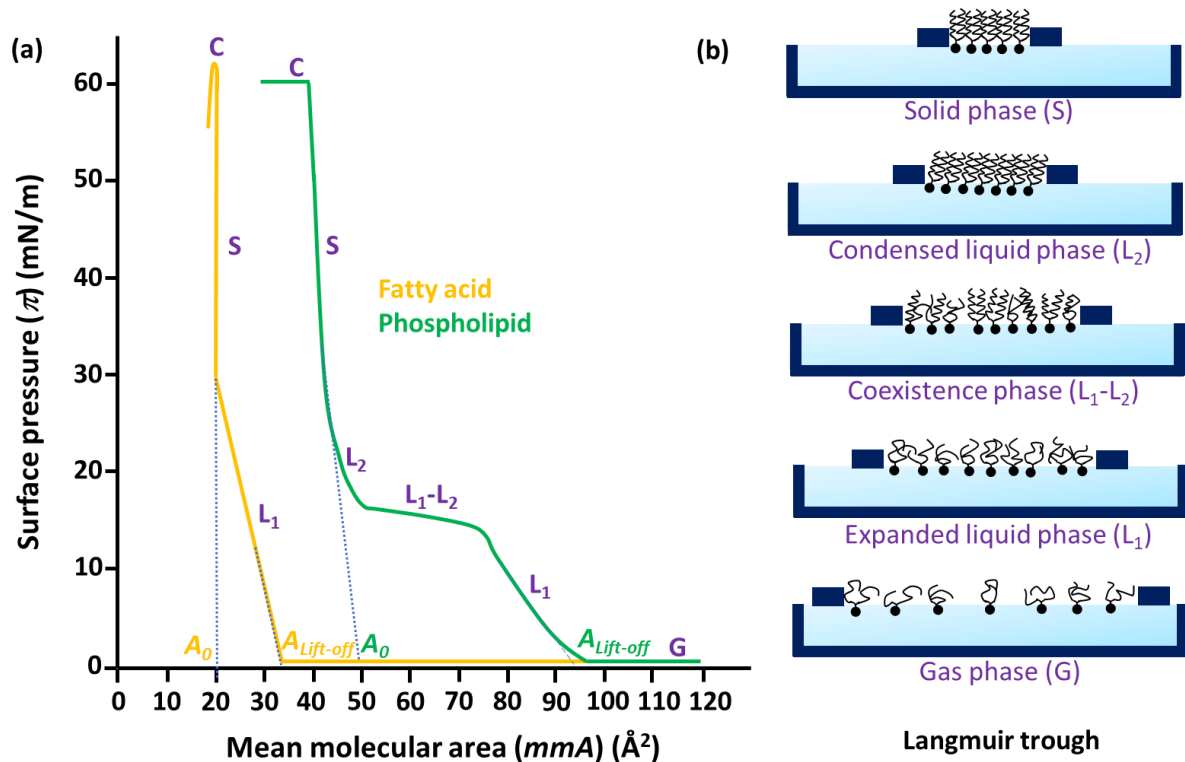


**Figure 5:** (a) Typical  $\pi$ - $mmA$  isotherm of a fatty acid (stearic acid) and a phospholipid (dipalmitoylphosphatidylcholine-DPPC) on the water subphase at 20 °C<sup>[80,81]</sup> and (b) schematic presentation of a DPPC Langmuir film with different phases as marked by letters at the  $\pi$ - $mmA$  isotherm.

After spreading the amphiphiles to  $\pi \approx 0$  mN/m and solvent evaporation, a 2D gas-like phase is formed (Figure 5b, G zone). When the barriers are moved to reduce  $mmA$  of molecules, several phases depending upon molecular interaction can be generated. Drawing tangents (dotted lines) on the linear regions of the Langmuir isotherm and then extrapolating to  $\pi = 0$  mN/m, different phases can be identified. An expanded liquid phase ( $L_1$ ) is formed at the initial increase of  $\pi$  (at  $A_{\text{lift-off}}$ ), where the molecules start to exert forces among themselves. The reduction in  $mmA$  by compression then leads to a condensed liquid state ( $L_2$ ) (e.g., intermolecular distance is slightly larger than solid) and finally, to a solid phase. This transition (liquid to solid) sometimes appears as a plateau-like feature in the isotherm (e.g., no  $\pi$  change upon  $mmA$  reduction or horizontal line in the isotherm) known as the coexistence phase (Figure 5b,  $L_1$ - $L_2$  zone). This phase does not exist for many amphiphiles like stearic acid, but it is characteristic of liquid crystals.<sup>[64]</sup> Further reduction in  $mmA$ , when exceeding the limiting area of the molecule ( $A_0$ ), results in film collapse. It should be noted that the limiting area is the least area that a molecule occupies. This area depends on the chemical structure of amphiphiles and their orientation (e.g., flat/tilted/vertical) in the film. For example, stearic acid containing a

single hydrocarbon chain has a limited area of around  $\approx 18$  to  $21 \text{ \AA}^2$  when oriented vertically in the Langmuir film relative to the water surface.<sup>[64]</sup> Using the space-filling method, one can theoretically calculate the least area of molecules.<sup>[64]</sup> The  $\pi$ - $mmA$  isotherm, however, provides the limiting area value experimentally. Once the film collapses,  $\pi$  drops immediately, or a plateau typically high  $\pi$  in the  $\pi$ - $mmA$  isotherm appears. The film collapse usually occurs through the formation of multiple layers or vesicles<sup>[82]</sup> (Figure 6). The morphology of the collapsed film is very interesting, which includes folding, buckling, cracking, and wrinkling.

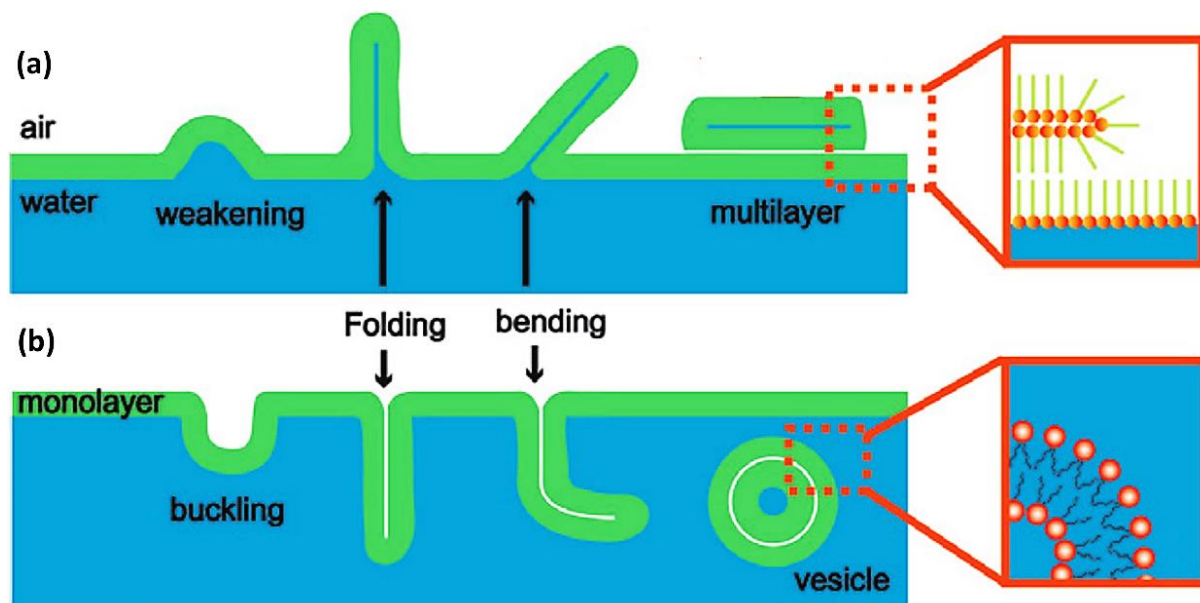


**Figure 6:** Langmuir film collapse mechanism of small amphiphilic molecules. The figure is adapted from the reference.<sup>[82]</sup>

It should be noted that Gibbs film is another type of monolayer, which is also formed by the adsorption process. This monolayer is an equilibrium system in which the solute concentration drives the film formation rather than the compression as seen in Langmuir film.<sup>[83]</sup> Instead of water-insoluble amphiphilic materials, compounds that are soluble in one phase (for example in water) are used. Surface pressure is recorded as a function of time to confirm the monolayer formation. The typical film formation process is that the material is 1<sup>st</sup> dissolved in the water subphase, and as time passes, molecules migrate from the water phase to the air-water interface. When this migration process reaches equilibrium, a plateau zone appears in the surface pressure vs. time ( $\pi$ - $t$ ) diagram, indicating the formation of a Gibbs monolayer.<sup>[84]</sup>



## 1.4 Behavior of amphiphilic polymers on the water surface of a Langmuir trough

Small amphiphilic molecules were used for most of the early work on Langmuir and LB films. Except for the discovery of ordered films with various morphologies, these were not so attractive for industrial applications. Langmuir film fabrication was therefore extended to non-classical amphiphiles including polymers<sup>[85–87]</sup> and other classes of materials as summarized in several review articles.<sup>[75,88]</sup> Polymers that are amphiphilic and water-insoluble can form stable Langmuir films. The film formation varies significantly from small amphiphiles since the macromolecules can adopt different architectures (e.g., coils, pancakes, and helices) on the water surface due to their conformational flexibility.<sup>[74]</sup> The variation starts with the initial adsorption process. Once the amphiphiles of small molecules are spread, all hydrophilic parts anchor to the water surface, resulting in complete adsorption.<sup>[80]</sup> However, this is hardly possible for polymers due to their long-chain nature and different adsorption properties.<sup>[89]</sup>

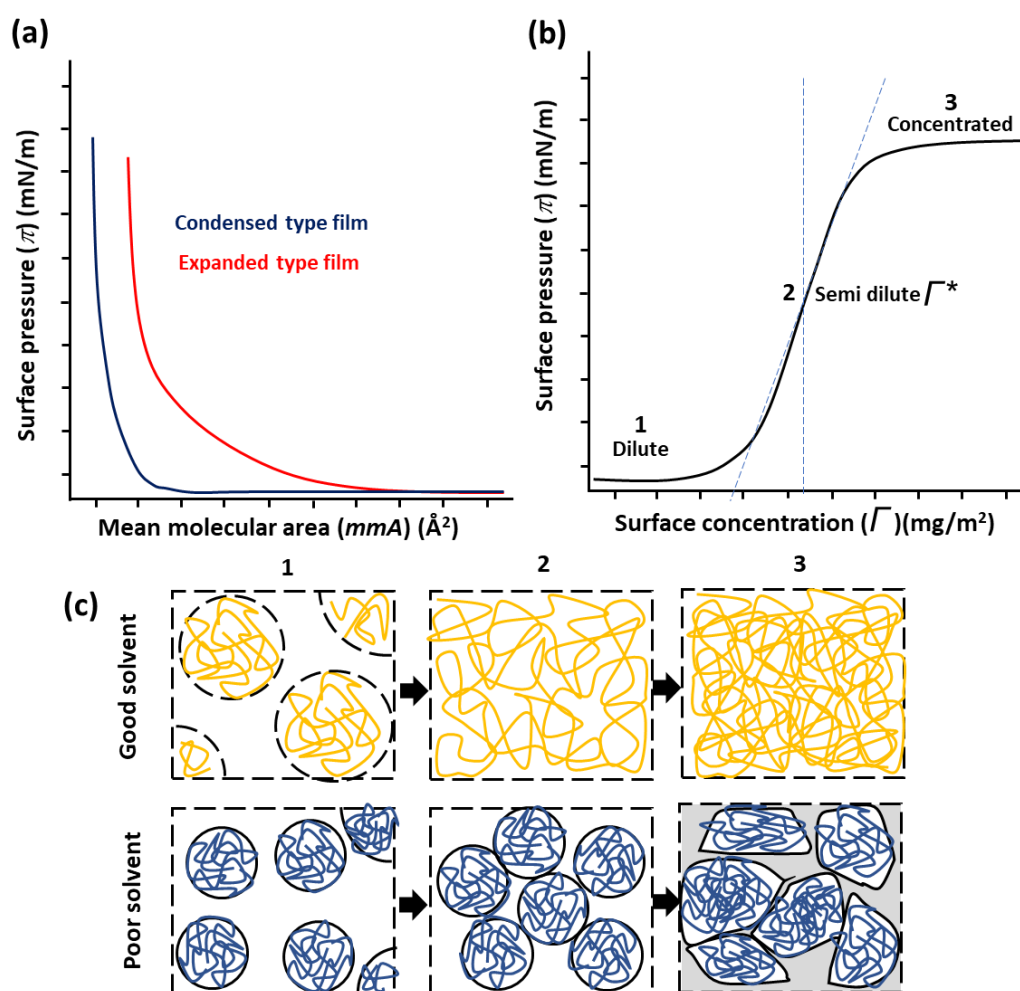


**Figure 7:** Schematic presentation of a typical (a)  $\pi$ - $mmA$ , (b)  $\pi$ - $\Gamma$  isotherm, and (c) the polymer chains on the water surface at different  $\Gamma$ . The figures are reconstructed from several references.<sup>[88,90]</sup>

The behavior of different amphiphilic polymers on the water surface can be studied by measuring  $\pi$ - $mmA$  isotherms (Figure 7a). Some polymers show an extended  $mmA$  in the isotherms with a gentle increase in  $\pi$  during compression (Figure 7a, red trace). These are expanded type films caused by strong interactions between polymer chains and the water surface.<sup>[85]</sup> However, stronger interactions between the polymer segments compared to the water surface result in condensed type films. In this case,  $\pi$  increases sharply at a small  $mmA$  value during compression (Figure 7a, blue trace).<sup>[85,86]</sup> The  $\pi$ - $mmA$  isotherm of polymers also shows a hysteresis behavior. This implies that the 1<sup>st</sup> compression isotherm does not match with the 2<sup>nd</sup> or higher-order isotherms. This happens due to the irreversible structure formation during the 1<sup>st</sup> compression. Another way of understanding the behavior of polymers on the water surface is the  $\pi$  vs. surface concentration ( $\Gamma$ ) ( $\pi$ - $\Gamma$ ) plot as shown in Figure 7b. Here, the change of  $\pi$  is monitored either by increasing polymer concentration while keeping the  $mmA$  constant<sup>[91]</sup> or reducing the trough area by barrier movement (e.g., compression).<sup>[88]</sup> Two types of behavior can be seen in such measurements.<sup>[92]</sup> For example, if the water surface acts like a good solvent, then at dilute  $\Gamma$ , polymer chains adopt an expanded structure (1). When the  $\Gamma$  increases to  $\Gamma^*$  (overlapping concentration), interpenetration of the chains happens, resulting in a semi-dilute system (2). Above this  $\Gamma^*$ ,  $\pi$  saturates and a concentrated film is generated (3) (Figure 7c, image: good solvent). The behavior is different when the water surface behaves like a poor solvent. At dilute  $\Gamma$ , polymer chains stay partially collapsed on the water surface (1). No chain interpenetration occurs upon increasing  $\Gamma$  to  $\Gamma^*$  (2), rather than the deformation of the collapsed chains above  $\Gamma^*$  concentration (3) (Figure 7c, image: poor solvent).

Polymer Langmuir films also show structure formation immediately after spreading the polymer solution on the water surface. For instance, isotactic poly(methyl methacrylate) (i-PMMA)<sup>[23]</sup> and poly(D-lactide) (PDLA)/poly(L-lactide) (PLLA)<sup>[93]</sup> form helical conformations on the water surface and then crystallize during compression. Polymers can be copolymerized or grafted with different materials to create novel amphiphiles.<sup>[94-97]</sup> Unique phase transitions that are not present in small amphiphilic molecules can be seen. One interesting behavior observed in PEO-based block or grafted materials is the pancake to mushroom and then to brush transition.<sup>[95,98,99]</sup> It should also be noted that the Langmuir film formation of polymers is sometimes more difficult as compared to small amphiphiles. The success of film formation relies on the ability to spread polymer solution on the water surface. Sometimes, it is difficult to find suitable solvents for polymers as well as for other non-classical amphiphiles.<sup>[75]</sup> The aggregate formation is also an issue for polymer Langmuir films. The final problem is to

achieve uniform films on the solid support, particularly when the films may be too stiff for transfer. Despite these challenges, the interest in Langmuir/LB films is still growing considerably due to the possibility of generating mechanically robust films with a wide range of applications, especially in the production of devices and sensors.<sup>[100]</sup>

### **1.5 Crystallization of homopolymers on the water surface of a Langmuir trough**

The Langmuir technique utilizes the self-assembly process of molecules to create ultrathin films at the air-water interface. The films undergo several phase transitions including crystallization during compression and melting during expansion. Not all polymers can form a stable Langmuir film, which limits the crystallization studies at the air-water interface. Poly( $\epsilon$ -caprolactone) (PCL) is one of the most studied polymers that crystallizes on the water surface of a Langmuir trough during compression. The mechanism of crystallization has been discussed in detail elsewhere.<sup>[101–104]</sup> The crystallization was studied by spreading PCL on the water surface from chloroform solution and measuring the  $\pi$ - $mmA$  isotherm at isothermal condition upon compression after solvent evaporation (Figure 8, black color trace). Initially, the ester groups of PCL polymer adsorbed to the water surface, forming an amorphous 2D monolayer. During compression above a certain  $mmA$  value, some of the ester groups left the water surface, resulting in a 3D film. This process appeared as a plateau-like feature at  $\pi \approx 9$ -12 mN/m in the isotherm related to the formation of butterfly-like single crystallites as seen by Brewster angle microscopy (BAM) (Figure 8, image a). Interestingly, the crystallites disappeared when the barriers were moved to their original position (expansion). This phenomenon was denoted as a melting process. So, the crystallization only happens upon compression above a certain  $mmA$  value. The crystallization was found to be diffusion-controlled growth,<sup>[92]</sup> which is typical for thin film crystallization.<sup>[41]</sup> The crystallite size was influenced by the molar mass of PCL and the compression speed of the trough.<sup>[102]</sup> Large crystals were observed for low or intermediate molar mass due to the high mobility of the chains compared to the higher molar mass PCL. The higher compression speed also generated small crystals. Electron diffraction on the crystallites transferred to a solid support revealed a vertical chain orientation of PCL with respect to the solid support. Recently, some studies show that the chains in the crystallites are tilted with respect to the water surface.<sup>[90]</sup> In addition, the melting temperature of these crystallites was found to be higher than the bulk crystalline PCL.<sup>[105]</sup> Another polymer that can be crystallized on the Langmuir trough is PEO.<sup>[106]</sup> A concentrated aqueous salt solution instead of a water subphase was used. The  $\pi$ - $mmA$  isotherm of PEO showed a plateau-like feature at  $\approx 30$  mN/m

(Figure 8, red color trace). This plateau was assigned to the crystallization of PEO with the help of BAM. However, unlike PCL, crystallization in PEO was a very slow process that was initiated by several compression-expansion cycles and keeping the barriers constant at a certain surface pressure in the plateau region for some minutes to hours. BAM showed dendritic features of the crystallites on the aqueous salt solution (Figure 8, image b). Once the crystallites formed, they disappeared completely like PCL upon barrier expansion. This process is similar to that one can see in bulk when crystallites melt with increasing temperature. The crystallization of PEO was also confirmed directly on the aqueous salt surface of the Langmuir trough with the help of GI-WAXS.<sup>[107]</sup> Almost vertical chain orientation with respect to the subphase surface was found.

Other polymers which crystallized on the water surface are PDLA/PLLA<sup>[93,108,109]</sup> and i-PMMA<sup>[23]</sup>. A short description of their crystallization at the air-water interface is provided. PDLA/PLLA showed  $\pi$ -*mmA* isotherm with a plateau zone at a surface pressure of  $\approx 9$  mN/m (Figure 8, light blue color trace). A film-like feature can be seen by BAM without obvious morphological details (Figure 8, image c). Crystallization was confirmed by infrared reflection absorption spectroscopy (IRRAS) at the air-water surface<sup>[109]</sup> and atomic force microscopy (AFM) after transferring the films/crystallites to solid supports.<sup>[93]</sup> Different morphologies can be observed depending on the molar mass of the polymer.<sup>[93,109]</sup> A parallelly oriented fiber-like morphology was commonly found in low molar mass PDLA.<sup>[93]</sup> In the case of i-PMMA,  $\pi$ -*mmA* isotherm with a pseudo plateau at  $\approx 8$  mN/m was observed (Figure 8, green color trace). BAM could not reveal any structure formation in the plateau region of the  $\pi$ -*mmA* isotherm due to the limited resolution of the instrument. Crystallization was, therefore, confirmed by IRRAS at the air-water surface<sup>[90]</sup> as well as by AFM<sup>[23]</sup> in LB films. Lamellae or even the double helices parallel to the solid support were identified within the lamellae.<sup>[23,110]</sup> So, it is evident that PCL and PEO crystallize on the water surface, where the polymer chains in the crystallites remain vertical with respect to the subphase surface. The scenario is opposite for PDLA/PLLA and i-PMMA polymers, where the chains in the crystallites stay parallel to the water subphase or solid support surface. Different chain orientations on the water surface were explained based on the stiffness of the polymers. For instance, PDLA and i-PMMA, due to their chain stiffness, have a higher tendency to remain parallel to the water surface than flexible polymers like PCL.<sup>[110]</sup>

There are also some reports on the Langmuir/LB film formation of polymer blends.<sup>[103,111]</sup> The common blends are poly(styrene) (PS) with PCL,<sup>[103]</sup> PS with poly(methyl methacrylate)

(PMMA),<sup>[112]</sup> and *i*-PMMA mixed with syndiotactic poly(methyl methacrylate) (*s*-PMMA)<sup>[113]</sup>. Two common behaviors were found in such blend systems. A 1:2 mixture of *i*-PMMA and *s*-PMMA showed a  $\pi$ -*mmA* isotherm with a plateau region corresponding to the co-crystallization of the polymers.<sup>[113]</sup> The isotherm showed only one plateau region at a slightly lower  $\pi$  value compared to the isotherm of pure *i*-PMMA. Most interestingly, no phase separation was observed. A uniform film with evidence of helical strands made of both polymers (*i*- and *s*-PMMA) can be seen by AFM after transferring the film to a solid support above the plateau region of the  $\pi$ -*mmA* isotherm.

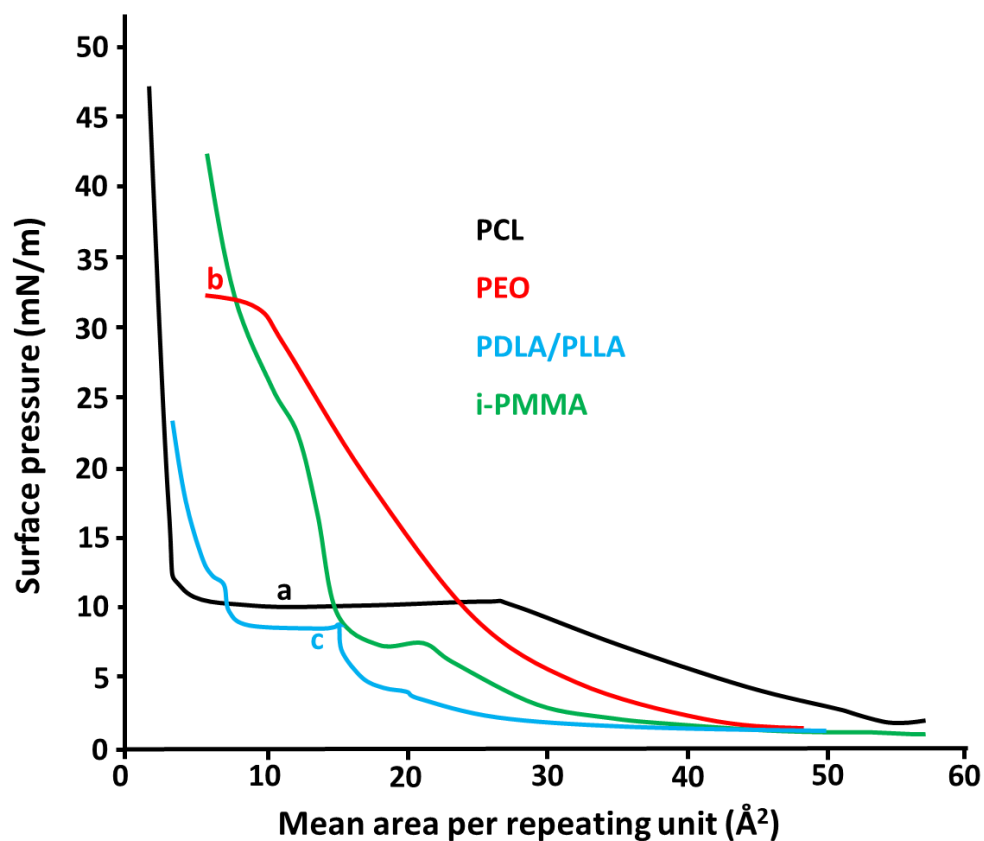


**Figure 8:**  $\pi$ -*mmA* isotherms of some homopolymers recorded on the water surface (PEO on aqueous salt solution surface) of a Langmuir trough (top) and BAM images taken at the plateau region of the isotherms as marked by letters (bottom). Isotherms and images are reconstructed using several references.<sup>[92,93,108,110]</sup>

In other types of blends, such as PCL/PS, depending on the ratio of the polymers, strong phase separation can be seen.<sup>[103,112]</sup> PCL/PS blend showed nucleation and crystal growth of PCL molecules in the plateau region of the isotherm when the PCL content is significantly high.<sup>[103]</sup> However, an entirely different behavior emerges, an isotherm with no plateau region and a small *mmA* value when the PS content was increased. Most interestingly, PCL crystallization was strongly inhibited. PS nanoaggregates in the liquid PCL film can only be seen by BAM. In short, phase separation occurred in Langmuir films of polymer blends when non-amphiphilic materials were blended with amphiphilic materials. In that case, hydrophobic nanoscale aggregates are the common features at the air-water interface. Crystallization can only be observed when the amphiphilic components of the blends reach a certain concentration.<sup>[103]</sup>

### **1.6 Structure formation of block copolymers on the water surface of a Langmuir trough**

Block copolymers are well known for their unique morphologies such as cubic, cylindrical, lamellar, and hexagonal in selective solvents, thin films, and bulk.<sup>[114,115]</sup> These are the microphase-separated structures formed by self-organization<sup>[116]</sup> and can be controlled by varying the lengths of the copolymer blocks, changing the nature of one of the blocks, and using the different preparation methods<sup>[117]</sup> including Langmuir trough. There are many publications on the structure formation of amphiphilic block copolymers at the air-water interface.<sup>[105,117]</sup> The majority of the reported block copolymers are diblock systems such as poly(ethylene oxide)-*b*-poly( $\epsilon$ -caprolactone), poly(styrene)-*b*-poly(ethylene oxide), poly(butadiene)-*b*-poly(ethylene oxide), poly(styrene)-*b*-poly(4-vinyl pyridine), poly(styrene)-*b*-poly(tert-butyl acrylate), poly(styrene)-*b*-poly(acrylic acid) and many more.<sup>[115,118–120]</sup> Some triblock,<sup>[95,121]</sup> pentablock,<sup>[122]</sup> and random<sup>[123]</sup> copolymers were also reported.  $\pi$ -*mmA* isotherms of diblock copolymers showed different regions related to various phase transitions and surface structures of the diblock copolymers at the air-water interface.<sup>[95,124]</sup> These structures are strongly influenced by the ratio of the hydrophobic/hydrophilic contents of the block copolymers, spreading solvents, and compression states.<sup>[115]</sup> At low surface pressure/compression, PEO-based diblock copolymers formed monolayers just like the PEO homopolymer.<sup>[115,125]</sup> However, surface micellization was reported for poly(styrene)-based block copolymers under the same conditions.<sup>[126,127]</sup> Other structures, such as planar-aggregates, strands or ribbons, and nanodots or circular micelles, can also be observed depending on the compression states of the block copolymers (at different *mmA* values) (Figure 9).<sup>[115,127,128]</sup> Now concerning crystallization, the majority of the studies were done in bulk, solutions, or thin films as

summarized in the review article.<sup>[129]</sup> Only a few studies have been published on the crystallization of block copolymers at the air-water interface. Crystallization can be seen in PEO-*b*-PCL diblock copolymer.<sup>[105,119]</sup> The  $\pi$ -*mmA* isotherm showed a plateau region at above  $\approx 15$  mN/m depending upon PCL content of the block copolymer. Crystallization occurred only in PCL block at the plateau region of the isotherm. PEO, on the other hand, immersed in the subphase and stayed amorphous.<sup>[119,130]</sup> Even after transferring the films onto a solid substrate, only PCL crystallites can be seen. Different crystallite morphologies such as spherulite, dendritic, and needle-like structures were found.<sup>[119,130]</sup> These structures were different compared to the crystallites of PCL homopolymer at the air-water interface.<sup>[101]</sup> This diverse structural variation is because crystallization in block copolymers is not only controlled by the parameters that define the crystallization in homopolymers (e.g., chemical structures, crystallization conditions) but also governed by the block lengths and amounts of the water soluble/insoluble blocks.<sup>[131,132]</sup> In most studies, amorphous hydrophobic polymers like poly(styrene) (PS) are block copolymerized with a hydrophilic PEO in order to introduce new types of amphiphiles. Unlike typical aggregates, no crystallization was observed for such diblock copolymers.<sup>[133–135]</sup>

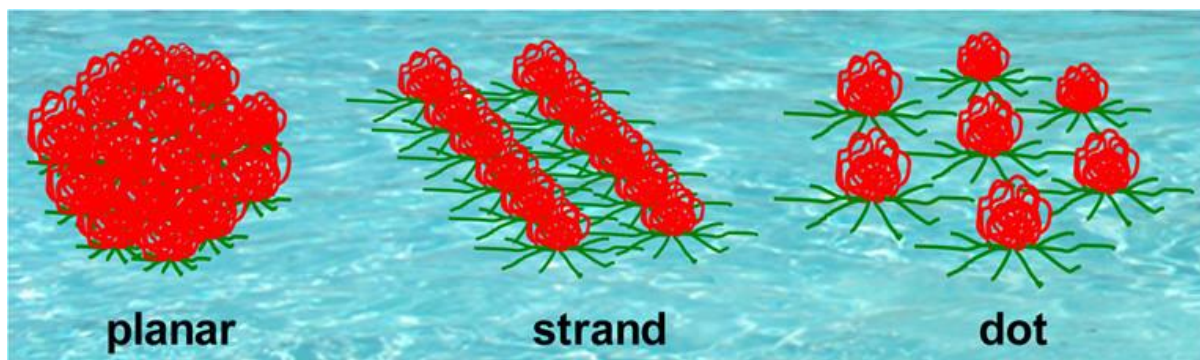


**Figure 9:** Common morphologies of diblock copolymers during Langmuir film formation as illustrated schematically. Red and green colors indicate the hydrophobic and hydrophilic blocks of diblock copolymers, respectively. The figure is adapted from the reference.<sup>[115]</sup>

## 1.7 Motivation, aim, and outline of the Thesis

So far, the limited number of suitable polymers is a major issue in Langmuir monolayer and LB film fabrication. Polymers must have a polar group in the repeating unit in order to prevent immediate collapse of the molecules on the water surface and they should also be water-insoluble.<sup>[85,86]</sup> Some polymers such as PCL, PDLA/PLLA, and i-PMMA meet the requirements and are used in Langmuir film fabrication.<sup>[23,93,101]</sup> Poly(ethylene) (PE), one of the simplest polymers with many industrial applications, is not suitable for Langmuir studies. Thin film research of PE on the water surface was reported, but the crystallization was unsuccessful.<sup>[136]</sup> When PE spread on the water surface, 3D aggregates were formed rather than a monolayer film. This is due to the lack of a polar group per repeating unit of the polymer. Polar groups can be introduced in various ways including surface modification or polymerization.<sup>[137,138]</sup> Some approaches result in highly branched PE with randomly dispersed polar groups in the polymer backbone or side chains with large polydispersities. Acyclic diene metathesis (ADMET) polymerization allows synthesizing of linear PE-like materials with polar groups (e.g., halogens, acetyls, and esters) in the polymer backbone with moderate polydispersities.<sup>[139]</sup> These polymers are commonly known as precision or ADMET PE and the groups in the polymer backbone can also be considered as chain defects. They contain precisely separated polar groups in the backbone of the polymer. Crystallizing them in bulk, solvent-cast films, and melt-grown domains have previously been reported.<sup>[139]</sup> Precision PE is very similar to conventional PE materials. This motivated us to study the polymer at the air-water interface. The polymers used are poly(ethylene)s (PEs) with various phosphoester group defects at the 21<sup>st</sup> position of the methylene backbone (main chain), referred to as Phenoxy- and Ethoxy- PPE (polyphosphoester).<sup>[140,141]</sup> Methyl-PPE-*co*-decadiene, another type of PE, has phosphoester defects at every 21<sup>st</sup> or 29<sup>th</sup> position of the backbone.<sup>[142]</sup> The first aim of this Thesis is to understand the Langmuir film formation of these precision PEs and then their crystallization behavior at the air-water interface. A Langmuir trough is therefore employed since it provides the air-water interface necessary for the studies. The films are fabricated by spreading the polymer solutions on the water surface of a Langmuir trough and compressing them by moving the barriers after solvent evaporation.<sup>[142]</sup> Several  $\pi$ -*m*mA isotherms are measured to understand the film formation. The morphologies of the films/crystals are explored by real-time monitoring with BAM and epifluorescence microscopy (EFM). IRRAS is used to confirm the phase transitions of the films at different compression states of the  $\pi$ -*m*mA isotherms. AFM is used to reveal film morphologies and thicknesses. Grazing incidence wide-angle X-ray scattering (GI-



WAXS) is employed to identify the crystal structure and chain orientation of the crystallites relative to the solid support. The basic working principle of these tools (e.g., BAM, AFM, GI-WAXS) is briefly described in chapter 2. In the papers I and II of chapter 3, the results of PEs crystallization at the air-water interface are presented. This includes a detailed discussion on  $\pi$ -*mma* isotherms, starting of crystallization, crystallites growth, crystallite morphologies, transferring of the crystallites by the LB method, thickness measurements, and finally, estimating chain orientations relative to the solid support.

Poly( $\epsilon$ -caprolactone) (PCL) can form a stable Langmuir film and crystallize with butterfly-like domains formation at the plateau region (9-12 mN/m) of the  $\pi$ -*mma* isotherm.<sup>[101]</sup> The majority of the studies used BAM experiments to confirm the crystallization on the water surface and some used electron diffraction after transferring the films to a solid support.<sup>[101]</sup> However, the chain orientation of PCL in the crystallites at various compression states of the  $\pi$ -*mma* remains unexplored. This Thesis explores the chain orientations of PCL crystallites directly on the water surface at different compression states using two sophisticated tools such as GI-WAXS and IRRAS. The chain orientation is also measured after transferring the crystallites from the water surface to the solid support by GI-WAXS. Paper III in chapter 3 contains these results.

As previously stated, extensive research has been conducted on Langmuir film formation of poly(ethylene glycol) (PEG) based amphiphilic block copolymers at the air-water interface.<sup>[90,143]</sup> This is because they have distinct interfacial properties than PEG homopolymer. The previous focus was on organic-organic block copolymers with different lengths of hydrophilic and hydrophobic blocks.<sup>[144]</sup> The behavior of organic-inorganic hybrid amphiphilic block copolymers has received less attention. An example of such system is a diblock copolymer of PEG with inorganic polyhedral oligomeric silsesquioxane containing methacrylate (MA-POSS). The block copolymers can form rigid Langmuir films with different interesting morphologies. The second aim of this Thesis is to understand the Langmuir film formation along with the ordering behavior of a series of hybrid diblock copolymers made of PEG and MA-POSS. In all block copolymers, the PEG molar mass is kept at 5000 g/mol (113 repeat units) and the MA-POSS block is varied from 4000 to 21000 g/mol (4 to 21 repeat units) [PEG<sub>5k</sub>-*b*-P(MA-POSS)<sub>4 to 21</sub>]. Initially, several  $\pi$ -*mma* isotherms are measured to understand the film formation. Again, BAM and IRRAS are employed to observe the film morphologies and reveal the molecular ordering at different compression states of the  $\pi$ -*mma* isotherms. In order to better understand the film formation process, several LB films are made at different  $\pi$  values and investigated by AFM to see the film morphology and estimate the film thickness.

Among all the investigated diblock block copolymers, only PEG<sub>113</sub>-*b*-P(MA-POSS)<sub>21</sub> showed film fragments with sharp edges in the collapse state of the  $\pi$ -*m*mA isotherm. Several compression-expansion cycles are applied to the fragments and the morphological changes are monitored by EFM. The fragments are also transferred to solid supports to investigate the film morphology by AFM and the molecular ordering by GI-WAXS. All of the results are published and can be found in papers IV and V of chapter 3.

Finally, in chapter 4, the findings are summarized and a general conclusion is provided along with a future outline of the crystallization or structure formation of homopolymers and hybrid diblock copolymers at the air-water interface of a Langmuir trough.

## 2 Experimental methods

The methods used in this Thesis were already presented in the material and method section of each paper in chapter 3. This chapter will therefore only cover the basic working principle of the instruments used. The Langmuir trough as the main technique employed to crystallize the polymers on the water surface is described in detail. The other complementary techniques such as BAM, EFM, and IRRAS utilized to monitor the film morphology and crystallization progress are briefly reviewed. The trough is equipped with a LB transfer unit, which is also addressed. Finally, AFM and GI-WAXS techniques used to assess the thickness and crystallite orientation relative to the substrate surface are shortly described.

### 2.1 Langmuir trough and Langmuir-Blodgett (LB) transfer

The Langmuir trough depicted in Figure 3 is mainly a rectangular trough made of Teflon. It holds a liquid called “subphase”. Water is mostly used as a subphase due to its non-miscibility with amphiphiles and high surface tension.<sup>[65]</sup> Buffer solutions, solvent mixtures, and aqueous salt solutions can also be used as subphases.<sup>[64,65]</sup> Other parts of the trough are two moveable symmetrical barriers (can also be one barrier) and a surface pressure Wilhelmy sensor. The surface pressure is a 2D analog of 3D pressure of the ideal gas law expressed as follows,

$$\pi A = k_B T \quad (1)$$

where  $\pi$ ,  $A$ ,  $k_B$  and  $T$  are the surface pressure, the molecular area, the Boltzmann constant, and the absolute temperature, respectively.

$\pi$  is calculated from the difference between the surface tension of pure water and the water surface covered by adsorbed molecules,

$$\pi = \gamma_0 - \gamma \quad (2)$$

where  $\pi$ ,  $\gamma_0$  and  $\gamma$  are the surface pressure, the surface tension of pure water (72.75 mN/m at 20 °C), and the surface tension of water with adsorbed molecules, respectively.

A Wilhelmy plate made of filter paper or platinum is used to measure  $\pi$ . The plate is partially immersed in water as depicted in Figure 10. The forces acting on the plate are gravity, surface tension, and buoyancy. The former two forces act downwards and the latter force acts upwards.

So the force balance equation can be expressed as follows,<sup>[145]</sup>

$$F_0 = F_{gravity} + F_{surface\ tension} - F_{buoyancy} \quad (3)$$

$$F_0 = \rho_M g l b d + 2\gamma_0 (b + d) \cos\theta - \rho_L g h b d \quad (4)$$

where  $F_0$  is the net downward force exerted by the pure water.  $\gamma_0$  and  $\theta$  are the surface tension of pure water and the contact angle of water on the Wilhelmy plate, respectively.  $\rho_M$ ,  $l$ ,  $b$  and  $d$  are the density, length, width, and thickness of the Wilhelmy plate, respectively.  $g$  is the gravitational constant. The immersion depth of the Wilhelmy plate is  $h$ , and the density of the subphase is  $\rho_L$ . The net downward force ( $F$ ) exerted by the adsorbed molecular film is,

$$F = \rho_M g l b d + 2\gamma (b + d) \cos\theta - \rho_L g h b d \quad (5)$$

If the liquid completely wets the plate, then  $\theta$  becomes zero (i.e.,  $\cos 0 = 1$ ). The thickness ( $d$ ) can also be ignored since it is much smaller than the width of the Wilhelmy plate. The surface pressure is then obtained by simply measuring the change of force acting on the plate with and without an adsorbed molecular film present at the surface from the following equations,<sup>[146]</sup>

$$F_0 - F = 2(\gamma_0 - \gamma)(b + d) \quad (6)$$

$$\pi = \gamma_0 - \gamma = \frac{F_0 - F}{2(b + d)} = \frac{F_0 - F}{2b} \quad (7)$$

Finally, a sensitive microbalance linked to the plate measures changes in mass to determine the force.

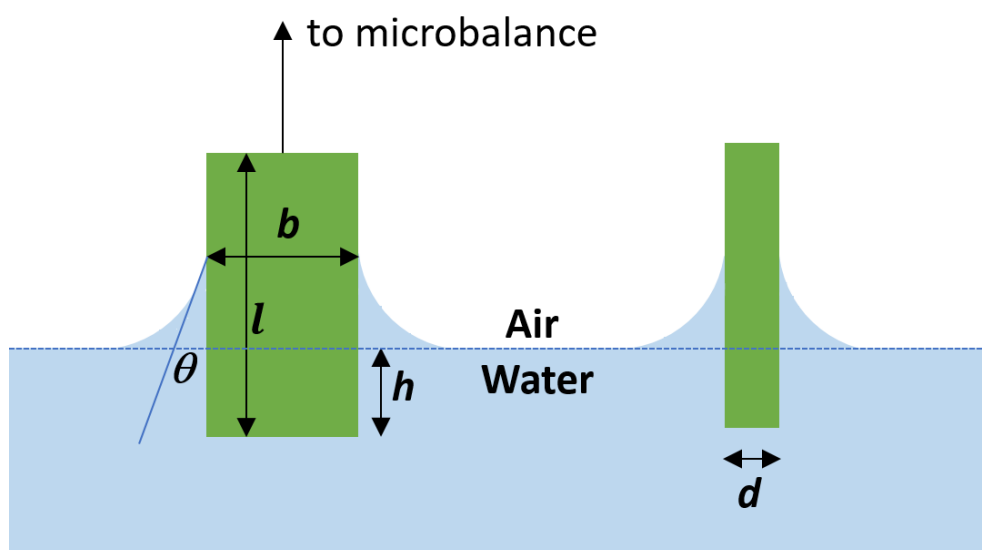


**Figure 10:** Front (left) and side (right) view of a Wilhelmy plate immersed in water.

As already mentioned, Langmuir films are prepared by spreading solutions of amphiphilic molecules from a volatile solvent up to a desired  $mmA$  value. The value is calculated by dividing the trough surface area between the barriers by the total number of molecules spread. This can be derived from the following relation,<sup>[146]</sup>

$$mmA[\text{\AA}^2] = \frac{M_n[\text{g mol}^{-1}] \times A_{\text{trough}}[\text{\AA}^2]}{V[\text{ml}] \times C[\text{g ml}^{-1}] \times N_A[\text{mol}^{-1}]} \quad (8)$$

where  $mmA$  is the mean molecular area.  $M_n$  is the number average molar mass of the polymer.  $A_{\text{trough}}$  is the trough area between the barriers.  $V$  and  $C$  are the volume and the concentration of the polymer solution spread at the air-water interface.  $N_A$  is Avogadro's constant.

When the solvent evaporates, polar heads of the amphiphiles due to electrostatic interactions anchor to the interfacial water molecules. The hydrophobic chains repulse the water surface and stay in the air. The film formation is now achieved by reducing the trough area by moving the barriers at a constant rate (e.g., compression at 1 cm<sup>2</sup>/min). During the compression,  $\pi$  is recorded at constant temperature and plotted as a function of  $mmA$  known as  $\pi$ - $mmA$  isotherm. The slope change in  $\pi$ - $mmA$  isotherm helps to identify the molecular phases in the Langmuir film. This change is sometimes not so obvious. A first-order derivative of the  $\pi$ - $mmA$  isotherm can therefore be taken into account, which shows maxima in the isotherm related to various phase transitions. Multiplying the  $mmA$  with the first-order derivative of  $\pi$ - $mmA$  gives the elastic modulus ( $\varepsilon_S$ ) and the inverse of it is called the compressibility modulus ( $C^{-1}$ ). Both of these terms help to understand the mechanical behavior of the films. For instance, while the film is liquid, it has high compressibility but low modulus. When the film changes to a solid-state, the modulus increases (i.e., the film becomes stiffer), but the compressibility decreases since the solid cannot be compressed more than a liquid. Note that the plot of modulus or compressibility possesses strong scattering of data points, which is typically reduced by data smoothing using an adjacent-averaging approach.

$$\varepsilon_S = C^{-1} = -mmA \left( \frac{\partial \pi}{\partial mmA} \right) \quad (9)$$

Where  $\varepsilon_S$ ,  $C^{-1}$ ,  $mmA$  and  $\frac{\partial \pi}{\partial mmA}$  are the elastic modulus, the compressibility modulus, the mean molecular area, and the 1<sup>st</sup> derivative of the  $\pi$ - $mmA$  isotherm, respectively.

So far, the  $\pi$ - $mmA$  isotherm measurements only provide initial information about the Langmuir monolayer. For example, the increase of  $\pi$  tells about the film formation, the  $mmA$  values give

rough hints of the molecular orientations in the film, and the plateaus in the isotherm depict a phase transition or film collapse. Besides, various experimental techniques are also used to reveal more details about film formation. The molecular-level interactions, chain orientations, and phases of the film at different compression states can be revealed by IRRAS or sum-frequency generation (SFG) spectroscopy.<sup>[75]</sup> The monolayer crystallization is studied by X-ray or neutron reflectometry. The electrical properties of the monolayer can be studied by surface potential and electrical conduction measurements.<sup>[75]</sup> Morphology and topography of the films are investigated by BAM and AFM. Some instruments can be used either directly or coupled with a Langmuir trough during film compression or after transferring the film to solid supports.<sup>[75]</sup> LB is the most commonly used technique for film transfer. The working principle is very simple such as a cleaned substrate (e.g., silicon wafer) is cut to the desired shape (e.g., circle or rectangle) and hooked vertically to the arm of the transfer unit. The substrate is immersed to a certain depth (some mm) into the subphase before spreading the solutions and a transfer pressure is set. After trough preparation (e.g., spreading polymer solution and solvent evaporation), the trough surface is then compressed. When the compression reaches the transfer pressure, the substrate is slowly pulled upward (e.g., 1 mm/min) by the transfer unit. As a result, the Langmuir films (or crystals) present on the water surface are transferred to both sides of the solid support.<sup>[64]</sup> The barriers of the trough move slowly (change in trough area) in order to maintain  $\pi$  constant during the film transfer experiment. This area change of the trough when divided by the substrate area (area dipped in the subphase) gives a value called transfer ratio (equation 10). Alternatively, the film transfer can also be done while keeping the  $mmA$  constant.

$$\tau = \frac{\Delta A_L}{A_S} \quad (10)$$

Where  $\tau$ ,  $\Delta A_L$  and  $A_S$  are the transfer ratio, the area change of the trough during the transfer process to keep  $\pi$  constant, and the substrate area dipped into the subphase, respectively.

$\tau \approx 1$  is considered an ideal homogeneous transfer. This indicates that the orientation of the molecules in the Langmuir film did not change during the transfer. Values outside 0.8-1.2 are related to a poor homogeneity of the transferred films.<sup>[65]</sup> Sometimes, negative  $\tau$  can also be seen that happens due to the removal of films from the substrate surface rather than transfer during multiple dipping process.  $\tau$  depends on many factors such as types of amphiphilic molecules, monolayer phases (gas or solid), dipping rate, subphase composition (pH), solid substrate qualities, and deposition surface pressure.<sup>[64]</sup>

Among them, solid substrates are described shortly here. Common substrates used in the LB transfer are silicon wafer, mica, glass, and graphite.<sup>[64]</sup> Substrates are usually chosen based on the desired purpose or characterization method. Mica, for example, is used for AFM, and glass is used for optical analysis. The type of substrates and dipping directions (e.g., up or downstroke) determine which part (e.g., hydrophilic or hydrophobic) of the amphiphilic molecules should link to the substrate during the transfer process. For example, polar head groups of the amphiphilic molecules adhere to the polar substrate. Figure 11 demonstrates the LB film preparation using two different ways. The substrate can also be dipped many times in the trough to create multiple layers. Generally, the LB technique is very popular since it can be used for homogeneous film deposition over a large substrate area, multi-layered film fabrication, and the possibility of using any solid supports. Another way of film transferring involves touching the film horizontally by the substrate and then pulling it upward. This was introduced by Vincent Schaefer from Langmuir's team at General Electric (GE) in the USA.<sup>[147]</sup> These films are known as Langmuir-Schaefer (LS) films.<sup>[64]</sup> This method becomes very effective when the Langmuir films are difficult to transfer by the LB method due to their stiffness.<sup>[75]</sup>

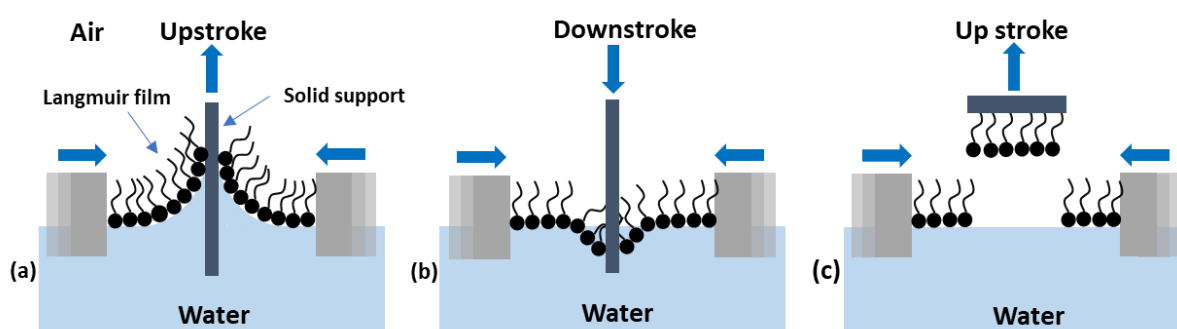


**Figure 11:** Schematic presentation of the Langmuir-Blodgett (LB) transfer of amphiphilic molecules using (a) upstroke, (b) downstroke, and (c) illustration of the Langmuir-Schaefer (LS) transfer method.

In addition to the characterization tools indicated above, molecular dynamics simulations were also utilized to investigate the structure and dynamics of the Langmuir monolayer.<sup>[148–150]</sup> The experimental results were also sometimes compared to the simulated data. Small amphiphiles (e.g., stearic acid) and their interactions with bioactive substances (e.g., proteins) were primarily simulated.<sup>[150,151]</sup> The findings include entire  $\pi$ - $m$ A isotherms, electron density profiles, and the distribution of gauche defects in the hydrophobic parts. Simulations revealed that the polar head groups should be anchored at the air-water interface, and the hydrophobic parts (e.g., methylene groups) should be completely out of the water. With increasing density, the hydrophobic parts were organized from a random state to an ordered structure.<sup>[150]</sup>

## 2.2 Brewster angle microscopy (BAM)

BAM uses an optical microscope that applies the reflectance properties of light to visualize Langmuir films in real-time. The morphologies, phase transitions, and domain/crystallite shapes of the Langmuir films can be seen. BAM is based on Brewster's law, which states that p-polarized light is completely refracted (i.e., no reflection) when guided to the liquid surface at the Brewster's angle ( $\theta_B$ ).<sup>[152]</sup> It was first introduced in 1991 by different research groups to examine Langmuir films of small amphiphiles on the water surface.<sup>[153,154]</sup> Figure 12 shows a setup of BAM coupled with a Langmuir trough. The p-polarized light (i.e., wave vector of the electric field is parallel to the plane of the incidence, denoted here as red arrows) is guided towards the water surface of a Langmuir trough at  $\theta_B$ . As expected, no light is reflected (i.e., all light is refracted) from the water surface, which results in zero contrast on the monitor<sup>[153,154]</sup> (Figure 12a). When the Langmuir film is formed during compression, it modifies Brewster's condition (i.e., changes in the local refractive index), which results in small amounts of light being reflected. A charge-coupled device (CCD) camera captures the optical signals and visualizes the film on the monitor (Figure 12b).

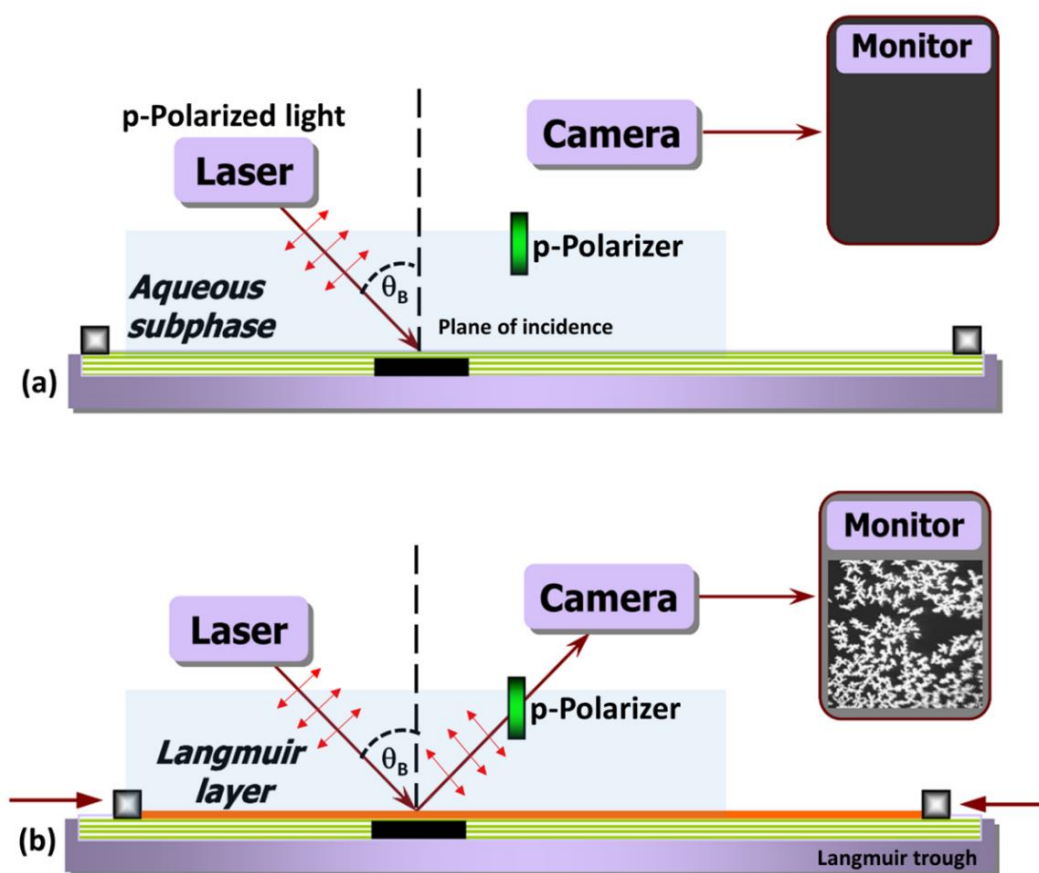


**Figure 12:** Schematic diagrams of a BAM coupled with a Langmuir trough (a) for the pure water surface and (b) a film-covered surface. The figure is reconstructed from reference.<sup>[92]</sup>



Snell's law can be used to calculate  $\theta_B$  using the following relation,

$$\theta_B = \arctan \frac{n_2}{n_1} \quad (11)$$

where  $\theta_B$ ,  $n_1$  and  $n_2$  are the Brewster angle, the refractive index of air, and water, respectively.  $n_1 = 1$  and  $n_2 = 1.333$ , which give a  $\theta_B$  of  $53.1^\circ$  for the water surface.

Since p-polarized light is refracted at Brewster angle, which is then scattered from the Teflon surface. This scattered light interferes with the signal coming from the Langmuir film. A reflective silicon wafer (black rectangular bar in Figure 12) is therefore placed on the Teflon surface to direct the scattering light out of the detector.<sup>[146]</sup> There are some advantages of using BAM, for example, it visualizes Langmuir films without using any dyes that would interfere with the film formation. A large surface area of the film can also be seen by BAM, which is very helpful in understanding the overall conditions (e.g., morphology) of the film on the water surface. However, there are also some limitations of BAM. Such as the reflectance of p-polarized light depends on film thickness, as a result, the contrast can only be seen when the film gains a certain thickness during compression.<sup>[152]</sup> Individual domains sometimes cannot be resolved well due to the limited lateral resolution of the microscope.<sup>[142]</sup>

### 2.3 Epifluorescence microscopy (EFM)

EFM is a particular form of optical microscopy that uses the fluorescence properties of molecules to generate images. EFM is frequently used to examine biological specimens.<sup>[155]</sup> Langmuir films of small amphiphiles<sup>[156]</sup> or polymers<sup>[142]</sup> can be monitored in real-time with better resolution than BAM. Figure 13 shows a possible setup of the microscope. A fluorophore (e.g., dye) is added to the subphase at a low concentration<sup>[142]</sup> or mixed with the spreading solution<sup>[157]</sup>, or even covalently attached to the amphiphiles<sup>[69]</sup> to enable surface imaging. Through an objective lens, high-intensity light of a particular wavelength is guided to excite the dye. The dye absorbs photons, which causes electrons to move to a higher energy state. The electrons, later on, lose energy and return to their ground state upon emitting light with a longer wavelength. The emission is then collected through the same objective lens and separated from its original excitation light with a combination of filter sets. Finally, a magnified image of the film under examination can be seen. Since the microscope uses the same objective lens to excite the dye and collect the emitted light, it is called epifluorescence, the Greek word “epi” means “same”. Details on the absorption and emission mechanisms of different fluorophores can be found elsewhere.<sup>[155]</sup>

During the film formation, the dye molecules are either absorbed or excluded from the Langmuir films compared to the subphase. This fluctuation in dye concentration generates bright-dark contrast, which allows to distinguish e.g., crystalline or amorphous phases of the Langmuir film. For example, the subphase and amorphous films can initially have the same contrast (e.g., bright). When the crystallites form in Langmuir films during compression, dye molecules are excluded from these domains, which results in dark contrast.<sup>[142]</sup> Obviously, dark contrast can also be caused by dye quenching (e.g., losing fluorescent properties due to high dye concentration).<sup>[158]</sup> It should be noted that the bright or dark contrast depends on the dye's nature. Some dyes only show contrast when interacting with any molecules present in the subphase. In that case, the subphase initially appears dark (e.g., Bis-ANS dye), and when the Langmuir films form, the contrast changes to bright color. The main advantage of EFM is the possibility to use objective lenses (e.g., 50x) with high magnifications to resolve the crystallites with better resolution.<sup>[142]</sup> However, the dye molecules can act like impurities and affect the isotherms as well as the morphology of the crystallites. The subphase purity must be checked and the isotherm recorded with and without the dye subphase should be compared. Sometimes stiffer Langmuir films cover the subphase, resulting in poor contrast. Therefore, partially soluble dyes in both phases (e.g., subphase and film phase) give a better imaging environment.

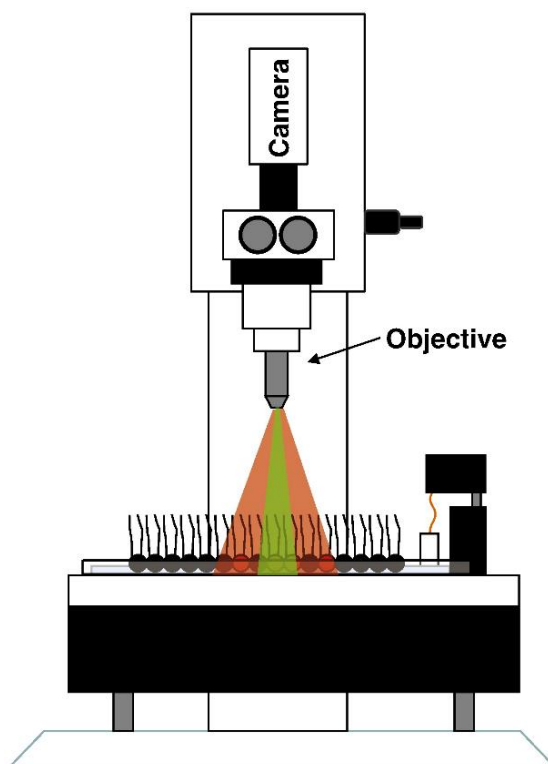


**Figure 13:** Illustration of an epifluorescence microscope coupled with a Langmuir trough. The figure is adapted from the reference.<sup>[159]</sup>

## 2.4 Infrared reflection absorption spectroscopy (IRRAS)

IRRAS is a surface-sensitive infrared (IR) spectroscopy technique that allows to investigate adsorbed molecules or thin layers present on a surface.<sup>[160]</sup> This technique provides information on the chemical composition, conformation, and orientation of the adsorbed molecules. It was first introduced in 1966 to investigate organic layers on metallic surfaces.<sup>[161]</sup> IRRAS can also be coupled with a Langmuir trough to study the behavior of small amphiphilic molecules and polymers at different compression states of the  $\pi$ - $mmA$  isotherm.<sup>[162,163]</sup> Unlike typical IR spectroscopy, IRRAS is measured in the external reflection mode rather than transmission. A possible setup of the instrument is shown in Figure 14.

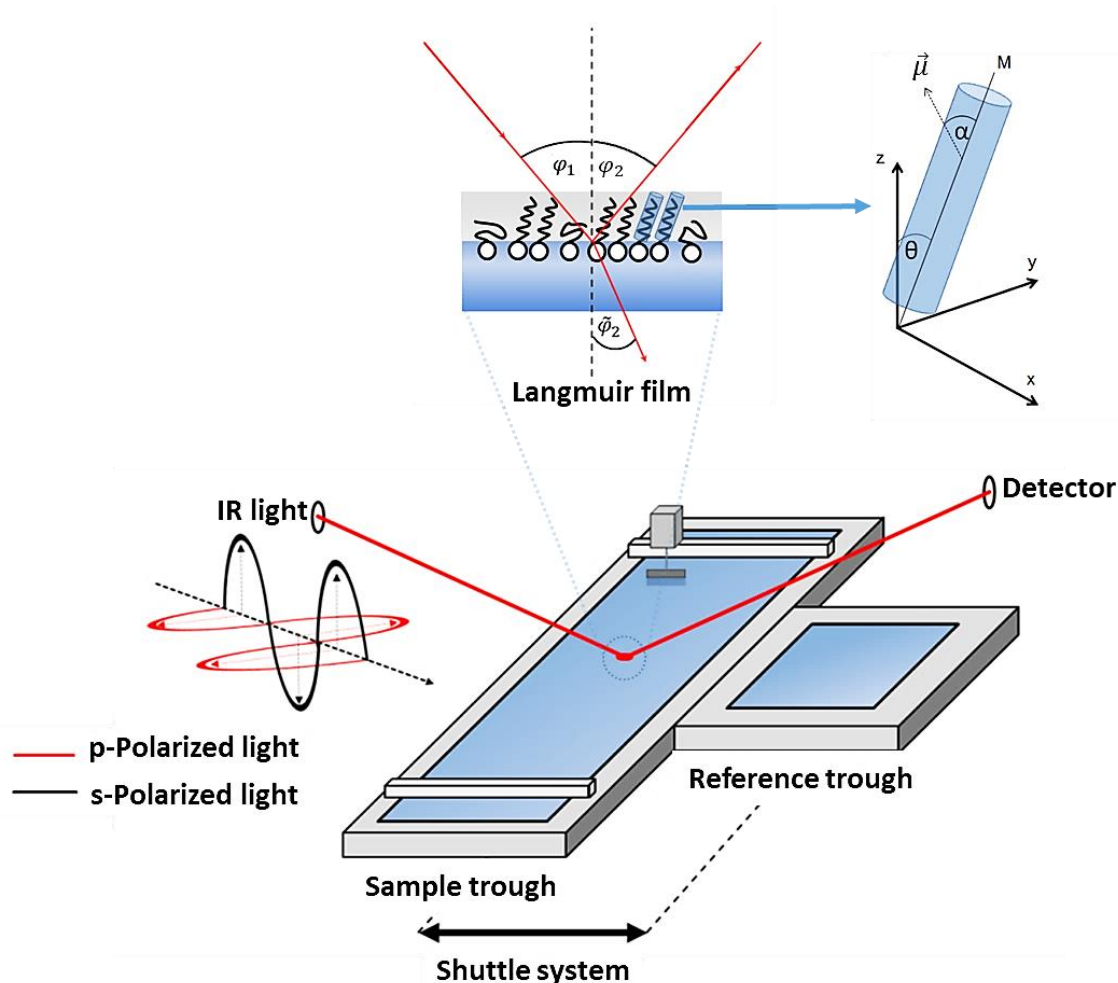


**Figure 14:** Illustration of an IRRAS setup with its working principle. The insets show a schematic drawing of the Langmuir film with molecular chains on the x, y, and z-axis.  $\varphi_1, \varphi_2$  and  $\tilde{\varphi}_2$  are the angles of incidence, reflection, and refraction of the IR light, respectively.  $\theta$  is the tilt angle relative to the surface normal z.  $\alpha$  is the angle between the molecular chain (M) and the transition dipole moment ( $\vec{\mu}$ ).<sup>[90]</sup>

First, polarized (s- and p-) IR light at a certain incidence angle, usually between 10° and 80°, is guided to the reference trough containing only pure water and then switched to the sample trough of Langmuir film with the help of a shuttle system. The reflected IR light is then detected and used to calculate the reflectance-absorbance (RA) spectra by the following relation,

$$RA = -\lg \frac{R}{R_0} \quad (12)$$

where  $R$  is the reflectivity of the film and  $R_0$  is the reflectivity of the pure water surface.

In the final IRRA spectra, the water vapor signal is eliminated by subtracting the reference spectra from the sample spectra. IRRA spectra contain information about phases, molecular orientation, and film thicknesses. The position of IRRA bands provides information about the film phases (e.g., liquid/solid).<sup>[164]</sup> The orientations of molecules in the films are calculated from the direction (e.g., positive or negative sign) and the intensity of the IRRA bands.<sup>[165]</sup> For example, at a given angle of incidence, IRRA bands become positive when the transition dipole moments (TDMs) of molecular vibrations are orientated preferentially perpendicular to the water surface. However, they change to negative bands when the TDMs are oriented parallel to the water surface.<sup>[90,166]</sup> The presence of intermediate TDMs results in a band with neighboring positive and negative components. This happens since the intensity of certain vibrational bands is enhanced or attenuated due to the direction of TDMs of molecules relative to the electric field vector of the IR light. An enhanced IRRA intensity is observed when both (e.g., TDMs and electric field vectors) stay in the same direction. Obviously, other factors such as incidence angle and polarization influence the sign as well as the intensity of the IRRA bands.<sup>[167]</sup> With the help of simulation, it is possible to generate theoretical spectra of a certain band.<sup>[168]</sup> The intensity of this band is then compared with the experimental IRRA spectra to calculate the average chain orientation with respect to the surface normal. A detailed discussion regarding the models to simulate IRRA spectra for a specific molecular vibration and fitting with experimental data to evaluate molecular orientations can be found elsewhere.<sup>[168]</sup>

## 2.5 Atomic force microscopy (AFM)

AFM is a powerful imaging tool for analyzing surfaces at high resolution.<sup>[169,170]</sup> The microscope can be used to examine the morphology and thickness of Langmuir films transferred to solid supports.<sup>[171]</sup> Figure 15 depicts the basic working setup of an AFM. A cantilever, typically made of silicon with a sharp tip at the end, either in contact or intermittent contact or even in non-contact with the sample surface, scans across the surface line by line at a constant tip-sample interaction. A feedback system controls the interaction force by maintaining a constant deflection or oscillation amplitude of the cantilever called setpoint. The position of the cantilever movement during the scan is followed by a laser beam and a photodetector system. When the cantilever experiences different roughness on the surface, it bends, or the oscillation amplitude changes. The feedback controller moves the piezoelectric scanner to keep the setpoint constant. Finally, the coordinates that an AFM tip tracks during the scans are translated to a height image. This image contains height, roughness, and topography information of the surface. Other common types of imaging that can be done in AFM are phase by AC mode and modulus/adhesion/deformation by PeakForce mode.<sup>[172]</sup> When the cantilever scans the surface with up and down oscillations at a particular amplitude (intermittent contact mode), depending on the surface properties (e.g., elasticity/friction), different oscillation lags/leads (phase shifts) occur, which are then translated into a phase image. Some features of the surface that are not well resolved in the height image can be seen better in the phase image due to the enhanced contrast of the image.<sup>[23]</sup>

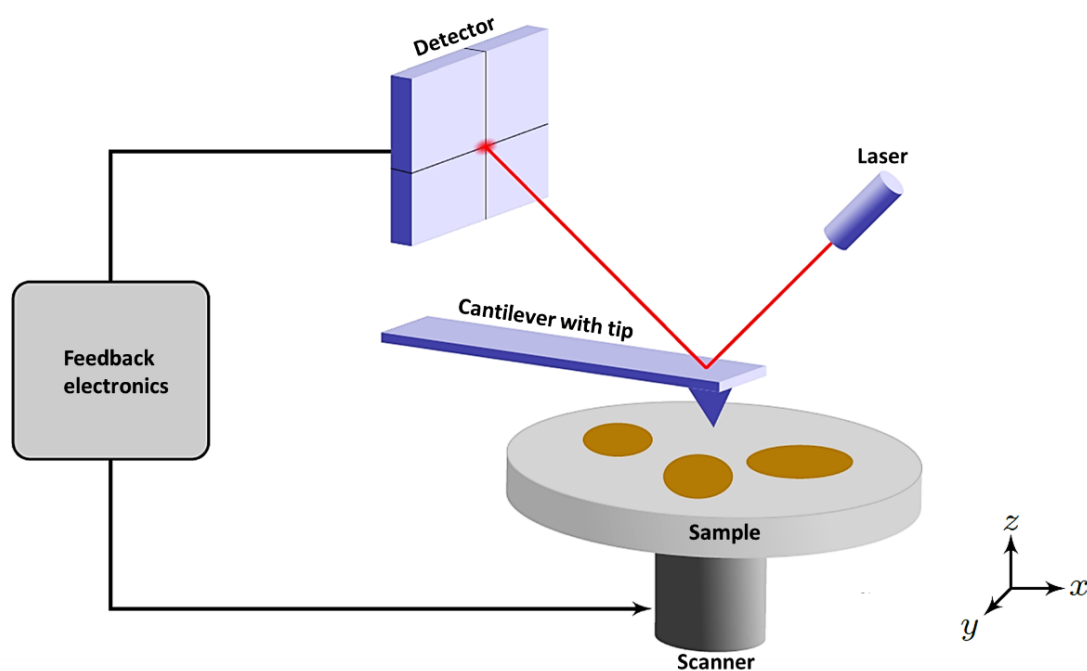


**Figure 15:** Schematic presentation of an AFM setup with the working principle.<sup>[50]</sup>

## 2.6 Grazing incidence wide-angle X-ray scattering (GI-WAXS)

GI-WAXS is an X-ray scattering technique for studying the crystallinity of surfaces and thin films.<sup>[173]</sup> Langmuir films can also be probed by GI-WAXS, either while the films are being compressed on the water surface of the Langmuir trough or after transferring to the solid supports. The measurement geometry of the GI-WAXS technique is depicted in Figure 16 (left). A coordinate system can be seen with the x-axis pointing to the X-ray beam, the y-axis parallel to the sample surface, and the z-axis along the surface normal. An X-ray beam impinges onto the Langmuir/LB film at a small angle  $\alpha_i$ , typically below  $1^\circ$  with respect to the xy plane, and is scattered at an angle  $\alpha_f$  and  $\psi$  relative to the xy and xz plane, respectively. This scattering intensity is collected with the help of a two-dimensional area detector (Figure 16, left). GI-WAXS measurements are performed at a constant incidence angle and detector position, which is different compared to a  $\theta$ - $2\theta$  geometry in regular WAXS measurements, where both the X-ray source and the detector move simultaneously along the angular range. Due to the fixed shallow  $\alpha_i$ , the method is called grazing incidence WAXS. So, the selection of  $\alpha_i$  is crucial. This should be slightly larger than the critical angle ( $\alpha_c$ ) for the total external reflection of the materials to probe only the sample surface. In the case of PCL thin films on the silicon substrate, the  $\alpha_i$  is set between  $0.17$  to  $0.2^\circ$  to get scattering only from the polymer since PCL has a  $\alpha_c$  of  $0.16^\circ$  and silicon has  $0.22^\circ$  with Cu  $K\alpha$  radiation.<sup>[50,174]</sup> Since the X-rays come at a grazing angle and illuminate a large area of the film, splitting occurs in reflections due to different crystallites to detector distances. The detected scattering image is converted to the reciprocal space of the sample coordinates as described in the result parts of the papers (I and III) in chapter 3. The GI-WAXS image contains a large amount of information including the lattice plane of the crystallites, their orientations relative to the surface, and the crystallite sizes. The former one is used to determine the crystal structure. The position of the Bragg reflections in the GI-WAXS image reveals the crystal orientation and the peak width helps to calculate crystal sizes by the Scherrer formalism.<sup>[107]</sup> Figure 16 (right) shows the position of the Bragg reflections with the expected orientations of the crystallites. The horizontal out-plane reflections (out of the scattering plane) at  $q_y$  appear when the crystallites are vertical to the substrate surface, and the vertical in-plane reflections at  $q_z$  occur when the lattice plane is parallel to the substrate (Figure 16 right, a). When both are present in the film, Bragg reflections appear along with the  $q_y$  and  $q_z$  directions (Figure 16 right, b). Broad Bragg peaks appear in the vertical direction due to the angular distribution of the crystallites (Figure 16 right, c). The isotropic distribution of the crystallites results in Debye Scherrer rings (Figure 16 right, d).

It should be noted that the GI-WAXS studies performed in this Thesis are mostly taken after transferring the Langmuir films or crystallites to a solid support, except for PCL, where both water and solid surfaces were used. All GI-WAXS measurements aim to confirm the crystallization of the polymers in the plateau region of the  $\pi$ -*m*m*A* isotherm and estimate the chain orientation in the crystallites or films relative to the water surface or solid support.

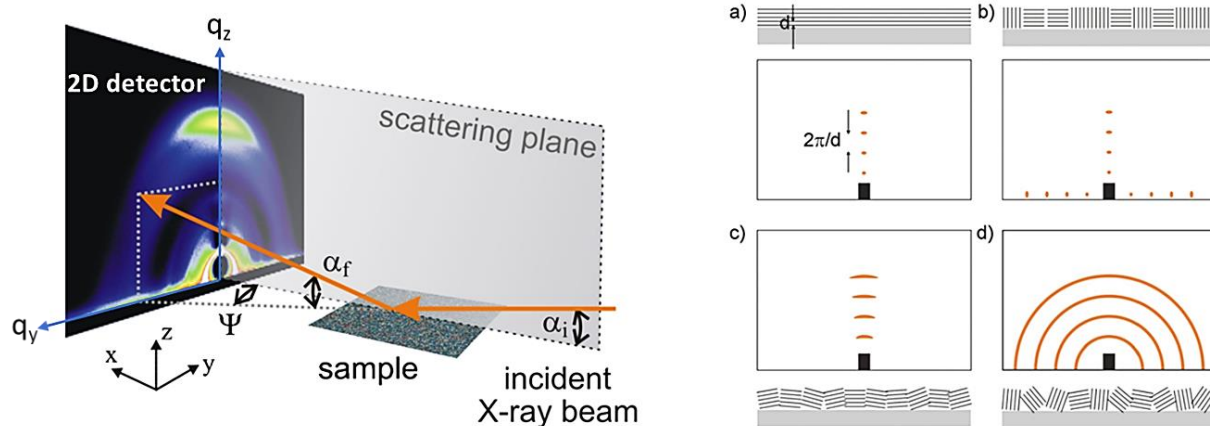


**Figure 16:** Schematic presentation of GI-WAXS setup with a 2D detector<sup>[175]</sup> (left) and the expected scattering patterns corresponding to the orientations of crystallites in thin films<sup>[173]</sup> (right).

### 3 Results

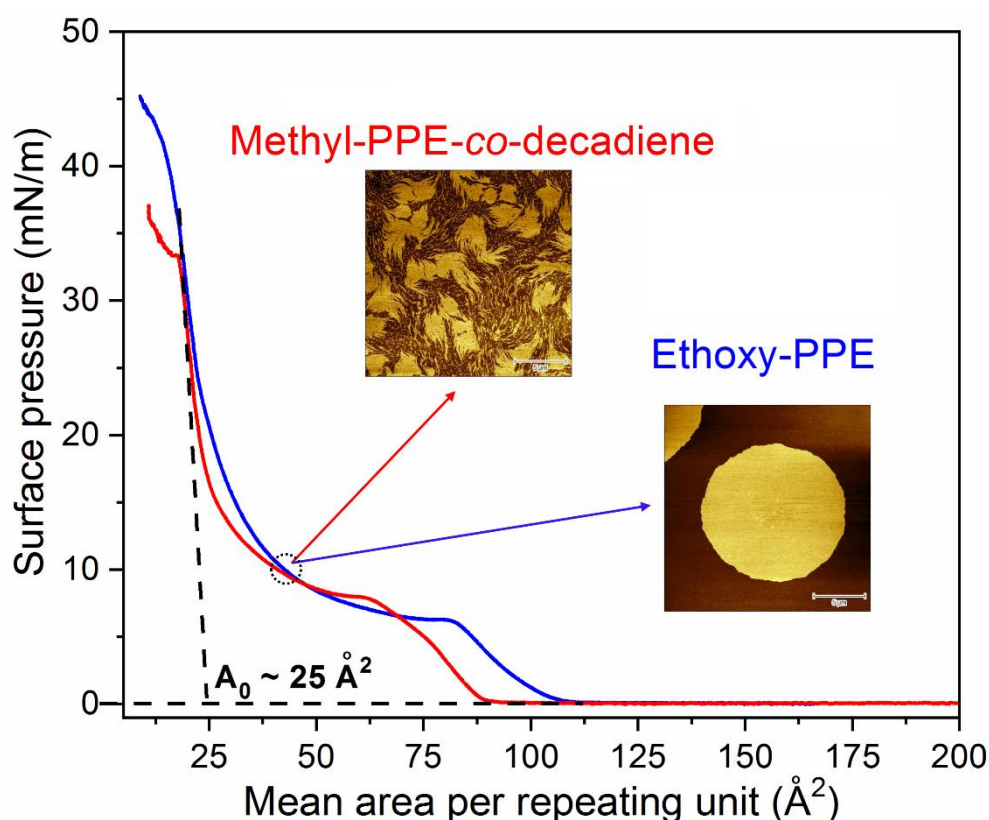
#### 3.1 Paper I

Crystallization of poly(ethylene)s with regular phosphoester defects studied at the air-water interface<sup>1</sup>

Nazmul Hasan, Karsten Busse, Tobias Haider, Frederik R. Wurm and Jörg Kressler

Polymers 2020, 12, 2408, <https://doi.org/10.3390/polym12102408>

Graphical abstract:



Poly(ethylene) (PE) cannot form stable Langmuir films<sup>[85]</sup> and is unable to crystallize at the air-water interface.<sup>[136]</sup> This is due to the lack of polar groups in the PE structure. Ethoxy-PPE or Methyl-PPE-co-decadiene is similar to PE, containing regular phosphoester polar groups (e.g., defects) in the methylene backbone, can be an alternative, as demonstrated in this publication. The Langmuir films were prepared by spreading the polymer solution on the water surface of a Langmuir trough and compressing them after solvent evaporation. Both Ethoxy-PPE and Methyl-PPE-co-decadiene crystallized with different morphologies during compression as characterized by  $\pi$ - $mmA$  isotherm measurements, BAM, and EFM. Crystallites were further investigated by AFM and GI-WAXS techniques after transferring them from the water surface



to the solid support. Different morphologies of the PPEs crystallites related to different crystal structures were confirmed.

The author contributions to the following article are: N. Hasan and J. Kressler designed the research. T. Haider and F. Wurm synthesized the polymers. N. Hasan performed the following experiments as Langmuir isotherms, LB transfer, BAM, EFM, AFM, FTIR, DSC, and WAXS. N. Hasan analyzed the data and wrote the draft manuscript. K. Busse did GI-WAXS experiments. N. Hasan, K. Busse, F. R. Wurm, and J. Kressler discussed the results, reviewed them, and finalized the paper.

---

<sup>1</sup>The following article [N. Hasan et al., *Polymers* 2020, 12, 2408] has been published under the terms of the Creative Commons Attributions 4.0 International License (CC BY 4.0) that permits unrestricted use, distribution, and reproduction in any medium under the specification of the author's name (Nazmul Hasan, Karsten Busse, Tobias Haider, Frederik R. Wurm, and Jörg Kressler) and the source (*Polymers*; <https://doi.org/10.3390/polym12102408>). The link to the article on the publisher's website is: <https://www.mdpi.com/2073-4360/12/10/2408>. Supporting information can be found at: <https://www.mdpi.com/2073-4360/12/10/2408/s1?version=1603108727>. No changes were made.

Article

# Crystallization of Poly(ethylene)s with Regular Phosphoester Defects Studied at the Air–Water Interface

Nazmul Hasan<sup>1</sup>, Karsten Busse<sup>1</sup>, Tobias Haider<sup>2</sup>, Frederik R. Wurm<sup>3</sup> and Jörg Kressler<sup>1,\*</sup> 

<sup>1</sup> Institute of Chemistry, Martin Luther University Halle-Wittenberg, D-06099 Halle, Germany; nazmul.hasan@chemie.uni-halle.de (N.H.); karsten.busse@chemie.uni-halle.de (K.B.)

<sup>2</sup> Max Planck Institute for Polymer Research, Ackermannweg 10, D-55128 Mainz, Germany; haider@mpip-mainz.mpg.de

<sup>3</sup> Sustainable Polymer Chemistry Group, MESA+ Institute for Nanotechnology, Faculty of Science and Technology, Universiteit Twente, P.O. Box 217, 7500 AE Enschede, The Netherlands; frederik.wurm@utwente.nl

\* Correspondence: joerg.kressler@chemie.uni-halle.de; Tel.: +49-345-552-5800

Received: 29 September 2020; Accepted: 16 October 2020; Published: 19 October 2020



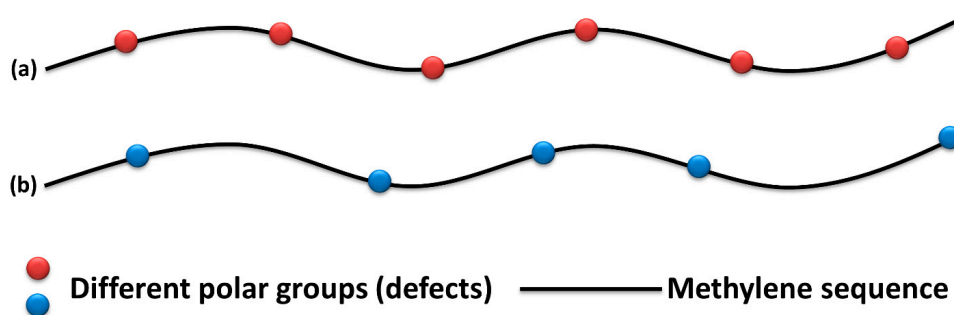
**Abstract:** Poly(ethylene) (PE) is a commonly used semi-crystalline polymer which, due to the lack of polar groups in the repeating unit, is not able to form Langmuir or Langmuir–Blodgett (LB) films. This problem can be solved using PEs with hydrophilic groups arranged at regular distances within the polymer backbone. With acyclic diene metathesis (ADMET) polymerization, a tool for precise addition of polar groups after a certain interval of methylene sequence is available. In this study, we demonstrate the formation of Langmuir/LB films from two different PEs with regular phosphoester groups, acting as crystallization defects in the main chain. After spreading the polymers from chloroform solution on the water surface of a Langmuir trough and solvent evaporation, the surface pressure is recorded during compression under isothermal condition. These  $\pi$ - $A$  isotherms, surface pressure  $\pi$  vs. mean area per repeat unit  $A$ , show a plateau zone at surface pressures of  $\sim$  (6 to 8) mN/m, attributed to the formation of crystalline domains of the PEs as confirmed by Brewster angle and epifluorescence microscopy. PE with ethoxy phosphoester defects (Ethoxy-PPE) forms circular shape domains, whereas Methyl-PPE-*co*-decadiene with methyl phosphoester defects and two different methylene sequences between the defects exhibits a film-like morphology. The domains/films are examined by atomic force microscopy after transferring them to a solid support. The thickness of the domains/films is found in the range from  $\sim$  (2.4 to 3.2) nm depending on the transfer pressure. A necessity of chain tilt in the crystalline domains is also confirmed. Grazing incidence X-ray scattering measurements in LB films show a single Bragg reflection at a scattering vector  $q_{xy}$  position of  $\sim$  15.1 nm<sup>-1</sup> known from crystalline PE samples.

**Keywords:** poly(ethylene); Langmuir–Blodgett film; crystallization; AFM and GI-WAXS

## 1. Introduction

Polymer crystallization in thin films has been studied with respect to basic research [1–8] and applications [9,10] for the last few decades. Various polymer properties change with film thickness compared to their bulk state influencing polymer crystallization as molecular mobility [11,12], glass transition temperature [3,13–18], and chain orientation [19,20]. Thin solid films are usually prepared by spin coating a polymer solution onto a solid substrate [11,21]. An alternative approach for the preparation of polymer thin films is spreading the polymer solution on aqueous surfaces of a Langmuir trough, followed by solvent evaporation [22,23]. These films are also known as Langmuir films [24]. Finally, Langmuir film compression yields various film thicknesses in the Å- to nm-range

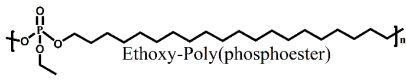
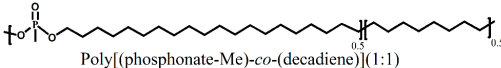
connected with different states of order. This method also provides the option to control crystallization kinetics by changing parameters of the Langmuir trough as the barrier compression–expansion speed and subphase temperature or even replacing the water subphase with aqueous salt solutions [25]. The formation of butterfly-like crystals of poly( $\epsilon$ -caprolactone) (PCL) [26] or dendritic morphology of poly(ethylene oxide) (PEO) [25] Langmuir films are notable. The Langmuir films can be transferred to solid supports using the Langmuir–Blodgett (LB) technique [24]. The LB films allow to study the surface morphology with high lateral resolution, e.g., by atomic force microscopy (AFM). The observation of the double helix of isotactic poly(methyl methacrylate) (i-PMMA) is one of the most impressive examples [27,28]. A major drawback for the preparation of Langmuir films and finally LB films is the limited number of suitable polymers [22,23]. They must contain a polar group in the repeating unit, which helps to anchor the polymer chain to the water surface to avoid immediate collapse [29]. Some polymers such as PCL, poly(L-lactic acid) (PLA), and i-PMMA fulfill this requirement with their ester groups and are used for the preparation of Langmuir or LB films [26,27,30,31]. However, Langmuir or LB film formation of poly(ethylene) (PE) was not successful and crystallization studies were not reported. Some thin film studies have been done using medium-density PE [32,33]. The issue regarding PE Langmuir/LB film formation is the lack of polar groups in the repeating unit. Different approaches are reported to introduce polar groups to PE such as surface modification of PE [34,35], copolymerization [36], and living polymerization [37]. Some approaches yield highly branched PEs with randomly distributed polar groups in the polymer backbone or side chain with high polydispersities [38]. Acyclic diene metathesis (ADMET) polymerization [39] allows to synthesize linear PE-like materials with polar groups (defects) in the polymer backbone (Scheme 1) with moderate polydispersities [40,41]. These polymers are called precision polymers [40,41]. Their crystallization behavior in bulk and solvent cast films or melt grown domains has already been reported in detail elsewhere [41,42]. The crystallization of such a polymer on the surface of water has been reported by our group. We reported the crystallization of a PE with a phosphoester defect in the main chain at every 21st position of the  $\text{CH}_2$  backbone (Phenoxy-PPE) at the air-water interface [43]. After spreading this polymer from the chloroform solution on the surface of water, some polymer chains immediately crystallize at  $\pi$  of 0 mN/m, but the final crystallization of most of the polymer chains occurs upon compression in the expanded plateau zone of the Langmuir isotherm ( $\pi \sim 4.5$  mN/m). Crystallization is monitored directly on the surface of water with Brewster angle microscopy (BAM) and epifluorescence microscopy. Single crystallites with hexagonal shape are observed. Most of the crystallites have a thickness of  $\sim 2.6$  nm with an elevated region in the center of the crystal measured in LB films [43].



**Scheme 1.** Schematic illustration of (a) Ethoxy-PPE and (b) Methyl-PPE-co-decadiene.

In this study, Langmuir films of different PEs namely Ethoxy-PPE and Methyl-PPE-co-decadiene (see Table 1) are prepared by spreading the polymer solutions on the water surface of a Langmuir trough and compressing them after solvent evaporation. The morphology of the films is monitored by BAM and epifluorescence microscopy during the compression. Finally, LB films are prepared by transferring the film from the water surface to a solid support to study the film thickness by atomic force microscopy (AFM) and crystallization by grazing incidence wide-angle X-ray scattering (GI-WAXS).

**Table 1.** List of the polymers under investigation with their chemical structure, short naming, and number average molar mass  $M_n$ .

Polymer Name and Chemical Structure	Abbreviated as	$M_n^*$ (g/mol)	$M_w/M_n^*$
 Ethoxy-Poly(phosphoester)	Ethoxy-PPE	9900	2.30
 Poly[(phosphonate-Me)-co-(decadiene)](1:1)	Methyl-PPE-co-decadiene	8500	2.08

\* Determined by gel permeation chromatography (GPC) (Tetrahydrofuran; THF, Poly(styrene); PS) standard).

## 2. Materials and Methods

### 2.1. Materials

PEs with regular phosphoester defects in the main chain under investigation are listed in Table 1. All polymers were synthesized by ADMET polymerization. Ethoxy-PPE has 20 CH<sub>2</sub> units in each repeat unit. Methyl-PPE-co-decadiene contains randomly (20 to 28) CH<sub>2</sub> units in every repeat unit since it is a (1:1) random copolymer obtained by copolymerization of an equimolar mixture of 1,9-decadiene and di(undec-10-en-1-yl) methylphosphonate. The synthesis of the Ethoxy-PPE is described elsewhere [42]. Characterization data for the Methyl-PPE-co-decadiene copolymer can be found in the supporting information (Figures S1–S3). All polymers are semi-crystalline in bulk and thin films, where only the methylene chains crystallize [41,42]. The DSC traces, the X-ray diffraction (XRD) patterns, and the FTIR spectra of the polymers can be found in Figures S4–S5 of the supporting information.

### 2.2. Langmuir Isotherms Measurement

The  $\pi$ -A isotherms were recorded using a Langmuir trough (Riegler & Kirstein GmbH, Potsdam, Germany) with a maximum trough area of 545 cm<sup>2</sup>. The trough was equipped with two moveable barriers and a Wilhelmy plate made of filter paper. The entire trough was covered by a Plexiglas box to maintain an equilibrium environment. Millipore water was used as a subphase for the experiment. The temperature of the subphase was kept at 20 °C using a thermostat. Before spreading the polymer solution, the purity of the subphase was checked by surface pressure measurement at maximum barrier compression ( $\pi < 0.15$  mN/m). Polymer solutions with a concentration of ~2 mg/mL were prepared in chloroform and spread dropwise in some random locations on the subphase using a Hamilton digital syringe. After a 20 min waiting time for complete solvent evaporation, the trough surface was compressed at a speed of 50 Å<sup>2</sup>/(molecule min) to record the pressure–area isotherm.

### 2.3. Microscopic Studies on Langmuir Films

To monitor the water surface during compression, a Brewster angle microscope (NFT Mini BAM, Nanofilm Technologies, Valley View, OH, USA) coupled with a Langmuir trough of 142 cm<sup>2</sup> was used. The lateral resolution of the microscopy was 20  $\mu$ m with a field view of 4.8  $\times$  6.4 mm<sup>2</sup>. The images were captured using the software WinTV (Hauppauge Inc, Hauppauge, NY, USA). The imaging of the Langmuir film was done at different surface pressures during the film compression at a rate of 50 Å<sup>2</sup>/(molecule min). Epifluorescence images were recorded with an Axio Scope A1 Vario epifluorescence microscope (Carl Zeiss MicroImaging, Jena, Germany). The microscope was equipped with an EC Epiplan-NEOFLUAR 50x objective and a Hamamatsu EM-CCD digital camera. A film balance (Riegler & Kirstein GmbH, Potsdam, Germany) with a maximum trough area of 258 cm<sup>2</sup> covered with a Plexiglas chamber was used. The temperature of the subphase was kept at 20 °C. To enable the experiment, the aqueous subphase contained 50 nM Rhodamine B fluorescence dye ([9-(2-carboxyphenyl)-6-diethylamino-3-xanthenylidene]-diethylammonium chloride). The dye was excited using a 100 W mercury arc lamp through a combination of BP 546/12 nm window and a beam

splitter FT 560 nm. The emission was detected via a BP 575–640 nm (filterset 20, Carl Zeiss AG, Jena, Germany). The imaging of the monolayer was done during the film compression with a speed of 50 Å<sup>2</sup>/(molecule min) at different surface pressures.

#### 2.4. Langmuir–Blodgett (LB) Film Transfer, AFM, and GI-WAXS

Silicon wafer with a size of 20 × 10 mm<sup>2</sup> was cleaned and mounted to a film transfer unit (KSV Instruments, Helsinki, Finland) to prepare LB films. The film was made at π of 10 mN/m and 15 mN/m, respectively. The substrate was attached vertically to the transfer unit and immersed into the subphase ~8 mm. The polymer solution was then spread on the water surface and compressed up to the transfer pressure. When the transfer pressure was reached, the submerged silicon substrate was moved upward at a speed of 0.5 mm/min, while the surface pressure was kept constant. This process transfers a film of the polymer on the substrate surface. The film was then dried at room temperature and stored in a sealed box for AFM and GI-WAXS measurements. AFM studies were carried out in AC mode by NanoWizard 4 (JPK, Berlin, Germany) instrument in air. A silicon cantilever with a spring constant of 40 N/m and a resonance frequency of 325 kHz was used. The captured images were then processed by JPK and Gwyddion software. A Retro-F SAXSLAB setup (SAXSLAB, Copenhagen, Denmark) equipped with an AXO microfocus X-ray source (AXO DRESDEN GmbH, Dresden, Germany) and a DECTRIS PILATUS3 R 300K detector (DECTRIS Ltd, Baden-Daettwil, Switzerland) was used to perform GI-WAXS measurements on the LB films of PEs. Figure 1 provides a schematic presentation of the setup used. Measurements were conducted at room temperature under vacuum condition in reflection mode. The incidence angle α<sub>i</sub> of CuKα radiation (λ = 1.5418 Å) was ~0.2°. The detector images were converted to sample coordinates according to Equation (1) and the condition n<sub>XR</sub> = cos(α<sub>c</sub>) cos(α<sub>i</sub>)1 with the critical angle α<sub>c</sub> [26].

$$\begin{pmatrix} q_x \\ q_y \\ q_z \end{pmatrix} = \frac{k_0}{n_{XR}} \begin{pmatrix} \cos \varphi_f \cos \alpha_f - n_{XR} \\ \frac{\sin \varphi_f \cos \alpha_f}{\sqrt{n_{XR}^2 - \cos^2 \alpha_f}} \\ \end{pmatrix} \quad (1)$$

where q<sub>x</sub>, q<sub>y</sub>, and q<sub>z</sub> are the scattering vector in x, y, and z coordinates, n<sub>XR</sub> is the refractive index, k<sub>0</sub> is the wavenumber, α<sub>f</sub> and φ<sub>f</sub> are the vertical and horizontal scattering angle, respectively.

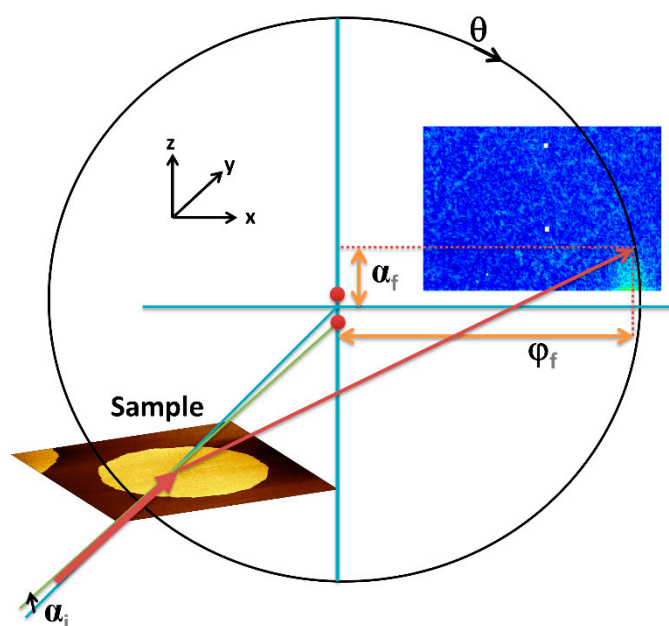
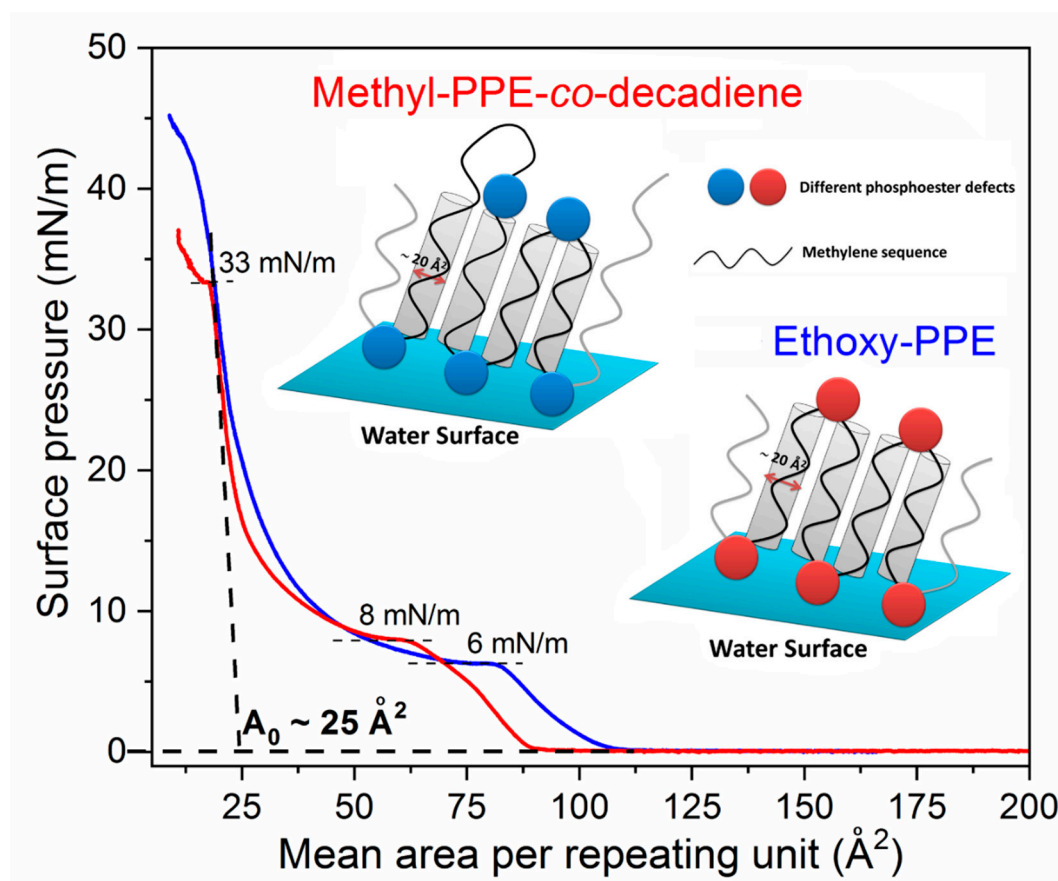


Figure 1. Sample geometry for GI-WAXS measurements.

The horizontal part of the scattering vector  $q$  is given with  $q_{xy} = \sqrt{q_x^2 + q_y^2}$ .

### 3. Results and Discussion

Figure 2 depicts the surface pressure vs. mean area per repeat unit ( $\pi$ - $A$ ) isotherms of two different PEs that are recorded after spreading the polymers from chloroform solution on the water subphase of a Langmuir trough to  $\pi = 0$  mN/m ( $A \sim 200 \text{ \AA}^2$ ) and compressing them with a rate of  $50 \text{ \AA}^2/(\text{molecule min})$  after solvent evaporation under isothermal condition.



**Figure 2.**  $\pi$ - $A$  isotherms of two different PEs measured at a subphase temperature of  $20 \text{ }^\circ\text{C}$  with a compression rate of  $50 \text{ \AA}^2/(\text{molecule min})$ . The insets show the possible chain orientation of the PEs at  $A_0$  position.

The isotherm of Ethoxy-PPE shows that with decreasing  $A$ , the  $\pi$  begins to increase from an  $A$  value of  $\sim 106 \text{ \AA}^2$ , followed by an extended plateau region at  $\sim 6$  mN/m and finally reaches  $\sim 45$  mN/m. The isotherm is slightly different for Methyl-PPE-co-decadiene, with an increase of  $\pi$  starting at  $\sim 90 \text{ \AA}^2$  and reaches finally a surface pressure of  $\sim 37$  mN/m. The plateau appears at a slightly higher pressure of  $\sim 8$  mN/m and a kink at a surface pressure of  $\sim 33$  mN/m. Thus, both PEs form Langmuir films where both PEs adopt different phases such as an amorphous film phase before the plateau and a crystalline solid phase after the plateau as already known from Phenoxy-PPE [43]. Therefore, the plateaus are obviously related to a 1st order phase transition from an amorphous phase to a crystalline state. Both plateaus end with a limiting area per repeating unit  $A_0$  of  $\sim 25 \text{ \AA}^2$ . This is calculated by drawing a tangent to the Langmuir isotherm after the crystallization plateau and extrapolation to zero surface pressure. The value is almost equal to the space required for a phosphate group ( $\sim 24 \text{ \AA}^2$ ) [44,45], but significantly larger than the area of a methylene sequence in zig-zag conformation ( $19 \text{ \AA}^2$ ) or in the rotator phase ( $21 \text{ \AA}^2$ ) [46]. Since the  $\text{CH}_2$  sequences are not sufficiently long for back folding,



more likely is a Langmuir monolayer formation for PEs where every second phosphoester defect is located on the water surface, while the hydrophobic methylene sequences (20–28 CH<sub>2</sub> units) avoid water contact in the air. They are aligned slightly tilted to the surface of the water as will be discussed in detail below. Every second phosphoester defect is placed at the polymer–air interface (see the insets of Figure 2). This orientation might be slightly different for Methyl-PPE-*co*-decadiene since the methylene sequences have a different length between the defects (see the insets of Figure 2). Finally, the area ratio of the methylene chain, e.g., at  $A_0 \sim 25 \text{ \AA}^2$ , in zig-zag conformation of  $19 \text{ \AA}^2$  or in the rotator phase of  $21 \text{ \AA}^2$ , gives an average tilt angle of  $37^\circ$  ( $\arccos 19 \text{ \AA}^2/25 \text{ \AA}^2$  or  $21 \text{ \AA}^2/25 \text{ \AA}^2$ ) with respect to the surface normal. Note that chain tilt is a very common phenomenon in Langmuir films and has been described extensively for polymers [26] and small molecules [47]. This can also be found in crystalline lamellae of oligomers [48] as well as polymers in bulk [49] and thin-films [50]. Chain tilt is typically caused by chain folding [49], the presence of defects in the main chain [48], or packing of end groups [48]. The chains in the polymer crystals reach a higher density than the amorphous chains due to the chain tilt. This has been confirmed for PE and discussed in detail elsewhere [49]. In the case of Langmuir films, a common reason for chain tilting is the packing of head groups. It is observed that molecules with bulky head groups often form tilted conformations of long alkyl chains in Langmuir films [51,52]. Here, the bulky head groups hinder the chain packing perfectly normal to the surface. Thus, the molecules must be tilted to preserve the close contact between the chains in crystallographic order [51]. Furthermore, chain tilting in Langmuir film depends on the compression state, e.g., PCL under various compressional conditions shows a chain tilt in the range of  $21^\circ$  to  $38^\circ$  [26]. Altogether, one can say that the observed limiting area values confirm the monolayer formation of these hydrophobic polymers with tilted methylene chains normal to the water surface and the polar chain defects which act as anchor groups to the water surface. In contrast, hydrophobic polymers show an extremely small limiting in the range of (0.2 to 2)  $\text{ \AA}^2$  [53], related to 3D film formation or aggregation [29,54].

Now, various microscopic techniques will be used to observe the film morphology of the PEs on the water surface. Figure 3 shows BAM images of the Langmuir film of PEs captured during the compression.

No morphological features are observed before reaching the plateaus of the Langmuir isotherms of both PEs, indicating a homogeneous film formation within the lateral resolution of the BAM equipment (Figure 3a, b, left-side images). When the plateau region is reached during the compression, the Ethoxy-PPE shows many bright domains (Figure 3a, right-side image). These domains are separated from each other, indicating a two-phase system with the solid tiny domains surrounded by the thin liquid film. For Methyl-PPE-*co*-decadiene sample, no domain formation is observed before and after the plateau region is reached (Figure 3b images), even compressing the film up to its collapse phase at  $\pi$  of  $\sim 33 \text{ mN/m}$ . The kink at  $\sim 33 \text{ mN/m}$  of this polymer is assigned to film collapse by BAM (see Figure S6 of supporting information). Note that domains formation in Langmuir experiments for semi-crystalline polymers is typically related to crystallization [43,54] and can be resolved by BAM, e.g., butterfly-like crystals of PCL [54]. In our case, the domains are too small to identify their exact morphology by BAM (Figure 3a, right-side image). Thus, epifluorescence microscope with the magnification of 40 times compared to BAM is employed for further investigations. A 50 nM aqueous solution of Rhodamine-B dye was used as subphase. Here, initially a bright contrast was observed from the dye subphase, but a dark contrast was generated when the domains appear upon compression. This is due to the exclusion of the dye from domains caused by crystallization [55–58]. Note that the dye molecules are just like an impurity in the subphase, which might influence the  $\pi$ - $A$  isotherms or even the domain morphology [55–58]. In our case, no influence of the dye subphase on the  $\pi$ - $A$  isotherm was detected (supporting information Figure S7).

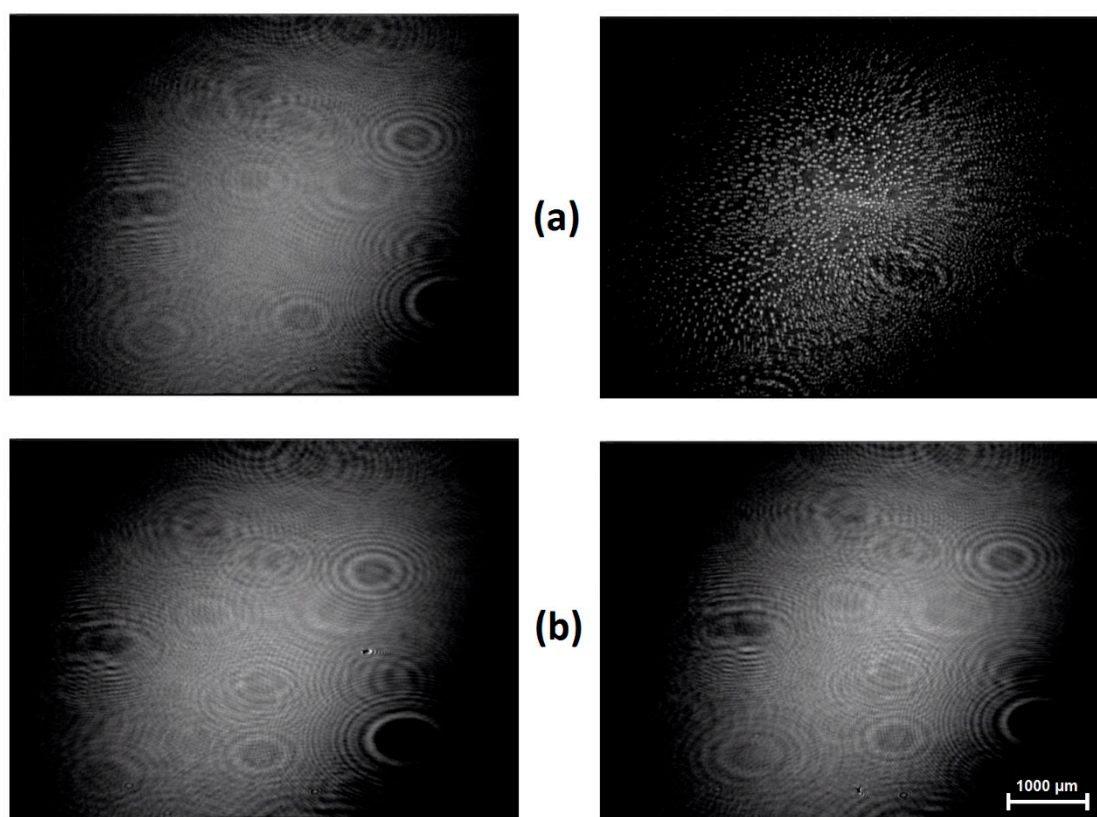


**Figure 3.** Brewster angle microscopy (BAM) images of (a) Ethoxy-PPE at  $\pi$  of 2 mN/m,  $A \sim 96 \text{ \AA}^2$  (left) and 7 mN/m,  $A \sim 63 \text{ \AA}^2$  (right), and (b) Methyl-PPE-*co*-decadiene at  $\pi$  of 2 mN/m,  $A \sim 84 \text{ \AA}^2$  (left) and 9 mN/m,  $A \sim 47 \text{ \AA}^2$  (right). All images were captured with a compression rate of  $50 \text{ \AA}^2/(\text{molecule min})$ . The image size is  $4.8 \times 6.4 \text{ mm}^2$ .

Figure 4 shows epifluorescence images of the PEs recorded on the dye subphase at two different compression states. These images resolve the morphology of the domains formed at the plateau zone and simultaneously indicate some tiny pre-domain formation before reaching the plateau region of the Langmuir isotherms. We observe some dark spots (Figure 4a,b, left-side images) after spreading the polymers solution on the dye subphase, solvent evaporation, and compressing them to initial increase of the surface pressure at 2 mN/m. For the Methyl-PPE-*co*-decadiene sample, the number of spots is larger and more clearly visible compared to Ethoxy-PPE. Note that the dark contrast of the domain is typically related to crystallization caused by the dye exclusion [43,55–58]. Thus, some crystallization may occur for both PEs immediately after spreading the polymer solutions and solvent evaporation. This behavior has also been observed for arachidic acid (C20 compound) [59]. In our case, we cannot confirm crystallization at this compression state by GI-WAXS experiment since this method is not sensitive enough for these small amounts of crystalline material. Continuing the film compression from 2 mN/m to the beginning of the plateau of the  $\pi$ - $A$  isotherm, no detectable changes on the subphase surface are observed. When the plateau starts upon compression, lots of dark domains are observed (not shown here). Upon further compression, these domains become large and the morphology becomes distinguishable, e.g., circular- or hexagonal-shaped domains of Ethoxy-PPE appear (Figure 4a, right-side image). Methyl-PPE-*co*-decadiene forms too small domains that are still difficult to resolve by epifluorescence microscopy (Figure 4b, right-side image). Therefore, the domains of both PEs are transferred from the water surface to silicon wafer and examined by AFM.



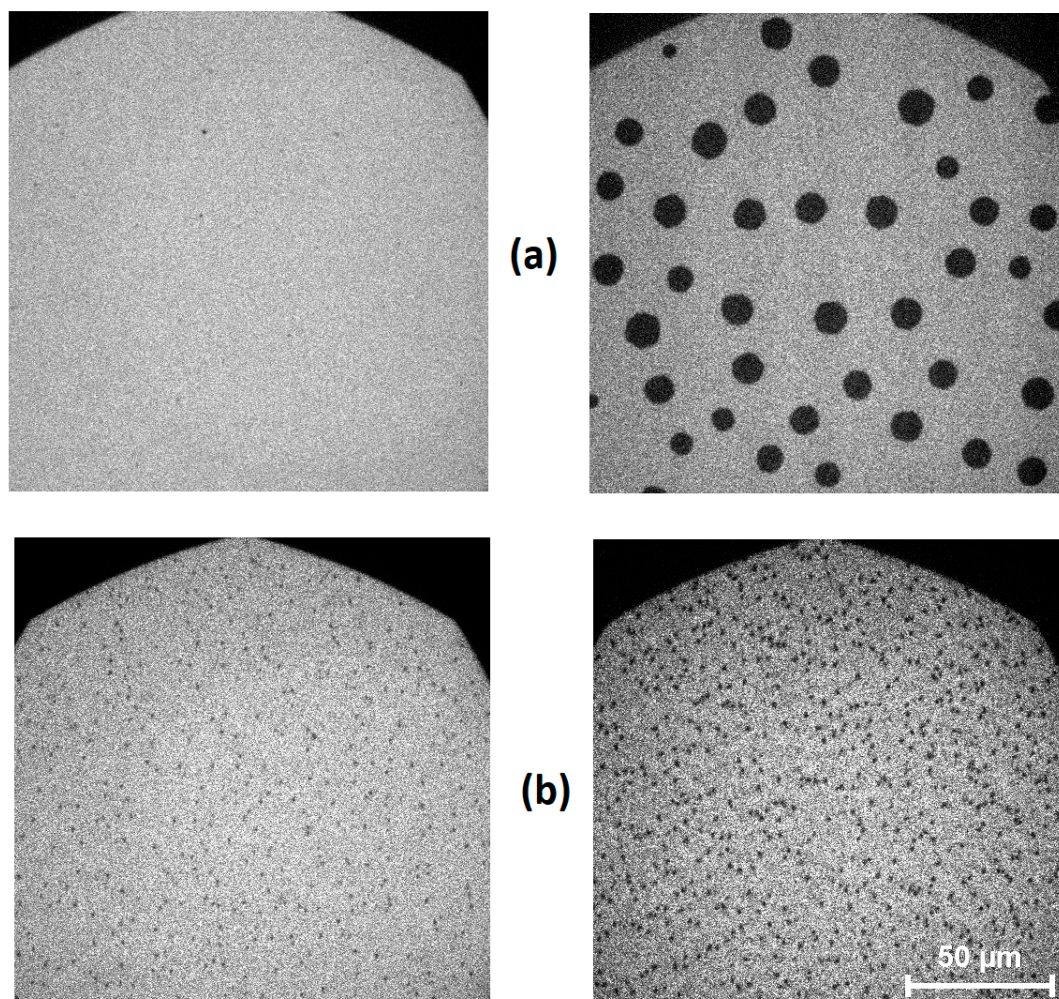


**Figure 4.** Epifluorescence images of (a) Ethoxy-PPE at  $\pi$  of 2 mN/m,  $A \sim 96 \text{ \AA}^2$  (left) and 7 mN/m,  $A \sim 63 \text{ \AA}^2$  (right), and (b) Methyl-PPE-*co*-decadiene at  $\pi$  of 2 mN/m,  $A \sim 84 \text{ \AA}^2$  (left) and 9 mN/m,  $A \sim 47 \text{ \AA}^2$  (right). The images are captured during the film compression at a compression rate of  $50 \text{ \AA}^2/(\text{molecule min})$ . The image size is  $164 \times 164 \text{ \mu m}^2$ .

Figure 5 shows AFM height images of the PE LB films transferred at 10 mN/m. A circular-shaped crystalline domain with a diameter of more than  $15 \text{ \mu m}$  is observed for Ethoxy-PPE (Figure 5a). Note that PE typically forms a lozenge-shaped single crystal due to the slowest growth of  $\{110\}$  planes [60]. There are also a truncated lozenge-shaped or lenticular-shaped crystal habits associated with supercooling temperature-dependent growth rates of the crystal planes [61,62]. Obviously, other factors are also involved in different crystal habits such as geometrical confinement [63], soft epitaxy [64], or molecular fractionation [61,65]. For the Methyl-PPE-*co*-decadiene sample, the morphology is very different compared to Ethoxy-PPE. Completely irregular-shaped large domains surrounded by small domains are observed (Figure 5b). These small domains can be related to the low molar mass fraction of the polymer as known from PE [61,65]. All domains together form a film-like morphology when the LB film is transferred at slightly higher surface pressure (Figure 6b). The irregularity in Methyl-PPE-*co*-decadiene domains can also be explained based on polymer stiffness. The stiffer backbone of Methyl-PPE-*co*-decadiene together with the random distribution of the length of the methylene sequences may hinder the growth of large regular domains. Note that Methyl-PPE-*co*-decadiene is stiffer than the Ethoxy-PPE known from  $T_g$  data as measured by DSC (see Figure S4 of the supporting information). Chain length-dependent morphologies of melt/solution grown crystals also show tiny irregular crystallites for Ethoxy-PPE with 20  $\text{CH}_2$  units [42]. This changes

to a dendritic or branch-like feature when the chain length between the Ethoxy-PPE defects increases to 40 CH<sub>2</sub> units [42]. It can be concluded that the morphologies of the PEs in Langmuir and finally in LB films can be tuned by increasing the length of the methylene sequence in between the phosphoester defects.

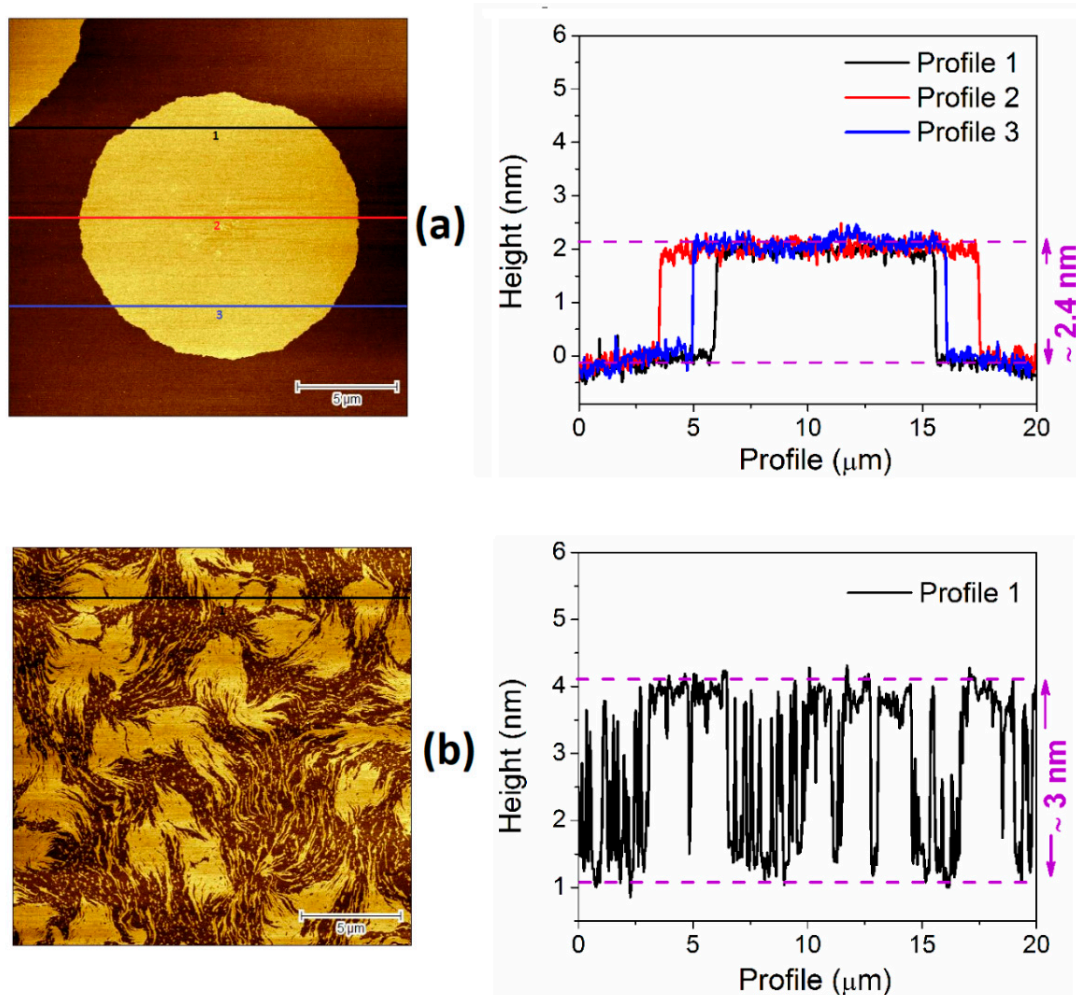


**Figure 5.** AFM height images (left) with the line profiles (right) of the LB film transferred at a  $\pi$  of 10 mN/m for (a) Ethoxy-PPE mN/m and (b) Methyl-PPE-co-decadiene. The image size is  $20 \times 20 \mu\text{m}^2$ . Enlarged AFM images of Methyl-PPE-co-decadiene can be found in Figure S8 of the supporting information.

Domain/film thicknesses are also estimated by drawing line profiles on the AFM images of the LB films. A maximum value in the range of  $\sim(2.4$  to  $3)$  nm is observed (see Figure 5). This value is almost equal to the length of the methylene sequence (20 to 28 CH<sub>2</sub> units) in a fully extended state. However, the theoretically calculated maximum length for Ethoxy-PPE is  $\sim 3.5$  nm. This is estimated considering two phosphoester defects (one defect is  $\sim 0.5$  nm) on both sides of the 20 CH<sub>2</sub> groups (2.5 nm) with a fully extended state (see discussion below). The small thickness obtained by AFM measurements might have two possibilities; either the phosphoester defects might be accommodated inside the crystalline domains, or the polymer chains in the domains are tilted by some degrees with respect to the substrate normal. Thus, the length ratio, e.g., thickness from AFM (2.4 nm) and the theoretically calculated maximum length (3.5 nm), gives a chain tilt of  $\sim 47^\circ$  ( $\arccos 2.4 \text{ nm}/3.5 \text{ nm}$ ) with respect to the substrate normal. The value is also consistent with the chain tilt angle value calculated from the limiting area of the  $\pi$ -A isotherm. The chain tilt can be further analyzed when the domains/films are transferred at a slightly higher surface pressure of  $\sim 15$  mN/m (see Figure 6a). A slight increase ( $2.7 \text{ nm} - 2.4 \text{ nm} = 0.3 \text{ nm}$ ) in domain thickness is observed which might be related to



the decrease in the chain tilt from  $\sim 47^\circ$  to  $\sim 40^\circ$  ( $\arccos 2.7 \text{ nm}/3.5 \text{ nm}$ , i.e., thickness from AFM (2.7 nm) divided by the theoretically calculated maximum length (3.5 nm)) due to the compression.

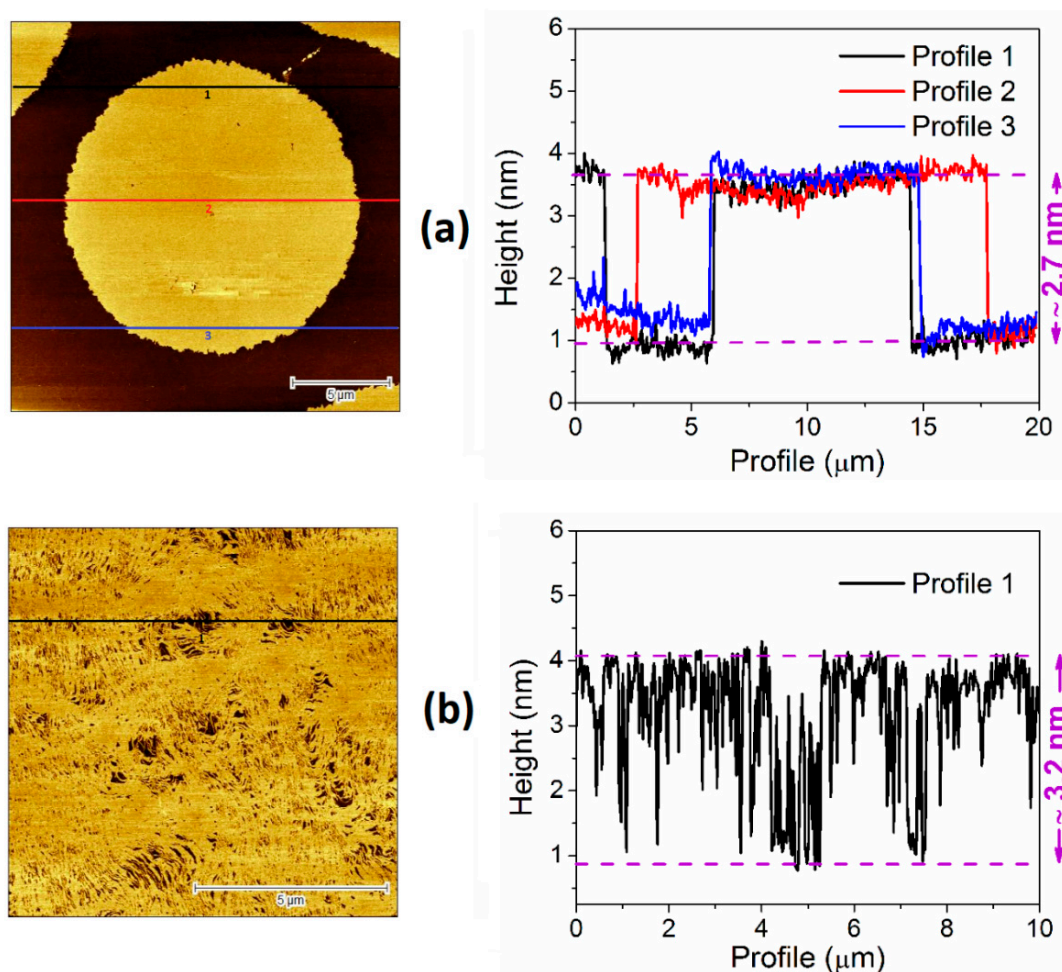


**Figure 6.** AFM height images (left) with the line profiles (right) of the LB film transferred at a  $\pi$  of 15 mN/m for (a) Ethoxy-PPE mN/m and (b) Methyl-PPE-*co*-decadiene.

Finally, GI-WAXS experiments are performed with the LB films to reveal more details of the crystallization process. LB films are transferred at a surface pressure  $\pi$  of 15 mN/m. At this surface pressure, the substrate surface is mostly covered with domains or film without breaking or multilayer formation as confirmed by AFM. Figure 7 shows the GI-WAXS pattern of the LB film of Ethoxy-PPE. A single Bragg reflection in the horizontal direction ( $q_{xy}$  axis) and Kiessig fringes [66] in the vertical direction ( $q_z$  axis) are observed. The horizontal reflection at  $q_{xy}$  positions of  $\sim 15.1 \text{ nm}^{-1}$  ( $d = 0.41 \text{ nm}$ ) is related to lateral chain packing of the methylene sequence with a nearest neighbor spacing [41,42] which occurs also as a rotator phase  $R_{II}$  known from *n*-alkanes [67–69]. Note that Langmuir films of long-chain hydrocarbon or phospholipids under GI-WAXS investigation show a similar type of Bragg reflection at the horizontal direction with a  $q_{xy}$  value in the range of 14.8 to  $15.1 \text{ nm}^{-1}$ , which is typically assigned to side by side chain packing with a nearly vertical rod-like orientation [70]. The Ethoxy-PPE sample was also studied by wide-angle X-ray scattering (WAXS) in the bulk state (see Figure S4). A single Bragg reflection at  $2\theta \sim 21.91^\circ$  ( $q \sim 15.4 \text{ nm}^{-1}$ ) is observed, indicating almost the same nearest neighbor spacing as observed in GI-WAXS. This suggests that the LB film of Ethoxy-PPE possesses a similar chain packing as its bulk state. Melt grown and solvent cast crystals of Ethoxy-PPE also show a single Bragg reflection and the crystal structure was assigned to pseudo-hexagonal [42,71,72]. GI-WAXS pattern of Methyl-PPE-*co*-decadiene has also a single Bragg reflection at a similar  $q_{xy}$  position

of  $\sim 15.1 \text{ nm}^{-1}$  as Ethoxy-PPE (Figure S9 of supporting information). The WAXS pattern of this modified PE in bulk state possesses two Bragg reflections at  $2\theta$  of  $\sim 21.54^\circ$  and  $\sim 23.91^\circ$  (see Figure S4), which can be identified as an orthorhombic rotator phase  $R_I$  of the methylene sequence [67–69]. This reflection is not visible in the GI-WAXS image, even measuring the sample for a long time. This is because the footprint of GI-WAXS spot is around  $0.2 \times 10 \text{ mm}^2$ , resulting in a broad distribution in the detected signals due to the scattering from several locations of the film [73]. It is worth mentioning that the crystal structure of these PEs is different, e.g., rotator phase  $R_{II}$  for Ethoxy-PPE and orthorhombic rotator phase  $R_I$  for Methyl-PPE-*co*-decadiene.

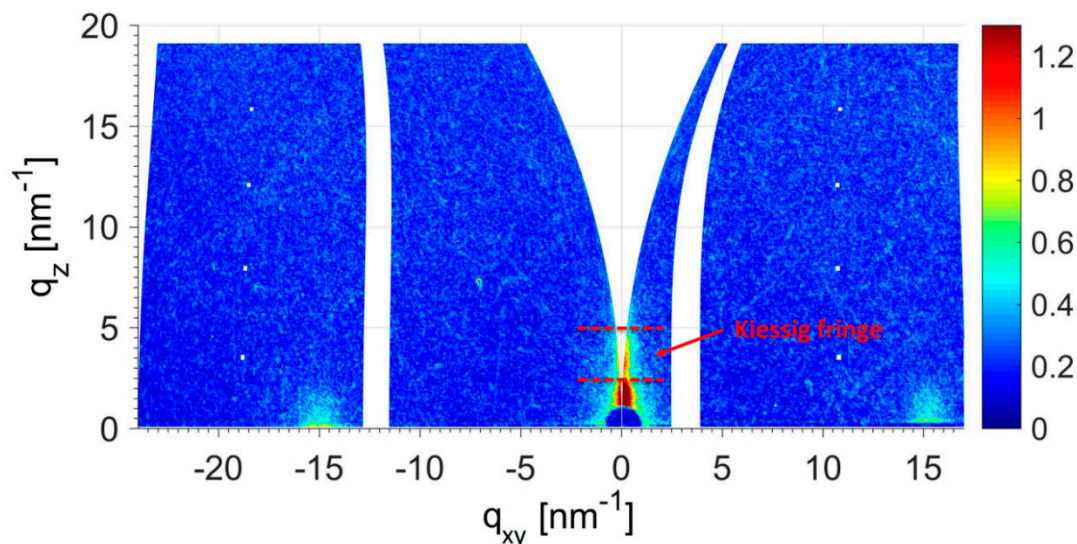


**Figure 7.** 2D GI-WAXS pattern of the LB film of Ethoxy-PPE transferred at 15 mN/m (after the plateau zone) of the  $\pi$ -A isotherm. The two vertical bands in the image are the empty space between the detectors and appear as blank. The dotted red lines are drawn in to the  $q_z$  axis to guide the range of the Kiessig fringe.

Besides, the vertically oriented reflections in the GI-WAXS image along  $q_z$  axis are the Kiessig fringes [66], which can be used to calculate the film thickness by  $d = 2\pi/\Delta q$ , where  $d$  is the layer thickness and  $\Delta q$  is the fringe width, i.e., the difference between two minima or maxima of the fringes. A film thickness of  $\sim 2.7 \text{ nm}$  is estimated for Ethoxy-PPE, which is consistent with the film thickness obtained by AFM measurement at the same transfer pressure. However, for Methyl-PPE-*co*-decadiene, a film thickness of  $(5.2 \pm 0.5) \text{ nm}$  is observed. This value significantly deviates from the value obtained by AFM measurement ( $\sim 3.2 \text{ nm}$ ). The origin of this difference is unknown. It should also be noted that the thickness estimation using X-ray measurements and AFM usually result in some differences [74].

#### 4. Conclusions

This study shows the possibility to prepare Langmuir/LB film from two different hydrophobic polymers. Using ADMET polymerization, the issue regarding the lack of polar groups in PE chains can be solved. The film morphology can also be tuned when changing the polar groups or increasing the length of methylene sequence between the polar groups (defects). We show the Langmuir/LB film formation of two different PEs (see Table 1), containing regularly spaced polar phosphoester defects in the main chain. The films are prepared by spreading the polymers from chloroform solution on the water surface of a Langmuir trough and compression after solvent evaporation by moving the barriers of the Langmuir trough (Figure 8).

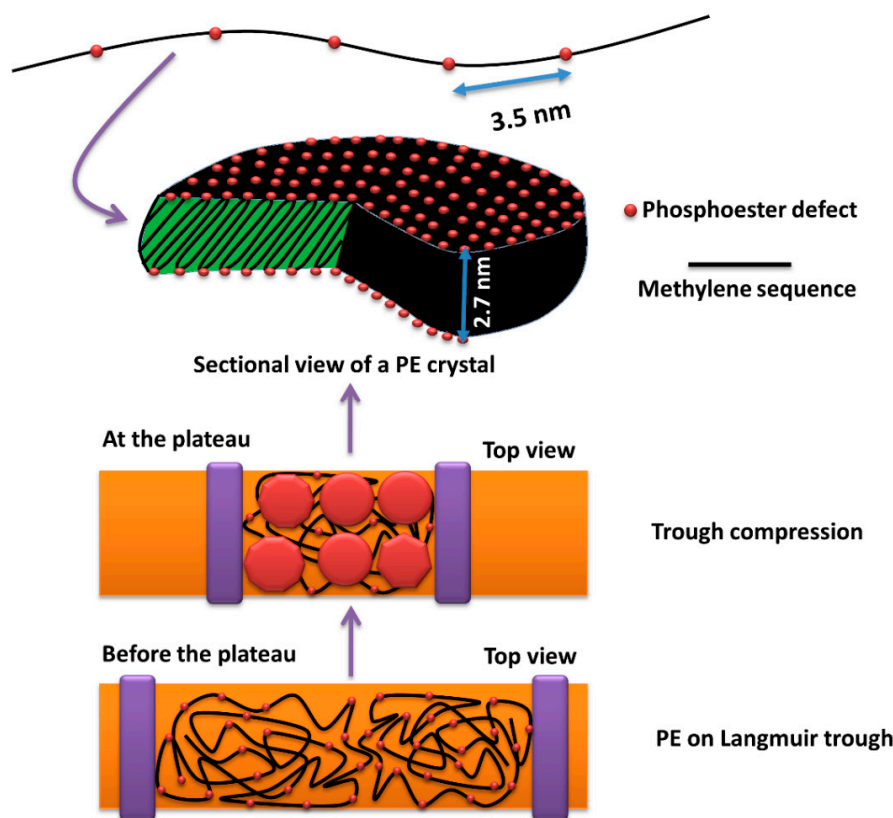


**Figure 8.** Schematic illustration of the chain organization of Ethoxy-PPE at the air–water interface during compression.

The surface pressure vs. area per repeating unit isotherms are recorded. They show a plateau zone in the surface pressure range of  $\sim(6$  to  $8)$  mN/m, assigned to crystalline domain formation by BAM and epifluorescence microscopy. The shape of the domains depends on the defects and the methylene chain length between the defects. PE with ethoxy phosphoester defects shows mostly circular shape domain. The domains turn to a film-like morphology when the chain length between the methyl phosphoester defects increases and when the length of the methylene chains within the PE is different. The thickness of the domains/film is in between  $\sim(2.4$  to  $3.2)$  nm, depending on the transfer pressure. Finally, GI-WAXS investigations on the domains or film on solid support show a single Bragg reflection at a  $q_{xy}$  position of  $\sim 15.1$  nm $^{-1}$  known from crystalline PE samples.

**Supplementary Materials:** The following are available online at <http://www.mdpi.com/2073-4360/12/10/2408/s1>, Figure S1:  $^1\text{H}$  NMR spectra of Methyl-PPE-*co*-decadiene, Figure S2:  $^{31}\text{P}$  NMR spectrum of Methyl-PPE-*co*-decadiene, Figure S3: GPC elugram of Methyl-PPE-*co*-decadiene, Figure S4: DSC and XRD of PEs, Figure S5: FTIR spectra of the investigated PEs and the reactants, Figure S6: BAM image of Methyl-PPE-*co*-decadiene at collapsed phase, Figure S7:  $\pi$ - $A$  isotherms of Ethoxy-PPE on different subphases, Figure S8: AFM images of the LB film of Methyl-PPE-*co*-decadiene and Figure S9: 2D GI-WAXS pattern of the LB film of Methyl-PPE-*co*-decadiene.

**Author Contributions:** Conceptualization, N.H.; methodology, N.H.; investigation, N.H., T.H., F.R.W., K.B.; writing—original draft preparation, N.H.; writing—review and editing, N.H., K.B., J.K.; supervision, J.K.; project administration, J.K.; funding acquisition, J.K. All authors have read and agreed to the published version of the manuscript.

**Funding:** This research was funded by Deutsche Forschungsgemeinschaft (DFG, German Research Foundation) Project number 189853844 TRR 102.

**Acknowledgments:** AFM and GI-WAXS measurements were carried out within the cooperation of the SFB TRR 102 (project B03, Thomas Thurn-Albrecht). We thank Oleksandr Dolynchuk for the conversion of GI-WAXS images.

**Conflicts of Interest:** The authors declare no conflict of interest.

## References

1. Reiter, G. Dewetting of thin polymer films. *Phys. Rev. Lett.* **1992**, *68*, 75–78. [[CrossRef](#)] [[PubMed](#)]
2. Factor, B.J.; Russell, T.P.; Toney, M.F. Grazing incidence X-ray scattering studies of thin films of an aromatic polyimide. *Macromolecules* **1993**, *26*, 2847–2859. [[CrossRef](#)]
3. Keddie, J.L.; Jones, R.A.L.; Cory, R.A. Interface and surface effects on the glass-transition temperature in thin polymer films. *Faraday Discuss.* **1994**, *98*, 219–230. [[CrossRef](#)]
4. Hobbs, J.K.; Humphris, A.D.L.; Miles, M.J. In-situ atomic force microscopy of polyethylene crystallization. 1. crystallization from an oriented backbone. *Macromolecules* **2001**, *34*, 5508–5519. [[CrossRef](#)]
5. Si, L.; Massa, M.V.; Dalnoki-Veress, K.; Brown, H.R.; Jones, R.A.L. Chain entanglement in thin freestanding polymer films. *Phys. Rev. Lett.* **2005**, *94*, 127801–127804. [[CrossRef](#)]
6. Ma, Y.; Hu, W.; Reiter, G. Lamellar crystal orientations biased by crystallization kinetics in polymer thin films. *Macromolecules* **2006**, *39*, 5159–5164. [[CrossRef](#)]
7. Kossack, W.; Seidlitz, A.; Thurn-Albrecht, T.; Kremer, F. Interface and confinement induced order and orientation in thin films of poly( $\epsilon$ -caprolactone). *Macromolecules* **2016**, *49*, 3442–3451. [[CrossRef](#)]
8. Flieger, A.-K.; Schulz, M.; Thurn-Albrecht, T. Interface-induced crystallization of polycaprolactone on graphite via first-order prewetting of the crystalline phase. *Macromolecules* **2018**, *51*, 189–194. [[CrossRef](#)]
9. *Polymer Thin Films*; Hashim, A.A. (Ed.) In-Tech: Vukovar, Croatia, 2010; pp. 1–309.
10. Nagaraja, A.; Jalageri, M.D.; Puttaiahgowda, Y.M. A thirst for polymeric antimicrobial surfaces/coatings for diverse applications. In *Engineered Antimicrobial Surfaces. Materials Horizons: From Nature to Nanomaterials*; Snigdha, S., Thomas, S., Radhakrishnan, E.K.N., Eds.; Springer: Singapore, 2020; pp. 13–31.
11. Reiter, G. Dewetting as a probe of polymer mobility in thin films. *Macromolecules* **1994**, *27*, 3046–3052. [[CrossRef](#)]
12. Tseng, K.C.; Turro, N.J.; Durning, C.J. Molecular mobility in polymer thin films. *Phys. Rev. E* **2000**, *61*, 1800–1811. [[CrossRef](#)]
13. Bunn, C.W. The crystal structure of long-chain normal paraffin hydrocarbons. The “shape” of the CH<sub>2</sub> group. *Trans. Faraday Soc.* **1939**, *35*, 482–491. [[CrossRef](#)]
14. Forrest, J.A.; Dalnoki-Veress, K.; Dutcher, J.R. Interface and chain confinement effects on the glass transition temperature of thin polymer films. *Phys. Rev. E* **1997**, *56*, 5705–5716. [[CrossRef](#)]
15. De Gennes, P.G. Glass transitions in thin polymer films. *Eur. Phys. J. E* **2000**, *2*, 201–205.
16. Tsui, O.K.C.; Zhang, H.F. Effects of chain ends and chain entanglement on the glass transition temperature of polymer thin films. *Macromolecules* **2001**, *34*, 9139–9142. [[CrossRef](#)]
17. Roth, C.B.; Dutcher, J.R. Glass transition and chain mobility in thin polymer films. *J. Electroanal. Chem.* **2005**, *584*, 13–22. [[CrossRef](#)]
18. Inoue, R.; Kanaya, T.; Nishida, K.; Tsukushi, I.; Telling, M.T.F.; Gabrys, B.J.; Tyagi, M.; Soles, C.; Wu, W.-L. Glass transition and molecular mobility in polymer thin films. *Phys. Rev. E* **2009**, *80*, 031802. [[CrossRef](#)]
19. Jones, R.L.; Kumar, S.K.; Ho, D.L.; Briber, R.M.; Russell, T.P. Chain conformation in ultrathin polymer films. *Nature* **1999**, *400*, 146–149. [[CrossRef](#)]
20. Kraus, J.; Müller-Buschbaum, P.; Kuhlmann, T.; Schubert, D.W.; Stamm, M. Confinement effects on the chain conformation in thin polymer films. *Europhys. Lett.* **2000**, *49*, 210–216. [[CrossRef](#)]
21. Hall, D.B.; Underhill, P.; Torkelson, J.M. Spin coating of thin and ultrathin polymer films. *Polym. Eng. Sci.* **1998**, *38*, 2039–2045. [[CrossRef](#)]
22. Crisp, D.J. Surface films of polymers. Part I. Films of the fluid type. *J. Colloid Sci.* **1946**, *1*, 49–70. [[CrossRef](#)]
23. Crisp, D.J. Surface films of polymers. Part II. Films of the coherent and semi-crystalline type. *J. Colloid Sci.* **1946**, *1*, 161–184. [[CrossRef](#)]
24. Petty, M.C. *Film Deposition*; Cambridge University Press: Cambridge, UK, 1996; pp. 12–64.
25. Busse, K.; Fuchs, C.; Hasan, N.; Pulst, M.; Kressler, J. Crystallization of poly(ethylene oxide) on the surface of aqueous salt solutions studied by grazing incidence wide-angle X-ray scattering. *Langmuir* **2018**, *34*, 12759–12763. [[CrossRef](#)] [[PubMed](#)]
26. Hasan, N.; Fuchs, C.; Schwiager, C.; Busse, K.; Dolynchuk, O.; Kressler, J. Crystallization of poly( $\epsilon$ -caprolactone) at the air-water interface studied by IRRAS and GI-WAXS. *Polymer* **2020**, *196*, 122468. [[CrossRef](#)]



27. Kumaki, J.; Kawauchi, T.; Yashima, E. Two-dimensional folded chain crystals of a synthetic polymer in a Langmuir–Blodgett film. *J. Am. Chem. Soc.* **2005**, *127*, 5788–5789. [[CrossRef](#)]
28. Kumaki, J. Observation of polymer chain structures in two-dimensional films by atomic force microscopy. *Polym. J.* **2016**, *48*, 3–14. [[CrossRef](#)]
29. Gaines, G.L. Monolayers of polymers. *Langmuir* **1991**, *7*, 834–839. [[CrossRef](#)]
30. Watanabe, K.; Kumaki, J. Extended-chain crystallization and stereocomplex formation of polylactides in a Langmuir monolayer. *Polym. J.* **2020**, *52*, 601–613. [[CrossRef](#)]
31. Fuchs, C.; Busse, K.; Flieger, A.-K.; Kressler, J. Polymer crystallization on the surface of water or aqueous salt solution. *Chem. Eng. Technol.* **2016**, *39*, 1333–1340. [[CrossRef](#)]
32. Sorokin, A.V.; Bai, M.; Ducharme, S.; Poulsen, M. Langmuir–Blodgett films of polyethylene. *J. Appl. Phys.* **2002**, *92*, 5977–5981. [[CrossRef](#)]
33. Nakanishi, K.; Suzuki, H.; Katoh, T.; Imai, S.; Nakayama, Y.; Miki, H. Deposition of polyethylene thin films using synchrotron radiation ablation. *Jpn. J. Appl. Phys.* **1999**, *38*, 863–867. [[CrossRef](#)]
34. Chung, T.C.; Lu, H.L.; Li, C.L. Synthesis and functionalization of unsaturated polyethylene: Poly(ethylene-co-1,4-hexadiene). *Macromolecules* **1994**, *27*, 7533–7537. [[CrossRef](#)]
35. Hong, M.; Liu, J.-Y.; Li, B.-X.; Li, Y.-S. Facile functionalization of polyethylene via click chemistry. *Macromolecules* **2011**, *44*, 5659–5665. [[CrossRef](#)]
36. Boffa, L.S.; Novak, B.M. Copolymerization of polar monomers with olefins using transition-metal complexes. *Chem. Rev.* **2000**, *100*, 1479–1494. [[CrossRef](#)] [[PubMed](#)]
37. Zhang, Y.; Wang, C.; Mecking, S.; Jian, Z. Ultrahigh branching of main-chain-functionalized polyethylenes by inverted insertion selectivity. *Angew. Chem.* **2020**, *132*, 14402–14408. [[CrossRef](#)]
38. Long, B.K.; Eagan, J.M.; Mulzer, M.; Coates, G.W. Semi-crystalline polar polyethylene: Ester-functionalized linear polyolefins enabled by a functional-group-tolerant, cationic nickel catalyst. *Angew. Chem. Int. Ed.* **2016**, *55*, 7106–7110. [[CrossRef](#)] [[PubMed](#)]
39. Wagener, K.B.; Boncella, J.M.; Nel, J.G. Acyclic diene metathesis (ADMET) polymerization. *Macromolecules* **1991**, *24*, 2649–2657. [[CrossRef](#)]
40. Few, C.S.; Wagener, K.B.; Thompson, D.L. Systematic studies of morphological changes of precision polyethylene. *Macromol. Rapid Commun.* **2014**, *35*, 123–132. [[CrossRef](#)]
41. Zheng, Y.-R.; Tee, H.T.; Wei, Y.; Wu, X.-L.; Mezger, M.; Yan, S.; Landfester, K.; Wagener, K.; Wurm, F.R.; Lieberwirth, I. Morphology and thermal properties of precision polymers: The crystallization of butyl branched polyethylene and polyphosphoesters. *Macromolecules* **2016**, *49*, 1321–1330. [[CrossRef](#)]
42. Haider, T.; Suraeva, O.; O’Duill, M.L.; Mars, J.; Mezger, M.; Lieberwirth, I.; Wurm, F.R. Controlling the crystal structure of precisely spaced polyethylene-like polyphosphoesters. *Polym. Chem.* **2020**, *11*, 3404–3415. [[CrossRef](#)]
43. Hasan, N.; Schwieger, C.; Tee, H.T.; Wurm, F.R.; Busse, K.; Kressler, J. Crystallization of a polyphosphoester at the air-water interface. *Eur. Polym. J.* **2018**, *101*, 350–357. [[CrossRef](#)]
44. Stumm, W.W.; Morgan, J.J. *Aquatic Chemistry: Chemical Equilibria and Rates in Natural Waters*; John Wiley & Sons: Hoboken, NJ, USA, 1996; p. 528.
45. Kobayashi, Y.; Amano, T.; Taga, K.; Yamamoto, Y.; Shervani, Z.; Yamamoto, M. Surface properties of novel surfactant, dihexadecyl gemini phosphate, monolayers on water surface by dropping method. *J. Biophys. Chem.* **2017**, *08*, 39–50. [[CrossRef](#)]
46. Kaganer, V.M.; Möhwald, H.; Dutta, P. Structure and phase transitions in Langmuir monolayers. *Rev. Mod. Phys.* **1999**, *71*, 779–819. [[CrossRef](#)]
47. Amado, E.; Kerth, A.; Blume, A.; Kressler, J. Infrared reflection absorption spectroscopy coupled with Brewster angle microscopy for studying interactions of amphiphilic triblock copolymers with phospholipid monolayers. *Langmuir* **2008**, *24*, 10041–10053. [[CrossRef](#)] [[PubMed](#)]
48. Pulst, M.; Schneemann, C.; Ruda, P.; Golitsyn, Y.; Grefe, A.-K.; Stühn, B.; Busse, K.; Reichert, D.; Kressler, J. Chain tilt and crystallization of ethylene oxide oligomers with midchain defects. *ACS Macro Lett.* **2017**, *6*, 1207–1211. [[CrossRef](#)]
49. Fritzsche, K.J.; Mao, K.; Schmidt-Rohr, K. Avoidance of density anomalies as a structural principle for semicrystalline polymers: The importance of chain ends and chain tilt. *Macromolecules* **2017**, *50*, 1521–1540. [[CrossRef](#)]

50. Elzein, T.; Nasser-Eddine, M.; Delaite, C.; Bistac, S.; Dumas, P. FTIR study of polycaprolactone chain organization at interfaces. *J. Colloid Interface Sci.* **2004**, *273*, 381–387. [[CrossRef](#)]
51. Kraack, H.; Tamam, L.; Sloutskin, E.; Deutsch, M.; Ocko, B.M. Alkyl-thiol Langmuir films on the surface of liquid mercury. *Langmuir* **2007**, *23*, 7571–7582. [[CrossRef](#)] [[PubMed](#)]
52. Mendelsohn, R.; Mao, G.; Flach, C.R. Infrared reflection–absorption spectroscopy: Principles and applications to lipid–protein interaction in Langmuir films. *Biochim. Biophys. Acta-Biomembr.* **2010**, *1798*, 788–800. [[CrossRef](#)] [[PubMed](#)]
53. Aoki, A.; Fukayama, S. Organic thin film solar cell composed of hetero-deposited Langmuir-Blodgett films. *Electrochemistry* **2010**, *78*, 178–180. [[CrossRef](#)]
54. Li, B.; Wu, Y.; Liu, M.; Esker, A.R. Brewster angle microscopy study of poly( $\epsilon$ -caprolactone) crystal growth in Langmuir films at the air/water interface. *Langmuir* **2006**, *22*, 4902–4905. [[CrossRef](#)]
55. Lösche, M.; Möhwald, H. Fluorescence microscope to observe dynamical processes in monomolecular layers at the air/water interface. *Rev. Sci. Instrum.* **1984**, *55*, 1968–1972. [[CrossRef](#)]
56. Lösche, M.; Rabe, J.; Fischer, A.; Rucha, B.U.; Knoll, W.; Möhwald, H. Microscopically observed preparation of Langmuir-Blodgett films. *Thin Solid Films* **1984**, *117*, 269–280. [[CrossRef](#)]
57. Lösche, M.; Möhwald, H. Impurity controlled phase transitions of phospholipid monolayers. *Eur. Biophys. J.* **1984**, *11*, 35–42. [[CrossRef](#)]
58. Helm, C.A.; Möhwald, H.; Kjaer, K.; Als-Nielsen, J. Phospholipid monolayers between fluid and solid states. *Biophys. J.* **1987**, *52*, 381–390. [[CrossRef](#)]
59. Kajiyama, T.; Oishi, Y. Novel concepts of aggregation structure of fatty acid monolayers on the water surface. In *New Developments in Construction and Functions of Organic Thin Films*; Kajiyama, T., Aizawa, M., Eds.; Elsevier: Amsterdam, The Netherlands, 1996; pp. 15–16.
60. Organ, S.J.; Keller, A. Solution crystallization of polyethylene at high temperatures. *J. Mater. Sci.* **1985**, *20*, 1571–1585. [[CrossRef](#)]
61. Gedde, U.W.; Hedenqvist, M.S. *Fundamental Polymer Science*; Springer Nature: Cham, Switzerland, 2019; pp. 251–321.
62. Weber, C.H.M.; Chiche, A.; Krausch, G.; Rosenfeldt, S.; Ballauff, M.; Harnau, L.; Göttker-Schnetmann, I.; Tong, Q.; Mecking, S. Single lamella nanoparticles of polyethylene. *Nano Lett.* **2007**, *7*, 2024–2029. [[CrossRef](#)] [[PubMed](#)]
63. Misra, R.D.K.; Depan, D.; Shah, J. The effect of dimensionality of nanostructured carbon on the architecture of organic–inorganic hybrid materials. *Phys. Chem. Chem. Phys.* **2013**, *15*, 12988. [[CrossRef](#)]
64. Li, L.; Li, C.Y.; Ni, C. Polymer crystallization-driven, periodic patterning on carbon nanotubes. *J. Am. Chem. Soc.* **2006**, *128*, 1692–1699. [[CrossRef](#)]
65. Gedde, U.W.; Jansson, J.-F. Molecular fractionation in melt-crystallized polyethylene: 3. Microscopy of solvent-treated samples. *Polymer* **1984**, *25*, 1263–1267. [[CrossRef](#)]
66. Geuchies, J.J.; Soligno, G.; Geraffy, E.; Hendriks, C.P.; van Overbeek, C.; Montanarella, F.; Slot, M.R.; Konovalov, O.V.; Petukhov, A.V.; Vanmaekelbergh, D. Unravelling three-dimensional adsorption geometries of PbSe nanocrystal monolayers at a liquid-air interface. *Commun. Chem.* **2020**, *3*, 28. [[CrossRef](#)]
67. Denicolò, I.; Doucet, J.; Craievich, A.F. X-ray study of the rotator phase of paraffins (III): Even-numbered paraffins C<sub>18</sub>H<sub>38</sub>, C<sub>20</sub>H<sub>42</sub>, C<sub>22</sub>H<sub>46</sub>, C<sub>24</sub>H<sub>50</sub>, and C<sub>26</sub>H<sub>54</sub>. *J. Chem. Phys.* **1983**, *78*, 1465–1469. [[CrossRef](#)]
68. Wentzel, N.; Milner, S.T. Crystal and rotator phases of n-alkanes: A molecular dynamics study. *J. Chem. Phys.* **2010**, *132*, 044901. [[CrossRef](#)] [[PubMed](#)]
69. Weiss, V.M.; Naolou, T.; Amado, E.; Busse, K.; Mäder, K.; Kressler, J. Formation of structured polygonal nanoparticles by phase-separated comb-like polymers. *Macromol. Rapid Commun.* **2012**, *33*, 35–40. [[CrossRef](#)] [[PubMed](#)]
70. Bera, P.K.; Kandar, A.K.; Krishnaswamy, R.; Fontaine, P.; Impéror-Clerc, M.; Pansu, B.; Constantin, D.; Maiti, S.; Sanyal, M.K.; Sood, A.K. Grazing incidence X-ray diffraction studies of lipid–peptide mixed monolayers during shear flow. *ACS Omega* **2020**, *5*, 14555–14563. [[CrossRef](#)] [[PubMed](#)]
71. Qiu, W.; Sworen, J.; Pyda, M.; Nowak-Pyda, E.; Habenschuss, A.; Wagener, K.B.; Wunderlich, B. Effect of the precise branching of polyethylene at Each 21st CH<sub>2</sub> group on its phase transitions, crystal structure, and morphology. *Macromolecules* **2006**, *39*, 204–217. [[CrossRef](#)]
72. Cankaya, A.; Steinmann, M.; Bülbül, Y.; Lieberwirth, I.; Wurm, F.R. Side-chain poly(phosphoramidate)s via acyclic diene metathesis polycondensation. *Polym. Chem.* **2016**, *7*, 5004–5010. [[CrossRef](#)]



73. Smilgies, D.-M. Scherrer grain-size analysis adapted to grazing-incidence scattering with area detectors. *J. Appl. Crystallogr.* **2009**, *42*, 1030–1034. [[CrossRef](#)] [[PubMed](#)]
74. Su, H.C.; Lee, C.H.; Lin, M.Z.; Huang, T.W. A comparison between X-ray reflectivity and atomic force microscopy on the characterization of a surface roughness. *Chin. J. Phys.* **2012**, *50*, 291–300.

**Publisher's Note:** MDPI stays neutral with regard to jurisdictional claims in published maps and institutional affiliations.



© 2020 by the authors. Licensee MDPI, Basel, Switzerland. This article is an open access article distributed under the terms and conditions of the Creative Commons Attribution (CC BY) license (<http://creativecommons.org/licenses/by/4.0/>).

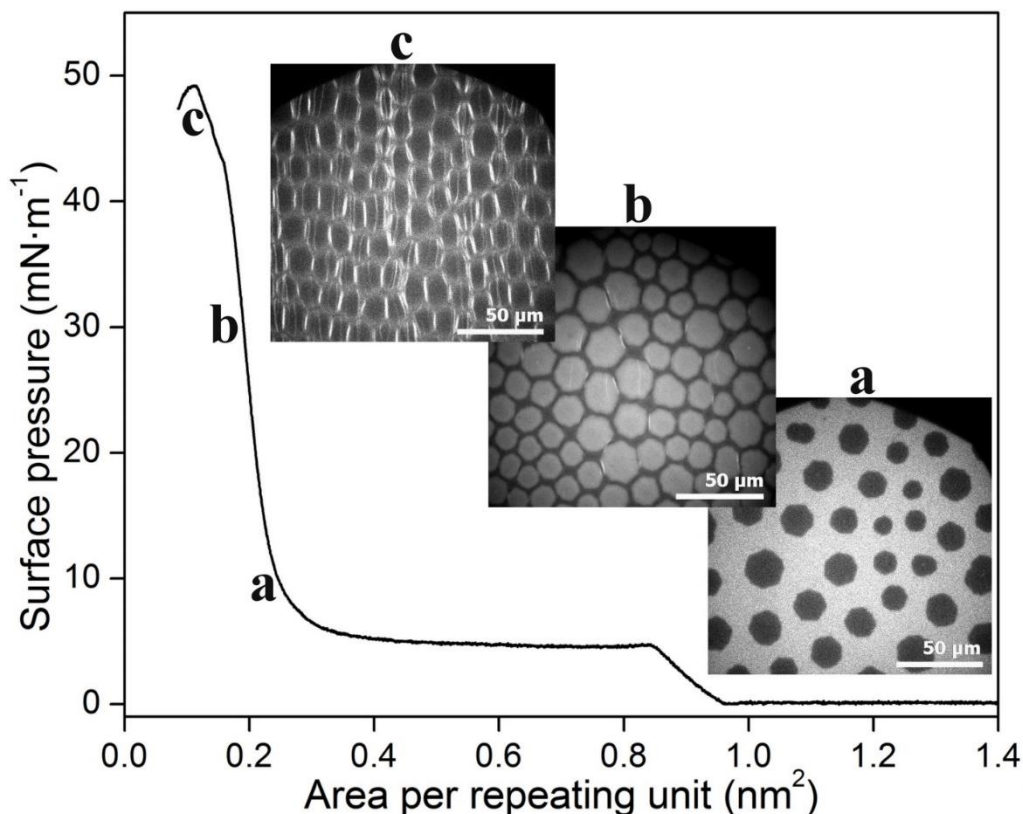
### 3.2 Paper II

#### Crystallization of a polyphosphoester at the air-water interface<sup>2</sup>

Nazmul Hasan, Christian Schwieger, Hisaschi T. Tee, Frederik R. Wurm, Karsten Busse, and Jörg Kressler

Eur. Polym. J. 2018, 101, 350, <https://doi.org/10.1016/j.eurpolymj.2018.03.001>

Graphical abstract:



This paper shows the crystallization of a polyphosphoester (PPE) in Langmuir/LB film. The polymer is similar to poly(ethylene) (PE) with a regular bulky phenoxy-phosphoester defect in the main chain. The polymer was dissolved in chloroform, spread on the water surface, and compressed after solvent evaporation. EFM revealed that the PPE develops hexagonal crystallites at the extended plateau zone of the  $\pi$ - $m$  isotherm followed by crystal collapse at maximum compression. IRRAS confirmed that the ordering happens in the methylene sequence of the PPE. After transferring the crystallites at different compression states to the solid support, AFM was used to observe the crystal morphology and estimate the thickness in order to understand more details about the crystallization process.

The author contributions to the following article are: N. Hasan and J. Kressler designed the research. H. T. Tee and F. R. Wurm synthesized the polymer. N. Hasan performed the following experiments as Langmuir isotherms, LB transfer, BAM, EFM, IRRAS, AFM, and FTIR. N. Hasan analyzed the data (C. Schwieger analyzed the IRRAS data) and wrote the draft manuscript (a part by J. Kressler). N. Hasan, C. Schwieger, K. Busse, F. Wurm, and J. Kressler discussed the results, reviewed them, and finalized the paper.

---

<sup>2</sup>The following article is reprinted (adapted) with permission from Eur. Polym. J. 2018, 101, 350, <https://doi.org/10.1016/j.eurpolymj.2018.03.001>. Copyright (2018) Elsevier. The link to the article on the publisher's website is: <https://www.sciencedirect.com/science/article/pii/S001430571830106X?via%3Dihub>. Supporting information is available at: <https://ars.els-cdn.com/content/image/1-s2.0-S001430571830106X-mmc1.docx>. No changes were made.



## Crystallization of a polyphosphoester at the air-water interface

Nazmul Hasan<sup>a</sup>, Christian Schwieger<sup>a</sup>, Hisaschi T. Tee<sup>b</sup>, Frederik R. Wurm<sup>b</sup>, Karsten Busse<sup>a</sup>, Jörg Kressler<sup>a,\*</sup>

<sup>a</sup> Department of Chemistry, Martin Luther University Halle-Wittenberg, D-06099 Halle (Saale), Germany

<sup>b</sup> Max Planck Institute for Polymer Research, Ackermannweg 10, D-55128 Mainz, Germany

### ARTICLE INFO

#### Keywords:

Polyphosphoester  
Langmuir film  
LB film  
IRRAS  
Crystallization

### ABSTRACT

A polyphosphoester (PPE) with phenyl phosphate groups separated by precisely 20 CH<sub>2</sub> groups in its backbone was dissolved in chloroform and spread on the water surface of a Langmuir trough. The surface pressure vs area per monomer unit ( $\pi$ -A) Langmuir isotherm together with epifluorescence and Brewster angle microscopy suggested that some crystallization occurred already at zero surface pressure immediately after solvent evaporation of the spread polymer solution. The extended plateau region of the Langmuir isotherm in the range of  $\pi \approx 4.5 \text{ mN m}^{-1}$  corresponds to the 2D crystallization of most polymer chains. Brewster angle and epifluorescence microscopy show that during the crystallization of PPE in the Langmuir film single crystal like hexagonal entities are formed with lateral dimensions of up to 20  $\mu\text{m}$ . These entities break upon compression beyond the limiting area per monomer unit which leads to a decrease of the elasticity modulus of the Langmuir film. The morphology of the single crystals and their failure upon compression are also observed in Langmuir-Blodgett films by atomic force microscopy. The thickness of the crystals is about 2.5 nm at the end of the plateau range and reaches 3.0 nm upon further compression. The polymer crystallization on the water surface is also confirmed by infrared reflection absorption spectroscopy.

### 1. Introduction

Many fundamental studies on polymer crystallization from melt or solution have used various types of polyethylene (PE) [1–4]. Typically, PE forms chain folded lamella crystals with an orthorhombic unit cell [5,6]. However, depending on the crystallization conditions also hexagonal [7] or monoclinic [8] unit cells have been reported. Recently, it has been emphasized that there is a necessity for the PE chains to be tilted when packed into lamella crystals [9–11]. The crystallization of a PE was also investigated in aqueous dispersions [12,13] or at the air/water interface [14]. Due to the lack of any polar group which could anchor the PE chains at the water surface, they do not form stable Langmuir monolayers but rather thick layers with a small degree of crystallinity. Several other completely hydrophobic polymers show a similar behavior [15]. However, hydrophobic and water insoluble polymers with polar entities in the polymer chain as e.g. an ester group in poly( $\epsilon$ -caprolactone) (PCL) or isotactic poly(methyl methacrylate) (i-PMMA) can form stable Langmuir layers at the air/water interface [16–18]. Upon compression in a Langmuir trough, a first order phase transition in their surface pressure vs area ( $\pi$ -A) isotherms indicative for 2D polymer crystallization was observed [17]. Another possibility to form stable Langmuir layers of hydrophobic polymers on the air-water

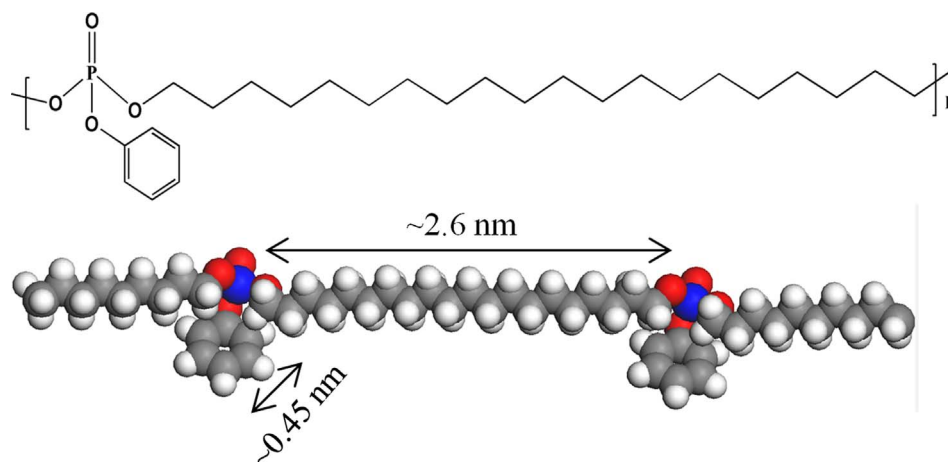
interface is given in amphiphilic block copolymers where the hydrophilic block functions as anchor [19].

With the advent of acyclic diene metathesis (ADMET) polymerization [20], it became possible to synthesize PE-like materials with a polar group in equidistant positions between the CH<sub>2</sub> groups [21,22]. This reduces the crystallinity and these polymers crystallize mainly into a pseudohexagonal unit cell [23]. In this study, we employ a precision polymer synthesized by ADMET. It contains a phenylphosphate group separated by exactly 20 CH<sub>2</sub> groups in its repeat unit (see Scheme 1). The length of a monomer unit  $L_{mu}$  is approximately 3 nm, the length of the 20 CH<sub>2</sub> groups 2.6 nm.

The crystallization of this polyphosphoester (PPE) in bulk and in thin films on solid supports was already reported elsewhere [23]. Here, we spread the PPE from chloroform solution on the water surface in a Langmuir trough. Then, the  $\pi$ -A compression isotherms are observed. The morphology change in the Langmuir films is directly visualized by Brewster angle microscopy (BAM) and epifluorescence microscopy. The ordering behavior of the CH<sub>2</sub> chains upon PPE film compression is studied by infrared reflection absorption spectroscopy (IRRAS) and quantitatively evaluated. The morphology of Langmuir-Blodgett (LB) films, obtained after film transfer onto mica substrates, is studied by atomic force microscopy (AFM).

\* Corresponding author.

E-mail address: [joerg.kressler@chemie.uni-halle.de](mailto:joerg.kressler@chemie.uni-halle.de) (J. Kressler).



**Scheme 1.** Repeat unit of the polyphosphoester (PPE) under investigation and the respective space filling model (color code: grey – carbon, white – hydrogen, red – oxygen, blue – phosphorus). (For interpretation of the references to colour in this figure legend, the reader is referred to the web version of this article.)

## 2. Experimental

### 2.1. Materials

The polyphosphoester ( $M_w = 17,800 \text{ g mol}^{-1}$ ,  $D = 2.29$ ) (PPE) was synthesized by ADMET polymerization. Synthesis and characterization details can be found elsewhere [22,23]. The melting temperature of the polymer in bulk is  $44^\circ\text{C}$ .

### 2.2. Methods

#### 2.2.1. Langmuir trough measurements

Pressure-area ( $\pi$ -A) isotherms were measured with a KSV 2000 Langmuir trough (Helsinki, Finland) which has a maximum surface area of  $76,050 \text{ mm}^2$ . It is equipped with symmetrically moving barriers and a platinum Wilhelmy plate. Langmuir troughs (Riegler and Kirstein, Berlin, Germany) with a surface area of  $14,800 \text{ mm}^2$  and  $26,212 \text{ mm}^2$ , respectively, were employed for BAM and epifluorescence microscopy. Here, filter paper was used instead of a Pt plate for surface pressure measurements. The subphase used for the experiments was prepared from deionized water (TKA GenPure Labor & Reinstwassertechnik Christian Wiesenack, Jena, Germany) with a conductivity of  $< 0.056 \mu\text{S cm}^{-1}$ . Before the experiments, the subphase purity was checked by measuring the surface pressure at maximum surface compression ( $\pi < 0.15 \text{ mN m}^{-1}$ ). To obtain the  $\pi$ -A isotherms, polymer solutions with different concentration of  $0.5\text{--}4 \text{ mg ml}^{-1}$  were prepared by dissolving them in HPLC grade chloroform. The solutions were stable at room temperature for several weeks. They were spread on the subphase using a digital syringe. After spreading the solutions, there was a 20 min waiting time for complete solvent evaporation. The compression rate used for recording the Langmuir isotherm was  $120 \text{ \AA}^2 \text{ molecule}^{-1} \text{ min}^{-1}$ , whereas the BAM and epifluorescence images were recorded with a compression rate of  $80 \text{ \AA}^2 \text{ molecule}^{-1} \text{ min}^{-1}$ .

#### 2.2.2. Microscopy

BAM (NFT Mini BAM, Nano-film technology, Valley View, USA) provided images of the morphology of the Langmuir films with a lateral resolution of  $5 \mu\text{m}$ . Epifluorescence images were recorded with an Axio Scope A1 Vario epifluorescence microscope (Carl Zeiss Microimaging, Jena, Germany) equipped with an EC Epiplan-NEOFLUAR 50x objective and a Hamamatsu EM-CCD digital camera. The images were contrast adjusted during the *in situ* observations. The aqueous subphase contained  $0.1 \text{ mg mL}^{-1}$  rhodamine 123 fluorescence dye (6-amino-9-(2-methoxycarbonylphenyl)xanthen-3-ylidene]azanium chloride). AFM

images of the Langmuir-Blodgett films were obtained in tapping mode using a Multimode 8 AFM (Bruker, Santa Barbara, USA) and a standard silicon cantilever (NSC15, Mikromash, Ore, USA) with a resonance frequency of  $325 \text{ kHz}$  and spring constant of  $40 \text{ N m}^{-1}$ . Drive amplitude of  $8.0\text{--}30 \text{ mV}$ , set point of  $350\text{--}400 \text{ mV}$ , and a scan rate of  $1 \text{ Hz}$  were used as settings for the AFM instrument. The captured AFM images were processed by Gwyddion software.

#### 2.2.3. Langmuir-Blodgett (LB) film transfer

For the preparation of LB films, freshly cleaved mica was used as solid support. The transfer was performed using a KSV Langmuir trough (Helsinki, Finland) equipped with an automated substrate holder. During the transfer the surface pressure was kept constant. The substrate was vertically fixed to the holder and immersed in the subphase (around  $8 \text{ mm}$ ). When the surface pressure reached the transferring pressure, the submerged substrate was moved upward with a speed of  $0.1 \text{ mm min}^{-1}$  which resulted in a PPE monolayer being transferred to the substrate. After that, the substrate was dried at room temperature and stored in a sealed box for later measurements.

#### 2.2.4. Infrared reflection absorption spectroscopy (IRRAS)

IRRAS experiments were performed using a Bruker Vector 70 FT-IR spectrometer combined with a Langmuir trough (Riegler & Kirstein, Germany) of  $30 \times 6 \text{ cm}^2$  and a circular reference trough ( $d = 6 \text{ cm}$ ) to measure the spectrum of the bare water surface. The Langmuir trough was equipped with a Wilhelmy pressure sensor and two movable barriers to permit film compression. The temperature was kept constant at  $20^\circ\text{C}$  by a circulating water bath. To obtain the spectra, a polarized IR beam was directed to the air-water interface of the Langmuir trough at a particular angle of incidence  $\varphi$  relative to the surface normal. The reflected IR beam was detected using a liquid nitrogen-cooled MCT detector. The reflectance absorbance (RA) spectra shown here were calculated following the relation  $RA = -\lg(R/R_0)$ , where  $R$  and  $R_0$  represent the IR reflectivity of the sample and the reference trough, respectively. The reflectivity spectra were repeatedly recorded in the sequence: one reference spectrum ( $R_0$ ) followed by 5 sample spectra ( $R$ ), while the Langmuir film was continuously compressed with a small compression rate of  $25 \text{ \AA}^2 \text{ molecule}^{-1} \text{ min}^{-1}$ . The resolution, the scanner speed and the number of scans in all experiments were  $4 \text{ cm}^{-1}$ ,  $160 \text{ kHz}$  and  $1000$ , respectively. A zero filling factor of two was applied before Fourier transformation of the averaged interferograms resulting in a nominal spectral resolution of  $2 \text{ cm}^{-1}$ . Spectra were recorded with the p-polarized IR beam at an angle of incidence of  $40^\circ$ .

### 3. Results and discussion

#### 3.1. The Langmuir isotherm

Fig. 1 shows the surface pressure-area per monomer unit ( $\pi$ - $A$ ) Langmuir isotherm of PPE together with the elastic modulus as a function of  $A$  (see inset). The surface pressure starts to increase at  $A = 0.95 \text{ nm}^2$  and reaches about  $4.5 \text{ mN m}^{-1}$  at  $A = 0.85 \text{ nm}^2$ . After the solvent evaporation the polymer chains form pancake-like island separated by water and compression does not lead to an increase of  $\pi$ . At  $A = 0.95 \text{ nm}^2$  the pancakes come into contact and form a continuous polymer film, a process that is finished at  $A = 0.85 \text{ nm}^2$ . The inflection point of the Langmuir isotherm can be obtained from the elastic modulus  $\epsilon$ , which is calculated from the  $\pi$ - $A$  isotherm using equation (1) as a function of  $A$  and the change in surface pressure with area per repeating unit  $\frac{d\pi}{dA}$ . A maximum at  $\pi \approx 2.3 \text{ mN m}^{-1}$  and  $A \approx 0.89 \text{ nm}^2$  (see inset of Fig. 1) is determined as characteristic values for this transition. Details for the determination of the elastic modulus can be found in the supporting document (S1).

$$\epsilon = -A \left( \frac{d\pi}{dA} \right)_{T=\text{const}} \quad (1)$$

Further compression leads to an extended plateau in the isotherm indicative for a thermodynamic 1st order phase transition in two-dimensional systems [24]. The occurrence of the plateau is obviously related to the crystallization of the PPE, i.e. the crystallographic packing of the n-alkane chains between the phosphate groups. The plateau region ends at a limiting area of  $A_0 = 0.24 \text{ nm}^2$  per repeating unit. It is given by the intersection of the maximum slope line of the  $\pi$ - $A$  isotherm and the slope of the plateau region. The cross-sectional area of an alkyl chain in the pseudo-hexagonal or rotator phase without tilt is  $0.2 \text{ nm}^2$  [23,25,26]. The minor difference of the values can be explained by a tilt of the alkyl chain by  $34^\circ$  with respect to the surface normal ( $\cos(34^\circ) = 0.2 \text{ nm}^2 / 0.24 \text{ nm}^2$ ) [27]. The limiting area is also in the range of the space requirement of a phosphate group of  $0.23 \text{ nm}^2$  [28]. Upon further compression, a sharp increase of the surface pressure up to  $\sim 48 \text{ mN m}^{-1}$  is observed. The occurrence of an additional maximum of the elastic modulus of the Langmuir film at  $25 \text{ mN m}^{-1}$  (see inset of Fig. 1) indicates another process in the Langmuir film. For the assignment of this process microscopic techniques will be employed.

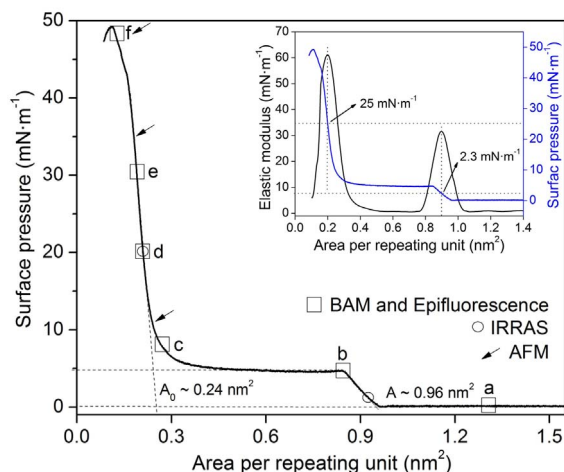


Fig. 1.  $\pi$ - $A$  isotherm of the polyphosphoester at  $20^\circ\text{C}$  measured with a compression speed of  $120 \text{ \AA}^2 \text{ molecule}^{-1} \text{ min}^{-1}$ . The squares indicate  $\pi$ - $A$  values where BAM and epifluorescence images are captured. The arrows mark  $\pi$ - $A$  values where LB films are transferred for AFM measurements. IRRAS spectra are recorded in the  $\pi$ - $A$  range between the two circles. The inset shows the elastic modulus and surface pressure as a function of the area per repeating unit.

#### 3.2. BAM and epifluorescence microscopy

BAM and epifluorescence microscopy images taken at different points of the Langmuir isotherm are shown in Fig. 2. The BAM image at  $\pi = 0 \text{ mN m}^{-1}$  and  $A = 1.3 \text{ nm}^2$  shows a homogeneous film without phase separation within the resolution limit of BAM (Fig. 2a, left). However, the corresponding epifluorescence microscopy image shows already some tiny dark spots (Fig. 2a, right) which have a diameter of  $\sim 0.5 \mu\text{m}$ . Obviously, some small crystalline entities are formed after spreading the polymer solution on the water surface and chloroform evaporation [12]. The dark color indicates that crystallization leads to an exclusion of the fluorescence dye initially located in the amorphous regions of the polymer. This is in agreement with the enrichment of rhodamine 123 in lipid membranes [29]. After further compression at  $\pi = 4.6 \text{ mN m}^{-1}$  and  $A = 0.85 \text{ nm}^2$  a complete polymer monolayer is formed. The crystalline areas increase in size and thus they are also observable by BAM (Fig. 2b, left). Some of these domains have a hexagonal appearance in the epifluorescence microscopy images (Fig. 2b, right). Further compression across the plateau region of the Langmuir isotherm to  $\pi = 8.0 \text{ mN m}^{-1}$  and  $A = 0.27 \text{ nm}^2$  leads to a further increase of the crystalline domains in the polymer film (Fig. 2c). All observed domains have an almost hexagonal habit in the epifluorescence microscopy image shown in Fig. 2c, right. Thus, the plateau region can be assigned unambiguously to the crystallization process of PPE in the Langmuir film.

A further series of BAM and epifluorescence microscopy images is taken after passing the limiting area of  $A_0 = 0.24 \text{ nm}^2$  of the Langmuir isotherm upon film compression (Fig. 3).

All images show a heterogeneous film structure caused by polymer crystallization. Most striking compared to the previous images shown in Fig. 2 is the fact that a contrast inversion appeared in the epifluorescence microscopy images taken at  $20$  and  $30 \text{ mN m}^{-1}$ , respectively. Now the crystals appear bright and the surrounding film is dark. This is obviously caused by the disintegration of the polymer crystals upon compression which leads to an influx of fluorescence dye into the crystalline areas of the polymer film. The cracks or folds in the crystals are most obvious in the epifluorescence microscopy image of Fig. 3e and indicated by yellow arrows. This is in agreement with the decrease of the elasticity modulus in this range of the Langmuir isotherm as shown in inset of Fig. 1. After further compression until the complete film collapse at  $\pi = \sim 48 \text{ mN m}^{-1}$  and  $A = 0.13 \text{ nm}^2$  a complete change of the crystalline entities from a hexagonal structure to a fibrillary structure is observed in BAM and epifluorescence microscopy (see Fig. 3f). After these changes the crystals appear now dark in epifluorescence images again and the surrounding area is bright. These are apparently fractured crystals floating on the water subphase.

#### 3.3. LB film characterization by AFM

The Langmuir film is transferred to mica by the Langmuir-Blodgett (LB) technique at different  $\pi$ - $A$  values as indicated in Fig. 1. The LB films are studied by AFM as shown in Fig. 4. The overall morphology of the LB films is in good agreement with the epifluorescence microscopy images captured directly on the water surface. Fig. 4a shows the crystalline entities obtained after LB film transfer at  $\pi = 10 \text{ mN m}^{-1}$  and  $A = 0.25 \text{ nm}^2$ . All crystals with a lateral dimension of  $10$ – $20 \mu\text{m}$  have in their center a tiny nucleation side. It has a larger height of  $15$ – $30 \text{ nm}$  compared to the other parts of the crystal. It should be noted that the AFM images were recorded with a resolution of  $512 \times 512$  pixels of the  $50 \mu\text{m} \times 50 \mu\text{m}$  image, where one pixel line has  $\sim 98 \text{ nm}$  size and the diameter of this 3D tiny entity is  $\sim 600 \text{ nm}$ . Therefore, the central features are roughly resolved. Nevertheless, these central features are always present in the crystals under investigation and also reported in literature [30]. It seems possible that these three dimensional nuclei are formed during the solvent evaporation after spreading the polymer solution on the water surface [15] which is in agreement with the



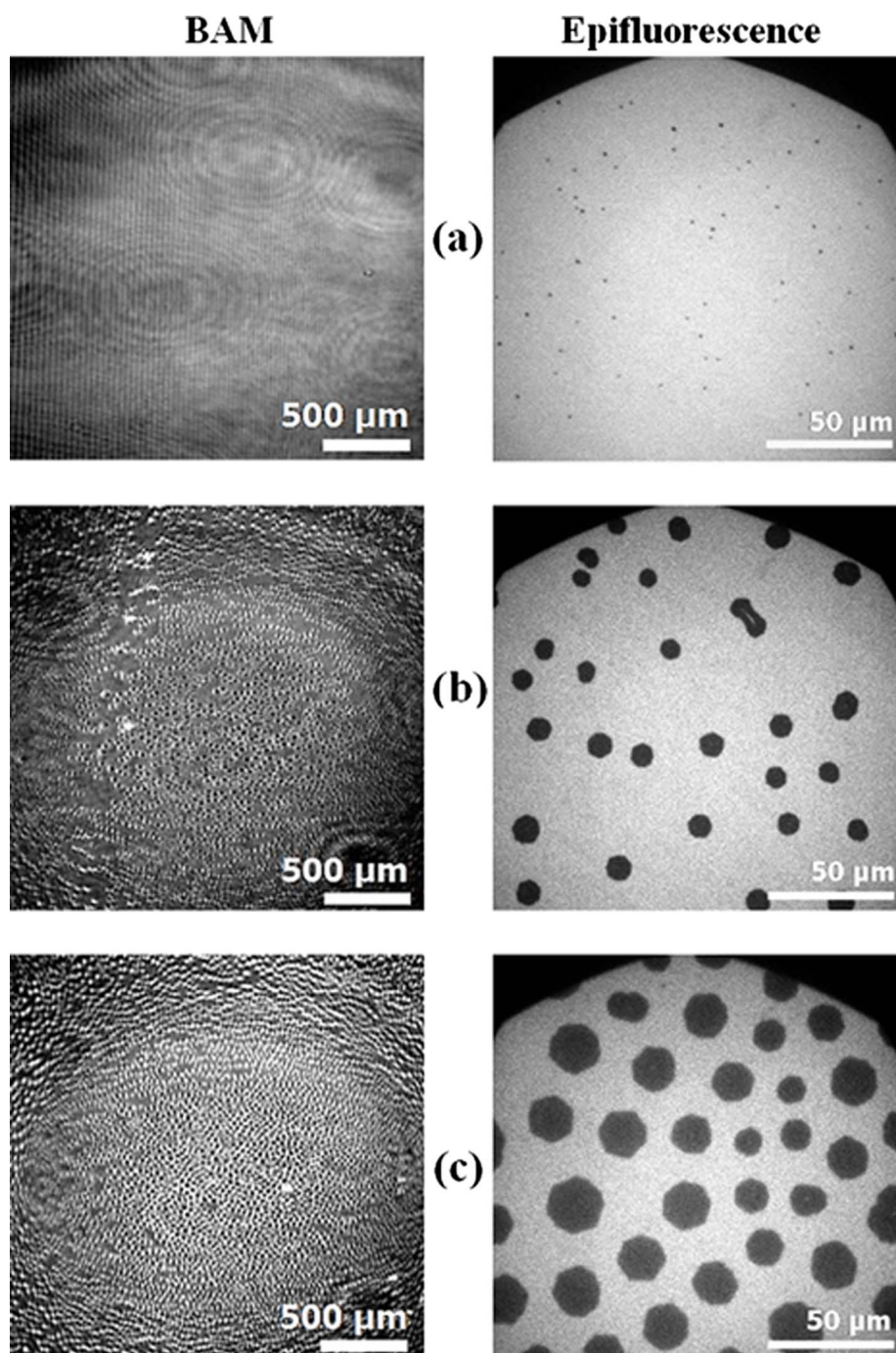


**Fig. 2.** BAM images (left) and epifluorescence microscopy images (right) of PPE captured during film compression on the Langmuir trough at selected  $\pi$  and  $A$  values. (a)  $0 \text{ mN m}^{-1}$ ,  $1.3 \text{ nm}^2$ , (b)  $4.6 \text{ mN m}^{-1}$ ,  $0.85 \text{ nm}^2$ , (c)  $8.0 \text{ mN m}^{-1}$ ,  $0.27 \text{ nm}^2$ .

epifluorescence image as shown in Fig. 2 (a). Additionally, this nucleus is sometimes surrounded by an area of  $5 \text{ nm}$  height. The thickness of the crystals themselves is usually in the range of  $2.5 \text{ nm}$  as can be seen in the height profile of Fig. 4a. Thus, the crystal thickness is determined by the length of the polymer repeat unit. The crystal is formed by the regular arrangement of the  $(\text{CH}_2)_{20}$  groups mainly in all-trans conformation as it is observed in bulk by the wide angle X-ray scattering pattern [6]. The polyethylene like crystals formed on the water surface have than on their fold surfaces the phenylphosphate groups located. The slightly smaller crystal thickness compared to the length of a monomer unit can be explained by the chain tilt, a phenomenon well established for polyethylene crystals [9–11]. The estimated chain tilt angle  $\phi$  is  $\sim 34^\circ$  ( $\phi = \arccos 2.5 \text{ nm}/3 \text{ nm}$ ) which is calculated

following the relation (2)

$$\phi = \arccos\left(\frac{L_c}{L_{mu}}\right) \quad (2)$$

where  $L_c$  and  $L_{mu}$  represent the lamella thickness and the length of a monomer unit.

These data agree very well with the Langmuir film measurements discussed above. Fig. 4b shows an AFM image of an LB film transferred at  $\pi = 35 \text{ mN m}^{-1}$  and  $A = 0.18 \text{ nm}^2$ . Two typical phenomena are observed. The crystals show folds with a larger height than the crystal and some cracks appear too. These phenomena are also observed in crystals of the Langmuir film directly on the water surface by epifluorescence microscopy (cf. Fig. 3e). The cracks allow for the

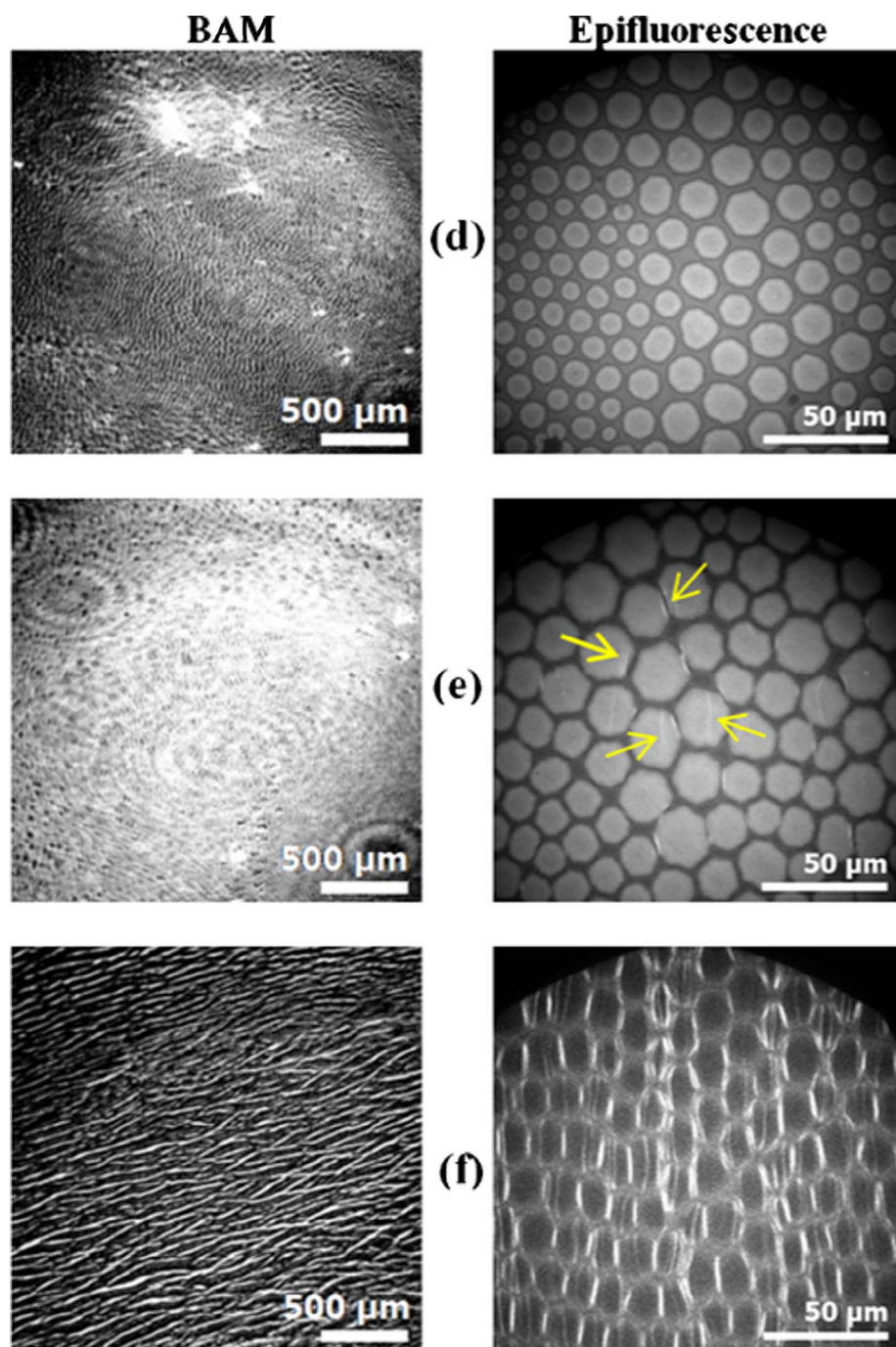


**Fig. 3.** BAM images (left) and epifluorescence microscopy images (right) of PPE captured during film compression on the Langmuir trough at selected  $\pi$  and  $A$  values. (d)  $20 \text{ mN m}^{-1}$ ,  $0.20 \text{ nm}^2$ , (e)  $30 \text{ mN m}^{-1}$ ,  $0.19 \text{ nm}^2$ , the yellow arrows indicate cracks and folds in the crystals, (f)  $48 \text{ mN m}^{-1}$ ,  $0.13 \text{ nm}^2$ .

determination of the crystal thickness which is now in the range of  $\sim 3 \text{ nm}$  (see height profile of Fig. 4b). Since this is approximately the length of a monomer unit, the  $(\text{CH}_2)_{20}$  chains are now oriented perpendicular to the water surface and the chain tilt angle is now  $0$  ( $\phi = \arccos 3 \text{ nm}/3 \text{ nm}$ ). This phenomenon has been observed for the small molecules as well as for polymers [31,32] and can be related to the intracrystalline mobility [33] as well as the sliding of crystalline blocks. Finally, LB films are prepared at  $\pi = 48 \text{ mN m}^{-1}$  and  $A = 0.13 \text{ nm}^2$ , the range of the complete collapse of the Langmuir film (see Fig. 4c). Several ribbon-like crystals have formed with non-uniform heights.

#### 3.4. Infrared reflection absorption spectroscopy

IRRAS is a powerful tool to study the behavior of polymers in Langmuir films on the air-water interface [19,34,35]. Polymers with long  $(\text{CH}_2)_n$  chains in their backbone are especially suitable for IRRAS studies since their methylene stretching vibrations give rise to intense reflection-absorption bands, whose position depends on the alkyl chain conformation and whose intensity depends on surface density and chain orientation. The ordering behavior of polymethylene chains has extensively been studied in Langmuir films of fatty acids and



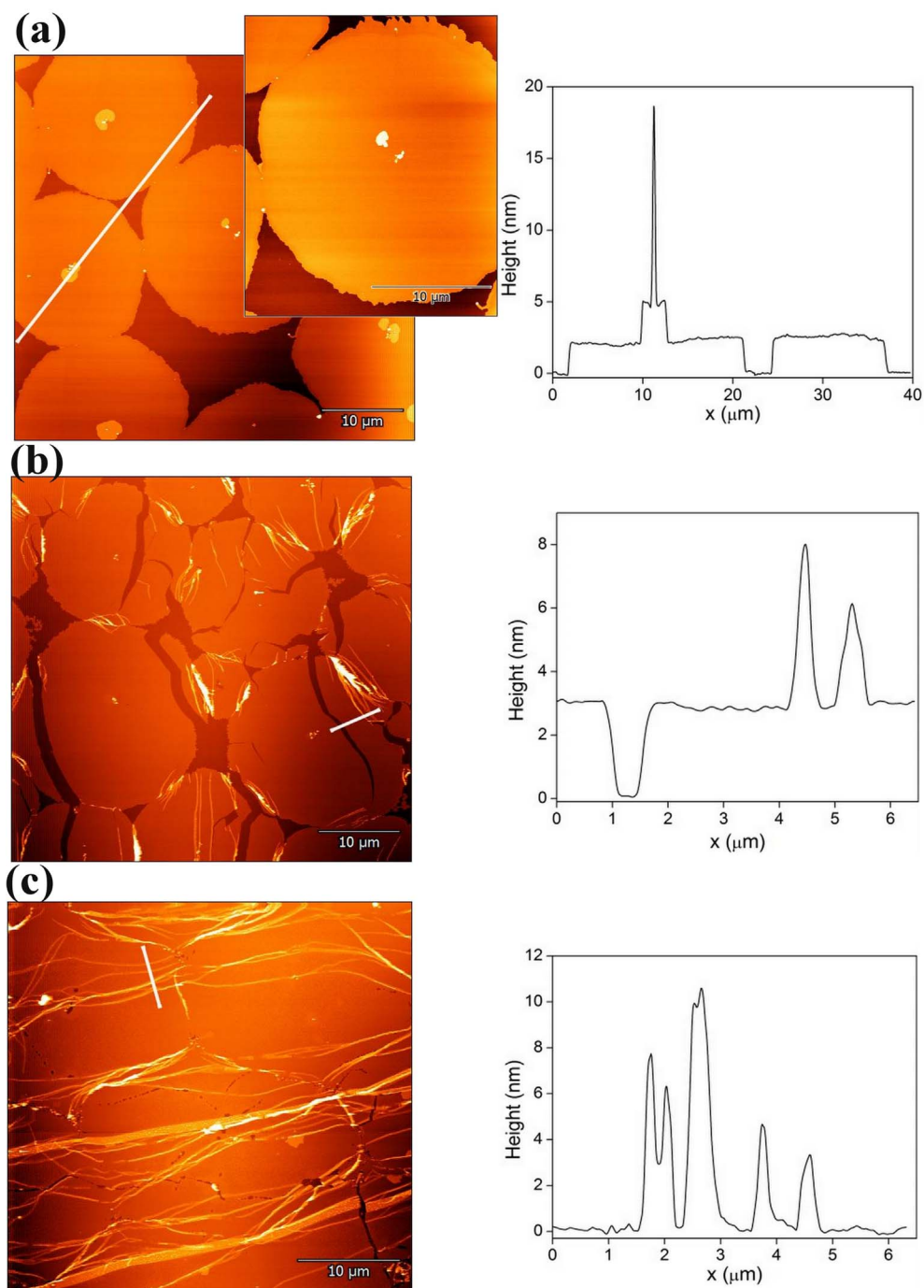


Fig. 4. AFM height image of LB films transferred at (a)  $\pi = 10 \text{ mN m}^{-1}$  and  $A = 0.25 \text{ nm}^2$ , inset shows the zooming of the middle crystal (b)  $\pi = 35 \text{ mN m}^{-1}$  and  $A = 0.18 \text{ nm}^2$ , (c)  $\pi = 48 \text{ mN m}^{-1}$  and  $A = 0.13 \text{ nm}^2$ . The respective height profiles are taken along the lines shown in the AFM images. Additionally, the consistency of the thickness measurements before and after the cracks with several line profiles is shown in supporting document (S2).

phospholipids [36–38]. Fig. 5a shows the IRRA spectra of PPE measured on the water surface at the angle of incidence of  $40^\circ$  with p-polarized radiation. The spectra were recorded during continuous compression of the PPE Langmuir film from an area per repeating unit of  $A = 0.94 \text{ nm}^2$  and a surface pressure  $\pi = 1.2 \text{ mN m}^{-1}$  to  $A = 0.2 \text{ nm}^2$  and  $\pi = 20 \text{ mN m}^{-1}$ , a range which covers the extended plateau region of the Langmuir isotherm (cf. Fig. 1). The assignment of the IR bands shown in Fig. 5a is done according to the literature [39–42]. The shift of the  $\text{CH}_2$  symmetric and antisymmetric stretching bands ( $\nu_s$  and  $\nu_{as}$ ) as a function of  $\pi$  (see Fig. 5b) provides information on the ordering behavior of the n-alkyl chains [36,38,43]. It can be seen that at low surface pressures, the  $\text{CH}_2$  stretching vibration bands are observed at high wave

numbers of  $\nu_{as} = 2926.9 \text{ cm}^{-1}$  and  $\nu_s = 2856.8 \text{ cm}^{-1}$ . These high wavenumbers reveal the fluid-like state of PPE n-alkyl chains with a high content of gauche conformations at low compression, i.e. at surface pressures smaller than the plateau value. This has also been reported for long-chain hydrocarbon molecules [36,38,43]. When increasing the surface pressure upon compression, the bands are shifted to lower wavenumbers ( $\nu_{as} = 2916.5 \text{ cm}^{-1}$  and  $\nu_s = 2849.7 \text{ cm}^{-1}$ ) at a surface pressure of  $4.5 \text{ mN m}^{-1}$ , i.e. the plateau pressure of the compression isotherm. This indicates a liquid to solid phase transition (i.e., crystallization) where the  $(\text{CH}_2)_{20}$  chains are densely packed in stretched all-trans conformations within the solid phase. The extremely low wavenumbers of the stretching vibrational bands are indicative for intense

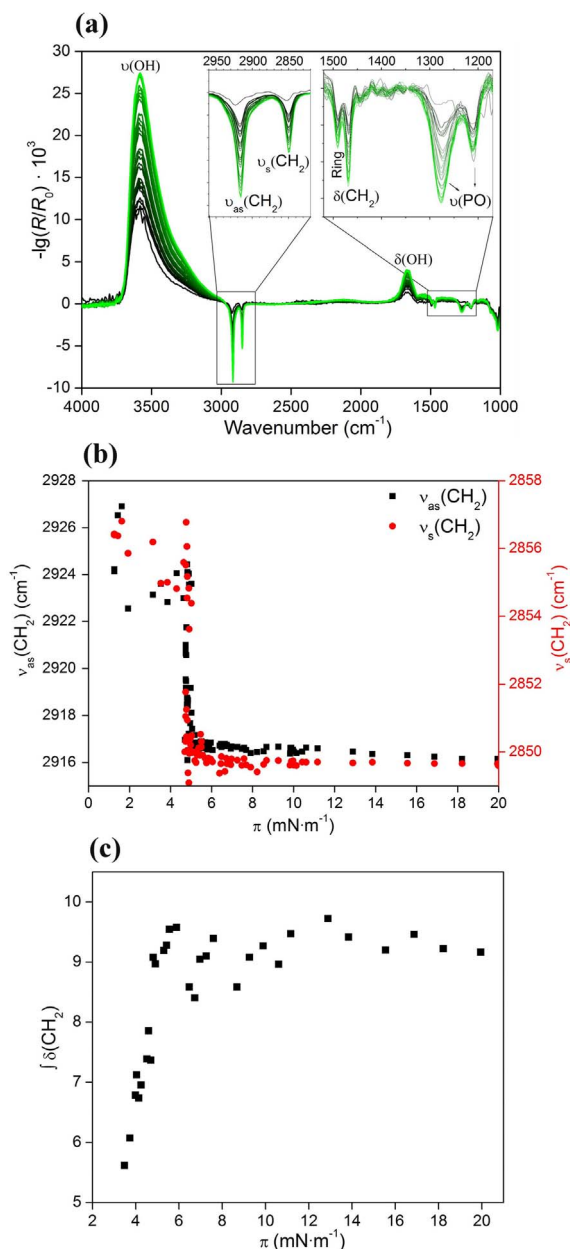


Fig. 5. (a) IRRA spectra of PPE recorded an angle of incidence  $\varphi = 40^\circ$  with p-polarization during continuous compression from  $0.94 \text{ nm}^2$  per repeat unit (black) to  $0.2 \text{ nm}^2$  per repeat unit (green). The insets show a zoom of the most prominent bands, which are assigned in the figure. (b) Shift of the position of antisymmetric (black, left scale) and symmetric (red, right scale)  $\text{CH}_2$  stretching vibrational bands as a function of surface pressure. (c) Integral intensity of the  $\text{CH}_2$  symmetric bending vibrational band normalized to the molecular area density within the film as a function of surface pressures. (For interpretation of the references to colour in this figure legend, the reader is referred to the web version of this article.)

inter-chain vibrational coupling, which only occurs when the rotation about the chain main axis is restricted, i.e., in a crystalline packing of the alkyl chains. A further compression beyond the plateau region to  $A = 0.20 \text{ nm}^2$  and  $\pi = 20 \text{ mN m}^{-1}$  shows no further shift of the  $\text{CH}_2$  bands which reveals that the polymer crystallization in the Langmuir film is finished at the end of the plateau region. Another indication of crystallization can be revealed by focusing on the intensity of  $\text{CH}_2$  symmetric bending vibrational band (scissoring).

The integral intensity of the  $\delta(\text{CH}_2)$  band normalized to the molecular area density within the Langmuir film is shown in Fig. 5c. Due to normalization any intensity variations can be attributed to molecular

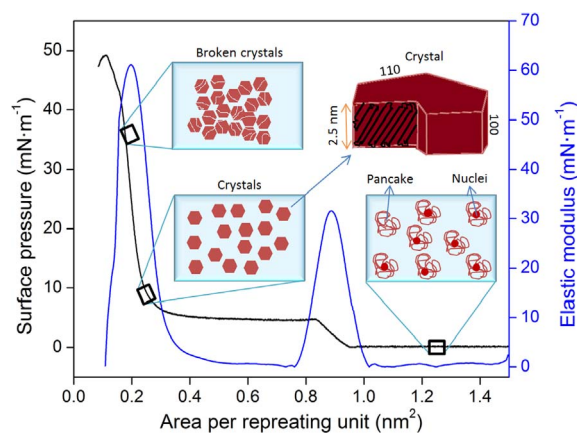


Fig. 6. Schematic presentation of the ordering behavior of PPE on the water surface upon compression.

rearrangements affecting the absorption coefficient of the vibration. The normalized band intensity increases in the range of the plateau pressure ( $3\text{--}5 \text{ mN m}^{-1}$ ) and stays constant at any further compression. The increases of the intensity of this band with increasing crystallinity is typical and has also been reported for PE [44,45]. Thus the  $\delta(\text{CH}_2)$  band intensity can be used as another marker for PPE crystallization upon compression. Additionally, the  $\text{CH}_2$  scissoring band at  $\sim 1469 \text{ cm}^{-1}$  could be an indication of hexagonal crystal packing [46]. However, it should be noted that the solution cooling and the melt crystallization of this polymer studied by electron diffraction reveal a pseudo-hexagonal crystal packing [23].

#### 4. Conclusions

The experimental results are summarized in Fig. 6.

After spreading the polymer solution and evaporation of the solvent, the polymer coils form pancakes and first nuclei of polymer crystals appear. When the pancakes come into contact upon compression the surface pressure increases together with the elasticity modulus indicating that a uniform Langmuir film is formed. During further compression in the plateau range of the Langmuir isotherm, PPE forms single crystal like entities with mainly hexagonal habit. The  $(\text{CH}_2)_{20}$  chains are tilted. The crystallization process can also be followed by IRRAS. Especially the  $\nu_s$  and  $\nu_{as}$   $\text{CH}_2$  bands are sensitive to follow the crystallization process. AFM studies of LB films indicate that the crystal thickness is determined by the length of a polymer repeat unit containing one phenylphosphate group and 20  $\text{CH}_2$  groups. Further compression leads to a steep increase of the surface pressure and the elasticity modulus. In this range the chain tilt disappears and the chains arrange perpendicular to the water surface. After reaching a maximum, the elasticity modulus decreases again as a result of the destruction of the single crystal like entities. The surface pressure increases up to  $48 \text{ mN m}^{-1}$  indicating that PPE is a real amphiphilic polymer with a hydrophilic phenylphosphate group and the lipophilic  $\text{CH}_2$  groups. For further analyses for the effect of the chain defect (phenyl phosphate group) on the crystallographic behavior [47], it is necessary to employ GI-WAXS measurement [48]. This is also caused by the fact that a hexagonal habit of the macroscopic crystal does not necessarily mean that a crystallographic hexagonal phase is present [49].

#### Notes

The authors declare no competing financial interest.

## Acknowledgement

This work was supported by Deutsche Forschungsgemeinschaft (DFG, SFB TRR 102, project B07). AFM measurements were carried out within the cooperation of the SFB TRR 102 (project B03, Thomas Thurn-Albrecht).

## Appendix A. Supplementary material

Supplementary data associated with this article can be found, in the online version, at <https://doi.org/10.1016/j.eurpolymj.2018.03.001>.

## References

- [1] E.W. Fischer, Stufen- und spiralförmiges Kristallwachstum bei Hochpolymeren, *Z. Naturf. A* 12 (1957) 753–754.
- [2] A. Keller, A note on single crystals in polymers: evidence for a folded chain configuration, *Philos. Mag.* 2 (1957) 1171–1175.
- [3] P.J. Flory, On the morphology of the crystalline state in polymers, *J. Am. Chem. Soc.* 84 (1962) 2857–2867.
- [4] B. Wunderlich, T. Davidson, Extended-chain crystals. I. General crystallization conditions and review of pressure crystallization of polyethylene, *J. Polym. Sci. Part A-2 Polym. Phys.* 7 (1969) 2043–2050.
- [5] J. Hengstenberg, XLIII. Röntgenuntersuchungen über den Bau der C-Ketten in Kohlenwasserstoffen ( $C_nH_{2n+2}$ ), *Zeitschrift Für Krist. – Cryst. Mater.* 67 (1928) 583–594.
- [6] C.W. Bunn, The crystal structure of long-chain normal paraffin hydrocarbons. The shape of the  $CH_2$  group, *Trans. Faraday Soc.* 35 (1939) 482–491.
- [7] D.C. Bassett, S. Block, G.J. Piermarini, A high-pressure phase of polyethylene and chain-extended growth, *J. Appl. Phys.* 45 (1974) 4146–4150.
- [8] P.W. Teare, D.R. Holmes, Extra reflections in the X-ray diffraction pattern of polyethylenes and polymethylenes, *J. Polym. Sci.* 24 (1957) 496–499.
- [9] K.J. Fritzsche, K. Mao, K. Schmidt-Rohr, Avoidance of density anomalies as a structural principle for semicrystalline polymers: the importance of chain ends and chain tilt, *Macromolecules* 50 (2017) 1521–1540.
- [10] C. Wutz, M.J. Tanner, M. Brookhart, E.T. Samulski, Where are the chain ends in semicrystalline polyethylene? *Macromolecules* 50 (2017) 9066–9070.
- [11] J.D. Hoffman, R.L. Miller, Kinetic of crystallization from the melt and chain folding in polyethylene fractions revisited: theory and experiment, *Polymer* 38 (1997) 3151–3212.
- [12] C.H.M. Weber, A. Chiche, G. Krausch, S. Rosenfeldt, M. Ballauff, L. Harnau, I. Gotker-Schnetmann, Q. Tong, S. Mecking, Single lamella nanoparticles of polyethylene, *Nano Lett.* 7 (2007) 2024–2029.
- [13] A. Godin, S. Mecking, Aqueous dispersions of multiphase polyolefin particles, *Macromolecules* 49 (2016) 8296–8305.
- [14] A.V. Sorokin, Langmuir-Blodgett films of polyethylene, *J. Appl. Phys.* 92 (2002) 5977–5981.
- [15] J. Kumaki, Monolayer of polystyrene monomolecular particles on a water surface studied by Langmuir-type film balance and transmission electron microscopy, *Macromolecules* 21 (1988) 749–755.
- [16] B. Li, Y. Wu, M. Liu, A.R. Esker, Brewster angle microscopy study of poly( $\epsilon$ -caprolactone) crystal growth in Langmuir films at the air/water interface, *Langmuir* 22 (2006) 4902–4905.
- [17] J. Kumaki, T. Kawauchi, E. Yashima, Two-dimensional folded chain crystals of a synthetic polymer in a Langmuir-Blodgett film, *J. Am. Chem. Soc.* 127 (2005) 5788–5789.
- [18] C. Fuchs, K. Busse, A.-K. Flieger, J. Kressler, Polymer crystallization on the surface of water or aqueous salt solutions, *Chem. Eng. Technol.* 39 (2016) 1333–1340.
- [19] C. Fuchs, H. Hussain, C. Schwieger, M. Schulz, W.H. Binder, J. Kressler, Molecular arrangement of symmetric and non-symmetric triblock copolymers of poly(ethylene oxide) and poly(isobutylene) at the air/water interface, *J. Colloid Interf. Sci.* 437 (2015) 80–89.
- [20] K.B. Wagener, J.M. Boncella, J.G. Nel, Acyclic diene metathesis (ADMET) polymerization, *Macromolecules* 24 (1991) 2649–2657.
- [21] K.N. Bauer, H.T. Tee, M.M. Velencoso, F.R. Wurm, Main-chain poly(phosphoester): history, syntheses, degradation, bio- and flame-retardant applications, *Prog. Polym. Sci.* 73 (2017) 61–122.
- [22] F. Marsico, M. Wagner, K. Landfester, F.R. Wurm, Unsaturated polyphosphoesters via acyclic diene metathesis polymerization, *Macromolecules* 45 (2012) 8511–8518.
- [23] Y.R. Zheng, H.T. Tee, Y. Wei, X.L. Wu, M. Mezger, S. Yan, K. Landfester, K. Wagener, F.R. Wurm, I. Lieberwirth, Morphology and thermal properties of precision polymers: the crystallization of butyl branched polyethylene and polyphosphoesters, *Macromolecules* 49 (2016) 1321–1330.
- [24] S. Ni, W. Lee, B. Li, A.R. Esker, Thermodynamics of the liquid expanded to condensed phase transition of poly(L-lactic acid) in Langmuir monolayers, *Langmuir* 22 (2006) 3672–3677.
- [25] N. Wentzel, S.T. Milner, Crystal and rotator phases of n-alkanes: a molecular dynamics study, *J. Chem. Phys.* 132 (2010) 44901–44910.
- [26] V.M. Weiss, T. Naolou, E. Amado, K. Busse, K. Mäder, J. Kressler, Formation of structured polygonal nanoparticles by phase-separated comb-like polymers, *Macromol. Rapid Commun.* 33 (2012) 35–40.
- [27] M. Pulst, C. Schneemann, P. Ruda, Y. Golitsyn, A.K. Grefe, B. Stühner, K. Busse, D. Reichert, J. Kressler, Chain tilt and crystallization of ethylene oxide oligomers with midchain defects, *ACS Macro Lett.* 6 (2017) 1207–1211.
- [28] W. Stumm, J.J. Morgan, *Aquatic Chemistry: Chemical Equilibria and Rates in Natural Waters*, John Wiley & Sons, New Jersey, 1996.
- [29] L.B. Chen, Mitochondrial membrane potential in living cells, *Ann. Rev. Cell Biol.* 4 (1988) 155–181.
- [30] H. Zhang, M. Yu, B. Zhang, R. Reiter, M. Vielhauer, R. Mülhaupt, J. Xu, G. Reiter, Correlating polymer crystals via self-induced nucleation, *Phys. Rev. Lett.* 112 (2014) 237801–237805.
- [31] C. Stefanu, I. Vilotijevic, G. Brezesinski, P.H. Seeberger, D. Varón, Silva, A comparative structural study in monolayers of GPI fragments and their binary mixtures, *Phys. Chem. Chem. Phys.* 16 (2014) 9259–9265.
- [32] K. Busse, C. Peetla, J. Kressler, Water surface covering of fluorinated amphiphilic triblock copolymers: surface pressure-area and X-ray reflectivity investigations, *Langmuir* 23 (2007) 6975–6982.
- [33] R. Bärenwald, S. Goerlitz, R. Godehardt, A. Osichow, Q. Tong, M. Krumova, S. Mecking, K. Saalwächter, Local flips and chain motion in polyethylene crystallites: a comparison of melt-crystallized samples, reactor powders, and nanocrystals, *Macromolecules* 47 (2014) 5163–5173.
- [34] H. Hussain, A. Kerth, A. Blume, J. Kressler, Amphiphilic block copolymers of poly(ethylene oxide) and poly(perfluorohexylethyl methacrylate) at the water surface and their penetration into the lipid monolayer, *J. Phys. Chem. B.* 108 (2004) 9962–9969.
- [35] E. Amado, A. Kerth, A. Blume, J. Kressler, Infrared reflection absorption spectroscopy coupled with Brewster angle microscopy for studying interactions of amphiphilic triblock copolymers with phospholipid monolayers, *Langmuir* 24 (2008) 10041–10053.
- [36] M.L. Mitchell, R.A. Dluhy, In situ FT-IR investigation of phospholipid monolayer phase transitions at the air-water interface, *J. Am. Chem. Soc.* 110 (1988) 712–718.
- [37] R.G. Snyder, D.G. Cameron, H.L. Casal, D.A.C. Compton, H.H. Mantsch, Studies on determining conformational order in n-alkanes and phospholipids from the 1130  $cm^{-1}$  raman band, *Biochim. Biophys. Acta.* 684 (1982) 111–116.
- [38] R.D. Hunt, M.L. Mitchell, R.A. Dluhy, The interfacial structure of phospholipid monolayer films: an infrared reflectance study, *J. Mol. Struct.* 214 (1989) 93–109.
- [39] L.W. Daasch, D.C. Smith, Infrared spectra of phosphorus compounds, *Anal. Chem.* 23 (1951) 853–868.
- [40] S. Krimm, C.Y. Liang, G.B.B.M. Sutherland, Infrared spectra of high polymers. II. Polyethylene, *J. Chem. Phys.* 25 (1956) 549–562.
- [41] J.R. Nielsen, A.H. Woollett, Vibrational spectra of polyethylenes and related substances, *J. Chem. Phys.* 26 (1957) 1391–1400.
- [42] M. Gliboff, L. Sang, K.M. Kesting, M.C. Schalnau, A. Mudalige, E.L. Ratcliff, H. Li, A.K. Sigdel, A.J. Giordano, J.J. Berry, D. Nordlund, G.T. Seidler, J.L. Brédas, S.R. Marder, J.E. Pemberton, D.S. Ginger, Orientation of phenylphosphonic acid self-assembled monolayers on a transparent conductive oxide: a combined NEXAFS PM-IRRAS, and DFT study, *Langmuir* 29 (2013) 2166–2174.
- [43] C. Schwieger, B. Chen, C. Tschierske, J. Kressler, A. Blume, Organization of t-shaped facial amphiphiles at the air/water interface studied by infrared reflection absorption spectroscopy, *J. Phys. Chem. B* 116 (2012) 12245–12256.
- [44] K. Tashiro, S. Sasaki, M. Kobayashi, Structural investigation of orthorhombic-to-hexagonal phase transition in polyethylene crystal: the experimental confirmation of the conformationally disordered structure by X-ray diffraction and infrared/raman spectroscopic measurements, *Macromolecules* 29 (1996) 7460–7469.
- [45] I. Noda, A.E. Dowrey, C. Marcott, G.M. Story, Y. Ozaki, Generalized two-dimensional correlation spectroscopy, *Appl. Spectrosc.* 54 (2000) 236A–248A.
- [46] M. Oguri, G.S. Gooris, K. Bito, J.A. Bouwstra, The effect of the chain length distribution of free fatty acids on the mixing properties of stratum corneum model membranes, *Biochim. Biophys. Acta* 2014 (1838) 1851–1861.
- [47] M. Pulst, M.H. Samiullah, U. Baumeister, M. Prehm, J. Balko, T. Thurn-Albrecht, K. Busse, Y. Golitsyn, D. Reichert, J. Kressler, Crystallization of poly(ethylene oxide) with a well-defined point defect in the middle of the polymer chain, *Macromolecules* 49 (2016) 6609–6620.
- [48] A. Hexemer, P. Müller-Buschbaum, Advanced grazing-incidence techniques for modern soft-matter materials analysis, *IUCrJ* 2 (2015) 106–125.
- [49] P.G. Orsini, B. Marchese, L. Mazzarella, Morphology of polyethylene single crystals, *J. Polym. Sci. Part A* 1 (1963) 1901–1908.

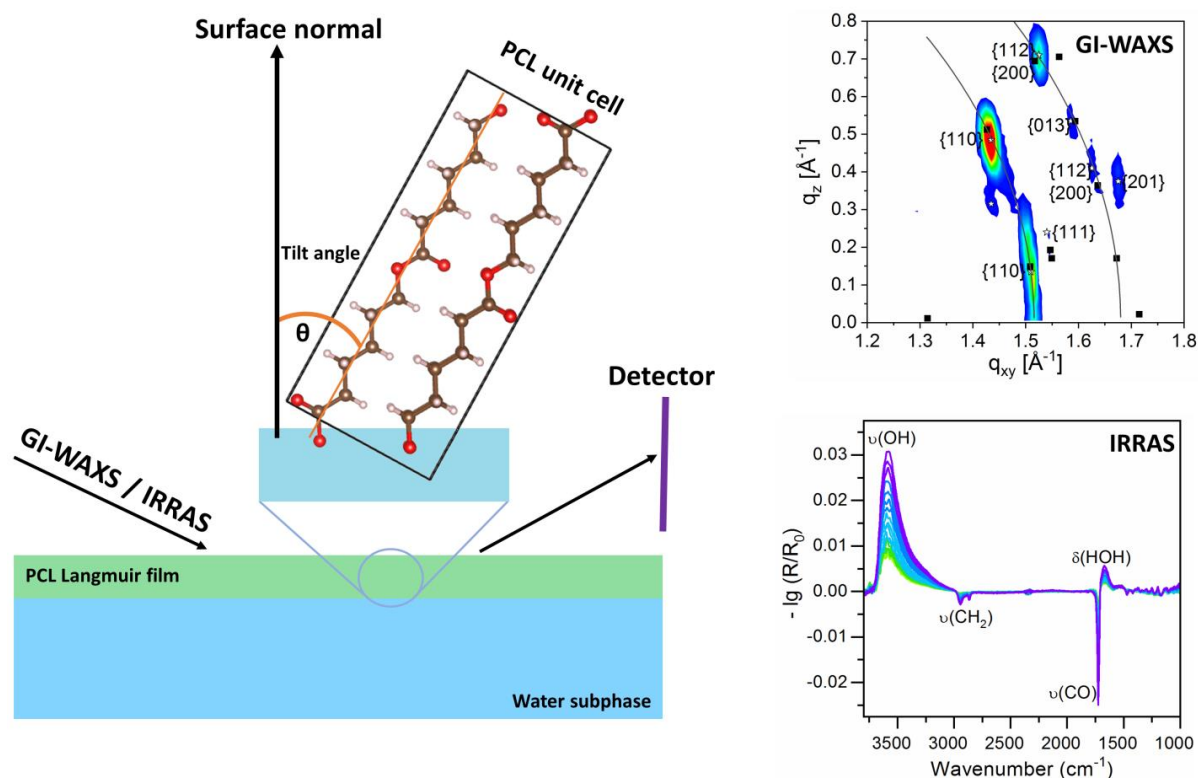
### 3.3 Paper III

#### Crystallization of poly( $\epsilon$ -caprolactone) at the air-water interface studied by IRRAS and GI-WAXS<sup>3</sup>

Nazmul Hasan, Christian Fuchs, Christian Schwieger, Oleksandr Dolynchuk, Karsten Busse, and Jörg Kressler

Polymer 2020, 196, 122468, <https://doi.org/10.1016/j.polymer.2020.122468>

Graphical abstract:



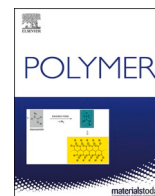
Many fundamental studies on poly( $\epsilon$ -caprolactone) (PCL) crystallization at the air-water interface of a Langmuir trough by measuring  $\pi$ -*mmA* isotherms together with BAM have been reported.<sup>[102,104]</sup> The following paper, however, demonstrates mainly the chain orientation of PCL Langmuir films (crystallites) revealed by IRRAS and GI-WAXS techniques. At various compression states of the  $\pi$ -*mmA* isotherm, chain tilting of PCL from  $\approx 21^\circ$  to  $38^\circ$  relative to the normal of the water surface was identified. The tilting orientation remained the same even when the crystallites were transferred to the solid support as confirmed by GI-WAXS studies.

The author contributions to the following article are: N. Hasan, K. Busse, and J. Kressler designed the research. N. Hasan performed the following experiments such as Langmuir isotherms, BAM, and LB transfer. C. Fuchs, and C. Schwieger did IRRAS. K. Busse and O. Dolynchuk did GI-WAXS experiments. N. Hasan wrote the draft manuscript (GI-WAXS part by K. Busse). All IRRAS figures are constructed from the Ph.D. Thesis (MLU-2017) data of C. Fuchs. All the authors discussed the results, reviewed them, and finalized the paper.

---

<sup>3</sup>The following article is reprinted (adapted) with permission from Polymer 2020, 196, 122468, <https://doi.org/10.1016/j.polymer.2020.122468>. Copyright (2020) Elsevier. The link to the article on the publisher's website is: <https://www.sciencedirect.com/science/article/pii/S0032386120303037?via%3Dihub>. Supporting information is at the link: <https://ars.els-cdn.com/content/image/1-s2.0-S0032386120303037-mmc1.docx>. No changes were made.





# Crystallization of poly( $\epsilon$ -caprolactone) at the air-water interface studied by IRRAS and GI-WAXS

Nazmul Hasan<sup>a</sup>, Christian Fuchs<sup>a</sup>, Christian Schwieger<sup>a,b</sup>, Karsten Busse<sup>a</sup>,  
Oleksandr Dolynchuk<sup>c</sup>, Jörg Kressler<sup>a,\*</sup>

<sup>a</sup> Institute of Chemistry, Martin Luther University Halle-Wittenberg, D-06099, Halle, Germany

<sup>b</sup> Interdisciplinary Research Center HALOmem, Institute for Biochemistry and Biotechnology, Martin Luther University Halle-Wittenberg, 06099, Halle, Germany

<sup>c</sup> Institute of Physics, Martin Luther University Halle-Wittenberg, D-06120, Halle, Germany

## ARTICLE INFO

### Keywords:

Poly( $\epsilon$ -caprolactone)  
Langmuir film  
Crystallization  
IRRAS  
GI-WAXS

## ABSTRACT

Poly ( $\epsilon$ -caprolactone) (PCL) dissolved in chloroform was spread on the water surface of a Langmuir trough and after solvent evaporation, the surface pressure vs area ( $\pi$ -A) Langmuir isotherm was recorded. An extended plateau region indicates a 1st order phase transition related to PCL crystallization as also confirmed by Brewster angle microscopy (BAM). Infrared reflection absorption spectroscopy (IRRAS) and grazing incidence wide angle X-ray scattering (GI-WAXS) reveal details of the PCL crystallization process on a molecular level. The IRRAS and GI-WAXS experiments confirm that crystallization occurs at the plateau region of the  $\pi$ -A Langmuir isotherm. GI-WAXS also confirms that the polymer chains in the crystals are tilted by  $\approx 21^\circ$  with respect to the water surface normal direction. This value is consistent with IRRAS data at a maximum compression state of  $\approx 2 \text{ \AA}^2$ .

## 1. Introduction

Poly( $\epsilon$ -caprolactone) (PCL) has been known to form stable Langmuir films at the air-water interface after spreading the polymer solution, solvent evaporation, and compression on a Langmuir trough [1–6]. This is difficult to understand when assuming that PCL is simply hydrophobic since most hydrophobic polymers as polyolefins or polystyrenes [7] do not form stable Langmuir films on water. They lack some polar groups able to form strong physical bonds with water which prevent the immediate film collapse upon compression. When looking on the chemical structure of PCL (Scheme 1), it becomes clear that this polymer is rather amphiphilic in nature [8,9].

Five hydrophobic  $\text{CH}_2$  groups separate the hydrophilic ester bond system in every repeat unit of PCL [4]. Thus, the  $\text{CH}_2$  groups prevent the water solubility and the polar ester bond system is sufficient to anchor PCL Langmuir films on the air-water interface. The crystallization of PCL has been reported in bulk [13,14], in blends [15–21], in thin films on solid support [22–26] and in Langmuir films [4,6,27–30]. Under all these conditions, PCL seems to crystallize in an orthorhombic unit cell. Each unit cell contains two polymer chains each having two monomer units with a nearly planar zigzag conformation [10–12]. Esker et al. studied extensively the crystallization of PCL on the water surface in

Langmuir films and in Langmuir-Schaefer (LS) films on a solid support [4]. It has been reported that the surface pressure-area ( $\pi$ -A) isotherm of PCL has a 1st order phase transition plateau at  $\approx 11 \text{ mN m}^{-1}$ . It indicates the transition from an amorphous monolayer to lamellar crystals upon isothermal film compression [4]. The mechanism involved in such transition is that upon compression some of the carbonyl groups of amorphous PCL detach from the air-water interface while the chain begins to fold back at the flexible ester linkage. This results in a 3D upright orientation of the PCL chains, being folded above the water surface [4]. This behavior is completely opposite to the Langmuir film of PLA [31] and *i*-PMMA [30,32], where chains stay in a 2D configuration (i.e. parallel to the water surface) due to the higher chain stiffness [30]. Brewster angle microscopy (BAM) reveals domains of butterfly morphology of the PCL crystals for low molar mass PCL (i.e., 2.8–10  $\text{kg mol}^{-1}$ ) [5,6,29]. The phase transition is reversible, i.e. crystalline dendrites disappear upon isothermal film expansion which is denoted as a melting process [4]. Electron diffraction on LS films transferred to a solid support (copper grid) at the end of the plateau region of the respective Langmuir isotherm reveals that the PCL chains are oriented perpendicular to the solid support in an orthorhombic unit cell known from bulk samples [4]. It should be noted that LS film preparation which includes film transferring on a solid substrate and the drying process

\* Corresponding author.

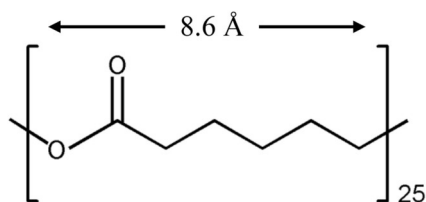
E-mail address: [joerg.kressler@chemie.uni-halle.de](mailto:joerg.kressler@chemie.uni-halle.de) (J. Kressler).

<https://doi.org/10.1016/j.polymer.2020.122468>

Received 13 January 2020; Received in revised form 27 March 2020; Accepted 7 April 2020

Available online 13 April 2020

0032-3861/© 2020 Elsevier Ltd. All rights reserved.



**Scheme 1.** A repeat unit of poly( $\epsilon$ -caprolactone). The length of one repeat unit is calculated from the crystallographic data of PCL [10–12]. The cross-sectional area in the crystalline state of a repeating unit is  $18.6 \text{ \AA}^2$  [6].

may alter the film morphology as well as chain orientation [33]. Therefore, in the present study, crystallization of PCL Langmuir film has been investigated directly on the water surface for the first time by grazing incidence wide angle X-ray scattering (GI-WAXS) and infrared reflection absorption spectroscopy (IRRAS). GI-WAXS is a suitable tool for *in situ* crystallization studies of polymers on the water surface. It provides information on crystallographic data including the chain orientation [34]. Additionally, infrared reflection absorption spectroscopy (IRRAS) [35] is employed which also provides quantitative information of PCL chain orientation with respect to water surface as well as the polymer mean film thickness as a function of the area occupied by PCL chains on the water surface. Thus, the combination of both techniques, i.e. GI-WAXS and IRRAS, allows for the observation of unprecedented details of polymer crystallization on the water surface. For comparison GI-WAXS measurement on PCL Langmuir-Blodgett (LB) films on solid supports have been carried out.

## 2. Experimental section

### 2.1. Materials

The poly( $\epsilon$ -caprolactone) under investigation has a number average molar mass  $M_n$  of  $2800 \text{ g mol}^{-1}$  (equivalent to a degree of polymerization of 25) and a polydispersity  $D$  of 1.33. It was synthesized by ring opening polymerization. The synthesis and the characterization details can be found elsewhere [6,36].

### 2.2. Langmuir isotherm measurement

The surface pressure – mean area per repeating unit ( $\pi$ -A) isotherm was measured using a Langmuir trough (KSV, Helsinki, Finland). The trough was equipped with two moveable barriers and a platinum Wilhelmy plate. The subphase used for the experiment was deionized water with a conductivity of  $<0.056 \text{ \mu S cm}^{-1}$ . The temperature of the subphase was kept at  $20 \text{ }^\circ\text{C}$ . The purity of the subphase was checked by surface pressure measurements at maximum surface compression ( $\pi < 0.15 \text{ mN m}^{-1}$ ). To obtain the  $\pi$ -A isotherms, PCL solutions with a concentration of  $1 \text{ mg ml}^{-1}$  were prepared in chloroform and spread dropwise on the subphase using a digital syringe. After a 20 min waiting time for complete solvent evaporation, the trough surface was compressed with a speed of  $\approx 1 \text{ \AA}^2 (\text{monomer unit})^{-1} \text{ min}^{-1}$  to record a part of the isotherm. These processes were repeated with different spreading volumes in order to obtain the complete isotherm.

### 2.3. Brewster angle microscopy (BAM)

A Brewster angle microscope (NFT Mini BAM, Nano-film engineering, Valley View, USA) was used to monitor the crystallization of PCL during compression. It had a lateral resolution of  $20 \text{ \mu m}$ , with a field view of  $4.8 \times 6.4 \text{ mm}^2$ . The images were captured using the software WinTV (Hauppauge, USA). The imaging of the monolayer was done during the film compression with a speed of  $0.6 \text{ \AA}^2 (\text{monomer unit})^{-1} \text{ min}^{-1}$  at different compression states.

### 2.4. Langmuir-Blodgett (LB) film transfer

A piece of silicon wafer ( $20 \times 10 \text{ mm}^2$ ) was cleaned and mounted to a KSV (Helsinki, Finland) film transfer unit to prepare LB films. The transfer pressure was set to  $\approx 11 \text{ mN m}^{-1}$  at  $A \approx 5 \text{ \AA}^2$ . The substrate was vertically attached to the transfer unit and immersed into the subphase about 8 mm. Afterwards, PCL solution was spread on the water surface and compressed up to the transfer pressure. When the transfer pressure was reached, the submerged silicon substrate was moved upward with a speed of  $0.1 \text{ mm min}^{-1}$ , while the surface pressure was kept constant. This process leads to transfer LB films of PCL on both sides of the substrate. The film was then dried at room temperature and stored in a sealed box for GI-WAXS measurements.

### 2.5. Infrared reflection absorption spectroscopy (IRRAS)

IRRAS experiments were performed in a setup consisting of a Vertex 70 FTIR spectrometer equipped with an A511 reflectance unit (both Bruker Optics, Germany) and a Langmuir trough system (Riegler & Kirstein, Germany) consisting of a  $30 \times 6 \text{ cm}^2$  sample trough and a circular reference trough ( $d = 6 \text{ cm}$ ). Both troughs can be brought into the focus of the IR beam by means of an automated shuttle system. The sample trough contained a Wilhelmy pressure sensor with a filter paper serving as Wilhelmy plate and two movable barriers to permit film compression. The subphase level in both troughs was kept constant by a home build laser controlled pumping system connected to reservoirs of  $\text{H}_2\text{O}$ , which served to compensate for subphase evaporation during the measurements. The troughs were covered with a closed plexiglass box to maintain a stable water vapor atmosphere. The temperature of the subphase was maintained at  $20 \text{ }^\circ\text{C}$  by a circulating water bath. The spectra were obtained by shining a polarized (s-perpendicular or p-parallel with respect to the plane of incidence) IR beam to the air-water interface of the Langmuir trough at a particular angle of incidence  $\varphi$  relative to the surface normal. The reflected IR beam was detected using a mercury-cadmium-telluride (MCT) detector. Reflectance absorbance (RA) spectra were calculated following the relation  $RA = -\log_{10}(R/R_0)$ , where  $R$  and  $R_0$  represent the IR reflectivity of the sample trough containing the film and the reference trough, respectively. Two different types of measurements were performed.

Firstly, PCL was dissolved in HPLC grade chloroform with a concentration of  $\approx 1.0 \text{ mg mL}^{-1}$  and spread dropwise on the water surface of the sample trough by a digital syringe (Hamilton 700 series) up to an initial  $\pi$  value of  $\approx 2 \text{ mN m}^{-1}$  at  $A \approx 60 \text{ \AA}^2 (\text{monomer unit})^{-1}$ . After 20 min equilibration time, the film was compressed up to a  $\pi$  value of  $\approx 11 \text{ mN m}^{-1}$  at  $A \approx 5 \text{ \AA}^2 (\text{monomer unit})^{-1}$  while IRRAS spectra were continuously recorded in p-polarization and an angle of incidence of  $40^\circ$ .

Secondly, a freshly prepared monolayer was compressed up to five different areas per repeating unit  $\approx 36 \text{ \AA}^2, \approx 14 \text{ \AA}^2, \approx 5 \text{ \AA}^2, \approx 3 \text{ \AA}^2$  and  $\approx 2 \text{ \AA}^2$  and IRRAS spectra were recorded at the given constant area at various angles of incidence in p-polarization and s-polarization. The angle of incidence  $\varphi$  varied in the measurement from  $25^\circ$  to  $70^\circ$  with an increment of  $3^\circ$  excluding  $52^\circ, 55^\circ$  and  $58^\circ$  due to the low reflectivity close to the Brewster angle [37]. Resolution and scanner speed used in all experiments were  $4 \text{ cm}^{-1}$  and  $80 \text{ kHz}$ , respectively. 500 and 1000 scans were collected for s-polarization and p-polarization measurements, respectively. A zero filling factor of two was applied before Fourier transformation of the averaged interferograms resulting in a nominal spectral resolution of  $2 \text{ cm}^{-1}$ .

Simulations of IRRAS bands were performed by MATLAB software using a script written by Schwieger et al. [38]. A 3-layer model (subphase/polymer film/air) developed by Kuzmin and Michailov [39,40] as described by Flach et al. [35] was used. The necessary parameters for the simulation such as wavelength dependent refractive indices ( $n$ ) as well as the absorption coefficient  $k$  of the subphase water were taken from literature [41,42]. For the polymer film, an isotropic refractive index  $n_H$

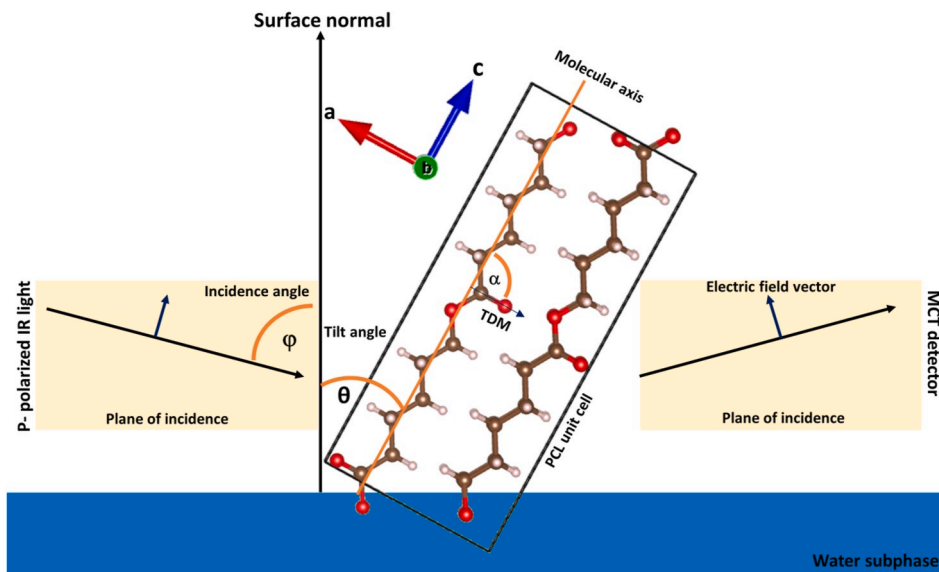


Fig. 1. Schematic presentation of the sample and measurement geometry for IRRAS measurements. The PCL unit cell is based on reference 12.

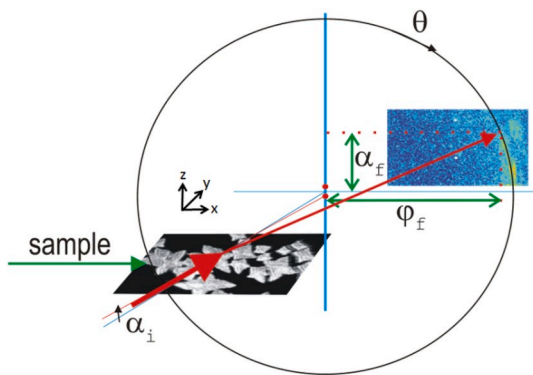


Fig. 2. Sample geometry for GI-WAXS measurements.

= 1.41 was used, as it is described for hydrocarbon molecules [35]. To fit the simulated spectra to the measured ones, several parameters were optimized such as the molecular tilt angle  $\theta$ , the polymer absorption coefficient  $k_{max}$ , and the full width at half height,  $fwhh$ . IRRA spectra

recorded at various angle of incidence  $\varphi$  and polarization (p- and s-) were fitted together in one global non-linear least squares fit using the Levenberg–Marquardt algorithm. The film thickness  $d$  was determined from a fit of the H<sub>2</sub>O stretching reflectance-absorbance (RA) band prior to the fit of the RA bands of the polymer film [38]. The procedure for the spectra simulation and its fit can be found in detail elsewhere [35,38]. An illustration of the sample and measurement geometry is given in Fig. 1.

2.6. Grazing incidence X-ray scattering (GI-WAXS)

GI-WAXS measurements on the water surface were performed at the ID10 EH1 – LSIS beam line ESRF Grenoble, France. The X-ray beam with 22 keV energy and the MYTHEN detector (1-dim, 1280 pixels) were used as describe elsewhere [43]. The incidence angle  $\alpha_i$  is at water critical angle  $\alpha_c = 0.056^\circ$  for 22 keV photons. The detailed experimental setup can be found elsewhere [34]. GI-WAXS measurements on solid support were performed using a Retro-F SAXSLAB setup (Copenhagen, Denmark). The setup was equipped with an AXO microfocus X-ray source (Dresden, Germany) and a DECTRIS PILATUS3 R 300K detector (Baden-Daettwil, Switzerland). Measurements were performed in a

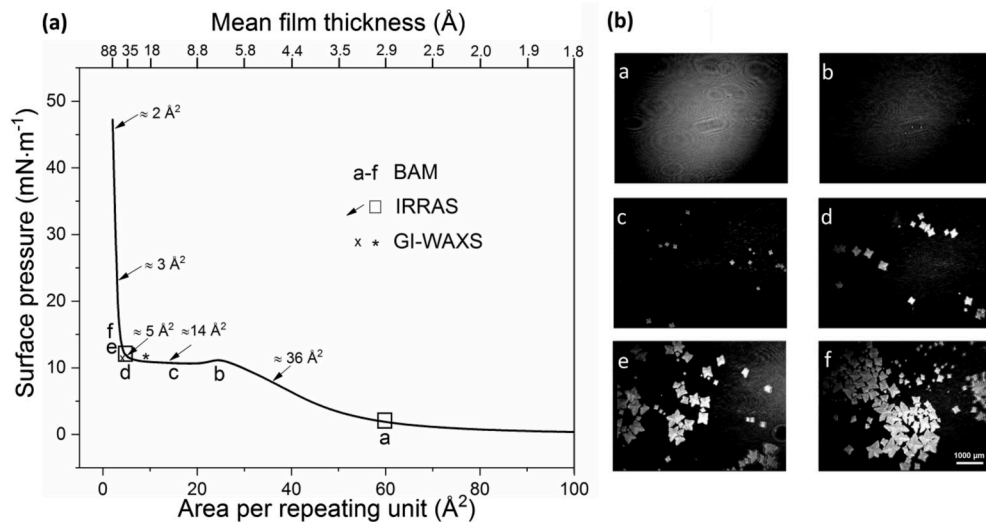
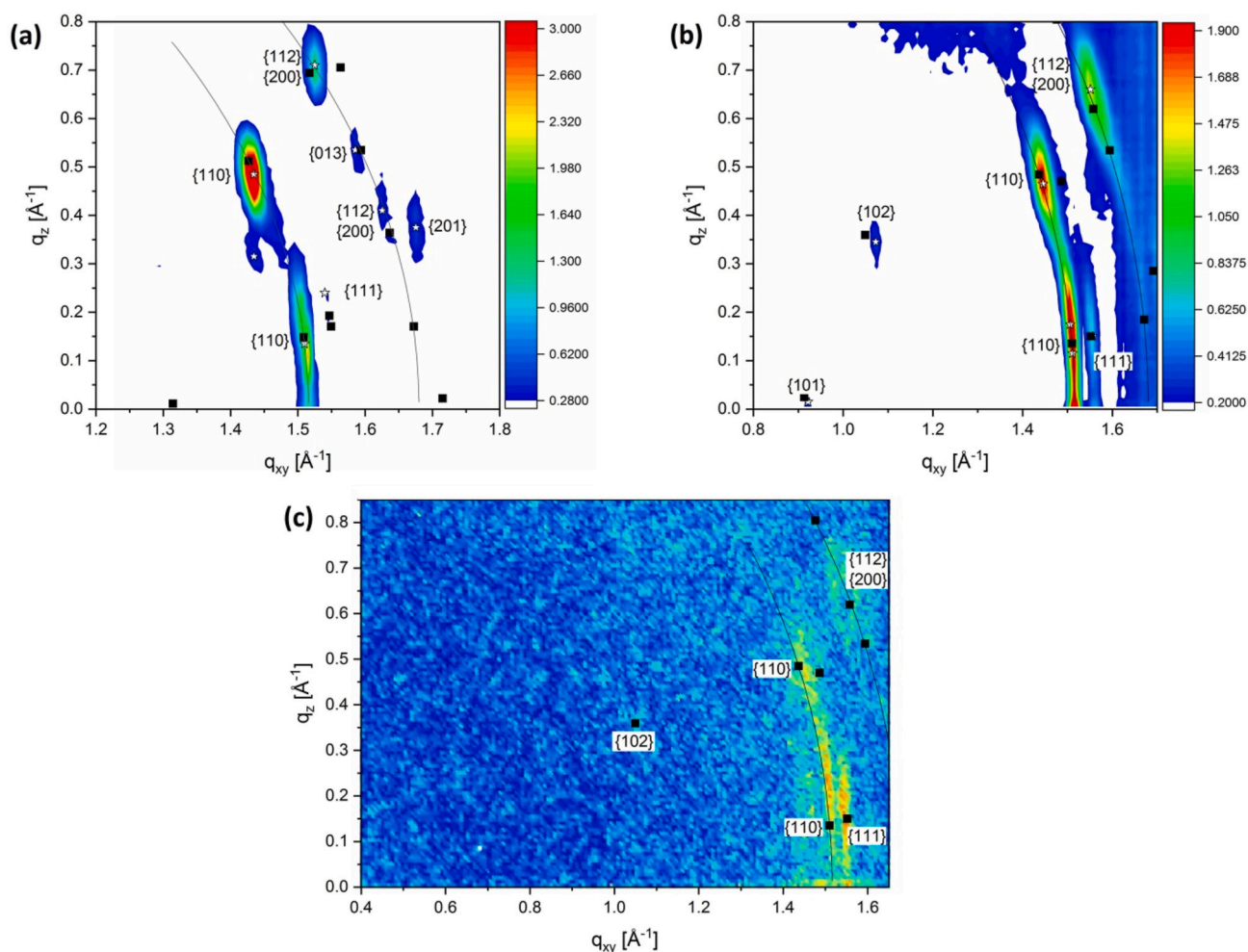


Fig. 3. (a)  $\pi$ -A isotherm of PCL measured at a subphase temperature of 20 °C with a compression rate of  $\approx 1 \text{ \AA}^2 (\text{monomer unit})^{-1} \text{ min}^{-1}$ . The letters (a to f) indicate the A value where BAM images are captured. The arrows show the  $\pi$  values where the IRRAS angle dependent measurements are carried out. The squares denote start and end of the  $\pi$  values range where IRRA spectra are recorded continuously during the film compression. The star denotes the  $\pi$  value where GI-WAXS measurements are performed on liquid support. The cross indicates the  $\pi$  value of 11  $\text{mN m}^{-1}$  at which a Langmuir film is transferred to a silicon wafer for analysis with GI-WAXS. (b) BAM images of PCL recorded at different states of compression, as a  $\approx 60 \text{ \AA}^2$ , b  $\approx 25 \text{ \AA}^2$ , c  $\approx 15 \text{ \AA}^2$ , d  $\approx 5 \text{ \AA}^2$ , e  $\approx 4 \text{ \AA}^2$ , and f  $\approx 3.4 \text{ \AA}^2$ . Dark areas represent amorphous regions of the PCL film and bright domains indicate crystallites.





**Fig. 4.** Two dimensional GI-WAXS patterns recorded at the plateau region (i.e.,  $9 \text{ \AA}^2$ ) during the compression of PCL. The asterisks indicate peak positions and corresponding peak indexation is given. Additionally, black lines at  $|q| = 1.516 \text{ \AA}^{-1}$  ( $\{110\}$  reflection) and  $|q| = 1.68 \text{ \AA}^{-1}$  ( $\{200\}$  and  $\{112\}$  reflections) are drawn to guide the eye. Black squares indicate expected peak positions for an orientation with  $19^\circ$  tilt angle in (a) and  $23^\circ$  tilt angle in (b) (See Fig. 1 for schematic presentation of the tilt angle). (c) GI-WAXS pattern of transferred LB film with same peak indexation as in (b). The film was transferred on a silicon wafer at  $11 \text{ mN m}^{-1}$ . (For interpretation of the references to colour in this figure legend, the reader is referred to the Web version of this article.)

reflection mode at room temperature under vacuum condition. The incidence angle was near silicon critical angle  $\alpha_c = 0.22^\circ$  for Cu K $\alpha$  radiation ( $\lambda = 1.5418 \text{ \AA}$ ).

All GI-WAXS data are given in sample coordinates according to equation (1), which were calculated from detector coordinates, depicted in Fig. 2, and the condition  $n_{XR} = \cos(\alpha_c) \approx \cos(\alpha_i) \approx 1$  with the critical angle  $\alpha_c$ .

$$\begin{pmatrix} q_x \\ q_y \\ q_z \end{pmatrix} = \frac{k_0}{n_{XR}} \begin{pmatrix} \cos \varphi_f \cos \alpha_f - n_{XR} \\ \sin \varphi_f \cos \alpha_f \\ \sqrt{n_{XR}^2 - \cos^2 \alpha_f} \end{pmatrix} \quad (1)$$

Horizontal q values are given with  $q_{xy} = \sqrt{q_x^2 + q_y^2}$ .

## 2.7. Fourier transform infrared (FTIR) spectroscopy

FTIR spectroscopy experiments were performed in transmission mode with a BRUKER Vector 22 (Bruker Optik GmbH, Germany) spectrometer. PCL was dissolved in chloroform and cast onto an IR window of CaF<sub>2</sub>. After allowing for evaporation of the solvent, 64 scans were collected with a resolution of  $4 \text{ cm}^{-1}$  in the temperature range of  $\approx 12^\circ\text{C}$ – $65^\circ\text{C}$ . The spectra were recorded in the wave number range of  $4000 \text{ cm}^{-1}$  to  $900 \text{ cm}^{-1}$ .

## 3. Results and discussion

### 3.1. Langmuir isotherm of PCL and BAM images

The Langmuir isotherm of PCL is measured after spreading polymer solution on the water subphase, solvent evaporation, and compression of the film by moving the barriers of the Langmuir trough. A surface pressure  $\pi$  vs area per repeating unit  $A$  isotherm which shows the increase of  $\pi$  with decreasing  $A$  is presented in Fig. 3 (a). It is seen that  $\pi$  increases to  $\approx 47 \text{ mN m}^{-1}$  with an extended plateau at  $\approx 11 \text{ mN m}^{-1}$  upon decreasing  $A$ . The extended plateau covers an area range per repeat unit of  $25 \text{ \AA}^2$  to  $5 \text{ \AA}^2$  including a little overshoot at the beginning of plateau, which is indicative for nucleation [5,29]. Detailed discussion about the isotherm can be found elsewhere [4,6,27–30]. The increase of  $\pi$  upon compression is common [44]. The appearance of a plateau in the  $\pi$ - $A$  isotherm of semicrystalline amphiphilic homopolymers is typically caused by crystallization [30–32,34,45,46]. It should be noted that the plateau region of the PCL isotherm has already been assigned to a monolayer to crystal lamellae transition [4].

Now, in order to obtain more information about the film organization, mean film thickness  $h$  is calculated at different  $A$  values by following the relation,

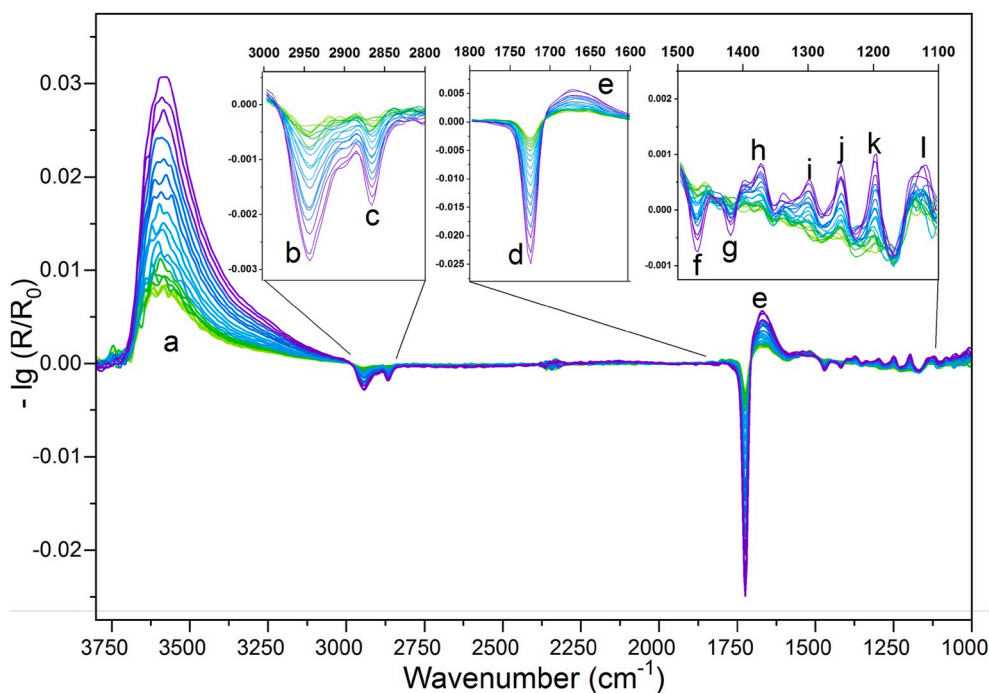


**Fig. 5.** IRRA spectra of PCL recorded at an angle of incidence  $\varphi = 40^\circ$  in p-polarization during a continuous compression from  $\approx 26 \text{ \AA}^2/(\text{repeat unit})$  (green) to  $\approx 7 \text{ \AA}^2/(\text{repeat unit})$  (violet), spectra recorded before the plateau are shown in Supporting Information, Fig. S1. The insets show magnifications of the selected bands. The assignment of the bands are as follows; (a)  $\nu(\text{OH})$ , (b)  $\nu_{\text{as}}(\text{CH}_2)$ , (c)  $\nu_{\text{s}}(\text{CH}_2)$ , (d)  $\nu(\text{CO})$ , (e)  $\delta(\text{HOH})$ , (f and g)  $\delta_{\text{s}}(\text{CH}_2)$ , (h)  $\tau(\text{CH}_2) + \gamma(\text{CH}_2)$ , (i)  $\nu(\text{CH}) + \nu(\text{CC})$  (j)  $\nu(\text{CCH}) + \nu(\text{OCH})$  (k)  $\nu_{\text{as}}(\text{COC})$ , (l)  $\nu_{\text{s}}(\text{COC})$  [55,57–60]. (For interpretation of the references to colour in this figure legend, the reader is referred to the Web version of this article.)

$$h = \frac{V_m}{A} \quad (2)$$

where  $V_m$  and  $A$  represent the molar volume per repeating unit of amorphous PCL and the mean area per repeating unit, respectively. The value of  $V_m = 175.3 \text{ \AA}^3$  is calculated from the density of the amorphous PCL,  $\rho = 1.081 \text{ g/cm}^3$ , and the molar mass of one repeating unit [47].

The compression of the polymer film to  $30 \text{ \AA}^2$  results in a calculated average thickness of  $\approx 5.8 \text{ \AA}$  (Fig. 3(a)). Such a thickness could correspond to a flat closely packed 2D monolayer of PCL, because  $5 \text{ \AA}$  is the thickness of a PCL chain [6]. However, when  $A$  is reduced to  $10 \text{ \AA}^2$  (nearly middle of the plateau) the predicted average film thickness increases to  $\approx 18 \text{ \AA}$  indicating a formation of a 3D monolayer on the water surface. The value is approximately in agreement with the length of two repeating units of PCL with some degrees of chain tilt [10–12]. In addition, BAM microscopy was employed during the film compression to monitor the water surface. The observations are presented in Fig. 3 (b). Before the plateau is reached, the monolayer is homogeneous, as expected (Fig. 3(b) a). First domains form directly at the beginning of the plateau, when the pressure relaxes from a metastable phase (Fig. 3(b)). Multiple domain formation and their lateral growth upon compression are evident in the plateau region of the Langmuir isotherm (Fig. 3(b) c-f). This indicates a two phase system of the PCL Langmuir film where crystallites appear as bright domains and the amorphous layer appears as dark area. Decrease of  $A$  to  $5 \text{ \AA}^2$  (end of the plateau), results in a predicted average film thickness of  $\approx 35 \text{ \AA}$ . In this state much larger domains on the water surface are visible (Fig. 3 (b) d). Atomic force microscopy investigation of these domains transferred to a solid support reveals a thickness of  $\approx 75 \text{ \AA}$  [4,30,48]. It should be noted that a dewetting process rather than crystallization occurs in thin films of PCL on solid support at a film thickness of  $40 \text{ \AA}$  [24,49].

In order to reveal more details of the crystallization, both GI-WAXS and IRRAS were employed. Thus, both the ordering behavior of the PCL chains and the average film thickness in the plateau region of the isotherm were determined.

### 3.2. GI-WAXS measurements

Now, to confirm the structural hypotheses developed above, several

GI-WAXS experiments have been performed. Among them, Fig. 4(a) and (b) show two typical 2D GI-WAXS patterns recorded at around  $9 \text{ \AA}^2$ , i.e., close to end of the plateau region of the  $\pi$ - $A$  isotherm. The other measurements (not shown here) exhibit a similar pattern. Besides the two most prominent Bragg reflections  $\{110\}$  and  $\{200\}/\{112\}$  several other reflections appear and can be identified. This finding confirms a polycrystalline nature of the PCL Langmuir film [23]. The reflections are assigned according to the orthorhombic unit cell of PCL with the lattice parameters  $a = 7.496 \text{ \AA}$ ,  $b = 4.974 \text{ \AA}$ ,  $c = 17.297 \text{ \AA}$  [12]. It should be noted that the  $\{200\}$  and  $\{112\}$  reflections have almost identical  $q$ -values of  $1.68 \text{ \AA}^{-1}$  and cannot be distinguished. The peak positions depicted in Fig. 4 cannot be assigned to a single orientation of PCL crystals, i.e., it must be assumed that we probe several crystals having different orientations with respect to the normal direction of the water surface. In general, it is possible to combine any two different peaks to estimate a crystal orientation, but in both cases crystal orientations were found, where at least the four most prominent peaks can be assigned together. In Fig. 4, two GI-WAXS measurements are shown, where the most prominent peaks can be assigned assuming a certain crystal orientation. In Fig. 4(a), the chain axis has a tilt of  $19^\circ$  with respect to the water surface normal direction and in the other the tilt is  $23^\circ$  (Fig. 4(b)). Most other measurements (not shown here) have also a characteristic  $\{110\}$  reflection in the range of  $q_z = 0.50 \text{ \AA}^{-1}$  (Fig. 4(a)) and  $q_z = 0.47 \text{ \AA}^{-1}$  (Fig. 4(b)), indicating that this is a preferred range of crystalline tilt angles. It should also be mentioned, that a small number of additional peaks were observed, which are not in agreement with a tilt angle of  $19$ – $23^\circ$ , but in these cases no orientation could be identified. Due to the large illuminated sample area (footprint of the beam is approximately  $2 \text{ cm} \times 300 \text{ \mu m}$ ), the position of the crystallite influences the final tilt angle determination, and a mean value of  $\approx 21^\circ$  for the tilt angle will be used.

The width in the  $q_z$ -direction,  $\Delta q_{\text{hkl},z}$  as the *fwhh* value, is directly related via the Scherrer equation to the thickness of the layer  $D_z$  with a Scherrer constant of  $K = 0.9$  [50].

$$D_z = \frac{2\pi K}{\Delta q_{\text{hkl},z}} \quad (3)$$

The two most prominent peaks ( $\{110\}$  and  $\{200\}$ ) lead to a thickness

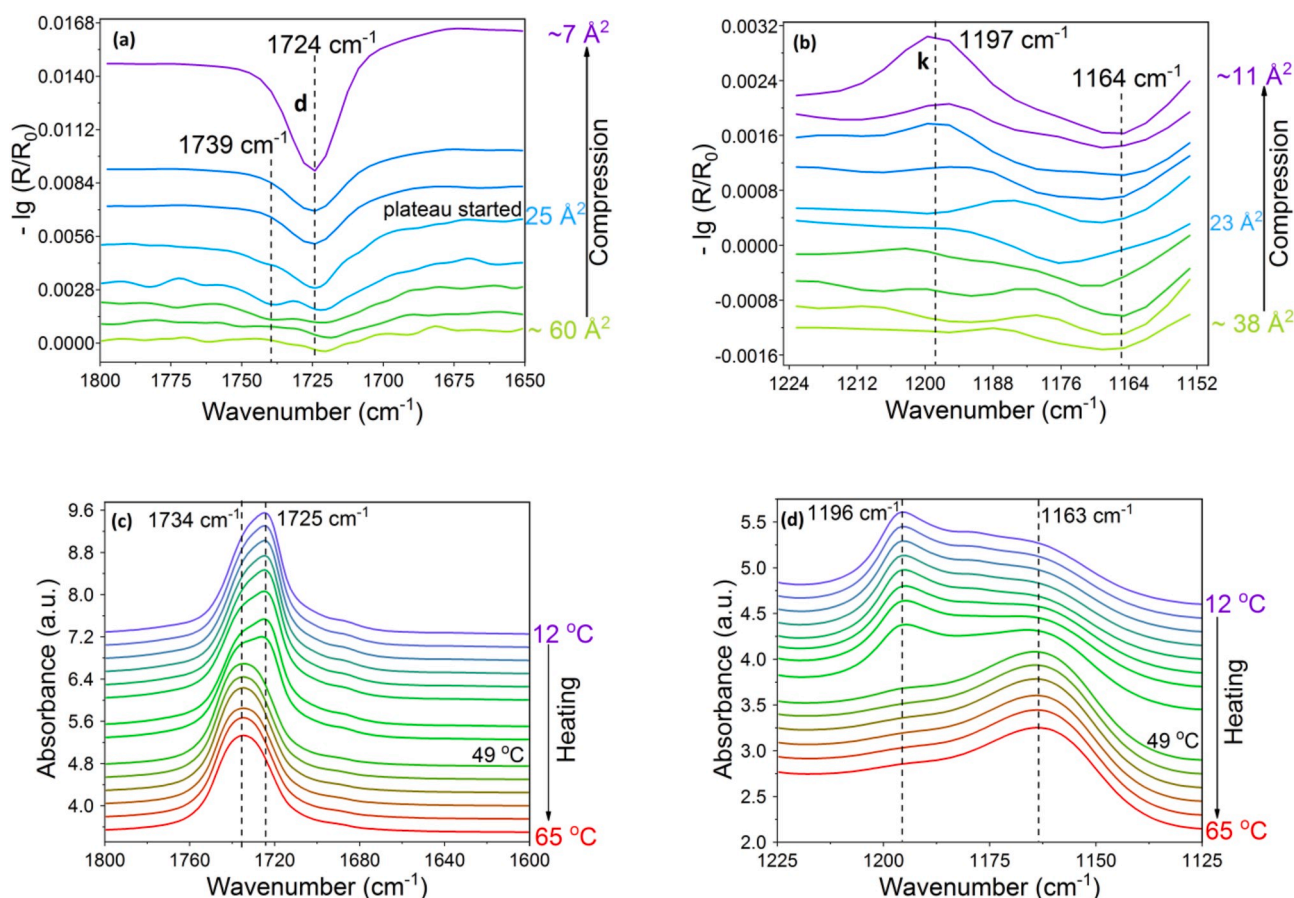


**Fig. 6.** IRRA spectra of (a)  $\nu(\text{CO})$  (band d) and (b)  $\nu_{\text{as}}(\text{COC})$  (band k) at different A, (c and d) transmission FTIR spectra of a thin film of PCL recorded at varying temperatures from 12 to 65 °C. The dotted lines should guide the eyes for crystalline component at a wavenumber of 1725  $\text{cm}^{-1}$  and 1196  $\text{cm}^{-1}$  as well as the amorphous component at 1734  $\text{cm}^{-1}$  and 1163  $\text{cm}^{-1}$  for  $\nu(\text{CO})$  and  $\nu_{\text{as}}(\text{COC})$  bands, respectively.

of 54 Å, which is very close to the values found by AFM measurements of the respective LB films [4,30].

In addition, PCL crystals were also transferred to a solid support and examined by GI-WAXS to see any effects in crystal orientation due to the transfer. In Fig. 4 (c) the GI-WAXS measurement of an LB film transferred at  $\approx 11 \text{ mN m}^{-1}$  is depicted. Within the experimental error, the data are in agreement with the crystal orientation observed in Fig. 4 (b), indicated by the black dots for the expected peak positions for 23° chain tilt angle. Therefore, we conclude that the chain tilt in PCL crystallites with respect to normal direction of interface is identical in Langmuir and Langmuir-Blodgett films. Thus, there is no apparent effect of the transfer process during LB film preparation on the crystal organization.

### 3.3. IRRAS measurements

#### 3.3.1. Crystallization studies

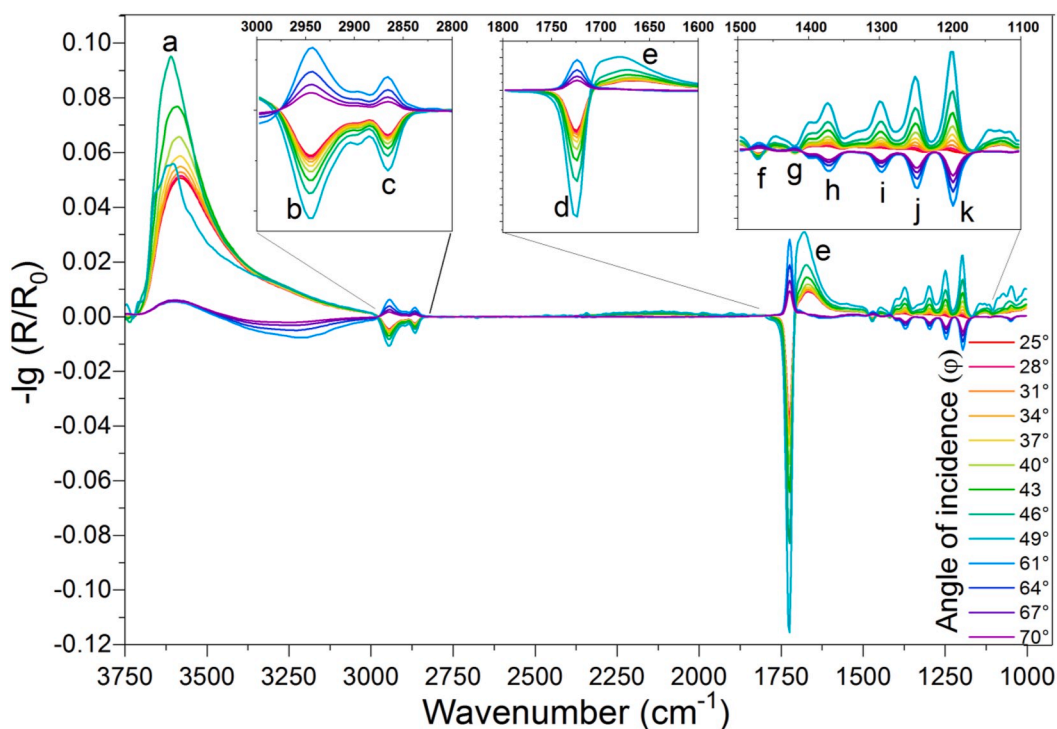
IRRAS is a powerful tool to study the behavior of Langmuir film on the water surface [51]. The method is widely reported for studying the crystallization as well as the chain orientation (e.g., chain tilt angle) of small molecules [38,52] and polymers [53,54]. From the IRRAS experiment, the reflectance-absorbance band intensity and band positions are evaluated. The band intensity is sensitive to the concentration as well as to the orientation of the polymer chains, whereas the band position is indicative for their conformation.

Fig. 5 shows IRRA spectra of PCL recorded during PCL film compression from an area of  $\approx 26 \text{ \AA}^2$ /(repeat unit) (green) to  $\approx 7 \text{ \AA}^2$ /(repeat unit) (violet), which covers the plateau region of the isotherm. The spectra reveal bands originating from the water subphase (a and e) and the polymer film (b to d and f to l). Some bands appear at positive

values and some at negative values of  $-\lg(R/R_0)$ . At the given angle of incidence ( $\varphi = 40^\circ$ ), positive bands are attributed to transition dipole moments (TDMs) orientated preferentially perpendicular to the surface, whereas negative bands are associated to TDMs rather parallel to the surface. A reflectance-absorbance intensity change is observed upon compression. The reflectance-absorbance of all bands including the crystallization sensitive band at  $\approx 1293 \text{ cm}^{-1}$  (i) [55] increases in its absolute values upon reducing A. The reflectance-absorbance increase is typically attributed to an increase of surface concentration and/or reorientation of the molecules resulting in a better alignment of the TDM of the respective vibration with the electrical field vector of the exciting IR light [56].

To confirm the crystallization of PCL in the plateau region, two IRRA bands (i.e.,  $\nu(\text{CO})$  and  $\nu_{\text{as}}(\text{COC})$ ) are selected and represented in Fig. 6(a and b) for different A. The Figures demonstrate that the  $\nu(\text{CO})$  and the  $\nu_{\text{as}}(\text{COC})$  bands at wavenumbers of 1724  $\text{cm}^{-1}$  and 1197  $\text{cm}^{-1}$ , respectively, increase in their absolute reflectance-absorbance upon compression within the plateau region. Their positions are indicative for the crystallinity of the sample. Looking to Fig. 6(c and d), similar band position for  $\nu(\text{CO})$  at 1725  $\text{cm}^{-1}$  and  $\nu_{\text{as}}(\text{COC})$  at 1196  $\text{cm}^{-1}$  are observed by transmission FTIR spectroscopy for a semi-crystalline thin film of PCL on  $\text{CaF}_2$ . However, at 49 °C both bands shift to different wavenumbers (i.e., 1734  $\text{cm}^{-1}$  and 1163  $\text{cm}^{-1}$ ) indicating a crystalline to melt phase transition. In line with this observation, it has been reported that the  $\nu(\text{CO})$  band in the solid state is composed of contributions from the crystalline state at 1725  $\text{cm}^{-1}$  and the amorphous state at 1735  $\text{cm}^{-1}$  [55,57,58,60,61]. We conclude that the appearance of the  $\nu(\text{CO})$  and  $\nu_{\text{as}}(\text{COC})$  IRRA bands at wavenumbers of 1724  $\text{cm}^{-1}$  and 1197  $\text{cm}^{-1}$ , respectively, upon film compression indicates a transition from an





**Fig. 7.** IRRA spectra of a Langmuir film of PCL recorded at various angles of incidence ( $\varphi = 25^\circ$ ; red to  $70^\circ$ ; violet) in p-polarization at  $A$  of  $\approx 3 \text{ \AA}^2$ . The insets show magnification of the selected bands. The assignments of the bands denoted by letters a to k are as given in the caption of Fig. 5. Additionally, IRRA spectra obtained at areas per repeating unit of  $\approx 36 \text{ \AA}^2$ ,  $\approx 14 \text{ \AA}^2$ ,  $\approx 5 \text{ \AA}^2$  and  $\approx 2 \text{ \AA}^2$  can be found in the Supporting Information, Figures S(2–5). (For interpretation of the references to colour in this figure legend, the reader is referred to the Web version of this article.)

amorphous phase to a crystalline state within the plateau region of the isotherm. Contrary to the crystalline bands, the bands being indicative for the amorphous phase are hardly visible in the IRRA spectra due to the low surface concentration of PCL at higher areas and possibly as well to a less favorable orientation of the PCL chains with respect to the interface. Indeed, the change in sign of the  $\nu_{\text{as}}(\text{COC})$  band during compression concomitant to the shift of the band position (Fig. 6 (b)) indicates a reorientation of the PCL chains during crystallization.

### 3.3.2. Chain orientation and film thickness estimation

It has already been reported for PCL spin coated thin films that the chains are tilted by  $17^\circ$  and  $22^\circ$  on the substrate with respect to the surface normal [58]. However, no quantitative information has yet been reported for PCL at the air-water interface. Thus, the question remains whether the substrate or the preparation technique influence the PCL chain orientation. Herein, chain orientations as quantified by the chain tilt angle and film thickness of a PCL film prepared directly at the air-water interface were determined at different compression states. In a typical analysis, IRRA spectra are recorded with varying angle of

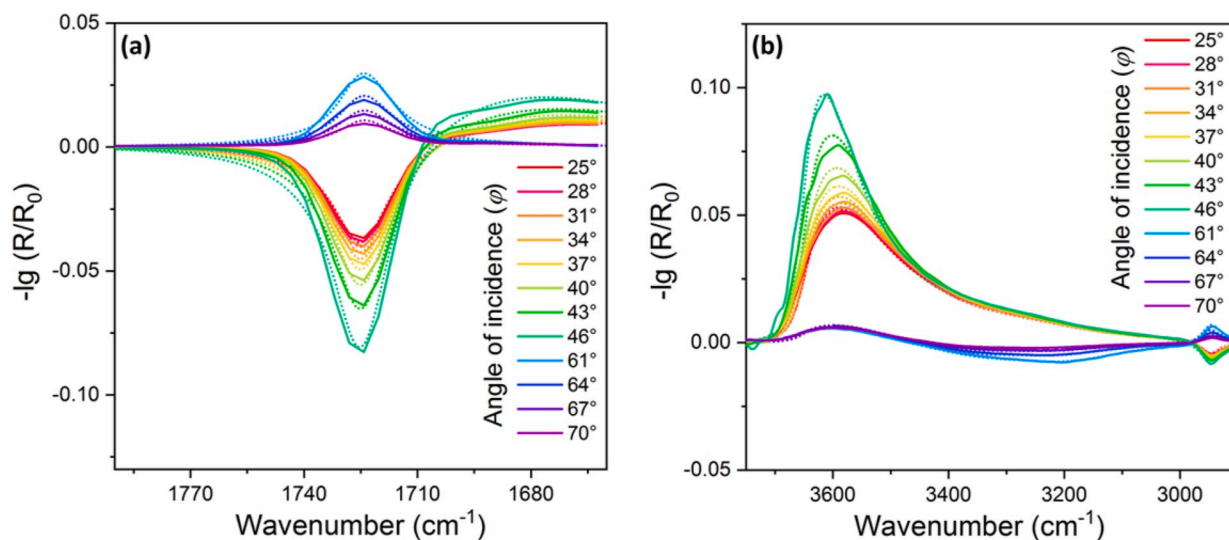


**Fig. 8.** Experimental (full lines) and best fitting simulated (dotted lines) IRRA spectra recorded in p-polarization and at various angles of incidence ( $\varphi = 25^\circ$ ; red to  $70^\circ$ ; violet) in the range of the (a)  $\nu(\text{CO})$  band and (b)  $\nu(\text{OH})$  band of a Langmuir film of PCL at  $A$  of  $\approx 3 \text{ \AA}^2$ . Tilt angle in the simulation is  $27^\circ$  and the film thickness is  $60 \text{ \AA}$ . (For interpretation of the references to colour in this figure legend, the reader is referred to the Web version of this article.)

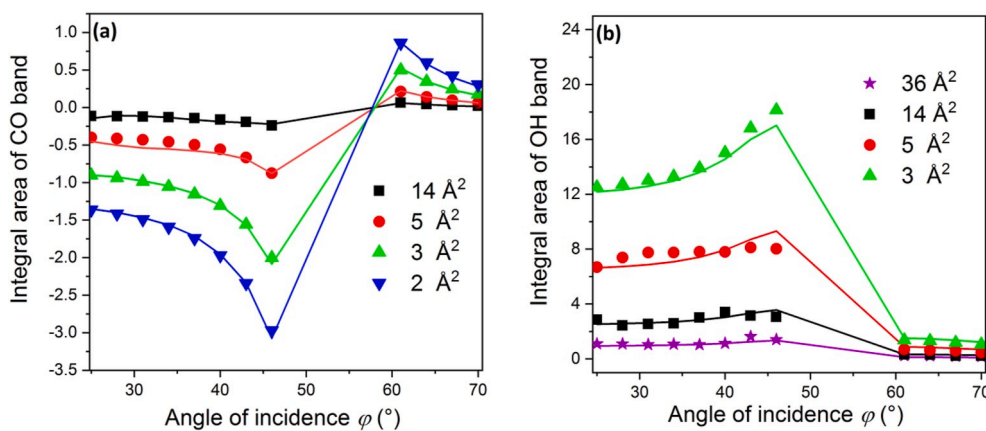


**Fig. 9.** The integral areas of the vibrational band of (a)  $\nu(\text{CO})$  ( $1747\text{ cm}^{-1} - 1697\text{ cm}^{-1}$ ) and (b)  $\nu(\text{OH})$  ( $3718\text{ cm}^{-1} - 2944\text{ cm}^{-1}$ ) from the experimental (symbols) and simulated (line) IRR spectra of the Langmuir film of PCL at different areas as a function of  $\varphi$  for p-polarization.

**Table 1**

PCL chain tilt angles and film thickness obtained from CO and OH stretching vibrational IRR band fitting along with thicknesses calculated according to equation (2).

Mean area/repeating unit ( $\text{\AA}^2$ )	Calculated thickness ( $\text{\AA}$ )	Thickness ( $\text{\AA}$ )	Tilt angle ( $^\circ$ )
$\approx 36$	4.8	4.6	–
$\approx 14$	13	12	28
$\approx 5$	35	32	38
$\approx 3$	59	60	27
$\approx 2$	88	89	23

incidence  $\varphi$  as well as polarization (p,s) and the bands with defined TDM orientations are fitted with simulated IRR spectra [35,38,52,62]. From the fitting, the chain tilt angle  $\theta$  with respect to surface normal can be obtained. In addition, the film thickness can be calculated from the fit of the OH stretching bands originating from the subphase water.

Fig. 7 shows IRR spectra of a PCL film at  $A$  of  $\approx 3\text{ \AA}^2$  recorded at various angles of incidence. The most prominent bands are the  $\nu(\text{CO})$  (d) and  $\nu(\text{OH})$  (a) bands. To extract the information on chain tilt angle ( $\theta$ ),

the  $\nu(\text{CO})$  bands and for the film thickness ( $d$ ) evaluation, the  $\nu(\text{OH})$  bands are further analyzed. The mathematical formalism used for the tilt angle calculation is described elsewhere [38]. The angle between the TDM of the  $\nu(\text{C}=\text{O})$  band with respect to the chain axis was set to  $\alpha = 90^\circ$  (see Fig. 1). The unknown parameters are  $k_{\text{max}}$  (polymer absorption coefficient),  $\theta$  and  $d$  which were obtained by a global nonlinear least squares fit of simulated IRR bands to the observed ones at all probed angles of incidence and polarizations (p,s). The simulated IRR spectra of these bands are plotted together with experimental IRR spectra in p-polarization as a function of  $\varphi$  in Fig. 8. It is evident that the simulated spectra denoted by dots mostly superimpose the experimental IRR spectra (bold lines). In this case ( $A \approx 3\text{ \AA}^2$ ) the chain tilt angle is found to be  $27^\circ$  and the average film thickness is  $\approx 60\text{ \AA}$  (see Supporting Information, Figs. S6–S8 for the fit of the bands at other compression states). In addition, two plots are shown in Fig. 9(a) and (b), where the integral area of  $\nu(\text{CO})$  and  $\nu(\text{OH})$  bands of the experimental and the simulated IRR spectra at different  $A$  are shown as a function of  $\varphi$  to evaluate the quality of the fit. The simulated spectra fit best to the experimental data when the tilt angle  $\theta$  is  $28^\circ$ ,  $38^\circ$ ,  $27^\circ$  and  $23^\circ$  for  $A$  of  $\approx 14\text{ \AA}^2$ ,  $\approx 5\text{ \AA}^2$ ,  $\approx 3\text{ \AA}^2$  and  $\approx 2\text{ \AA}^2$ , respectively (Table 1). These determined PCL chain tilt angles are calculated from average order parameters of all PCL chain segments, i.e. with contribution of remaining amorphous PCL as well as chain segments forming the folds in the crystals. Therefore, these values are slightly higher than the values determined by GI-WAXS, which senses only the crystalline fraction. Interestingly, the PCL chain tilt determined by IRRAS at highest compression ( $2\text{ \AA}^2$ ) is in good agreement with the GI-WAXS data (IRRAS:  $23^\circ$  vs. GI-WAXS:  $21^\circ$ ). This is reasonable because at this compression state, beyond the phase transition plateau, the amorphous content is negligible and thus the contribution of the crystalline component maximal. Thus, the IRRAS data nicely corroborate the GI-WAXS experiments. A similar chain tilt is also reported elsewhere [58]. It should be noted that, a perpendicular chain orientation ( $\theta = 0^\circ$ ) with respect to a solid support has been reported for PCL LS films [4]. The IRRAS band fitting could not be performed for the spectra recorded  $A$  of  $\approx 36\text{ \AA}^2$  due to a low signal to noise ratio at this lower surface coverage. Additionally, the average film thickness values obtained from the fitting of the  $\nu(\text{OH})$  IRR bands are listed in Table 1 along with the tilt angle. The obtained thickness values are in very good agreement with film thickness mentioned in Fig. 3(a) as calculated following equation (2), even though they are determined independent of the measured area value and any molecular volume assumptions.

At a compression state of  $36\text{ \AA}^2$ , i.e. before the plateau, the average film thickness is determined to be  $4.6\text{ \AA}$ , which corresponds to one molecular thickness and can thus be assigned to a 2D monolayer of PCL. Upon compression the average film thickness steadily increases and reaches  $\approx 60\text{ \AA}$  at  $3\text{ \AA}^2$ /(repeat unit), i.e. at the end of the plateau when

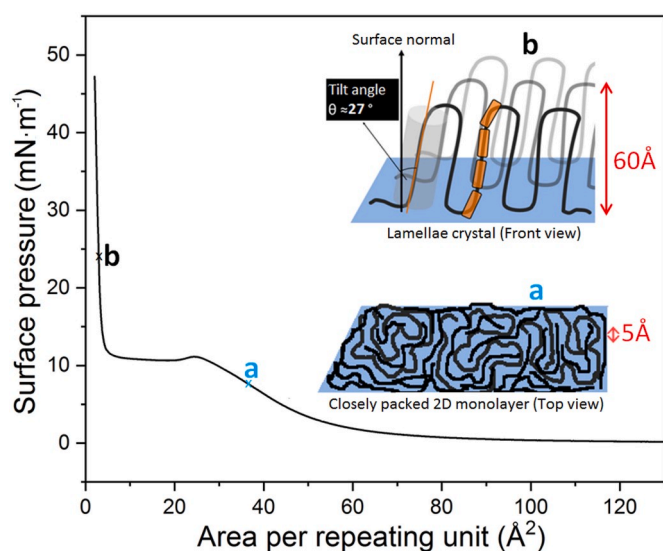


**Fig. 10.** Schematic presentation of the chain ordering (i.e., crystallization) of PCL on the water surface upon compression. One yellow rectangle is representing two repeating units of PCL. (For interpretation of the references to colour in this figure legend, the reader is referred to the Web version of this article.)

the film is completely crystalline. This thickness is equivalent to the length of  $\approx 8$  repeating units of PCL with a chain tilt of  $27^\circ$  and indicates a 3D film formation, which means that not all the monomer units are in contact with the air-water interface any more. This is also manifested in the mean areas per repeat unit, which are, at the end of the transition plateau, smaller than one PCL chain cross sectional area. Assuming a PCL chain cross-sectional area of  $20 \text{ \AA}^2$ , a PCL segment with 8 repeating units in a tilt angle of  $27^\circ$  would occupy an area of  $2.8 \text{ \AA}^2$ /(repeat unit), which is very close to the actual experimental area of  $3 \text{ \AA}^2$ /(repeat unit). Thus, IRRAS, film balance and GI-WAXS data nicely combine and support the assumption that the PCL crystallites formed at the air-water interface contain slightly tilted multiunit PCL stretches. Upon further compression, the determined average film thickness and thereby the theoretical calculated number of monomer units per fold increases to 89  $\text{\AA}$  and 11, respectively. Whether that is due to an increased crystal thickness or to a partial crystal stacking cannot be decided on basis of the data. However, considering the morphology of the film as determined by BAM (see Fig. 3(b) f) and the reported crystallite thickness after transfer and investigation by AFM [4,30,48], we assume that the latter is the case.

#### 4. Summary and conclusions

The crystallization of PCL at the air-water interface, as determined by film balance, IRRAS and GI-WAXS measurements, is summarized in Fig. 10. The process starts with spreading of the polymer solutions and compression of the formed PCL films after solvent evaporation. A flat closely packed unordered/amorphous 2D monolayer forms before the plateau is reached. This is confirmed by IRRAS thickness measurements after compression of the polymer film to  $A \approx 36 \text{ \AA}^2$  (indicated by a). Upon further compression to  $\approx 3 \text{ \AA}^2$  (indicated by b), we observe a transition from the 2D monolayer to a lamellar crystal with an average thickness of  $\approx 60 \text{ \AA}$ . This corresponds to a PCL stretch of 8 repeating units being tilted with respect to the surface normal by  $27^\circ$ . This amorphous to crystalline phase transition is responsible for the plateau in the surface pressure-area isotherm that expands from ca  $25 \text{ \AA}^2$  to ca  $5 \text{ \AA}^2$ . These values are indicative for the cross sectional areas of one flat lying PCL unit and a nearly upright multimeric PCL stretch, respectively. This shows that the PCL chains reorient for crystallization and partly detach from the water surface. The reorientation as well as the crystallite thickness that comprises multiple repeat units of PCL has been proven by IRRAS. Butterfly-like crystallites are formed upon compression in the plateau region, which are visible by Brewster angle microscopy. At the end of the transition plateau the chains are tilted by an average angle of  $27^\circ$  with respect to the water surface normal and with further compression to  $\approx 2 \text{ \AA}^2$ /(repeat unit), a chain tilt of  $23^\circ$  is obtained by multi-angle IRRA spectroscopy. In addition, GI-WAXS experiments confirmed that crystallization in the PCL film occurs in the plateau region upon compression. The formed crystallites possess an orthorhombic unit cell with a crystal orientation where the polymer chain axes are tilted by approximately  $21^\circ$  with respect to the water surface normal direction. This completely corroborated the results obtained by IRRA spectroscopy. Small differences in the obtained PCL chain tilt angles are due to the fact that GI-WAXS senses exclusively the crystalline part of the sample, whereas remaining amorphous parts or unordered folds contribute to the averaged spectroscopic signal. This study demonstrates that a pressure-induced crystallization of an amphiphilic polymer at the air-water interface can be studied by appropriate techniques without the need to transfer the film to solid supports. Herein, we used the Langmuir film balance technique combined with BAM, IRRA spectroscopy and GI-WAXS to obtain a consistent and precise understanding of the crystallization process at the air-water interface and the morphology of the formed crystallites.

#### Declaration of competing interest

The authors declare that they have no known competing financial interests or personal relationships that could have appeared to influence the work reported in this paper.

#### CRediT authorship contribution statement

**Nazmul Hasan:** Writing - original draft, Conceptualization, Investigation. **Christian Fuchs:** Investigation. **Christian Schwieger:** Writing - review & editing, Investigation, Software. **Karsten Busse:** Writing - review & editing, Investigation. **Oleksandr Dolynchuk:** Investigation. **Jörg Kressler:** Supervision, Writing - review & editing.

#### Acknowledgments

This work was supported by Deutsche Forschungsgemeinschaft (DFG, German Research Foundation) – Project number – 189853844 – TRR 102 and FOR 1145. The authors acknowledge the European Synchrotron Radiation Facility and would like to thank O. Kononov and G. Li Destri for assistance in using beamline ID10. We also thank Thomas Thurn-Albrecht for helpful discussion on the evaluation of GI-WAXS data.

#### Appendix A. Supplementary data

Supplementary data to this article can be found online at <https://doi.org/10.1016/j.polymer.2020.122468>.

#### References

- [1] W.K. Lee, J.A. Gardella, Hydrolytic kinetics of biodegradable polyester monolayers, *Langmuir* 16 (2000) 3401–3406.
- [2] W.K. Lee, R.W. Nowak, J.A. Gardella, Hydrolytic degradation of polyester blend monolayers at the air/water interface: effects of a slowly degrading component, *Langmuir* 18 (2002) 2309–2312.
- [3] A. Leiva, L. Gargallo, D. Radić, Interfacial properties of poly( $\epsilon$ -caprolactone) and derivatives, *J. Macromol. Sci. Part A* 41 (2004) 577–583.
- [4] B. Li, Y. Wu, M. Liu, A.R. Esker, Brewster angle microscopy study of poly( $\epsilon$ -caprolactone) crystal growth in Langmuir films at the air/water interface, *Langmuir* 22 (2006) 4902–4905.
- [5] B. Li, A.R. Esker, Molar mass dependent growth of poly( $\epsilon$ -caprolactone) crystals in Langmuir films, *Langmuir* 23 (2007) 2546–2554.
- [6] T. Naolou, K. Busse, B.D. Lechner, J. Kressler, The behavior of poly( $\epsilon$ -caprolactone) and poly(ethylene oxide)-*b*-poly( $\epsilon$ -caprolactone) grafted to a poly(glycerol adipate) backbone at the air/water interface, *Colloid Polym. Sci.* 292 (2014) 1199–1208.
- [7] J. Kumaki, Monolayer of polystyrene monomolecular particles on a water surface studied by Langmuir-type film balance and transmission electron microscopy, *Macromolecules* 21 (1988) 749–755.
- [8] M.A. Woodruff, D.W. Hutmacher, The return of a forgotten polymer - polycaprolactone in the 21st century, *Prog. Polym. Sci.* 35 (2010) 1217–1256.
- [9] A. Kulkarni, J. Reiche, K. Kratz, H. Kamusewitz, I.M. Sokolov, A. Lendlein, Enzymatic chain scission kinetics of poly( $\epsilon$ -caprolactone) monolayers, *Langmuir* 23 (2007) 12202–12207.
- [10] Y. Chatani, Y. Okita, H. Tadokoro, Y. Yamashita, Structural studies of polyesters. III. Crystal structure of poly- $\epsilon$ -caprolactone, *Polym. J.* 1 (1970) 555–562.
- [11] H. Hu, D.L. Dorset, Crystal structure of poly( $\epsilon$ -caprolactone), *Macromolecules* 23 (1990) 4604–4607.
- [12] H. Bittiger, R.H. Marchessault, Crystal structure of poly- $\epsilon$ -caprolactone, *Acta Crystallogr.* B26 (1970) 1923–1927.
- [13] W.-C. Ou-Yang, L.-J. Li, H.-L. Chen, J.C. Hwang, Bulk crystallization behavior of poly( $\epsilon$ -caprolactone) with a wide range of molecular weight, *Polym. J.* 29 (1997) 889–893.
- [14] H. Chen, L. Li, W.-C. Ou-Yang, J.C. Hwang, W. Wong, Spherulitic crystallization behavior of poly( $\epsilon$ -caprolactone) with a wide range of molecular weight, *Macromolecules* 30 (1997) 1718–1722.
- [15] Y.W. Cheung, R.S. Stein, Critical analysis of the phase behavior of poly( $\epsilon$ -caprolactone) (PCL)/polycarbonate (PC) blends, *Macromolecules* 27 (1994) 2512–2519.
- [16] J.M. Vion, R. Jérôme, P. Teyssié, M. Aubin, R.E. Prud'homme, Synthesis, characterization, and miscibility of caprolactone random copolymers, *Macromolecules* 19 (1986) 1828–1838.
- [17] S. Nojima, H. Tsutsui, M. Urushihara, W. Kosaka, N. Kato, T. Ashida, A dynamic study of crystallization of poly( $\epsilon$ -caprolactone) and poly( $\epsilon$ -caprolactone)/poly(vinyl chloride) blend, *Polym. J.* 18 (1986) 451–461.
- [18] J.M. Jonza, R.S. Porter, Bisphenol A polycarbonate/poly( $\epsilon$ -caprolactone) blends: melting point depression and reactivity, *Macromolecules* 19 (1986) 1946–1951.



- [19] A.A.C.M. Oudhuis, H.J. Thiewes, P.F. Hutten, G. Brinke, A comparison between the morphology of semicrystalline polymer blends of poly( $\epsilon$ -caprolactone)/poly(vinyl methyl ether) and poly( $\epsilon$ -caprolactone)/(styrene-acrylonitrile), *Polymer* 35 (1994) 3936–3942.
- [20] J. Kressler, P. Svoboda, T. Inoue, Influence of copolymer composition on the crystallization in PCL SAN blends, *Polymer* 34 (1993) 3225–3233.
- [21] K. Schulze, J. Kressler, H.W. Kammer, Phase behaviour of poly( $\epsilon$ -silon-caprolactone) (polystyrene-ran-acrylonitrile) blends exhibiting both liquid-liquid unmixing and crystallization, *Polymer* 34 (1993) 3704–3709.
- [22] S.A. Berrill, F. Heatley, J.H. Collett, D. Attwood, C. Booth, J.P.A. Fairclough, A. J. Ryan, K. Viras, A.J. Dutton, R.S. Blundell, Chain folding in poly( $\epsilon$ -caprolactone) studied by small-angle X-ray scattering and Raman spectroscopy. A strategy for blending in the crystalline state, *J. Mater. Chem.* 9 (1999) 1059–1063.
- [23] V.H. Mareau, R.E. Prud'homme, In-situ hot stage atomic force microscopy study of poly( $\epsilon$ -caprolactone) crystal growth in ultrathin films, *Macromolecules* 38 (2005) 398–408.
- [24] C. Qiao, J. Zhao, S. Jiang, X. Ji, L. An, B. Jiang, Crystalline morphology evolution in PCL thin films, *J. Polym. Sci., Part B: Polym. Phys.* 43 (2005) 1303–1309.
- [25] S.Y. Yu-Su, S.S. Sheiko, H. Lee, W. Jakubowski, A. Nese, K. Matyjaszewski, D. Anokhin, D.A. Ivanov, Crystallization of molecular brushes with block copolymer side chains, *Macromolecules* 42 (2009) 9008–9017.
- [26] A.-K. Flieger, M. Schulz, T. Thurn-Albrecht, Interface-induced crystallization of polycaprolactone on graphite via first-order prewetting of the crystalline phase, *Macromolecules* 51 (2018) 189–194.
- [27] B. Li, Surface Characterization of Poly ( $\epsilon$ -Caprolactone) at the Air/water Interface, Virginia Polytechnic Institute and State University, Master thesis, 2004.
- [28] B. Li, A.R. Esker, Blends of poly( $\epsilon$ -caprolactone) and intermediate molar mass polystyrene as Langmuir films at the air/water interface, *Langmuir* 23 (2007) 574–581.
- [29] B. Li, H. Marand, A.R. Esker, Dendritic growth of poly( $\epsilon$ -caprolactone) crystals from compatible blends with poly(*t*-butyl acrylate) at the air/water interface, *J. Polym. Sci., Part B: Polym. Phys.* 45 (2007) 3300–3318.
- [30] C. Fuchs, K. Busse, A.-K. Flieger, J. Kressler, Polymer crystallization on the surface of water or aqueous salt solution, *Chem. Eng. Technol.* 39 (2016) 1333–1340.
- [31] K. Watanabe, J. Kumaki, Extended-chain crystallization and stereocomplex formation of poly(lactides) in a Langmuir monolayer, *Polym. J.* (2020), <https://doi.org/10.1038/s41428-020-0312-2>.
- [32] J. Kumaki, T. Kawauchi, E. Yashima, Two-dimensional folded chain crystals of a synthetic polymer in a Langmuir-Blodgett film, *J. Am. Chem. Soc.* 127 (2005) 5788–5789.
- [33] A.-C. Schöne, T. Roch, B. Schulz, A. Lendlein, Evaluating polymeric biomaterial – environment interfaces by Langmuir monolayer techniques, *J. R. Soc. Interface* 14 (2017) 1–18.
- [34] K. Busse, C. Fuchs, N. Hasan, M. Pulst, J. Kressler, Crystallization of poly(ethylene oxide) on the surface of aqueous salt solutions studied by grazing incidence wide-angle X-ray scattering, *Langmuir* 34 (2018) 12759–12763.
- [35] C.R. Flach, A. Gericke, R. Mendelsohn, Quantitative determination of molecular chain tilt angles in monolayer films at the air/water interface: infrared reflection/absorption spectroscopy of behenic acid methyl ester, *J. Phys. Chem. B* 101 (1997) 58–65.
- [36] T. Naolou, A. Meister, R. Schöps, M. Pietzsch, J. Kressler, Synthesis and characterization of graft copolymers able to form polymersomes and worm-like aggregates, *Soft Matter* 9 (2013) 10364–10372.
- [37] R. Mendelsohn, External infrared reflection absorption spectrometry of monolayer films at the air-water interface, *Annu. Rev. Phys. Chem.* 46 (1995) 305–334.
- [38] C. Schwieger, B. Chen, C. Tschierske, J. Kressler, A. Blume, Organization of T-shaped facial amphiphiles at the air/water interface studied by infrared reflection absorption spectroscopy, *J. Phys. Chem. B* 116 (2012) 12245–12256.
- [39] V.L. Kuzmin, A.V. Mikhailov, Molecular theory of light reflection and applicability limits of the macroscopic approach, *Optic Spectrosc.* 51 (1981) 383–385.
- [40] V.L. Kuzmin, V.P. Romanov, A.V. Mikhailov, Reflection of light at the boundary of liquid systems and structure of the surface layer: a review, *Optic Spectrosc.* 73 (1992) 1–26.
- [41] J.E. Bertie, M.K. Ahmed, H.H. Eysel, Infrared intensities of liquids. 5. Optical and dielectric constants, integrated intensities, and dipole moment derivatives of H<sub>2</sub>O and D<sub>2</sub>O at 22 °C, *J. Phys. Chem.* 93 (1989) 2210–2218.
- [42] J.E. Bertie, Z. Lan, Infrared intensities of liquids XX: the intensity of the OH stretching band of liquid water revisited, and the best current values of the optical constants of H<sub>2</sub>O(l) at 25 °C between 15,000 and 1 cm<sup>-1</sup>, *Appl. Spectrosc.* 50 (1996) 1047–1057.
- [43] D.M. Smilgies, N. Boudet, B. Struth, O. Kononov, Troika II: a versatile beamline for the study of liquid and solid interfaces, *J. Synchrotron Radiat.* 12 (2005) 329–339.
- [44] R. Vilanove, F. Rondelez, Scaling description of two-dimensional chain conformations in polymer monolayers, *Phys. Rev. Lett.* 45 (1980) 1502–1504.
- [45] H. Bourque, I. Laurin, M. Pézolet, J.M. Klass, R.B. Lennox, G.R. Brown, Investigation of the poly(L-lactide)/poly(D-lactide) stereocomplex at the air-water interface by polarization modulation infrared reflection absorption spectroscopy, *Langmuir* 17 (2001) 5842–5849.
- [46] N. Hasan, C. Schwieger, H.T. Tee, F.R. Wurm, K. Busse, J. Kressler, Crystallization of a polyphosphoester at the air-water interface, *Eur. Polym. J.* 101 (2018) 350–357.
- [47] A.A.J. Ketelaars, Y. Papanitiou, K. Nakayama, Analysis of the density and the enthalpy of poly( $\epsilon$ -caprolactone) - polycarbonate blends: amorphous phase compatibility and the effect of secondary crystallization, *J. Appl. Polym. Sci.* 66 (1997) 921–927.
- [48] T.J. Joncheray, K.M. Denoncourt, C. Mathieu, M.A.R. Meier, U.S. Schubert, R. S. Duran, Langmuir and Langmuir-Blodgett films of poly(ethylene oxide)-*b*-poly( $\epsilon$ -caprolactone) star-shaped block copolymers, *Langmuir* 22 (2006) 9264–9271.
- [49] C. Qiao, S. Jiang, X. Ji, L. An, B. Jiang, Studies on confined crystallization behavior of poly( $\epsilon$ -caprolactone) thin films, *Front. Chem. China* 2 (2007) 343–348.
- [50] D.M. Smilgies, Scherrer grain-size analysis adapted to grazing-incidence scattering with area detectors, *J. Appl. Crystallogr.* 42 (2009) 1030–1034.
- [51] P. Hollins, Infrared reflection-absorption spectroscopy, *Encycl. Anal. Chem.* 3 (2006) 107–192.
- [52] C. Schwieger, X. Liu, M.P. Krafft, Self-assembled mesoscopic surface domains of fluorocarbon-hydrocarbon diblocks can form at zero surface pressure: Tilting of solid-like hydrocarbon moieties compensates for cross-section mismatch with fluorocarbon moieties, *Phys. Chem. Chem. Phys.* 19 (2017) 23809–23816.
- [53] C. Fuchs, H. Hussain, C. Schwieger, M. Schulz, W.H. Binder, J. Kressler, Molecular arrangement of symmetric and non-symmetric triblock copolymers of polyethylene oxide and polyisobutylene at the air/water interface, *J. Colloid Interface Sci.* 437 (2015) 80–89.
- [54] M.C. Fauré, P. Bassereau, B. Desbat, Orientation of grafted polymer chains at the air-water interface studied by PM-IRRAS, *Eur. Phys. J. E* 2 (2000) 145–151.
- [55] Y. Zhao, D. Keroack, R. Prud'homme, Crystallization under strain and resultant orientation of poly( $\epsilon$ -caprolactone) in miscible blends, *Macromolecules* 32 (1999) 1218–1225.
- [56] M. Jbeily, C. Schwieger, J. Kressler, Mixed Langmuir monolayers of perfluorostearic acid and stearic acid studied by epifluorescence microscopy using fluorinated rhodamines and infrared reflection absorption spectroscopy (IRRAS), *Colloids Surf., A* 529 (2017) 274–285.
- [57] M.M. Coleman, J. Zarian, Fourier-transform infrared studies of polymer blends. II. poly( $\epsilon$ -caprolactone)-poly(vinyl chloride) system, *J. Polym. Sci., Part B: Polym. Phys.* 17 (1979) 837–850.
- [58] T. Elzein, M. Nasser-Eddine, C. Delaite, S. Bistac, P. Dumas, FTIR study of polycaprolactone chain organization at interfaces, *J. Colloid Interface Sci.* 273 (2004) 381–387.
- [59] K. Holland-Moritz, H.W. Siesler, Infrared spectroscopy of polymers, *Appl. Spectrosc. Rev.* 11 (1976) 1–55.
- [60] H. Jiang, P. Wu, Y. Yang, Variable temperature FTIR study of poly(ethylene-co-vinyl alcohol)-graft-poly( $\epsilon$ -caprolactone), *Biomacromolecules* 4 (2003) 1343–1347.
- [61] M. Unger, S. Morita, H. Sato, Y. Ozaki, H. Siesler, Variable-temperature Fourier transform infrared spectroscopic investigations of poly(3-hydroxyalkanoates) and perturbation- correlation moving-window two-dimensional correlation analysis. Part II: study of poly( $\epsilon$ -caprolactone) homopolymer and a poly(3-hydroxybutyrate)-poly( $\epsilon$ -caprolactone) blend, *Appl. Spectrosc.* 63 (2009) 1034–1040.
- [62] X. Du, W. Miao, Y. Liang, IRRAS studies on chain orientation in the monolayers of amino acid amphiphiles at the air-water interface depending on metal complex and hydrogen bond formation with the headgroups, *J. Phys. Chem. B* 109 (2005) 7428–7434.

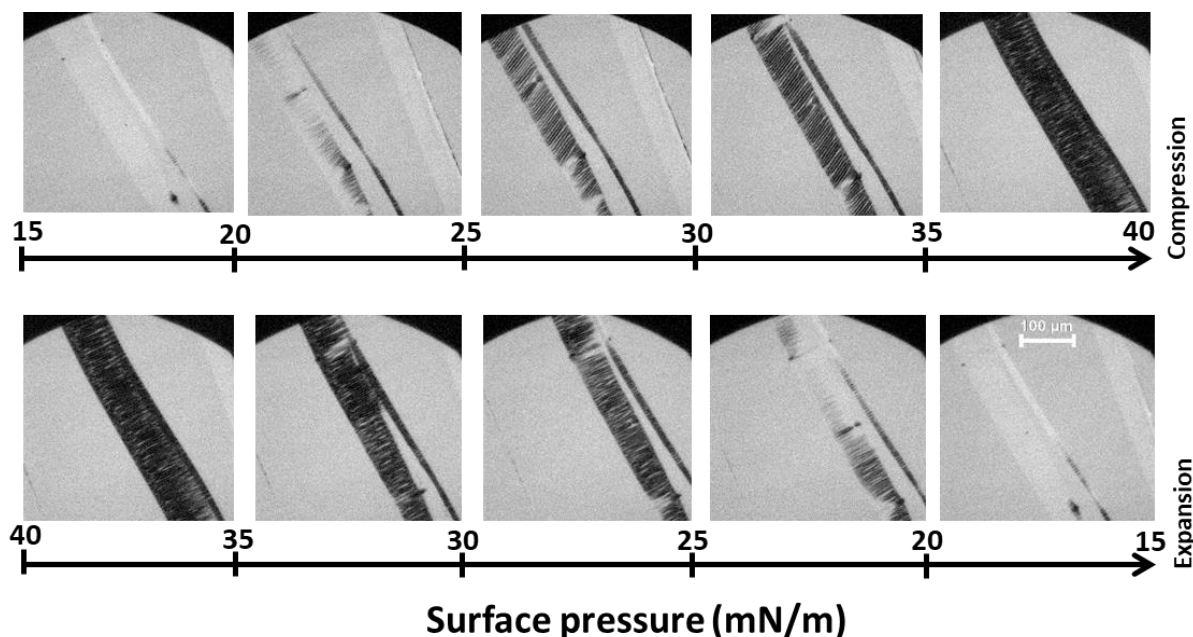
### 3.4 Paper IV

Formation of surface wrinkles in collapsed Langmuir films of a polyhedral oligomeric silsesquioxane containing diblock copolymer<sup>4</sup>

Nazmul Hasan, Karsten Busse, Asad Ullah, Hazrat Hussain, and Jörg Kressler

Langmuir 2021, 37, 13399, <https://doi.org/10.1021/acs.langmuir.1c02082>

Graphical abstract:



Poly(ethylene glycol) (PEG) cannot form stable Langmuir films above a surface pressure of  $\approx 10$  mN/m at room temperature.<sup>[106]</sup> A hybrid diblock copolymer, PEG<sub>113</sub>-*b*-P(MA-POSS)<sub>21</sub> can resolve this issue with unique wrinkle formation in the collapsed film fragments when subjected to several compression-expansion cycles. This wrinkle structure disappeared upon barrier expansion and reappeared again with compression. The  $\pi$ -*mmA* isotherm measurements together with EFM revealed more details of the structure formation. GI-WAXS confirmed the presence of two different orientations of the MA-POSS block in the collapsed film fragments. These orientations were found to be responsible for the wrinkle development.



The author contributions to the following article are: N. Hasan and J. Kressler designed the research. A. Ullah and H. Hussain synthesized the block copolymers. N. Hasan performed the following experiments as Langmuir isotherms, LB transfer, BAM, EFM, AFM, and WAXS. N. Hasan analyzed the data and wrote the draft manuscript. K. Busse performed and analyzed the GI-WAXS data and wrote the GI-WAXS part. N. Hasan, K. Busse, and J. Kressler discussed the results, reviewed them, and finalized the paper.

---

<sup>4</sup>The following article is reprinted (adapted) with permission from Langmuir 2021, <https://doi.org/10.1021/acs.langmuir.1c02082>. Copyright (2021) ACS. The link to the article on the publisher's website is <https://pubs.acs.org/doi/10.1021/acs.langmuir.1c02082>. The supporting information files can be found under the link below: [https://pubs.acs.org/doi/suppl/10.1021/acs.langmuir.1c02082/suppl\\_file/la1c02082\\_si\\_002.pdf](https://pubs.acs.org/doi/suppl/10.1021/acs.langmuir.1c02082/suppl_file/la1c02082_si_002.pdf). No changes were made.

# Formation of Surface Wrinkles in Collapsed Langmuir Films of a Polyhedral Oligomeric Silsesquioxane Containing Diblock Copolymer

Nazmul Hasan, Karsten Busse, Asad Ullah, Hazrat Hussain, and Jörg Kressler\*



Cite This: *Langmuir* 2021, 37, 13399–13408



Read Online

ACCESS |



Metrics & More

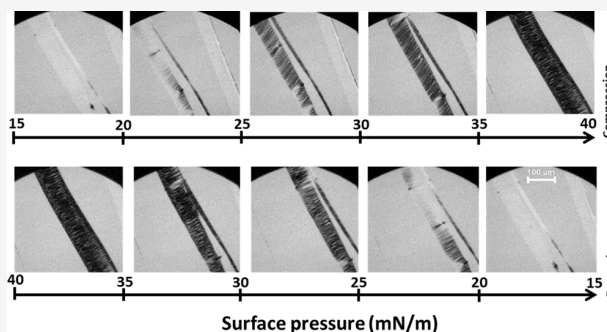


Article Recommendations



Supporting Information

**ABSTRACT:** Surface pressure versus mean molecular area isotherms of Langmuir films of a hybrid diblock copolymer of poly(ethylene glycol) (PEG) and poly(methacrylo polyhedral oligomeric silsesquioxane) P(MA-POSS) together with Brewster angle microscopy reveal details of the phase transitions. The formation of a periodic wrinkling pattern in collapsed films is observed by epifluorescence microscopy after applying several compression–expansion cycles above the surface pressure of  $\approx 18$  mN/m. The wrinkle formation is reversible upon compression and expansion of the Langmuir films. Two distinct orientations of POSS molecules are assumed in Langmuir films upon compression, vertically for chains close to the water surface and horizontally orientated upper layers with significant amounts of PEG in between them. Thus, the wrinkling forms mainly in the top stiffer MA-POSS blocks above a certain compressional stress. The wrinkles disappear during the Langmuir–Blodgett (LB) transfer. Nevertheless, atomic force microscopy and grazing incidence wide-angle X-ray scattering experiments reveal the formation of highly ordered POSS molecules in LB films.



## INTRODUCTION

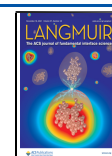
Strain-induced surface patterns have received increasing interest in recent years as a result of their applications in flexible electronics,<sup>1,2</sup> soft actuators,<sup>3</sup> stretchable random lasers,<sup>4</sup> smart adhesives,<sup>5</sup> optical grating,<sup>6</sup> and self-assembly microfabrication.<sup>7</sup> Surface wrinkles or undulations belong to a common type of spatial periodic pattern that develops in stiff thin films deposited on a soft elastic substrate and subjected to stress.<sup>8,9</sup> This can cause contraction of the substrate that reduces the projected area below the thin surface film.<sup>10</sup> A stiff substrate on the other hand might induce delaminating patterns, like buckles.<sup>11</sup> Furthermore, the application of biaxial compression to films can facilitate labyrinth patterns,<sup>12</sup> while uniaxial compression generates straight wrinkles.<sup>13</sup> Although the wrinkling pattern has several unique properties (e.g., optical and acoustic) caused by wave interference phenomena, the lack of controllable fabrication limits their applications.<sup>14–17</sup> A Langmuir trough with a controlled compression–expansion system might be suitable for well-defined wrinkle formation. The fabrication of polymeric Langmuir films begins with spreading solutions of amphiphilic polymers on aqueous surfaces of the trough, solvent evaporation, and applying symmetrical lateral compression by moving the barriers.<sup>18,19</sup> This approach enables controlled compression as well as real-time monitoring of the film morphology by different microscopic, spectroscopic, and scattering techniques.

Unfortunately, several amphiphilic polymers are not suitable for the fabrication of wrinkles. This is caused by their semi-crystalline nature, resulting in separated domains rather than a uniform solid film.<sup>20–23</sup> Some polymers or small molecules can form uniform solid films on the water surface,<sup>24</sup> but compression leads to film collapse followed by surface folds instead of periodic wrinkles.<sup>25</sup> This problem can be solved when an amphiphilic hybrid diblock copolymer of poly(ethylene glycol) (PEG) and poly(methacrylo polyhedral oligomeric silsesquioxane) P(MA-POSS) is used. Typically, closed cage POSS ( $T_8R_8$ ) is not suitable for Langmuir film studies<sup>26</sup> unless certain polar groups are attached,<sup>27,28</sup> the cage is opened [e.g.,  $T_7R_7(OH)_3$ ],<sup>29,30</sup> or a block copolymer, such as PEG-*b*-P(MA-POSS),<sup>31</sup> is used. The copolymer under investigation consists of a hydrophilic PEG block and a hydrophobic block of closed cage isobutyl POSS methacrylate [ $T_8(i-Bu)_7MA$ ] (Scheme 1). The Langmuir film behavior of this copolymer has been reported recently, where the size of the PEG block was kept constant (113 units) and the P(MA-

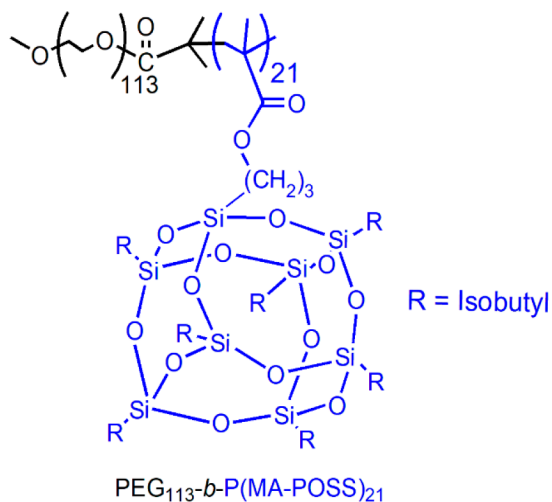
Received: August 5, 2021

Revised: October 8, 2021

Published: November 1, 2021



**Scheme 1. Chemical Structure of the Hybrid Diblock Copolymer PEG<sub>113</sub>-*b*-P(MA-POSS)<sub>21</sub>, Where the MA-POSS Block Is Composed of T<sub>8</sub>(i-Bu)<sub>7</sub>MA Units**



POSS) block was varied from 4 to 21 monomer units of T<sub>8</sub>(i-Bu)<sub>7</sub>MA.<sup>31</sup> Here, the hydrophilic PEG block anchors the hydrophobic P(MA-POSS) block on the water surface. A film stiffening at moderate surface compression was observed followed by film collapse at high compression.<sup>31</sup> Expansion from this state reveals separated fragments of the collapsed film on the water surface observed by Brewster angle microscopy (BAM).

The present study demonstrates that compression–expansion cycles induced a wrinkle pattern on the collapsed Langmuir films of PEG<sub>113</sub>-*b*-P(MA-POSS)<sub>21</sub> (Scheme 1). This wrinkling is reversible and reproducible. The fabrication process is similar to that of wrinkle formation in thin films by strain relieve.<sup>16,17,32–37</sup> Only a few reports use a liquid subphase,<sup>33,38,39</sup> but this is the first study of wrinkle formation in Langmuir films. We will, therefore, primarily focus on the sinusoidal wrinkle formation on collapsed films of PEG<sub>113</sub>-*b*-P(MA-POSS)<sub>21</sub> observed by epifluorescence microscopy. Prior to this, the phase behavior of the Langmuir film upon compression and expansion will thoroughly be characterized by surface pressure versus mean molecular area ( $\pi$ -*mmA*) isotherm measurements and BAM. Langmuir–Blodgett (LB) films will also be prepared at different compression states to reveal the film morphology by atomic force microscopy (AFM)<sup>40</sup> and the molecular ordering by grazing incidence wide-angle X-ray scattering (GI-WAXS).<sup>25</sup>

## EXPERIMENTAL SECTION

**Materials.** The PEG<sub>113</sub>-*b*-P(MA-POSS)<sub>21</sub> hybrid diblock copolymer (Scheme 1), with  $M_n \approx 25\,700$  g/mol, comprises a PEG block of 5000 g/mol (113 EG units) and a MA-POSS block [T<sub>8</sub>(i-Bu)<sub>7</sub>MA] of  $\approx 20\,700$  g/mol (21 MA-POSS units). The copolymer was synthesized by atom transfer radical polymerization (ATRP) using PEG as a macroinitiator. Synthesis details, characterization concerning crystallization in bulk, and Langmuir film formation of a series of PEG-*b*-P(MA-POSS) copolymers can be found elsewhere.<sup>31,41</sup>

**Langmuir Isotherms, BAM, and Epifluorescence Microscopy.** The  $\pi$ -*mmA* isotherms were measured using a R&K Langmuir trough (Potsdam, Germany) with a maximum trough area of 258 cm<sup>2</sup>. The trough was equipped with two moveable barriers and a filter paper, which acts as Wilhelmy plate. The whole trough was covered with a Plexiglas box to minimize the subphase evaporation. Deionized

water from TKA GenPure Labor & Reinstwassertechnik Christian Wiesenack (Jena, Germany) with a conductivity of 0.054  $\mu$ S/cm was used as a subphase in the experiment. The temperature of the subphase was maintained at 20 °C with a RCS 6 (Lauda, Germany) thermostat. The purity of the subphase was ensured by maintaining  $\pi$  less than 0.15 mN/m at maximum compression. The isotherms were recorded by spreading a certain amount of copolymer from chloroform solution with a concentration of 1 mg/mL on some random points of the subphase using a Hamilton (Reno, NV, U.S.A.) digital syringe. After 20 min of waiting time for complete solvent evaporation, the trough surface was compressed and expanded with a speed of  $\approx 50$  Å<sup>2</sup> molecule<sup>-1</sup> min<sup>-1</sup> to record the compression–expansion isotherms.

Epifluorescence images were recorded with an Axio Scope A1 Vario epifluorescence microscope from Carl Zeiss Microimaging (Jena, Germany), equipped with an EC Epiplan-NEOFLUAR objective 20–50 $\times$  and a Hamamatsu electron multiplying charge-coupled device (EM-CCD) digital camera. A Langmuir trough from R&K (Potsdam, Germany) with a maximum area of 258 cm<sup>2</sup> placed on a Märzhäuser *x*-*y*-*z* stage (Wetzlar, Germany) and Ludl Mac5000 (Hawthorne, NY, U.S.A.) controller was used. The temperature of the subphase was kept at 20 °C with a water-circulating thermostat. To enable the imaging of the Langmuir film, the tracer fluorescence dye rhodamine 123 ([6-amino-9-(2-methoxycarbonylphenyl)xanthen-3-ylidene]-azanium chloride)<sup>42</sup> was used. The dye was dissolved in  $\approx 140$  mL of water with a target concentration of  $\approx 50$  nM and then poured into the trough. As a result of its lipophilic nature,<sup>42</sup> some dye clusters were formed on the water surface, which were observed as bright spots in the epifluorescence microscope and then removed by sucking the upper layer of the subphase at maximum barrier compression using a pump system. The final dye concentration was not checked afterward, but it was sufficient for imaging. The purity of the subphase was confirmed by keeping  $\pi$  at smaller than  $\approx 0.2$  mN/m at maximum barrier compression. It should be mentioned that a completely water-soluble dye (rhodamine B) was also tested. However, this dye gave a very poor contrast of the film at high surface pressure and is not appropriate for imaging. Rhodamine 123 was excited using a HXP 120 C mercury arc lamp through a TRP-A filter set from Semrock (Rochester, NY, U.S.A.) with a combination of a FF01-280/20 nm window and a FT 310-Di01 nm dichroic mirror. The emission was detected via the FF01-357/44 nm window. The imaging of the film was performed as follows: (a) first, the film was compressed at a speed of  $\approx 50$  Å<sup>2</sup> molecule<sup>-1</sup> min<sup>-1</sup> to its collapsed state (42 mN/m), and imaging was carried out for every 2 mN/m increase of  $\pi$ , and (b) second, the film was expanded from its collapsed state to 0 mN/m, upon tracking several fragmented films. Then, several compression–expansion cycles were carried out upon monitoring these films with the speed range of  $\approx 10$ –50 Å<sup>2</sup> molecule<sup>-1</sup> min<sup>-1</sup>. The morphological changes were recorded in both video and image format.

A NFT Mini BAM from Nanofilm Technologies (Valley View, OH, U.S.A.) coupled with the R&K Langmuir trough (Potsdam, Germany) of 142 cm<sup>2</sup> was used to monitor the water surface during the compression–expansion experiments. The field view on the surface of the microscope was 4.8  $\times$  6.4 mm<sup>2</sup>. A WinTV module (Hauppauge, NY, U.S.A.) was used to capture the images at different surface pressures during the compression–expansion cycles at a speed of  $\approx 50$  Å<sup>2</sup> molecule<sup>-1</sup> min<sup>-1</sup>.

**LB Film Transfer, AFM, and GI-WAXS.** A KSV (Helsinki, Finland) film transfer unit coupled with a R&K Langmuir trough (Potsdam, Germany) with a trough area of 142 cm<sup>2</sup> was used to prepare the LB films. The films were made at several transfer pressures ranging from 8 to 42 mN/m. Cleaned silicon substrates with a dimension of 20  $\times$  10 mm<sup>2</sup> were attached vertically to the transfer unit and immersed into the subphase up to  $\approx 8$  mm. The copolymer solution was then spread on the water surface and, after chloroform evaporation, compressed up to the transfer pressure under isothermal conditions. When the transfer pressure was reached, the submerged silicon substrate was moved upward at a speed of 0.5 mm/min, while  $\pi$  was kept constant. The transferred film was then dried at room

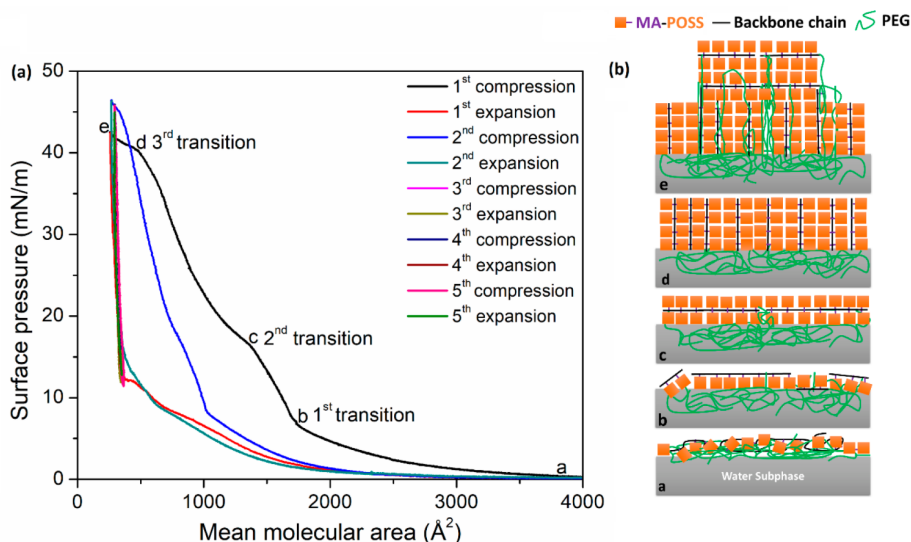


**Figure 1.** (a)  $\pi$ – $mma$  isotherms of a  $\text{PEG}_{113}$ - $b$ - $\text{P}(\text{MA-POSS})_{21}$  copolymer recorded on the water subphase at 20 °C with several compression–expansion cycles at a speed of  $\approx 50 \text{ \AA}^2 \text{ molecule}^{-1} \text{ min}^{-1}$  and (b) schematic presentation of the molecular orientations during the film compression.

temperature and stored in a sealed box for AFM and GI-WAXS studies.

AFM was performed using a Bruker Multimode 8 (Santa Barbara, CA, U.S.A.) instrument in peak-force tapping mode in air. A silicon cantilever of ScanAsyst-AIR from Bruker with a spring constant of 0.4 N/m and a resonance frequency of 75 kHz was used. Images were recorded with 512 pixels and at 1 Hz scan rate. The images were processed by Gwyddion software.

GI-WAXS measurements on the LB films were performed by a Retro-F SAXSLAB setup (Copenhagen, Denmark) equipped with an AXO microfocus X-ray source (Dresden, Germany) and a DECTRIS PILATUS3 R 300K detector (Baden-Daettwil, Switzerland). Measurements were carried out in reflection mode under vacuum at room temperature. The incidence angle  $\alpha_i$  of Cu  $K\alpha$  radiation ( $\lambda = 1.5418 \text{ \AA}$ ) was fixed at  $\approx 0.2^\circ$ . The conversion of the detector images to sample coordinates is described in detail elsewhere.<sup>21,22</sup>

## RESULTS AND DISCUSSION

### Langmuir Film, Collapse Phase, and Wrinkle Pattern.

Langmuir film formation of  $\text{PEG}_{113}$ - $b$ - $\text{P}(\text{MA-POSS})_{21}$  begins with spreading the copolymer solution on the water surface and compression after chloroform evaporation. Several  $\pi$ – $mma$  isotherms are recorded during compression–expansion cycles under isothermal conditions, as depicted in Figure 1a.

The lifting up of  $\pi$  starts from a  $mma$  of  $\approx 3800 \text{ \AA}^2$  during the first compression. This value is slightly larger than the area of 21 POSS molecules of the copolymer (lift-off area of one POSS is  $\approx 150 \text{ \AA}^2$ )<sup>28</sup> but significantly smaller than the area of 113 EG units of the PEG block (area of one EG is  $\approx 44 \text{ \AA}^2$ ).<sup>43</sup> As POSS is attached to a polymer backbone, a more detailed area estimation is carried out. The POSS core can be described by a box with  $\approx 5 \text{ \AA}$  side length (or  $\approx 0.25 \text{ nm}^2$  core area) with additional isobutyl groups in seven corners, increasing the side length to  $\approx 1 \text{ nm}$ .<sup>44</sup> At the eighth corner, POSS is attached via a  $\approx 1 \text{ nm}$  long spacer to the polymer backbone, and at each  $\approx 2.5 \text{ \AA}$  along the backbone, another MA-POSS follows. The exact area requirement depends upon the direction of the isobutyl groups; a horizontal orientation needs more space, while a vertical orientation needs less. A flat two-dimensional (2D) arrangement of 21 MA-POSS units can be obtained (images a and b of Figure 1b) when always a group of four

consecutive POSS units is arranged almost side by side perpendicular to the chain direction, possibly as a result of the spacer length, followed by the next group of four in chain direction. AFM measurements of transferred films at a low surface pressure show a very smooth layer with  $\approx 1.34 \text{ nm}$  thickness, confirming the monolayer formation (Figure S1 of the Supporting Information). It should be noted that the basal plane of hexagonally packed  $\text{T}_8(\text{i-Bu})_8$  would not fit this arrangement, but the dense-packed  $\{101\}$  plane does. Now upon further compression, a gradual increase of  $\pi$  to 8 mN/m can be seen. There is no hysteresis (Figure S2 of the Supporting Information) in the isotherm up to this point, which suggests the formation of a reversible liquid-like film. BAM or epifluorescence microscopy does not show any structure of the surface film. A LB film was therefore prepared, which reveals a flat surface with no distinct PEG and P(MA-POSS) phases.<sup>31</sup> When the compression continues, a sharp increase of  $\pi$  at a  $mma$  of  $\approx 1760 \text{ \AA}^2$  is observed. This reflects the rigidity of the POSS molecules,<sup>27</sup> and the area corresponds to  $\approx 0.84 \text{ nm}^2$  per POSS unit, which is possible if the isobutyl groups are oriented in a vertical direction. The PEG block is now submerged into the subphase at this  $mma$ . We can consider this as a first transition region, and the expected molecular orientation is depicted in image b of Figure 1b. Typically, the dissolution of PEG Langmuir films into the subphase happens at  $\pi \approx 8$ – $10 \text{ mN/m}$ , followed by a plateau in the isotherm.<sup>45,46</sup> The observed continuous increase of  $\pi$  is also an indication of a reorganization of the POSS layer. A pseudo-plateau or kink at  $\pi \approx 18 \text{ mN/m}$  or at  $mma$  of  $\approx 1300 \text{ \AA}^2$  ( $1.2 \text{ nm}^2$  for two POSS units) indicates the formation of a POSS double layer, where the polymer backbone probably forms an intermediate layer (image c of Figure 1b). This can be considered as a second transition. Further compression of the film then yields  $\pi$  values up to  $\approx 41 \text{ mN/m}$  until another pseudo-plateau (third transition) appears (Figure 1a). The area of  $\approx 500 \text{ \AA}^2$  per molecule corresponds to a staple of five POSS units; i.e., each POSS polymer block is now in a vertical orientation with four POSS units as the basal plane and five units high (image d of Figure 1b). A compression beyond this



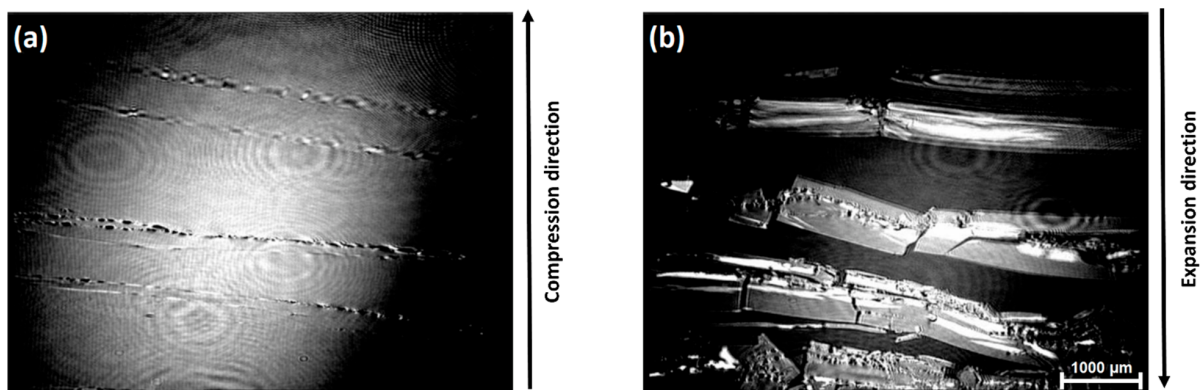


**Figure 2.** BAM images of the PEG<sub>113</sub>-*b*-P(MA-POSS)<sub>21</sub> copolymer captured on the water subphase at a  $\pi$  of (a)  $\approx 41$  mN/m during the first compression and (b)  $\approx 10$  mN/m during the first expansion from the collapsed state. In both cases, a compression–expansion rate of  $\approx 50$  Å<sup>2</sup> molecule<sup>-1</sup> min<sup>-1</sup> was used.

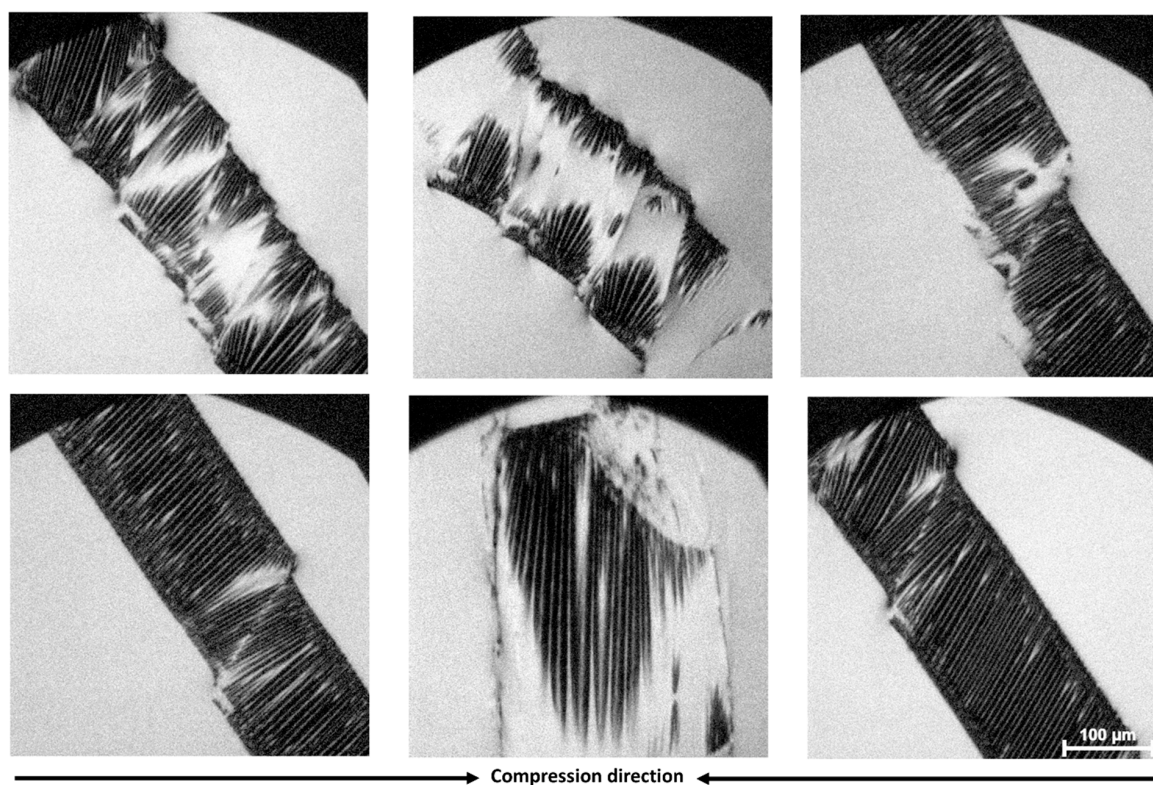


**Figure 3.** Epifluorescence images of PEG<sub>113</sub>-*b*-P(MA-POSS)<sub>21</sub> captured on an aqueous subphase with rhodamine 123 dye at  $\pi \approx 40$  mN/m at different locations of the Langmuir trough during the fifth compression cycle. A compression–expansion rate of  $\approx 50$  Å<sup>2</sup> molecule<sup>-1</sup> min<sup>-1</sup> was used. More images of collapsed films with wrinkles can be found in Figures S3–S5 of the Supporting Information.

area automatically leads to film collapse and multilayer formation with horizontally orientated POSS layers on top. Image e of Figure 1b illustrates a possible arrangement of the molecules in the collapsed state. Unfortunately, no film structure was observed by BAM or even by epifluorescence microscopy, with the exception of some strips in the third transition region ( $\approx 41$  mN/m), which was already identified as film collapse<sup>31</sup> (see Figure 2a). The second transition at  $\approx 18$  mN/m during the first compression cycle is, therefore, characterized after transferring Langmuir films onto a solid support as discussed in detail in the section of characterization of LB films.

Additionally, Figure 1a also shows  $\pi$ -*m*mA isotherms recorded during the expansion of the barriers from  $\pi$  of  $\approx 43$  to 0 mN/m. Immediately, a sharp drop of  $\pi$  (relaxation phenomenon)<sup>29</sup> to  $\approx 10$  mN/m followed by a gradual decrease to 0 mN/m can be seen. Both BAM (see Figure 2b) and epifluorescence microscopy show some collapsed film fragments of different shapes. The sharp edges are indicating some kind of molecular arrangement (POSS molecules are on top of the films), as illustrated in image e of Figure 1b. These fragments are not disappearing, even when  $\pi$  reaches 0 mN/m, caused by maximum barrier expansion. When the second compression is applied (Figure 1a), the  $\pi$  value now begins to

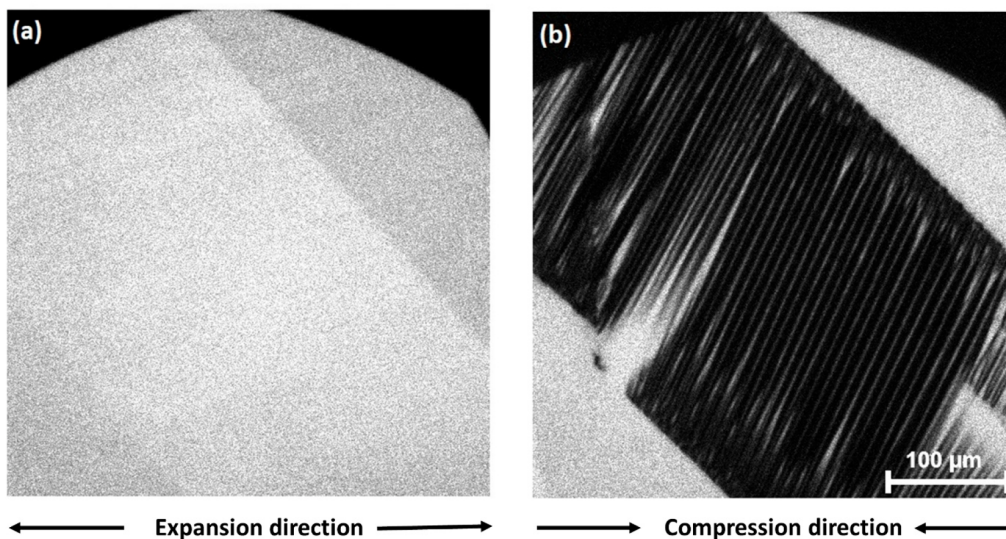


**Figure 4.** Epifluorescence images of  $\text{PEG}_{113}\text{-}b\text{-P}(\text{MA-POSS})_{21}$  captured at  $\pi$  of (a) 10 mN/m during the first expansion from the collapsed state and (b) 35 mN/m during the fifth compression cycle. For both cases, a compression–expansion rate of  $\approx 10 \text{ \AA}^2 \text{ molecule}^{-1} \text{ min}^{-1}$  was used.

increase from a smaller  $mmA$  of  $\approx 3000 \text{ \AA}^2$  and reaches a slightly higher  $\pi$  of 45 mN/m. This smaller  $mmA$  is expected because a stable structure (multilayers) on the water surface was formed. Now monitoring the collapsed films using epifluorescence microscopy reveals a very unique surface morphology when several compression–expansion cycles are applied. Many dark strips with spatial periodicity in the micrometer range, depending upon the shape of the films, are formed upon maximum compression. These structures become more and more visible when several compression–expansion cycles are performed. Figure 3 shows some epifluorescence images that are captured at  $\approx 40 \text{ mN/m}$  and at several locations of the trough.

It is expected that the dye molecules are mostly absorbed in MA-POSS parts of the block copolymer as a result of the lipophilic nature of rhodamine 123.<sup>42</sup> Thus, the bright white background of the images represents the dye-incorporated Langmuir film. The dark contrast in Figure 3 is the non-fluorescent or dye-free region of the collapsed films. This is because the compression either excludes (typical for crystallization)<sup>20,23,47–49</sup> or deactivates (self-quenching phenomenon)<sup>50</sup> the dye in this part of the Langmuir film. When the film area is expanded, the dark regions become bright very fast (Figure S9 of the Supporting Information), which is a good indication for the dye self-quenching mechanism. In the case of crystallization, upon film expansion, the domains would remain dark until the crystals vanish.

The darker regions in Figure 3 possess periodic patterns in different directions with respect to the direction of the compression. This pattern can be called wrinkles according to previously reported structures.<sup>14,16,32,51,52</sup> In short, wrinkles, folds, creases, and ridges are all examples of various surface structures caused by mechanical instabilities of soft materials. The last three examples are classified as extremely nonlinear types, i.e., non-uniform, self-contact with sharp indentation, period doubles, and narrow peaks.<sup>52</sup> However, the surface wrinkles, which have been well-identified in the past few years, show a relatively uniform wavy shape, spatial periodic pattern, or sinusoidal feature in the wavelength ( $\lambda$ ) range of 5–15  $\mu\text{m}$ .<sup>14,16,32,51,52</sup> As a result of their large dimension, these

features can be well-resolved by different microscopic techniques, such as optical microscopy or atomic force microscopy (AFM). In our case, the observed periodic pattern has fairly similar sinusoidal shapes and can be well-resolved by epifluorescence microscopy. Figures S3, S4, and S10 of the Supporting Information also provide some evidence for this structure. Thus, the term “wrinkle” is accurately describing our results. These wrinkles possess a periodicity of  $\lambda \approx 5\text{--}9 \mu\text{m}$  depending upon the compression speed of the barriers (Figures 3 and 4 and Figures S3–S5 of the Supporting Information). This is because slow compression results in bigger broken films, which results in a larger wavelength of the wrinkles. In addition, wrinkling is a fast process. Therefore, slow compression also provides better imaging conditions. Of course, there might be some kinetic effects that we cannot separate in this case. Regardless of the degree of compression, wrinkling only develops when the  $mmA$  reaches a certain value. Once the compression (applied stress) is released, the wrinkles disappear and reappear again after further compression, which indicates an elastic deformation.<sup>53</sup> In addition, we observed that the wrinkles are not apparent in BAM experiments (Figure S6 of the Supporting Information). This might be caused by the limited lateral resolution of BAM. In contrast, epifluorescence microscopy has a 10 $\times$  higher magnification than BAM. The dye used for the experiment has no significant influence on the  $\pi$ – $mmA$  isotherm (Figure S7 of the Supporting Information).

Now, to understand the formation of these wrinkles, we follow a single collapsed film during several compression–expansion cycles. The structural changes are recorded for every 2 mN/m increase or decrease of  $\pi$ . Figure 5 shows epifluorescence images recorded during the fifth compression–expansion cycle of a collapsed film in the  $\pi$  range from  $\approx 14$  to 42 mN/m.

The experiment exhibits dark nucleation sites at fragment edges of the collapsed film (bright stripes), starting at  $\pi \approx 14 \text{ mN/m}$  (top image 14 of Figure 5). When the compression is continued, many dark wrinkles appear up to the maximum barrier compression (top image 42 of Figure 5). The periodicity varies from  $\approx 5$  to 9  $\mu\text{m}$ . These features almost



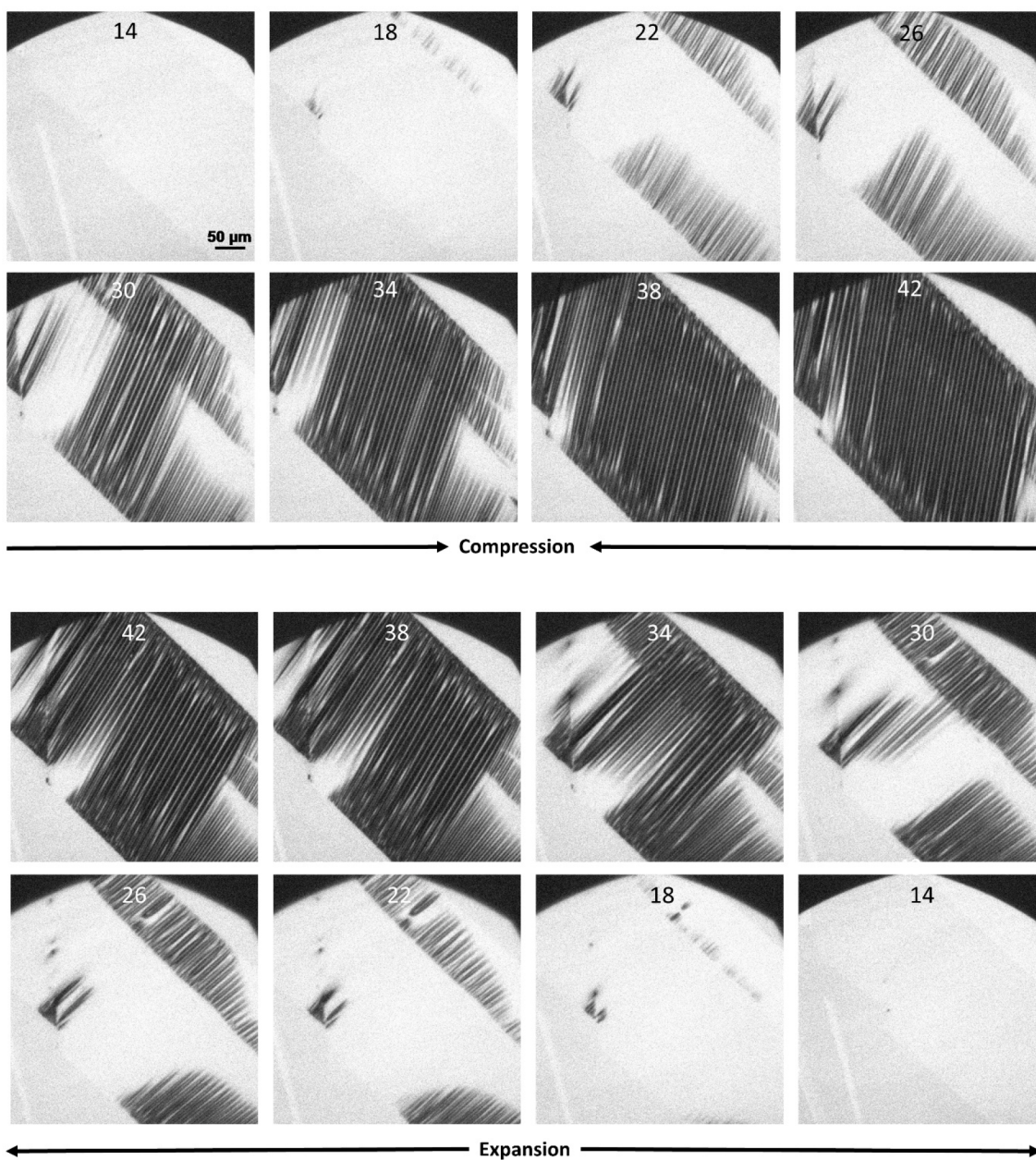


**Figure 5.** Epifluorescence images of  $\text{PEG}_{113}\text{-}b\text{-P}(\text{MA-POSS})_{21}$  captured at different surface pressures during the (top) fifth compression cycle and (bottom) fifth expansion cycle. The numbers in the images indicate  $\pi$ . For both cases, a compression–expansion rate of  $\approx 10 \text{ \AA}^2 \text{ molecule}^{-1} \text{ min}^{-1}$  was used. The whole process was recorded as a video, which can be found in Figure S9 of the Supporting Information, and similar wrinkled structures for other collapsed films can be seen in Figure S10 of the Supporting Information.

disappear below  $\pi$  of 18 mN/m during the expansion cycle (bottom image 14 of Figure 5) and reappear again with compression. This reversibility is typical for wrinkle formation in the elastic deformation region.<sup>53</sup> It is also clear from the images (Figures 3–5) that the wrinkling is independent from the compression direction of the barriers. This is because the compression by moving barriers of the Langmuir trough is not directly exerted to the collapsed film fragments rather than to the flexible thin film surrounding them. A similar behavior is observed for some systems where wrinkles are generated along cracks not in the deformation direction.<sup>14</sup> Generally, a stiffer thin layer on top of an elastic substrate exhibits wrinkling

during relaxation of the strained substrate connected with the transfer of elastic energy.<sup>8</sup> In our case, the vertically orientated MA-POSS blocks may act as a soft layer and the horizontally orientated MA-POSS blocks are the stiffer parts (Figure 1b). During the compression, a stress acts to the vertical MA-POSS layer anchored to the water surface. The vertically orientated MA-POSS layer then transfers the stress to the horizontally orientated MA-POSS blocks. The acting stress is then relieved by wrinkle formation. This is only occurring when a certain concentration of the MA-POSS molecules is present in the copolymer. For example, wrinkle formation was not observed in epifluorescence images for copolymers with MA-POSS

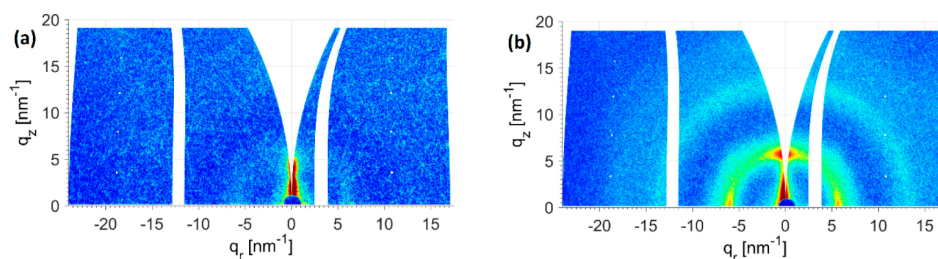


**Figure 6.** Two-dimensional GI-WAXS pattern of the LB film of PEG<sub>113</sub>-*b*-P(MA-POSS)<sub>21</sub> transferred at  $\pi$  of (a) 10 mN/m and (b) 25 mN/m.

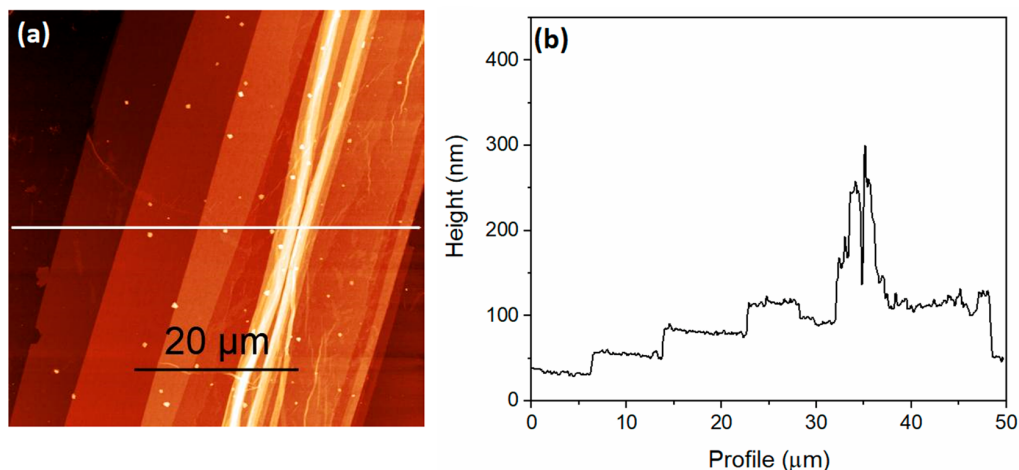


**Figure 7.** (a) AFM height image and (b) line profile of the LB film of PEG<sub>113</sub>-*b*-P(MA-POSS)<sub>21</sub> transferred at  $\pi \approx 42$  mN/m onto a silicon wafer during the fifth compression cycle.

concentrations in the range from PEG<sub>113</sub>-*b*-P(MA-POSS)<sub>4</sub> to PEG<sub>113</sub>-*b*-P(MA-POSS)<sub>8</sub>. This is because the collapsed films are not stiff enough to form wrinkles; i.e., they are fluid-like (Figure S8 of the Supporting Information). Now it is worth mentioning that the Langmuir trough technique is suitable for the fabrication of controlled wrinkling patterns, even though quantitative studies, such as modulus calculation, are not possible because the wrinkles are non-transferable to a solid support to estimate the amplitude information (height) of them.

**Characterization of LB Films.** To identify the structural changes that occurred during the Langmuir film compression, GI-WAXS experiments were conducted on LB films transferred at various  $\pi$ . Figure 6a shows a GI-WAXS image of the LB film transferred at the first transition region (first compression cycle) at  $\approx 10$  mN/m.

A very weak signal at the  $q_r$  position of  $\approx 5$  nm<sup>-1</sup> is observed in horizontal and vertical directions. This indicates a typical distance of  $d = 2\pi/q_r = 1.3$  nm, which is slightly more than the diameter of a POSS molecule. For LB films transferred above the second transition region at 25 mN/m, the Bragg reflection is slightly shifted to  $q_r \approx 5.75$  nm<sup>-1</sup>, again observed in horizontal and vertical directions (Figure 6b). This value is in good agreement with the {101} signal of POSS in the hexagonal crystal structure,<sup>44,54,55</sup> and in the vertical direction, it was expected as a result of its higher packing density; however, the peak directions do not fit: in a hexagonal lattice, a reflection from an equivalent plane (e.g., {01 $\bar{1}$ }) should show a tilt between both reflections, which is not 90°, as observed in our case. Additionally, in some measurements, a very weak signal at  $q_r \approx 8.13$  nm<sup>-1</sup> was observed at a tilt of  $\approx 45^\circ$ , leading

to the assumption of a simple cubic structure (sc) with the lattice parameter  $a = 1.09$  nm showing {100} and {110} and their equivalent reflections in the correct positions. Furthermore, in some measurements, the vertical direction is slightly shifted, forming a tetragonal lattice with a longer  $c$  direction. In this case, the isobutyl groups are more extended in the vertical direction, as discussed above. GI-WAXS on the collapsed film transferred at 42 mN/m shows similar patterns with a more intense signal as a result of the more transferred material and a lattice parameter of  $a = 1.03$  nm (Figure S11 of the Supporting Information).

Now looking at Figure 6b again, a broad ring at  $q_r \approx 14$  nm<sup>-1</sup> is observed. This is identified as an amorphous halo for the PEG block.<sup>41</sup> Thus, it is obvious that the second transition region at  $\approx 18$  mN/m is related to reorientation of POSS molecules of the P(MA-POSS) block. The PEG block on the other hand stays amorphous as a result of hydration or the presence of bulky MA-POSS groups, which restrict the molecular movement of the PEG chains necessary for crystallization.<sup>31</sup> Note that wide-angle X-ray scattering (WAXS) studies on this copolymer in the bulk show several Bragg reflections. Reflections at the  $2\theta$  position of  $8.18^\circ$  ( $d$  spacing of 1.08 nm) and  $11.03^\circ$  ( $d$  spacing of 0.8 nm) are in agreement with the {101} and {110} reflections for the POSS units in a hexagonal lattice,<sup>44,54,55</sup> but also a simple cubic or a tetragonal lattice is possible. Without more reflections, the crystal structure in bulk cannot be identified. The reflection at  $23.51^\circ$  is identified as the overlapping {112} and {032} signals for the PEG block (Figure S12 of the Supporting Information).<sup>44,54,55</sup> The reflection at  $2\theta$  of  $19.26^\circ$  can originate from both POSS and PEG blocks.<sup>41</sup> Thus, it is



obvious that several reflections cannot be identified in the GI-WAXS images. This is because of the broad distribution of the detected signals caused by the scattering from several locations of the film.<sup>56</sup> The same LB films were then investigated by AFM, as presented in Figure 7.

Several broken films with an elevated thickness from 25 to 32 nm are observed. In some regions, the thickness is more than 150 nm. These values are much larger compared to the film thickness (i.e.,  $\approx 3.0\text{--}3.5$  nm) of the LB film transferred at 25 mN/m.<sup>31</sup> We cannot distinguish the PEG or P(MA-POSS) blocks from the surface analysis. The AFM image also reveals no wrinkle structure of the collapsed films. We investigated several films, but in all cases, no wrinkles were observed, even after transferring the film directly after epifluorescence measurements at  $\approx 41$  mN/m (Figure S13 of the Supporting Information). This is because the wrinkles are only stable under lateral compression and disappear during the film-transferring process as a result of the relaxation of the stiffer POSS molecules. As a result, conducting GI-WAXS or infrared reflection absorption spectroscopic studies directly on the collapsed Langmuir films without moving them to the solid support are necessary for future work.

## CONCLUSION

Langmuir film formation of PEG<sub>113</sub>-*b*-P(MA-POSS)<sub>21</sub> with several plateaus in the  $\pi$ -*mmA* isotherm assigned to multilayer

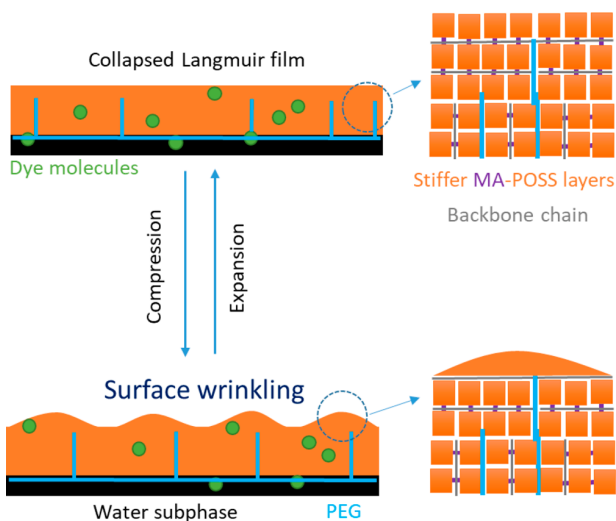


**Figure 8.** Schematic presentation of the surface wrinkling on the collapsed Langmuir film of PEG<sub>113</sub>-*b*-P(MA-POSS)<sub>21</sub> during compression. The orange color indicates POSS molecules; the blue color indicates PEG chains; the green color indicates dye molecules; and the black color indicates the water subphase. It should be mentioned that the length scale for the wrinkling with several micrometers is about 1000 times larger than the size of the POSS molecules. Therefore, the sketch of the wrinkling is simplified.

formation and film collapse has recently been reported.<sup>31</sup> The present study demonstrates the formation of a very unique surface structure in collapsed Langmuir films. It is observed that, when the films are subjected to several compression and expansion cycles, periodically arranged surface wrinkles above  $\pi$  of  $\approx 18$  mN/m appear as confirmed by epifluorescence microscopy. The wrinkles disappear upon barrier expansion and reappear again with compression. A schematic illustration

concerning the wrinkling on collapsed film fragments is shown in Figure 8. Two distinct orientations of POSS molecules are estimated, vertically for chains close to the water surface and horizontally orientated upper layers with significant amounts of PEG in between them. The wrinkled structure is thus believed to be formed mainly in the top stiffer MA-POSS molecules of the copolymer above a certain compressional stress.

The compression of the soft layer induces a stress in the stiff layer, which is relieved by forming wrinkles.<sup>17,32</sup> The wrinkles also exhibit dark contrast in the epifluorescence images as a result of dye exclusion or dye deactivation. Finally, the collapsed films are then transferred at a highly compressed state to the solid support, and AFM investigations do not reveal wrinkles on the films but ordering in POSS molecules as confirmed by GI-WAXS experiments. The Langmuir trough together with the hybrid diblock copolymer PEG<sub>113</sub>-*b*-P(MA-POSS)<sub>21</sub> can be used to fabricate different fascinating patterns, such as periodic surface wrinkles, in a controlled manner.

## ASSOCIATED CONTENT

### Supporting Information

The Supporting Information is available free of charge at <https://pubs.acs.org/doi/10.1021/acs.langmuir.1c02082>.

Wrinkle formation in video format (ZIP)

AFM measurement, hysteresis measurement of the  $\pi$ -*mmA* isotherm, epifluorescence and BAM images of the collapsed films,  $\pi$ -*mmA* isotherms and BAM images of the collapsed films,  $\pi$ -*mmA* isotherms at different sub-phases, BAM image of the PEG<sub>113</sub>-*b*-P(MA-POSS)<sub>8</sub> copolymer, epifluorescence images, GI-WAXS of the collapsed film and WAXS measurements in bulk, and AFM image of collapsed films (PDF)

## AUTHOR INFORMATION

### Corresponding Author

Jörg Kressler – Department of Chemistry, Martin Luther University Halle-Wittenberg, D-06099 Halle, Germany; [orcid.org/0000-0001-8571-5985](https://orcid.org/0000-0001-8571-5985); Email: [joerg.kressler@chemie.uni-halle.de](mailto:joerg.kressler@chemie.uni-halle.de)

### Authors

Nazmul Hasan – Department of Chemistry, Martin Luther University Halle-Wittenberg, D-06099 Halle, Germany  
 Karsten Busse – Department of Chemistry, Martin Luther University Halle-Wittenberg, D-06099 Halle, Germany; [orcid.org/0000-0003-4168-0957](https://orcid.org/0000-0003-4168-0957)  
 Asad Ullah – Department of Chemistry, Quaid-i-Azam University Islamabad, Islamabad 45320, Pakistan  
 Hazrat Hussain – Department of Chemistry, Quaid-i-Azam University Islamabad, Islamabad 45320, Pakistan

Complete contact information is available at: <https://pubs.acs.org/10.1021/acs.langmuir.1c02082>

### Notes

The authors declare no competing financial interest.

## ACKNOWLEDGMENTS

This work was supported by Deutsche Forschungsgemeinschaft (Project 189853844 TRR 102, Project B07). AFM and GI-WAXS measurements were carried out within the cooperation of SFB TRR 102 (Project B03, Thomas Thurn-Albrecht). The authors thank Dr. Oleksandr Dolynchuk for the conversion of GI-WAXS images. HH gratefully acknowledges

the financial support from Higher Commission (HEC) of Pakistan under NRP project No. 20-3074/NRP/UR&D/HEC/13 and the Alexander von Humboldt Foundation-Germany (Georg Forster Research Fellowship).

## REFERENCES

- (1) Sun, Y.; Choi, W. M.; Jiang, H.; Huang, Y. Y.; Rogers, J. A. Controlled Buckling of Semiconductor Nanoribbons for Stretchable Electronics. *Nat. Nanotechnol.* **2006**, *1*, 201–207.
- (2) Li, Y. Reversible Wrinkles of Monolayer Graphene on a Polymer Substrate: Toward Stretchable and Flexible Electronics. *Soft Matter* **2016**, *12*, 3202–3213.
- (3) Tokudome, Y.; Kuniwaki, H.; Suzuki, K.; Carboni, D.; Poologasundarampillai, G.; Takahashi, M. Thermoresponsive Wrinkles on Hydrogels for Soft Actuators. *Adv. Mater. Interfaces* **2016**, *3*, 1500802.
- (4) Hu, H.-W.; Haider, G.; Liao, Y.-M.; Roy, P. K.; Ravindranath, R.; Chang, H.-T.; Lu, C.-H.; Tseng, C.-Y.; Lin, T.-Y.; Shih, W.-H.; Chen, Y.-F. Wrinkled 2D Materials: A Versatile Platform for Low-Threshold Stretchable Random Lasers. *Adv. Mater.* **2017**, *29*, 1703549.
- (5) Chan, E. P.; Smith, E. J.; Hayward, R. C.; Crosby, A. J. Surface Wrinkles for Smart Adhesion. *Adv. Mater.* **2008**, *20*, 711–716.
- (6) Yu, C.; O'Brien, K.; Zhang, Y.-H.; Yu, H.; Jiang, H. Tunable Optical Gratings Based on Buckled Nanoscale Thin Films on Transparent Elastomeric Substrates. *Appl. Phys. Lett.* **2010**, *96*, 041111.
- (7) Yoo, P. J. Fabrication of Complexly Patterned Wavy Structures Using Self-Organized Anisotropic Wrinkling. *Electron. Mater. Lett.* **2011**, *7*, 17–23.
- (8) Groenewold, J. Wrinkling of Plates Coupled with Soft Elastic Media. *Phys. A* **2001**, *298*, 32–45.
- (9) Ares, P.; Wang, Y. B.; Woods, C. R.; Dougherty, J.; Fumagalli, L.; Guinea, F.; Davidovitch, B.; Novoselov, K. S. Van Der Waals Interaction Affects Wrinkle Formation in Two-Dimensional Materials. *Proc. Natl. Acad. Sci. U. S. A.* **2021**, *118*, No. e2025870118.
- (10) Deng, S.; Berry, V. Increased Hierarchical Wrinkles on Stiff Metal Thin Film on a Liquid Meniscus. *ACS Appl. Mater. Interfaces* **2016**, *8*, 24956–24961.
- (11) Audoly, B. Stability of Straight Delamination Blisters. *Phys. Rev. Lett.* **1999**, *83*, 4124–4127.
- (12) Yin, J.; Yagüe, J. L.; Eggenpieler, D.; Gleason, K. K.; Boyce, M. C. Deterministic Order in Surface Micro-Topologies through Sequential Wrinkling. *Adv. Mater.* **2012**, *24*, 5441–5446.
- (13) Chung, J. Y.; Nolte, A. J.; Stafford, C. M. Surface Wrinkling: A Versatile Platform for Measuring Thin-Film Properties. *Adv. Mater.* **2011**, *23*, 349–368.
- (14) Yu, S.; Zhang, X.; Xiao, X.; Zhou, H.; Chen, M. Wrinkled Stripes Localized by Cracks in Metal Films Deposited on Soft Substrates. *Soft Matter* **2015**, *11*, 2203–2212.
- (15) Jin, L. Mechanical Instabilities of Soft Materials: Creases, Wrinkles, Folds, and Ridges. Doctoral Dissertation, Harvard University, Cambridge, MA, 2014; pp 1–215.
- (16) Kim, P.; Abkarian, M.; Stone, H. A. Hierarchical Folding of Elastic Membranes under Biaxial Compressive Stress. *Nat. Mater.* **2011**, *10*, 952–957.
- (17) Schweikart, A.; Fery, A. Controlled Wrinkling as a Novel Method for the Fabrication of Patterned Surfaces. *Microchim. Acta* **2009**, *165*, 249–263.
- (18) Crisp, D. J. Surface Films of Polymers. Part I. Films of the Fluid Type. *J. Colloid Sci.* **1946**, *1*, 49–70.
- (19) Crisp, D. J. Surface Films of Polymers. Part II. Films of the Coherent and Semi-Crystalline Type. *J. Colloid Sci.* **1946**, *1*, 161–184.
- (20) Hasan, N.; Schwiager, C.; Tee, H. T.; Wurm, F. R.; Busse, K.; Kressler, J. Crystallization of a Polyphosphoester at the Air-Water Interface. *Eur. Polym. J.* **2018**, *101*, 350–357.
- (21) Busse, K.; Fuchs, C.; Hasan, N.; Pulst, M.; Kressler, J. Crystallization of Poly(Ethylene Oxide) on the Surface of Aqueous Salt Solutions Studied by Grazing Incidence Wide-Angle X-ray Scattering. *Langmuir* **2018**, *34*, 12759–12763.
- (22) Hasan, N.; Fuchs, C.; Schwiager, C.; Busse, K.; Dolynchuk, O.; Kressler, J. Crystallization of Poly( $\delta$ -Caprolactone) at the Air-Water Interface Studied by IRRAS and GI-WAXS. *Polymer* **2020**, *196*, 122468.
- (23) Hasan, N.; Busse, K.; Haider, T.; Wurm, F. R.; Kressler, J. Crystallization of Poly(Ethylene)s with Regular Phosphoester Defects Studied at the Air-Water Interface. *Polymers* **2020**, *12*, 2408.
- (24) Schöne, A.-C.; Schulz, B.; Richau, K.; Kratz, K.; Lendlein, A. Characterization of Langmuir Films Prepared from Copolyester-ethanes Based on Oligo( $\omega$ -Pentadecalactone) and Oligo( $\epsilon$ -Caprolactone) Segments. *Macromol. Chem. Phys.* **2014**, *215*, 2437–2445.
- (25) Baoukina, S.; Monticelli, L.; Risselada, H. J.; Marrink, S. J.; Tieleman, D. P. The Molecular Mechanism of Lipid Monolayer Collapse. *Proc. Natl. Acad. Sci. U. S. A.* **2008**, *105*, 10803–10808.
- (26) Deng, J.; Hottle, J. R.; Polidan, J. T.; Kim, H.-J.; Farmer-Creely, C. E.; Viers, B. D.; Esker, A. R. Polyhedral Oligomeric Silsesquioxane Amphiphiles: Isotherm and Brewster Angle Microscopy Studies of Trisilanolisobutyl-POSS at the Air/Water Interface. *Langmuir* **2004**, *20*, 109–115.
- (27) Lee, W.; Ni, S.; Deng, J.; Kim, B.-S.; Satija, S. K.; Mather, P. T.; Esker, A. R. Telechelic Poly(Ethylene Glycol)-POSS Amphiphiles at the Air/Water Interface. *Macromolecules* **2007**, *40*, 682–688.
- (28) Paczesny, J.; Binkiewicz, I.; Janczuk, M.; Wybrańska, K.; Richter, L.; Holyst, R. Langmuir and Langmuir-Blodgett Films of Unsymmetrical and Fully Condensed Polyhedral Oligomeric Silsesquioxanes (POSS). *J. Phys. Chem. C* **2015**, *119*, 27007–27017.
- (29) Deng, J.; Farmer-Creely, C. E.; Viers, B. D.; Esker, A. R. Unique Rodlike Surface Morphologies in Trisilanolcyclohexyl Polyhedral Oligomeric Silsesquioxane Films. *Langmuir* **2004**, *20*, 2527–2530.
- (30) Banerjee, R.; Sanyal, M. K.; Bera, M. K.; Gibaud, A.; Lin, B.; Meron, M. Reversible Monolayer-to-Crystalline Phase Transition in Amphiphilic Silsesquioxane at the Air-Water Interface. *Sci. Rep.* **2015**, *5*, 8497.
- (31) Hasan, N.; Ullah, A.; Ullah, S.; Kressler, J.; Hussain, H. Langmuir Film Formation of Amphiphilic Hybrid Block Copolymers Based on Poly(Ethylene Glycol) and Poly(Methacrylo Polyhedral Oligomeric Silsesquioxane). *Colloid Polym. Sci.* **2019**, *297*, 1149–1159.
- (32) Huang, H.; Chung, J. Y.; Nolte, A. J.; Stafford, C. M. Characterizing Polymer Brushes via Surface Wrinkling. *Chem. Mater.* **2007**, *19*, 6555–6560.
- (33) Pociavsek, L.; Dellsy, R.; Kern, A.; Johnson, S.; Lin, B.; Lee, K. Y. C.; Cerda, E. Stress and Fold Localization in Thin Elastic Membranes. *Science* **2008**, *320*, 912–916.
- (34) Ma, Y.; Xue, Y.; Jang, K.-I.; Feng, X.; Rogers, J. A.; Huang, Y. Wrinkling of a Stiff Thin Film Bonded to a Pre-Strained, Compliant Substrate with Finite Thickness. *Proc. R. Soc. London, Ser. A* **2016**, *472*, 20160339.
- (35) Feng, L.; Chen, M.; Qian, Y.; Tian, J.; Liu, J.; Niu, S.; Muhammad, H.; Dong, M.; Zhong, J. Wrinkles with Changing Orientation and Complexity in a Single Piece of Thin Film. *J. Appl. Phys.* **2019**, *125*, 245301.
- (36) Cutolo, A.; Pagliarulo, V.; Merola, F.; Coppola, S.; Ferraro, P.; Fraldi, M. Wrinkling Prediction, Formation and Evolution in Thin Films Adhering on Polymeric Substrata. *Mater. Des.* **2020**, *187*, 108314.
- (37) Li, Z.; Liu, Y.; Marin, M.; Yin, Y. Thickness-Dependent Wrinkling of PDMS Films for Programmable Mechanochromic Responses. *Nano Res.* **2020**, *13*, 1882–1888.
- (38) Huang, R.; Suo, Z. Instability of a Compressed Elastic Film on a Viscous Layer. *Int. J. Solids Struct.* **2002**, *39*, 1791–1802.
- (39) Chatterjee, S.; McDonald, C.; Niu, J.; Velankar, S. S.; Wang, P.; Huang, R. Wrinkling and Folding of Thin Films by Viscous Stress. *Soft Matter* **2015**, *11*, 1814–1827.
- (40) Fuchs, C.; Busse, K.; Flieger, A.-K.; Kressler, J. Polymer Crystallization on the Surface of Water or Aqueous Salt Solution. *Chem. Eng. Technol.* **2016**, *39*, 1333–1340.

- (41) Ullah, A.; Ullah, S.; Mahmood, N.; Shah, S. M.; Hussain, Z.; Hussain, H. Effect of Polyhedral Oligomeric Silsesquioxane Nanocage on the Crystallization Behavior of PEG<sub>sk</sub>-*b*-P(MA-POSS) Diblock Copolymers Achieved via Atom Transfer Radical Polymerization. *Polym. Cryst.* **2019**, *2*, No. e10058.
- (42) Forster, S.; Thumser, A. E.; Hood, S. R.; Plant, N. Characterization of Rhodamine-123 as a Tracer Dye for Use In In Vitro Drug Transport Assays. *PLoS One* **2012**, *7*, No. e33253.
- (43) Barentin, C.; Muller, P.; Joanny, J. F. Polymer Brushes Formed by End-Capped Poly(Ethylene Oxide) (PEO) at the Air-Water Interface. *Macromolecules* **1998**, *31*, 2198–2211.
- (44) Waddon, A. J.; Coughlin, E. B. Crystal Structure of Polyhedral Oligomeric Silsesquioxane (POSS) Nano-Materials: A Study by X-ray Diffraction and Electron Microscopy. *Chem. Mater.* **2003**, *15*, 4555–4561.
- (45) Kuzmenka, D. J.; Granick, S. Collapse of Poly(Ethylene Oxide) Monolayers. *Macromolecules* **1988**, *21*, 779–782.
- (46) Fuchs, C.; Hussain, H.; Amado, E.; Busse, K.; Kressler, J. Self-Organization of Poly(Ethylene Oxide) on the Surface of Aqueous Salt Solutions. *Macromol. Rapid Commun.* **2015**, *36*, 211–218.
- (47) Lösche, M.; Möhwald, H. Impurity Controlled Phase Transitions of Phospholipid Monolayers. *Eur. Biophys. J.* **1984**, *11*, 35–42.
- (48) Lösche, M.; Möhwald, H. Fluorescence Microscope to Observe Dynamical Processes in Monomolecular Layers at the Air/Water Interface. *Rev. Sci. Instrum.* **1984**, *55*, 1968–1972.
- (49) Lösche, M.; Rabe, J.; Fischer, A.; Rucha, B. U.; Knoll, W.; Möhwald, H. Microscopically Observed Preparation of Langmuir-Blodgett Films. *Thin Solid Films* **1984**, *117*, 269–280.
- (50) Huang, M.; Camara, A. K. S.; Stowe, D. F.; Qi, F.; Beard, D. A. Mitochondrial Inner Membrane Electrophysiology Assessed by Rhodamine-123 Transport and Fluorescence. *Ann. Biomed. Eng.* **2007**, *35*, 1276–1285.
- (51) Ebata, Y.; Croll, A. B.; Crosby, A. J. Wrinkling and Strain Localizations in Polymer Thin Films. *Soft Matter* **2012**, *8*, 9086.
- (52) Wang, Q.; Zhao, X. A Three-Dimensional Phase Diagram of Growth-Induced Surface Instabilities. *Sci. Rep.* **2015**, *5*, 8887.
- (53) Huang, J.; Juszkievicz, M.; de Jeu, W. H.; Cerda, E.; Emrick, T.; Menon, N.; Russell, T. P. Capillary Wrinkling of Floating Thin Polymer Films. *Science* **2007**, *317*, 650–653.
- (54) Leu, C.-M.; Chang, Y.-T.; Wei, K.-H. Polyimide-Side-Chain Tethered Polyhedral Oligomeric Silsesquioxane Nanocomposites for Low-Dielectric Film Applications. *Chem. Mater.* **2003**, *15*, 3721–3727.
- (55) Markovic, E.; Matison, J.; Hussain, M.; Simon, G. P. Poly(Ethylene Glycol) Octafunctionalized Polyhedral Oligomeric Silsesquioxane: WAXD and Rheological Studies. *Macromolecules* **2007**, *40*, 4530–4534.
- (56) Smilgies, D.-M. Scherrer Grain-Size Analysis Adapted to Grazing-Incidence Scattering with Area Detectors. *J. Appl. Crystallogr.* **2009**, *42*, 1030–1034.

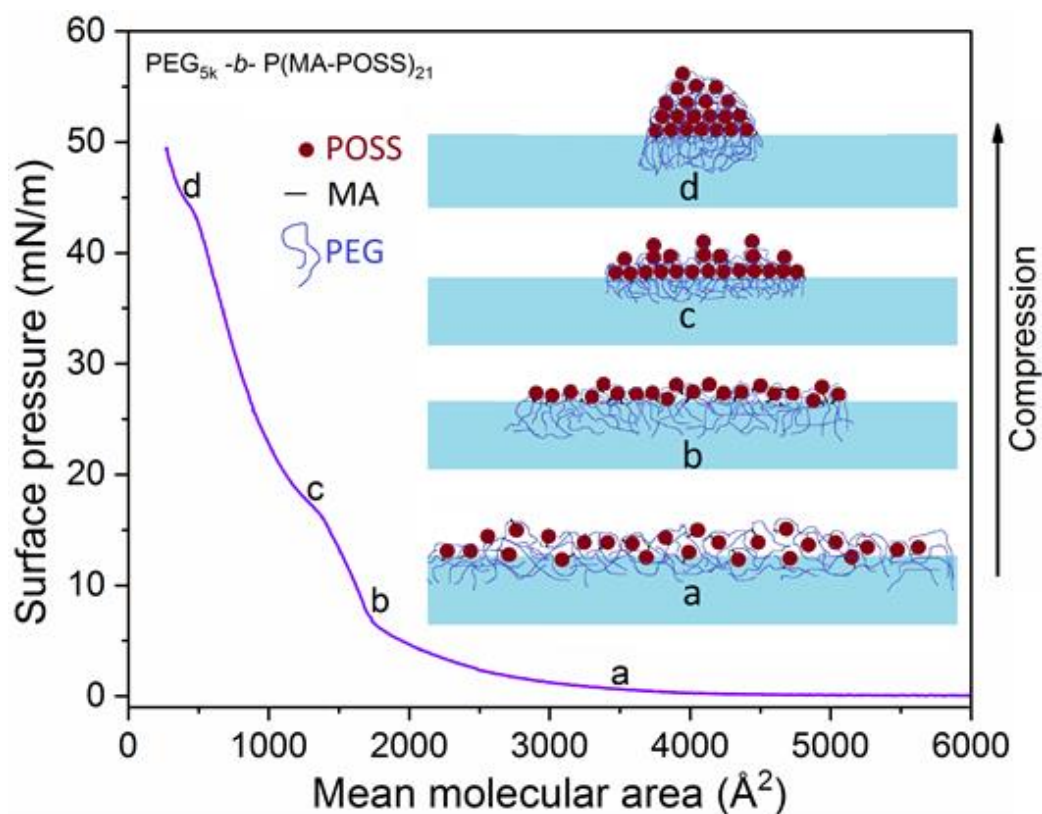
### 3.5 Paper V

Langmuir film formation of amphiphilic hybrid block copolymers based on poly(ethylene glycol) and poly(methacrylo polyhedral oligomeric silsesquioxane)<sup>5</sup>

Nazmul Hasan, Asad Ullah, Shakir Ullah, Jörg Kressler, and Hazrat Hussain

Colloid Polym. Sci. 2019, 297, 1149, <https://doi.org/10.1007/s00396-019-04517-2>

Graphical abstract:



Langmuir/LB film formation of a series of amphiphilic hybrid diblock copolymers based on poly(ethylene glycol) (PEG) and poly(methacrylo polyhedral oligomeric silsesquioxane) (PEG-*b*-P(MA-POSS)) is demonstrated in this publication. In contrast to PEG homopolymer, the investigated diblock copolymers form stable Langmuir films on the water surface as confirmed by  $\pi$ -*mmA* isotherm measurements. The IRRAS furthermore identified the ordering behavior of the diblock copolymers during compression. The morphologies and the thicknesses were then checked by AFM after transferring the films at different surface pressures to the solid supports in order to understand the film formation.



The author contributions to the following article are: N. Hasan and J. Kressler designed the research. A. Ullah, S. Ullah, and H. Hussain synthesized the diblock copolymers. N. Hasan performed all of the experiments (e.g., Langmuir isotherms, LB transfer, BAM, EFM, AFM, FTIR, and IRRAS). N. Hasan analyzed the data and wrote the draft manuscript. N. Hasan, H. Hussain, and J. Kressler discussed the results, reviewed them, and finalized the paper. N. Hasan and A. Ullah contribute equally.

---

<sup>5</sup>The following article is reprinted (adapted) with permission from *Colloid Polym. Sci.* 2019, 297, 1149, <https://doi.org/10.1007/s00396-019-04517-2>. Copyright (2021) Springer. The link to the article on the publisher's website is <https://link.springer.com/article/10.1007%2Fs00396-019-04517-2>. Supporting information is available at: [https://static-content.springer.com/esm/art%3A10.1007%2Fs00396-019-04517-2/MediaObjects/396\\_2019\\_4517\\_MOESM1\\_ESM.docx](https://static-content.springer.com/esm/art%3A10.1007%2Fs00396-019-04517-2/MediaObjects/396_2019_4517_MOESM1_ESM.docx). No changes were made.



# Langmuir film formation of amphiphilic hybrid block copolymers based on poly(ethylene glycol) and poly(methacrylo polyhedral oligomeric silsesquioxane)

Nazmul Hasan<sup>1</sup> · Asad Ullah<sup>2</sup> · Shakir Ullah<sup>2</sup> · Jörg Kressler<sup>1</sup> · Hazrat Hussain<sup>2</sup>

Received: 20 February 2019 / Revised: 12 April 2019 / Accepted: 7 May 2019 / Published online: 3 June 2019  
© Springer-Verlag GmbH Germany, part of Springer Nature 2019

## Abstract

The Langmuir film formation of poly(ethylene glycol) (PEG)- and poly(methacrylo polyhedral oligomeric silsesquioxane) P(MA-POSS)-based diblock copolymers (PEG<sub>5k</sub>-*b*-P(MA-POSS)<sub>x</sub>) at the air/water interface is investigated. While the Langmuir film formed by the PEG<sub>5k</sub> collapses at  $\pi \approx 8 \text{ mN m}^{-1}$ , the PEG<sub>5k</sub>-*b*-P(MA-POSS)<sub>x</sub> forms a stable film on the water surface revealing various phase transitions in surface pressure vs mean molecular area ( $\pi$ -*mmA*) isotherm—manifested by various pseudo-plateaus during compression. At higher surface coverage, the  $\pi$ -*mmA* isotherm exhibits a phase transition that is attributed to the transformation of the P(MA-POSS) monolayer into a multilayer film that is confirmed by AFM measurements of the Langmuir-Blodgett films fabricated before and after the phase transition and direct infrared reflection absorption spectroscopy of the Langmuir film during compression. At a still higher surface pressure, another pseudo-plateau is observed that is assigned to the ultimate film collapse as verified by the Brewster angle microscopy.

**Keywords** Langmuir film · POSS · Hybrid · Block copolymer · Langmuir-Blodgett · Amphiphilic

## Introduction

Poly(ethylene glycol) (PEG) is a hydrophilic polymer; nevertheless, it has the ability to form a Langmuir monolayer at the air/water interface when the molar mass exceeds  $1000 \text{ g mol}^{-1}$  [1, 2]. This is due to the fact that the (–CH<sub>2</sub>–CH<sub>2</sub>–O–) repeat unit of the PEG is amphiphilic in nature where the two CH<sub>2</sub> groups offer hydrophobicity while the oxygen atom is able to form hydrogen bonds with water molecules [1, 2]. The surface pressure vs mean molecular area ( $\pi$ -*mmA*) isotherm for the PEG Langmuir film suggests

a liquid expanded phase at lower surface pressure followed by a pancake conformation with compression and finally the film collapse in the pseudo-plateau region, i.e., dissolution of the PEG chain into the water subphase [3–5]. However, because of its good water solubility in bulk, the collapse surface pressure usually does not exceed  $\pi \approx 10 \text{ mN m}^{-1}$ . Most recently, the salting out effect was exploited by adding certain salts, such as K<sub>2</sub>CO<sub>3</sub>, to the subphase that not only led to the formation of a very stable film (up to  $\pi \approx 30 \text{ mN m}^{-1}$ ) but also led to unusual self-organization and PEG crystallization on the water surface [3, 6, 7]. In contrast to PEG homopolymer, many fundamental studies have also been reported concerning the behavior of PEG-based amphiphilic block copolymers at the air/water interface [4, 5, 8–10]. They exhibit different interfacial behaviors compared with the PEG homopolymer. Previously, the focus has been on organic/organic block copolymers where the lengths of the hydrophilic and hydrophobic blocks were varied [11, 12]. However, no attention has been paid to the behavior of organic/inorganic hybrid amphiphilic block copolymers of PEG at the air/water interface. Block copolymers of PEG and a block containing polyhedral oligomeric silsesquioxane (POSS) nanocages can be considered as a typical example.

---

Nazmul Hasan and Asad Ullah contributed equally to this work.

**Electronic supplementary material** The online version of this article (<https://doi.org/10.1007/s00396-019-04517-2>) contains supplementary material, which is available to authorized users.

✉ Hazrat Hussain  
hazrat.hussain@qau.edu.pk

<sup>1</sup> Department of Chemistry, Martin Luther University Halle-Wittenberg, 06099 Halle (Saale), Germany

<sup>2</sup> Department of Chemistry, Quaid-i-Azam University Islamabad, Islamabad 45320, Pakistan

The completely condensed POSS has a three-dimensional nanocage-like framework of silicon and oxygen atoms bonded in cubic shape (Scheme 1), where the  $R$  groups attached to the POSS core, as shown in Scheme 1, represent various organic moieties. The  $R$  groups are important for assimilation of the inorganic core with polymers and other organic matrices and facile functionalization for various applications. In addition to the typical applications of POSS derivatives, such as nanofiller in nanocomposites [15, 16], fluorescence sensors [17–19], photoresist materials [20], superhydrophobic surfaces [21], catalysts [22, 23], and low  $k$ -dielectric composites [24, 25], there is also a considerable interest in POSS for biomedical and pharmaceutical applications [26–29] and tissue engineering [30–33].

Several reports have appeared in the literature on the self-organization of POSS cages in thin films, including Langmuir films at the air/water interface and Langmuir-Blodgett (LB) films [34–44]. The POSS cages have a strong tendency of aggregation in thin films and the most effective tool to prevent that is to introduce the amphiphilic character to POSS. As an example, Paczesny et al. [43] investigated four unsymmetrical POSS cage derivatives with seven hydrophobic and one hydrophilic moiety (mercapto, glycerol, maleamic acid, or amino group) attached at the cage corner. The mercapto-POSS derivative was found to form aggregates and multilayer films on the water surface and complex nanostructures in LB films. The incompletely condensed trisilanol derivative of POSS with three unbonded hydroxyl groups forms a stable monolayer at the air/water interface with a rod-like multilayered morphology in the high surface pressure regime [13, 45, 46]. Mitsuishi et al. [34] reported the formation of ultra-thin LB films with a homogeneous distribution of the POSS cages by amphiphilic copolymers of *N*-dodecylacrylamide and a heptaphenyl POSS-containing comonomer. Lee et al. reported the interfacial behavior of telechelic POSS-PEG-POSS amphiphiles, with varying molar mass of the PEG chain ranging from 1 to 10 kg mol<sup>-1</sup>, at the air/water interface [2]. The PEG chain was forced to submerge into the water subphase upon

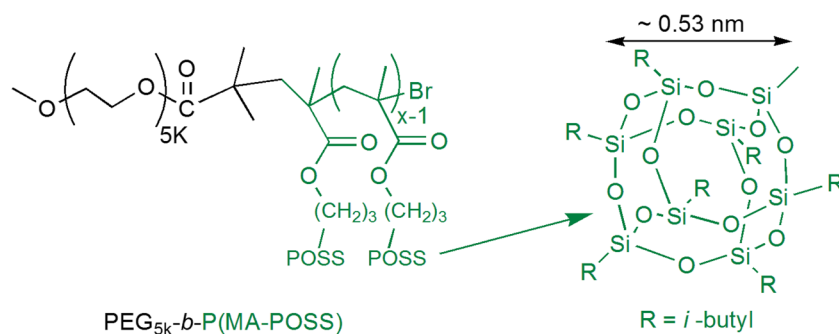
compression on the Langmuir trough while the POSS cages formed a closely packed film on the water surface at higher surface pressures. The POSS-containing amphiphilic block copolymers could have potential implications for the design and fabrication of hybrid nanoscale building blocks in thin films. The tuning of nanostructure formation by varying the composition of the amphiphilic hybrid copolymers could lead to a better understanding and the construction of the tailored nanobuilding blocks.

In the present work, we are reporting the molecular behavior of amphiphilic PEG<sub>5k</sub>-*b*-P(MA-POSS) hybrid diblock copolymers, where the subscript 5k represents the molar mass of the PEG chain (5 kg mol<sup>-1</sup>), corresponds to average degree of polymerization  $\approx 113$  and the degree of polymerization of the methacrylo-POSS (MA-POSS) segments varied from 4 to 21, in thin films at the air/water interface and in LB films. The  $\pi$ -*mma* isotherms have been measured coupled with Brewster angle microscopy (BAM), and infrared reflection absorption spectroscopy (IRRAS). This leads to a better understanding of the molecular arrangements of the block copolymer segments in Langmuir films and the phase transitions during compression. Langmuir-Blodgett (LB) films were also fabricated at various surface pressures during compression to interpret some of the observations made in the  $\pi$ -*mma* isotherms and to visualize the nanostructure morphology in thin films on a solid substrate by atomic force microscopy (AFM).

## Experimental part

### Materials

The investigated block copolymers of PEG and poly(methacrylo polyhedral oligomeric silsesquioxane) (PEG<sub>5k</sub>-*b*-P(MA-POSS)<sub>*x*</sub>) (Scheme 1) were synthesized via atom transfer radical polymerization with PEG<sub>5k</sub> as the macroinitiator [47] and have been thoroughly characterized for their self-assembly behavior in aqueous medium and in



**Scheme 1** Chemical structure of PEG<sub>5k</sub>-*b*-P(MA-POSS)<sub>*x*</sub> diblock copolymers, the colors indicate the hydrophilic block (black) and the hydrophobic block (green) of the copolymer. The core size of the POSS cage is  $\approx 0.53$  nm and the *i*-butyl part has a length of  $\approx 0.42$  nm. These

data are adopted from [4] as calculated by the molecular dynamics simulation. It should be noted that the diameter and the cross-sectional area of a POSS cage with different side groups range from 0.84 to 1.24 nm and from 1.40 to 1.80 nm<sup>2</sup>, respectively [2, 13, 14].

bulk, as described elsewhere [48–50]. The degree of polymerization  $x$  of the MA-POSS segments of the four PEG<sub>5k</sub>-*b*-P(MA-POSS) <sub>$x$</sub>  copolymers in the current study is in the range from 4 to 21 and the polydispersity indices are  $\approx 1.2$ – $1.3$  [48].

## Methods

### Langmuir trough measurements

The surface pressure  $\pi$  versus mean molecular area  $mmA$  isotherms of the investigated diblock copolymers were measured using a Langmuir trough (Riegler & Kirstein, Germany). The trough has a maximum available surface area of 26,212 mm<sup>2</sup> and is equipped with two symmetrical movable barriers as well as a Wilhelmy plate made from filter paper. The trough was covered with a closed plexiglass box to maintain a stable atmosphere and the temperature of the subphase was maintained at 20 °C by a circulating water bath. The subphase used for the experiments was prepared from deionized water (TKA GenPure Labor & Reinstwassertechnik Christian Wiesenack, Jena, Germany) with a conductivity of  $< 0.056 \mu\text{S cm}^{-1}$ . Before the experiments, the subphase purity was checked by measuring the surface pressure at maximum surface compression ( $\pi < 0.15 \text{ mN m}^{-1}$ ). To obtain the  $\pi$ - $mmA$  isotherms, the block copolymer solutions (concentration 1–2 mg ml<sup>-1</sup>) were prepared in HPLC grade chloroform and spread on the subphase using a digital microsyringe (Hamilton). After waiting 20 min for evaporation of the chloroform, the surface was compressed to record the  $\pi$ - $mmA$  isotherm. The compression speed used for all of the experiments was  $100 \text{ \AA}^2 \cdot \text{molecule}^{-1} \cdot \text{min}^{-1}$ , except for the BAM experiments where a slower compression rate of  $50 \text{ \AA}^2 \cdot \text{molecule}^{-1} \cdot \text{min}^{-1}$  was used for better imaging conditions [7].

### Brewster angle microscopy

To monitor the Langmuir film during compression, a Brewster angle microscope (NFT Mini BAM, Nano-film technology, Valley View, USA) was used. The instrument has a lateral resolution of  $\approx 20 \mu\text{m}$ , with a field of view of  $4.8 \times 6.4 \text{ mm}^2$ . The Langmuir trough used for this experiment has a maximum surface area of 14,800 mm<sup>2</sup>. The images were captured using the software WinTV (Hauppauge, USA).

### Atomic force microscopy

The atomic force microscopy (AFM) images of the LB films were acquired in tapping mode using a Multimode 8 AFM (Bruker, Santa Barbara, USA) and a standard silicon cantilever (NSC15, Mikromash, Ore, USA) with a resonance frequency of 325 kHz and a spring constant of  $40 \text{ N m}^{-1}$ . Drive amplitude of  $\approx 18 \text{ mV}$ , set point of 330–380 mV, and a

scan rate of 1 Hz were used. The captured AFM images were processed by Gwyddion software.

### Langmuir-Blodgett film transfer

A piece of circularly shaped mica ( $d = 10 \text{ mm}$ ) was cleaved from the middle and hooked to the substrate holder of the transferring unit from KSV (Helsinki, Finland) for preparation of the Langmuir-Blodgett (LB) film. During the transfer, the surface pressure was kept constant. The transfer pressures were set to  $8 \text{ mN m}^{-1}$  and  $25 \text{ mN m}^{-1}$ , respectively. The substrate was vertically fixed to the holder and immersed in the subphase (around 7 mm). Afterwards, the block copolymer solution was spread on the water surface, and after waiting for chloroform evaporation, the film was compressed to the required transfer pressure. After achieving the required surface pressure, the submerged mica substrate was automatically pulled upward with a speed of  $0.1 \text{ mm min}^{-1}$  which resulted in the block copolymer being transferred to the substrate. Furthermore, the transfer was confirmed by surface analysis of the mica substrate using AFM instrument and the transfer efficiency was realized from transfer ratio (TR) as calculated from reference [51]. The TR value (i.e.,  $\approx 1.05$ ) is close to the unity for both cases. The fabricated LB film was dried at room temperature in a desiccator and stored in a sealed box for later measurements.

### Infrared reflection absorption spectroscopy

The infrared reflection absorption spectroscopy (IRRAS) experiments were performed using a Bruker Vector 70 FTIR spectrometer equipped with a liquid nitrogen-cooled mercury-cadmium-telluride (MCT) detector and an A511 reflection unit (Bruker Optics, Germany). The setup was placed over two troughs such as a sample trough (Riegler & Kirstein, Germany) of  $30 \times 6 \text{ cm}^2$  and a circular reference trough ( $d = 6 \text{ cm}$ ). The sample trough contained a Wilhelmy pressure sensor made of filter paper and two movable barriers to permit film compression. The monolayer was prepared in this trough. The circular reference trough was used only to measure the spectrum of the bare water surface. Both troughs were connected to a water reservoir to maintain the same height level by an automated pumping system. The temperature of the subphase was maintained at 20 °C by a circulating water bath. Furthermore, the troughs were covered with a closed plexiglass box to keep a stable atmosphere. The IRRAS spectra were obtained by shining both troughs with an *s*-polarized IR beam at a particular angle of incidence  $\varphi$  relative to the surface normal. The reflectance-absorbance ( $RA$ ) spectra were calculated using the relation  $RA = -\log_{10}(R/R_0)$ , where  $R$  and  $R_0$  represent the IR reflectivity of the sample and the reference trough, respectively. The spectra were repeatedly recorded in the sequence: one reference spectrum ( $R_0$ ) followed by 5

sample spectra ( $R$ ), while the Langmuir film was continuously compressed with a small compression rate of  $25 \text{ \AA}^2 \cdot \text{molecule}^{-1} \cdot \text{min}^{-1}$ . The spectra were recorded with  $s$ -polarized IR beam at a  $60^\circ$  angle of incident. The resolution, the scanner speed, and the number of scans in all experiments were  $4 \text{ cm}^{-1}$ ,  $160 \text{ kHz}$ , and  $1000$ , respectively. A zero-filling factor of two was applied before the Fourier transformation of the averaged interferograms resulting in a nominal spectral resolution of  $2 \text{ cm}^{-1}$ .

### Fourier transform infrared spectroscopy

The Fourier transform infrared spectroscopy (FTIR) experiments were performed in transmission mode with a Vector 22 (Bruker Optik GmbH, Germany) spectrometer. The respective polymers were pressed into KBr pellets. The spectra were acquired with a resolution of  $4 \text{ cm}^{-1}$  with 64 scans in the wave number range of  $4000$  to  $400 \text{ cm}^{-1}$ .

## Results and discussion

The surface pressure vs mean molecular area ( $\pi$ - $mma$ ) isotherm that reveals various phases and phase transitions corresponding to different molecular conformations in Langmuir films on the water surface is recorded by measuring  $\pi$  during compression as a function of  $mma$ . Figure 1 depicts the  $\pi$ - $mma$  isotherm of  $\text{PEG}_{5k}$  homopolymer and the respective

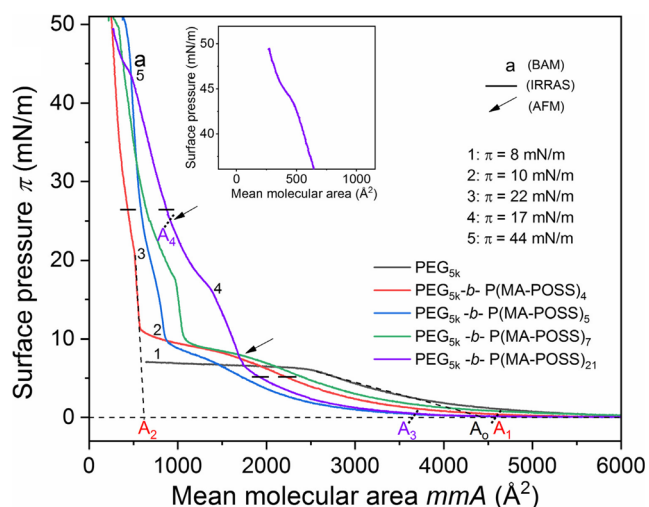


**Fig. 1**  $\pi$ - $mma$  isotherm of  $\text{PEG}_{5k}$  and the respective  $\text{PEG}_{5k}$ - $b$ - $\text{P}(\text{MA-POSS})_x$  diblock copolymers measured at  $20^\circ \text{C}$  with a compression speed of  $100 \text{ \AA}^2 \cdot \text{molecule}^{-1} \cdot \text{min}^{-1}$ . The inset shows a zoom of the  $\text{PEG}_{5k}$ - $b$ - $\text{P}(\text{MA-POSS})_{21}$  isotherm. The letter a and the arrows indicate the  $\pi$  values where observations with BAM and LB film transfer were carried out, respectively. The bold black lines on the isotherms represent the range of the IRRAS experiments for the respective film. The numbers denoted as 1, 2, 3, 4, and 5 guide the eyes to the plateaus of the respective isotherm. The dotted lines indicate some characteristic areas  $A_0$  to  $A_4$  of the isotherm (see text)

$\text{PEG}$ - $b$ - $\text{P}(\text{MA-POSS})_x$  diblock copolymers. For  $\text{PEG}_{5k}$ , the  $\pi$ - $mma$  isotherm depicts the typical PEG behavior on the water surface, starting with the liquid expanded state at lower surface pressure (low surface coverage), followed by the pancake region (where PEG chains lie in flattened conformation to maximize contact with the water surface) and then a pseudo-plateau—no further change in surface pressure upon film compression occurs. The pseudo-plateau is an indication of the removal of PEG chains from the water surface because of their dissolution into the water subphase during compression [3, 6, 7, 52]. The onset of the plateau is the surface pressure above which the PEG chains cannot retain their flattened conformation on the water surface; thus, they assume more and more extended conformation and penetrate the water bulk. The pseudo-plateau for  $\text{PEG}_{5k}$  homopolymer was observed at  $\approx 8 \text{ mN m}^{-1}$  (Fig. 1) in the current study; however, this may vary depending on the molar mass of the PEG employed [2]. The limiting pancake area,  $A_0$ , calculated from the extrapolation of the tangent of the pancake region to  $\pi = 0 \text{ mN m}^{-1}$ , is estimated  $\approx 4400 \text{ \AA}^2$ , corresponding to an area of  $(4400 \text{ \AA}^2 / 113) \approx 39 \text{ \AA}^2$  per ethylene oxide (EO) unit, which is close to the previously reported values of  $40$ – $48 \text{ \AA}^2$  per EO unit for PEG homopolymers [3, 9, 10].

After chain extension of  $\text{PEG}_{5k}$  with MA-POSS segments in  $\text{PEG}_{5k}$ - $b$ - $\text{P}(\text{MA-POSS})_x$  block copolymers, the behavior at the air/water interface changes drastically as depicted in Fig. 1 for the corresponding diblock copolymers, where the  $\pi$ - $mma$  isotherms of all the investigated block copolymer films reveal several pseudo-plateaus (indicated by the numbers 1 to 5) during compression. For  $\text{PEG}_{5k}$ - $b$ - $\text{P}(\text{MA-POSS})_4$  (with the smallest number of MA-POSS segments), the isotherm depicts a relatively well-defined pseudo-plateau 2 at  $\approx 10 \text{ mN m}^{-1}$  that is attributed to the dissolution of the  $\text{PEG}_{5k}$  chains upon compression. Upon further compression, a sharp increase in surface pressure appears with negligible change in the  $mma$  that can be assigned to the accumulation of MA-POSS segments on the water surface resulting in a compact film formation. This was also verified by a significant increase in the intensity of Si–O–Si ( $1108 \text{ cm}^{-1}$ ) band of POSS cages in IRRAS spectra during compression of the film after the plateau region (see supporting information Figure S1). The film is stable up to more than the recorded  $\pi \approx 50 \text{ mN m}^{-1}$ . The limiting brush area for the block copolymers increases with increasing the P(MA-POSS) content in the block copolymer. In the brush regime, at  $\pi \approx 22 \text{ mN m}^{-1}$ , a small deflection 3 can also be seen which transforms into a more prominent pseudo-plateau 4 in the isotherm of the  $\text{PEG}_{5k}$ - $b$ - $\text{P}(\text{MA-POSS})_{21}$  block copolymer.

It should be noted that the increase of  $\pi$  with reducing  $mma$  is trivial [53–55]; nevertheless, the plateaus for the block copolymers are indicative for phase transitions [3, 9]. As an example, in our recent study on the behavior of poly(isobutylene) (PIB) with small terminal PEO segments



(symmetric PEO<sub>3</sub>-PIB<sub>85</sub>-PEO<sub>3</sub> and non-symmetric PEO<sub>3</sub>-PIB<sub>85</sub>-PEO<sub>12</sub>, where the subscript represents the respective degrees of polymerization), a change in slope of the isotherm in the brush regime was observed that was attributed to a phase transition involving removal of the smaller PEO<sub>3</sub> segments from the water surface [3]. A similar deflection in the brush regime of the Langmuir isotherm of PFMA-*b*-PEO-*b*-PFMA triblock copolymers (PFMA represents poly(perfluorohexyl ethyl methacrylate)) with higher PFMA content was observed, which was attributed to the rearrangement of the PFMA segments at the air/water interface [8]. To clarify the phase transition in the current study, the area occupied by the repeat unit of the diblock copolymer chain at different surface pressures was calculated. Figure 1 depicts that the initial increase in surface pressure starts at  $\approx 4600 \text{ \AA}^2$  ( $A_1$ ) for PEG<sub>5k</sub>-*b*-P(MA-POSS)<sub>4</sub>. This corresponds to  $40 \text{ \AA}^2$  per EO unit, suggesting that the area occupied by the MA-POSS segments at the interface is negligible. One of the reasons for this could be the relatively small size of the P(MA-POSS)<sub>4</sub> block in this block copolymer. However, a similar behavior has also been observed for PEG-based amphiphilic block copolymers with relatively long hydrophobic segments [9, 11]. Additionally, the limiting area  $A_2$  is estimated as  $\approx 615 \text{ \AA}^2$  by drawing a tangent of the isotherm to zero surface pressure (dotted line) that corresponds to the cross-sectional area of  $\approx 4$  MA-POSS units [2, 13]. Since the diblock copolymer also contains the same number of MA-POSS units, it can, therefore, be argued that at this *mmA*, all PEG segments of the block copolymer must be submerged into the subphase with the air/water interface predominantly occupied by MA-POSS segments. For PEG<sub>5k</sub>-*b*-P(MA-POSS)<sub>21</sub> (block copolymer with the highest POSS content), the plateau that corresponds to the dissolution of the PEG chains could no longer be observed, indicating that the PEG chains have already submerged into the water subphase and that the interface is predominantly populated by the MA-POSS segments even at low surface pressure. Therefore, the initial increase of the surface pressure that started at  $\approx 3700 \text{ \AA}^2$  (indicated by  $A_3$ ) can be attributed to the area of  $\approx 21$  POSS units [2, 13], followed by two pseudo-plateaus at  $17 \text{ mN m}^{-1}$  4 and  $44 \text{ mN m}^{-1}$  5. The area  $A_4 \approx 912 \text{ \AA}^2$  after the plateau 4 corresponds to the cross-sectional area of  $\approx 5$  POSS units, indicating that several layers of the MA-POSS units have formed during the film compression up to this point in the isotherm. To support this statement, BAM microscopy is employed to monitor the water surface, especially plateau regions 4 and 5 during film compression.

BAM is an important tool to monitor the water surface during the  $\pi$ -*mmA* experiment on a Langmuir trough to visualize the formation of film domains on the water surface during compression [11, 56–58]. In the current study, the Langmuir films of the PEG<sub>5k</sub>-*b*-P(MA-POSS)<sub>4</sub> and PEG<sub>5k</sub>-*b*-P(MA-POSS)<sub>21</sub> were monitored with BAM during the compression from  $\pi \approx 0 \text{ mN m}^{-1}$  to  $\pi \approx 48 \text{ mN m}^{-1}$  and the

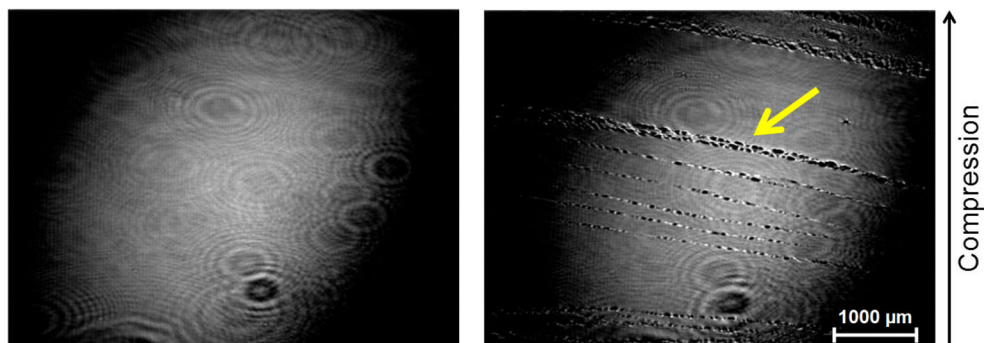
captured images are depicted in Fig. 2. It was observed that no film domain formation occurs in both of the films up to  $\pi \approx 42 \text{ mN m}^{-1}$  (see Supporting Information Figure S2). This reveals that no significant change in refractive indices takes place in the investigated region of the isotherm and hence no change in contrast of the BAM images could be detected [58]. The observation also inferred homogeneity of the Langmuir film. However, for the PEG<sub>5k</sub>-*b*-P(MA-POSS)<sub>21</sub> copolymer, at the 2nd plateau region 5, the appearance of strips to the compressional direction, (indicated by the yellow arrow) offers evidence of the film collapse (see Fig. 2 (right)). The strips might be composed of several layers of PEG and P(MA-POSS) blocks. A similar BAM observation has also been reported for the POSS-PEG<sub>1k</sub>-POSS telechelics, where the observed strips were assigned to the film collapse followed by multilayer formation of POSS units [2]. The pseudo-plateau 4 that started at  $\approx 18 \text{ mN m}^{-1}$ , however, could not be explained based on BAM observation. Therefore, several LB films were fabricated before and after the plateau 4 region and examined by AFM for changes in surface morphology and thickness.

Figure 3 depicts AFM images of the LB film of PEG<sub>5k</sub>-*b*-P(MA-POSS)<sub>21</sub> transferred at  $\pi \approx 8 \text{ mN m}^{-1}$ . The LB film transferred before the pseudo-plateau region 4 (see arrows in Fig. 1) shows a very compact and smooth surface morphology with a few holes in it. The maximum film thickness could be measured as  $\approx 0.70 \text{ nm}$ . The value is slightly smaller than the maximum height value (i.e.,  $\approx 0.95 \text{ nm}$ ) of *i*-butyl MA-POSS part, but, in the range of amorphous PEG Langmuir film, which is typically  $\approx (0.6\text{--}0.7) \text{ nm}$  in pancake region [6]. Now, looking to the phase image as shown in Fig. 3c reveals no phase difference (except the holes within the film), indicating a uniform and homogeneous surface morphology of the film with no distinct PEG and P(MA-POSS) phases. The morphology suggested a non-crystalline film where the stiffer POSS cage might be incorporated in the PEG layer that generates a smoother surface morphology with no change in image brightness. It should be noted that the crystalline thin film of PEG shows rough surface of lamella [59] and the stiffer region in the AFM phase image appeared as brighter than the softer region due to a positive phase shift [58]. The non-crystallinity of the film arises due to the hydrated nature of the PEG chain in LB film as well as their high affinity to the mica substrate which prevent aggregation and chain folding necessary for crystallization [60, 61].

Figure 4a depicts the LB film transferred after the plateau 4 region at  $25 \text{ mN m}^{-1}$  revealing a completely different surface morphology and film thickness. Two-layers film can be seen from the surface. The bottom layer indicated by blue arrow has an average film thickness value of  $\approx 1 \text{ nm}$ . The brighter part indicates the upper layer (red arrow) has an average thickness of  $\approx 1.7 \text{ nm}$ . The overall film thickness varies from  $\approx 0.70 \text{ nm}$  to  $\approx 2.7 \text{ nm}$  (Fig. 4b), suggesting a multilayer layer formation. However, due to strong anchoring force at the interface



**Fig. 2** BAM image of PEG<sub>5k</sub>-*b*-P(MA-POSS)<sub>4</sub> (left) and PEG<sub>5k</sub>-*b*-P(MA-POSS)<sub>21</sub> (right) captured during film compression on the Langmuir trough at  $\pi$  value of 45 mN m<sup>-1</sup> (indicated by a in Fig. 1). The yellow arrow indicates the strips caused by film collapse



of long hydrophilic PEG chains, this does not lead to the true film collapse. In addition, no visible strips in BAM images that are typically associated with the film collapse could be observed at  $\pi = 25$  mN m<sup>-1</sup> (see Supporting Information Figure S2(b) right). The ultimate film collapse happened at  $\pi \approx 44$  mN m<sup>-1</sup>, where the strips associated with the film collapse, could be clearly seen in BAM images (Fig. 2). Now looking to Fig. 4b, a very rough surface, i.e., inhomogeneous line profiles, with lots of elevated spike-like structures can be seen. The bright nanostructures in the phase image (Fig. 4c) and the elevated spike-like structures could be due to the MA-POSS segments, while the PEG blocks because of their high affinity for the mica surface are assumed to attain a flattened

conformation on the mica surface without aggregation or crystallization [60]. It should be noted that the POSS molecule has a very strong tendency for self-aggregation and crystallization into two-dimensional lamellar nanocrystals [13, 62, 63]. Finally, from the changes in surface morphology during compression, it can be argued that phase transition or aggregation processes take place in the plateau 4 regime.

Infrared reflection absorption spectroscopy (IRRAS) is a powerful tool for studying the Langmuir film directly at the air/water interface. IRRAS has been reported widely for investigating small amphiphiles as well as polymers at the water surface [11, 57, 64–73]. IRRAS is based on the principle that when *s*-polarized infrared radiation impinges onto a Langmuir

**Fig. 3** AFM measurements of the LB films of PEG<sub>5k</sub>-*b*-P(MA-POSS)<sub>21</sub> transferred at  $\pi \approx 8$  mN m<sup>-1</sup> **a** height image and **b**, **c** corresponding to height profile and phase image (see more AFM images in Supporting Information of Figure S3)

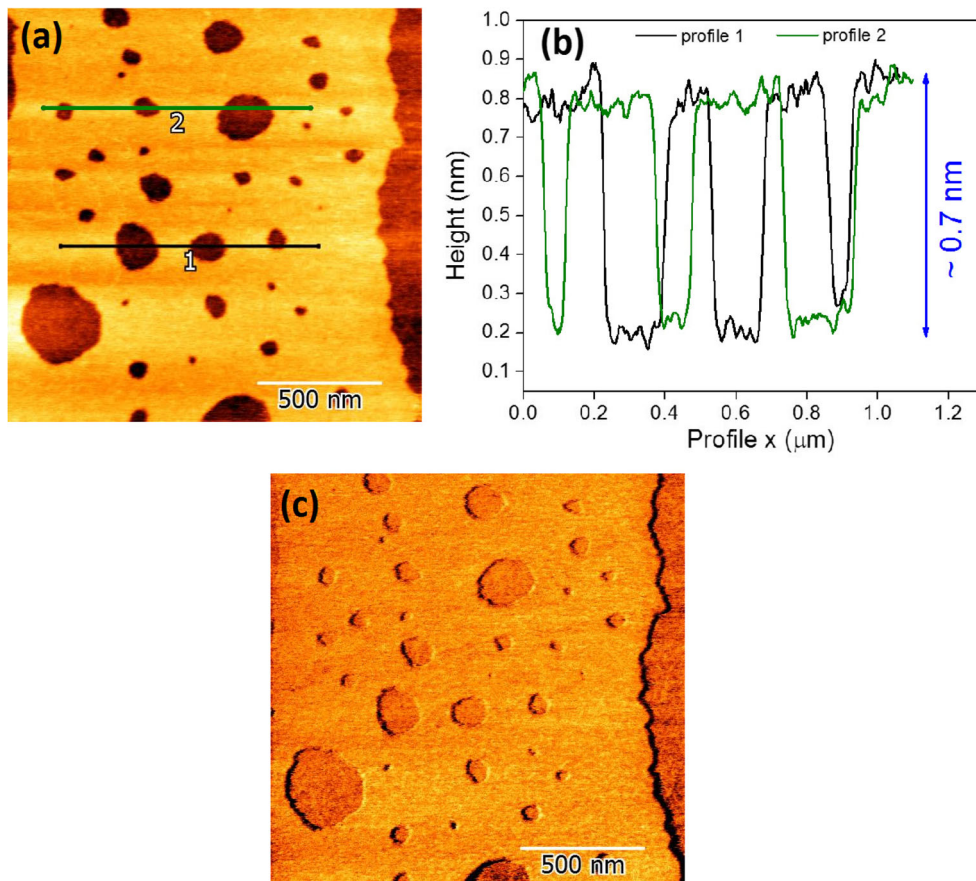
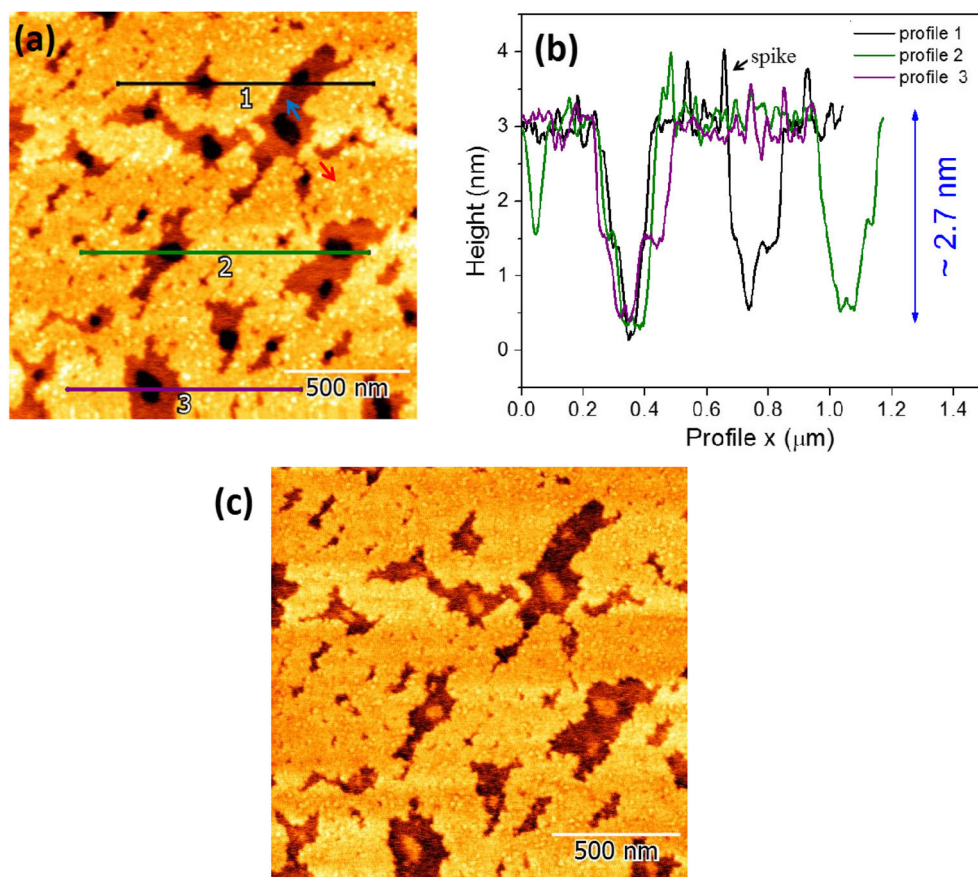


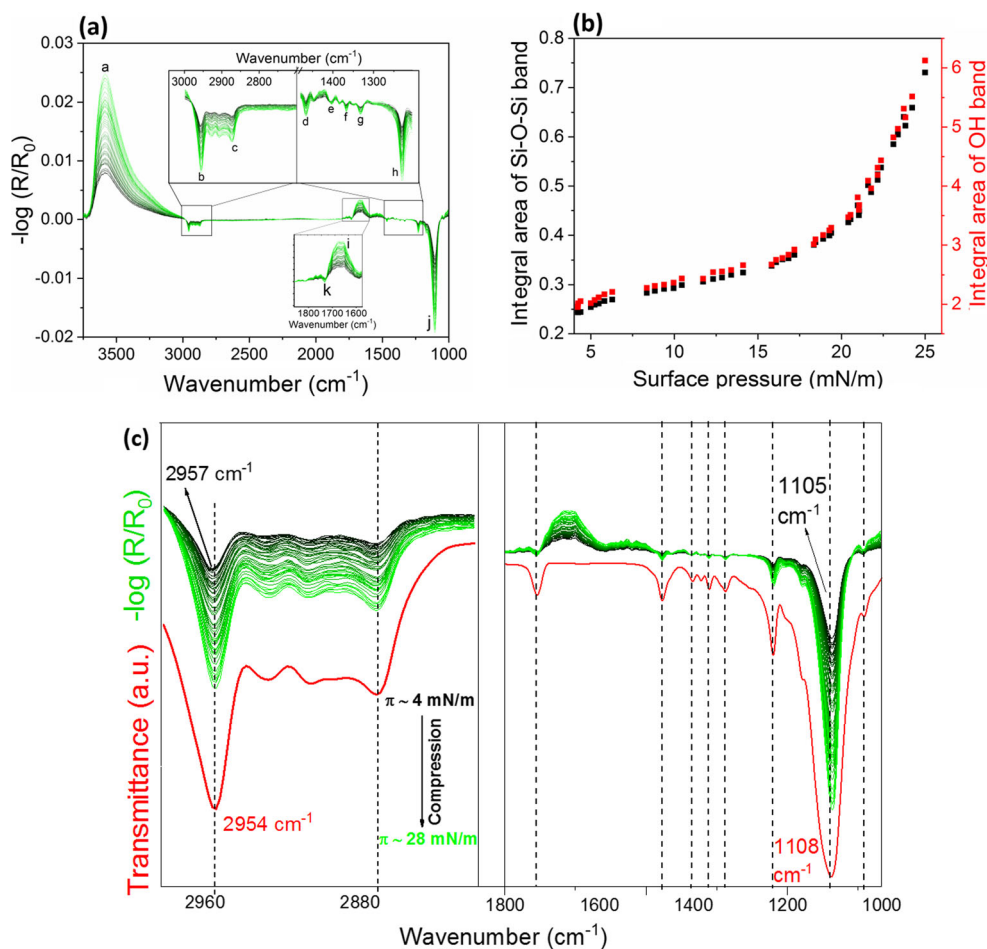
**Fig. 4** AFM measurements of the LB films of PEG<sub>5k</sub>-*b*-P(MA-POSS)<sub>21</sub> transferred at  $\pi \approx 25 \text{ mN m}^{-1}$  **a** height image (the arrows indicate different layers of the film) and **b**, **c** corresponding height profile and phase image, respectively (see more AFM images in Supporting Information of Figures S3 and S4)



film at the air/water interface, a small fraction of the light is reflected by the film. The IRRAS signals are recorded as a plot of reflectance-absorbance (RA) vs wavenumber, where RA is defined as  $-\log_{10}(R / R_0)$ , where  $R$  is the reflectivity of the Langmuir film-covered surface and  $R_0$  is the reflectivity of the pure water surface. In this study, IRRAS is employed to scan plateau region 4 of the isotherm of PEG<sub>5k</sub>-*b*-P(MA-POSS)<sub>21</sub> for any phase transition. Figure 5a shows the IRRAS spectra acquired during the film compression from  $\pi \approx 4 \text{ mN m}^{-1}$  (black) to  $\approx 28 \text{ mN m}^{-1}$  (green) to cover plateau region 4. The spectra reveal bands originating from vibrations of the water subphase, PEG, and MA-POSS segments of the block copolymer. The positive peaks (a) and (i) are due to the stretching and bending vibration, respectively, of the water molecules in the subphase. These bands are visible in the spectra due to the difference in reflectivity of the bare water surface and polymer populated water surface. Therefore, the reflectance-absorbance of these bands increases with the thickness of the interfacial polymer film. All the negative bands in the spectra (b) to (h) and (j) to (k) are due to the polymer chains on the water surface [12]. It is obvious that upon compression, the reflectance-absorbance of OH band from water and the negative bands from the polymer film increases in its absolute values as expected since the surface concentration of the constituents increases upon reducing *mmA* [69]. To support the statement

made above that plateau 4 could be due to the formation of several layers of MA-POSS segments on the water surface, the reflectance-absorbance changes of the  $\nu_{\text{as}}(\text{Si-O-Si})$  (j) and  $\nu(\text{OH})$  (a) band with compression were recorded and the data are depicted in Fig. 5b. The data reveal a significant change in the reflectance-absorbance of the  $\nu_{\text{as}}(\text{Si-O-Si})$  and  $\nu(\text{OH})$  bands in plateau regime ( $18\text{--}25 \text{ mN m}^{-1}$ ), which is a strong evidence of the increase in POSS concentration on the surface as well as the increase of film thickness in the plateau 4 regime [11]. This observation is also in agreement with the AFM images shown in Figs. 3 and 4 and the *mmA* calculation of the MA-POSS segments in Fig. 1. Furthermore, the band position of the IRRAS spectra has also been compared with that of the FTIR spectrum of the block copolymer in bulk as shown in Fig. 5c, where the position of the IRRAS bands matches with the position of the corresponding bands in the FTIR spectrum with a slight shift in the  $\nu_{\text{as}}(\text{CH})$  and  $\nu_{\text{as}}(\text{Si-O-Si})$  vibration bands, respectively, from  $2957 \text{ cm}^{-1}$  and  $1105 \text{ cm}^{-1}$  to  $2954 \text{ cm}^{-1}$  and  $1108 \text{ cm}^{-1}$ . Since most of the band positions of the IRRAS spectra at  $\pi \approx 28 \text{ mN m}^{-1}$  overlap with the corresponding bands of the FTIR spectrum of the bulk sample, it can be assumed that the Langmuir film preserves the conformations of the bulk phase. It should be noted that the higher wavenumbers of symmetric and antisymmetric CH bands (i.e., higher than  $\approx 2919 \text{ cm}^{-1}$ ,  $\nu_{\text{as}}(\text{CH}_2)$ ) and  $\approx 2850 \text{ cm}^{-1}$ ,  $\nu_{\text{s}}(\text{CH}_2)$ ) are indicative

**Fig. 5** **a** IRRA spectra of PEG<sub>5k</sub>-*b*-P(MA-POSS)<sub>21</sub> recorded during continuous compression from  $\pi \approx 4$  mN m<sup>-1</sup> (black) to 28 mN m<sup>-1</sup> (green). The insets show zooms of the selected bands. The assignment of the bands are as follows: (a)  $\nu(\text{OH})$ , (b)  $\nu_{\text{as}}(\text{CH}_2)$ , (c)  $\nu_{\text{s}}(\text{CH}_2)$ , (d)  $\delta_{\text{s}}(\text{CH}_2)$ , (e)  $\omega(\text{CH}_2)$ , (f)  $\omega(\text{CH}_2)$ , (g)  $\omega(\text{CH}_2)$ , (h)  $\nu(\text{CC})$ , (i)  $\delta(\text{OH})$ , (j)  $\nu(\text{Si-O-Si})$ , and (k)  $\nu(\text{CO})$  [11, 74–76]. **b** Integral area of the IRRA band of Si–O–Si at 1108 cm<sup>-1</sup> and OH at 3400 cm<sup>-1</sup> as a function of surface pressure. **c** Comparison of the IRRA (black to green) and the FTIR (red) spectrum of PEG<sub>5k</sub>-*b*-P(MA-POSS)<sub>21</sub>, the dotted lines are drawn to guide the eyes. The FTIR spectrum (red) of PEG<sub>5k</sub>-*b*-P(MA-POSS)<sub>21</sub> was acquired in a transmission mode using a KBr disc



of fluid-like film phase with high content of gauche conformations as reported for polymers and small amphiphilic molecules containing long-chain CH<sub>2</sub> units [57, 68, 73]. Since the

investigated copolymers contain small chain CH<sub>2</sub> unit, therefore, to understand the ordering behavior (i.e., crystallization) of the block copolymer with direct comparison of the CH band position is hardly possible; however, it could be possible by employing the GI-WAXS measurements [6].

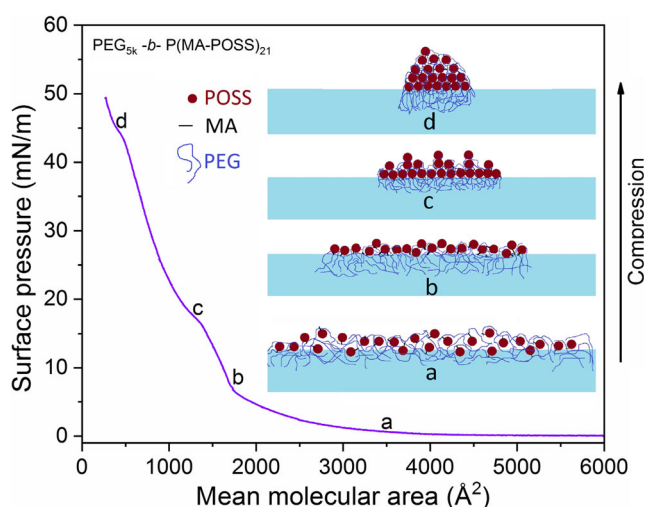


**Fig. 6**  $\pi$ - $m\mu\text{A}$  isotherm along with schematic presentation of the processes occur during the compression of the Langmuir film of PEG<sub>5k</sub>-*b*-P(MA-POSS)<sub>21</sub> on the water surface. The letters (a to d) are indicative of the  $\pi$  value of the isotherm related to the scheme

## Conclusion

The surface pressure vs mean molecular area ( $\pi$ - $m\mu\text{A}$ ) isotherms of the PEG<sub>5k</sub> homopolymer and the block copolymers were measured. Upon compression, the PEG<sub>5k</sub> Langmuir film was stable only up to a surface pressure of  $\approx 8$  mN m<sup>-1</sup>; however, all the investigated PEG<sub>5k</sub>-*b*-P(MA-POSS)<sub>x</sub> block copolymers could form an insoluble film on the water surface that revealed various phase transitions as manifested by various pseudo-plateaus during compression. The pseudo-plateau at  $\pi \approx 10$  mN m<sup>-1</sup> could be attributed to the removal of the PEG chains from the water surface. With increasing MA-POSS content, the pseudo-plateau that corresponds to the dissolution of the PEG chains into the subphase vanished progressively. Upon further compression, the MA-POSS segments formed a closely



packed compact film on the water surface—exhibited by a sharp rise in surface pressure. In the so-called brush regime, the isotherm reveals another phase transition as a pseudo-plateau. The corresponding AFM images of the LB films show a transformation in surface morphology from a homogeneous, compact, and thin film (thickness  $\approx 0.7$  nm) before the pseudo-plateau to a thick film (thickness  $\approx 2.7$  nm) with a rough surface morphology assigned to the multilayer film formation by the MA-POSS segments of the block copolymer. This was further corroborated by infrared reflection absorption spectra recorded during compression. The  $\pi$ -*mmA* isotherms of the block copolymers with high P(MA-POSS)<sub>x</sub> content display another phase transition at  $\pi \approx 44$  mN m<sup>-1</sup> that was confirmed by Brewster angle microscopy to be associated with film collapse. These observations are schematically summarized in Fig. 6 for PEG<sub>5k</sub>-*b*-P(MA-POSS)<sub>21</sub>.

**Acknowledgments** The AFM measurements were carried out within the cooperation of the SFB TRR 102 (project B03, Thomas Thum-Albrecht).

**Funding information** HH received financial support from the Higher Commission (HEC) of Pakistan under NRPU project no. 20-3074/NRPU/R&D/HEC/13 and QAU URF. JK received financial support from the Deutsche Forschungsgemeinschaft (SFB TRR 102, project B07).

## Compliance with ethical standards

**Conflict of interest** The authors declare that they have no conflict of interest.

## References

- Winterhalter M, Bürner H, Marzinka S, Benz R, Kasianowicz JJ (1995) Interaction of poly(ethylene-glycols) with air-water interfaces and lipid monolayers: investigations on surface pressure and surface potential. *Biophys J* 69:1372–1381
- Lee W, Ni S, Deng J, Kim BS, Satija SK, Mather PT, Esker AR (2007) Telechelic poly(ethylene glycol)-POSS amphiphiles at the air/water interface. *Macromolecules* 40:682–688
- Fuchs C, Hussain H, Amado E, Busse K, Kressler J (2015) Self-organization of poly(ethylene oxide) on the surface of aqueous salt solutions. *Macromol Rapid Commun* 36:211–218
- Deschênes L, Lyklema J, Danis C, Saint-Germain F (2015) Phase transitions in polymer monolayers: application of the Clapeyron equation to PEO in PPO–PEO Langmuir film. *Adv Colloid Interf Sci* 222:199–214
- James J, Ramalechume C, Mandal AB (2011) Two-dimensional surface properties of PEO-PPO-PEO triblock copolymer film at the air/water interface in the absence and presence of Tyr-Phe dipeptide, Val-Tyr-Val tripeptide, SDS and stearic acid. *Colloids Surf B: Biointerfaces* 82:345–353
- Busse K, Fuchs C, Hasan N, Pulst M, Kressler J (2018) Crystallization of poly(ethylene oxide) on the surface of aqueous salt solutions studied by GI-WAXS. *Langmuir* 34:12759–12763
- Fuchs C, Busse K, Flieger A-K, Kressler J (2016) Polymer crystallization on the surface of water or aqueous salt solution. *Chem Eng Technol* 39:1333–1340
- Peetla C, Graf K, Kressler J (2006) Langmuir monolayer and Langmuir–Blodgett films of amphiphilic triblock copolymers with water-soluble middle block. *Colloid Polym Sci* 285:27–37
- Gonçalves da Silva AM, Filipe EJM (1996) Interfacial behavior of poly(styrene)–poly(ethylene oxide) diblock copolymer monolayers at the air–water interface. Hydrophilic block chain length and temperature influence. *Langmuir* 12:6547–6553
- Barentin C, Muller P, Joanny JF (1998) Polymer brushes formed by end-capped poly(ethylene oxide) (PEO) at the air-water interface. *Macromolecules* 31:2198–2211
- Fuchs C, Hussain H, Schwieger C, Schulz M, Binder WH, Kressler J (2015) Molecular arrangement of symmetric and non-symmetric triblock copolymers of poly(ethylene oxide) and poly(isobutylene) at the air/water interface. *J Colloid Interface Sci* 437:80–89
- Feng H, Lu X, Wang W et al (2017) Block copolymers: synthesis, self-assembly, and applications. *Polymers* 9:1–31
- Deng J, Farmer-Creely CE, Viers BD, Esker AR (2004) Unique rodlike surface morphologies in trisilanocyclohexyl polyhedral oligomeric silsesquioxane films. *Langmuir* 20:2527–2530
- Kou X (2013) Synthesis of polyhedral oligomeric silsesquioxane (POSS) functionalized carbon nanotubes. Dissertation, University of Southern Mississippi
- Wang X, Xuan S, Song L, Yang H, Lu H, Hu Y (2012) Synergistic effect of POSS on mechanical properties, flammability, and thermal degradation of intumescent flame retardant polylactide composites. *J Macromol Sci Part B* 51:255–268
- Gnanasekaran D, Madhavpan K, Reddy RSR (2009) Developments of polyhedral oligomeric silsesquioxanes (POSS), POSS nanocomposites and their applications: a review. *J Sci Ind Res* 68:437–464
- Mohamed GM, Jheng Y-R, Yeh S-L et al (2017) Unusual emission of polystyrene-based alternating copolymers incorporating aminobutyl maleimide fluorophore-containing polyhedral oligomeric silsesquioxane nanoparticles. *Polymers* 9:1–20
- Mohamed MG, Hsu K-C, Hong J-L, Kuo S-W (2016) Unexpected fluorescence from maleimide-containing polyhedral oligomeric silsesquioxanes: nanoparticle and sequence distribution analyses of polystyrene-based alternating copolymers. *Polym Chem* 7:135–145
- Du F, Tian J, Wang H et al (2012) Synthesis and luminescence of POSS-containing perylene bisimide-bridged amphiphilic polymers. *Macromolecules* 45:3086–3093
- Lin H, Wan X, Jiang X, Wang Q, Yin J (2011) A nanoimprint lithography hybrid photoresist based on the thiol–ene system. *Adv Funct Mater* 21:2960–2967
- Tuteja A, Choi W, Ma M, Mabry JM, Mazzella SA, Rutledge GC, McKinley GH, Cohen RE (2007) Designing superoleophobic surfaces. *Science* 318:1618–1622
- Leng Y, Zhao J, Jiang P, Lu D (2016) POSS-derived solid acid catalysts with excellent hydrophobicity for highly efficient transformations of glycerol. *Catal Sci Technol* 6:875–881
- Létant SE, Herberg J, Dinh LN, Maxwell RS, Simpson RL, Saab AP (2007) Structure and catalytic activity of POSS-stabilized Pd nanoparticles. *Catal Commun* 8:2137–2142
- Liu Y-L, Fangchiang M-H (2009) Polyhedral oligomeric silsesquioxane nanocomposites exhibiting ultra-low dielectric constants through POSS orientation into lamellar structures. *J Mater Chem* 19:3643–3647
- Liu L, Yuan Y, Huang Y, Yu H, Yang J (2017) A new mechanism for the low dielectric property of POSS nanocomposites: the key role of interfacial effect. *Phys Chem Chem Phys* 19:14503–14511
- Loh XJ, Zhang Z-X, Mya KY, Wu YL, He CB, Li J (2010) Efficient gene delivery with paclitaxel-loaded DNA-hybrid polyplexes based on cationic polyhedral oligomeric silsesquioxanes. *J Mater Chem* 20:10634–10642

27. Pu Y, Zhang L, Zheng H et al (2013) Synthesis and drug release of star-shaped poly(benzyl L-aspartate)-block-poly(ethylene glycol) copolymers with POSS cores. *Macromol Biosci* 14:289–297
28. Pu Y, Zhang L, Zheng H, He B, Gu Z (2014) Drug release of pH-sensitive poly(L-aspartate)-b-poly(ethylene glycol) micelles with POSS cores. *Polym Chem* 5:463–470
29. Li Y, Xu B, Bai T, Liu W (2015) Co-delivery of doxorubicin and tumor-suppressing p53 gene using a POSS-based star-shaped polymer for cancer therapy. *Biomaterials* 55:12–23
30. Wang DK, Varanasi S, Strounina E, Hill DJT, Symons AL, Whittaker AK, Rasoul F (2014) Synthesis and characterization of a POSS-PEG macromonomer and POSS-PEG-PLA hydrogels for periodontal applications. *Biomacromolecules* 15:666–679
31. Pramudya I, Rico CG, Lee C, Chung H (2016) POSS-containing bioinspired adhesives with enhanced mechanical and optical properties for biomedical applications. *Biomacromolecules* 17:3853–3861
32. Wu J, Mather PT (2009) POSS polymers: physical properties and biomaterials applications. *Polym Rev* 49:25–63
33. Fadaie P, Atai M, Imani M, Karkhaneh A, Ghasaban S (2013) Cyanoacrylate-POSS nanocomposites: novel adhesives with improved properties for dental applications. *Dent Mater* 29:e61–e69
34. Wamke A, Dopierała K, Prochaska K, Maciejewski H, Biadasz A, Dudkowiak A (2015) Characterization of Langmuir monolayer, Langmuir–Blodgett and Langmuir–Schaefer films formed by POSS compounds. *Colloids Surf A Physicochem Eng Asp* 464:110–120
35. Dopierała K, Wamke A, Dutkiewicz M, Maciejewski H, Prochaska K (2014) Interfacial properties of fully condensed functional silsesquioxane: a Langmuir monolayer study. *J Phys Chem C* 118:24548–24555
36. Zhang Y, Zhao B, Li L, Nie K, Zheng S (2019) Polyhedral oligomeric silsesquioxane-capped poly(N-vinyl pyrrolidone) amphiphiles: synthesis, self-assembly, and use as porogen of nanoporous poly(vinylidene fluoride). *Colloid Polym Sci* 297:141–153
37. Rojewska M, Skrzypiec M, Prochaska K (2017) Surface properties and morphology of mixed POSS-DPPC monolayers at the air/water interface. *Colloids Surf B: Biointerfaces* 150:334–343
38. Skrzypiec M, Georgiev GA, Rojewska M, Prochaska K (2017) Interaction of polyhedral oligomeric silsesquioxanes and dipalmitoylphosphatidylcholine at the air/water interface: thermodynamic and rheological study. *Biochim Biophys Acta Biomembr* 1859:1838–1850
39. Li Z, Ma X, Guan X, Qiang X, Zang D, Chen F (2017) Aggregation behavior of star-shaped fluoropolymers containing polyhedral oligomeric silsesquioxane (POSS) at the air–water interface. *Colloid Polym Sci* 295:157–170
40. Dutkiewicz M, Karasiewicz J, Rojewska M, Skrzypiec M, Dopierała K, Prochaska K, Maciejewski H (2016) Synthesis of an open-cage structure POSS containing various functional groups and their effect on the formation and properties of Langmuir monolayers. *Chem Eur J* 22:13275–13286
41. Dopierała K, Maciejewski H, Prochaska K (2016) Interaction of polyhedral oligomeric silsesquioxane containing epoxy cyclohexyl groups with cholesterol at the air/water interface. *Colloids Surf B: Biointerfaces* 140:135–141
42. Mitsuishi M, Zhao F, Kim Y, Watanabe A, Miyashita T (2008) Preparation of ultrathin silsesquioxane nanofilms via polymer Langmuir - Blodgett films. *Chem Mater* 20:4310–4316
43. Paczesny J, Binkiewicz I, Janczuk M, Wybrańska K, Richter Ł, Hołyst R (2015) Langmuir and Langmuir-Blodgett films of unsymmetrical and fully condensed polyhedral oligomeric silsesquioxanes (POSS). *J Phys Chem C* 119:27007–27017
44. Xu S, Zhao B, Wei K, Zheng S (2018) Organic–inorganic polyurethanes with double decker silsesquioxanes in the main chains: morphologies, surface hydrophobicity, and shape memory properties. *J Polym Sci B Polym Phys* 56:893–906
45. Deng J, Hottle JR, Polidan JT, Kim HJ, Farmer-Creely CE, Viers BD, Esker AR (2004) Polyhedral oligomeric silsesquioxane amphiphiles: isotherm and Brewster angle microscopy studies of trisilanolisobutyl-POSS at the air/water interface. *Langmuir* 20:109–115
46. Deng J, Polidan JT, Hottle JR, Farmer-Creely CE, Viers BD, Esker AR (2002) Polyhedral oligomeric silsesquioxanes: a new class of amphiphiles at the air/water interface. *J Am Chem Soc* 124:15194–15195
47. Hussain H, Amado E, Kressler J (2011) Functional polyether-based amphiphilic block copolymers synthesized by atom-transfer radical polymerization. *Aust J Chem* 64:1183–1195
48. Ullah A, Ullah S, Mahmood N, et al (2019) Effect of polyhedral oligomeric silsesquioxane nanocage on the crystallization behavior of PEG<sub>sk</sub> - b -P(MA-POSS) diblock copolymers achieved via atom transfer radical polymerization. <https://doi.org/10.1002/pcr2.10058>
49. Tan BH, Hussain H, He CB (2011) Tailoring micelle formation and gelation in (PEG-P(MA-POSS)) amphiphilic hybrid block copolymers. *Macromolecules* 44:622–631
50. Hussain H, Tan BH, Seah GL, Liu Y, He CB, Davis TP (2010) Micelle formation and gelation of (PEG-P(MA-POSS)) amphiphilic block copolymers via associative hydrophobic effects. *Langmuir* 26:11763–11773
51. Perry MC (1996) *Langmuir-Blodgett films: an introduction*. Cambridge University Press, Cambridge
52. Tsukanova V, Salesse C (2004) On the nature of conformational transition in poly(ethylene glycol) chains grafted onto phospholipid monolayers. *J Phys Chem B* 108:10754–10764
53. Gaines GL (1991) Monolayers of polymers. *Langmuir* 7:834–839
54. Crisp DJ (1946) Surface films of polymers. Part II. Films of the coherent and semi-crystalline type. *J Colloid Sci* 1:161–184
55. Crisp DJ (1946) Surface films of polymers. Part I. Films of the fluid type. *J Colloid Sci* 1:49–70
56. Li B, Wu Y, Liu M, Esker AR (2006) Brewster angle microscopy study of poly( $\epsilon$ -caprolactone) crystal growth in Langmuir films at the air/water interface. *Langmuir* 22:4902–4905
57. Hasan N, Schwieger C, Tee HT, Wurm FR, Busse K, Kressler J (2018) Crystallization of a polyphosphoester at the air-water interface. *Eur Polym J* 101:350–357
58. Hoeng D, Moebius D (1991) Direct visualization of monolayers at the air-water interface by Brewster angle microscopy. *J Phys Chem* 95:4590–4592
59. Asada M, Jiang N, Sendogdular L, Sokolov J, Endoh MK, Koga T, Fukuto M, Yang L, Akgun B, Dimitriou M, Satija S (2014) Melt crystallization/dewetting of ultrathin PEO films via carbon dioxide annealing: the effects of polymer adsorbed layers. *Soft Matter* 10:6392–6403
60. Joncheray TJ, Denoncourt KM, Mathieu C, Meier MAR, Schubert US, Duran RS (2006) Langmuir and Langmuir-Blodgett films of poly(ethylene oxide)-b-poly( $\epsilon$ - caprolactone) star-shaped block copolymers. *Langmuir* 22:9264–9271
61. Cohn D, Stern T, Fernanda González M, Epstein J (2002) Biodegradable poly(ethylene oxide)/poly( $\epsilon$ -caprolactone) multiblock copolymers. *J Biomed Mater Res* 59:273–281
62. Carroll JB, Waddon AJ, Nakade H, Rotello VM (2003) “Plug and play” polymers. Thermal and x-ray characterizations of noncovalently grafted polyhedral oligomeric silsesquioxane (POSS)-polystyrene nanocomposites. *Macromolecules* 36:6289–6291
63. Zheng L, Waddon AJ, Farris RJ, Coughlin EB (2002) X-ray characterizations of polyethylene polyhedral oligomeric silsesquioxane copolymers. *Macromolecules* 35:2375–2379
64. Zheng J, Leblanc RM (2007) Advanced chemistry of monolayers at interfaces. In :Imae T (ed) *Infrared reflection absorption spectroscopy of monolayers at the air-water interface*, Academic Press, London, pp. 247–276



65. Wang H, Coss CS, Mudalige A, Polt RL, Pemberton JE (2013) A PM-IRRAS investigation of monorhamnolipid orientation at the air-water interface. *Langmuir* 29:4441–4450
66. Amado E, Kerth A, Blume A, Kressler J (2008) Infrared reflection absorption spectroscopy coupled with Brewster angle microscopy for studying interactions of amphiphilic triblock copolymers with phospholipid monolayers. *Langmuir* 24:10041–10053
67. Hussain H, Kerth A, Blume A, Kressler J (2004) Amphiphilic block copolymers of poly(ethylene oxide) and poly(perfluorohexylethyl methacrylate) at the water surface and their penetration into the lipid monolayer. *J Phys Chem B* 108:9962–9969
68. Schwieger C, Chen B, Tschierske C, Kressler J, Blume A (2012) Organization of T-shaped facial amphiphiles at the air/water interface studied by infrared reflection absorption spectroscopy. *J Phys Chem B* 116:12245–12256
69. Jbeily M, Schwieger C, Kressler J (2017) Mixed Langmuir monolayers of perfluorostearic acid and stearic acid studied by epifluorescence microscopy using fluorinated rhodamines and infrared reflection absorption spectroscopy (IRRAS). *Colloids Surf A* 529:274–285
70. Flach CR, Gericke A, Mendelsohn R (1997) Quantitative determination of molecular chain tilt angles in monolayer films at the air/water interface: infrared reflection/absorption spectroscopy of behenic acid methyl ester. *J Phys Chem B* 101:58–65
71. Elzein T, Nasser-Eddine M, Delaite C, Bistac S, Dumas P (2004) FTIR study of polycaprolactone chain organization at interfaces. *J Colloid Interface Sci* 273:381–387
72. Mao L, Ritcey AM, Desbat B (1996) Evaluation of molecular orientation in a polymeric monolayer at the air–water interface by polarization-modulated infrared spectroscopy. *Langmuir* 12:4754–4759
73. Schwieger C, Liu X, Krafft MP (2017) Self-assembled mesoscopic surface domains of fluorocarbon-hydrocarbon diblocks can form at zero surface pressure: tilting of solid-like hydrocarbon moieties compensates for cross-section mismatch with fluorocarbon moieties. *Phys Chem Chem Phys* 19:23809–23816
74. Liu W-C, Yang C-C, Chen W-C, Dai BT, Tsai MS (2002) The structural transformation and properties of spin-on poly(silsesquioxane) films by thermal curing. *J Non-Cryst Solids* 311:233–240
75. Tegou E, Bellas V, Gogolides E, Argitis P, Eon D, Cartry G, Cardinaud C (2004) Polyhedral oligomeric silsesquioxane (POSS) based resists: material design challenges and lithographic evaluation at 157 nm. *Chem Mater* 16:2567–2577
76. Zhu H, Ma Y, Fan Y, Shen J (2001) Fourier transform infrared spectroscopy and oxygen luminescence probing combined study of modified sol–gel derived film. *Thin Solid Films* 397:95–101

**Publisher's note** Springer Nature remains neutral with regard to jurisdictional claims in published maps and institutional affiliations.

#### 4 Summary, conclusion, and outlook

Crystallization in ultrathin films of different homopolymers such as PEs (i.e., Phenoxy-PPE, Ethoxy-PPE, and Methyl-PPE-*co*-decadiene) with regular phosphoester defects in the main chain, PCL, and hybrid diblock copolymers PEG-*b*-P(MA-POSS) was investigated at the air-water interface of a Langmuir trough. The polymers were dissolved in chloroform, spread on the water surface, and compressed by moving the barriers after solvent evaporation. The  $\pi$ -*mmA* isotherm measurements demonstrated the formation of stable Langmuir films with various phases during compression. Two completely different behaviors were observed from the investigated homopolymers and hybrid diblock copolymers. PEs crystallized in the plateau region of the  $\pi$ -*mmA* isotherms during compression as confirmed by BAM, EFM, and IRRAS as well as X-ray scattering techniques after transferring the films to the solid supports. PE with Ethoxy and Phenoxy defects in the 21<sup>st</sup> position of the methylene sequences formed separated circular/hexagonal single domains in the plateau region of the isotherm. These domains became bigger after the plateau region and then collapsed into broken parts at high surface compression. IRRAS measurements confirmed that the domains were the crystallites of PEs. These were transferred to a solid support and thoroughly investigated by AFM and GI-WAXS. Crystallites that were transferred in the plateau region have dimensions in the range of  $\approx 15$  to  $30 \mu\text{m}$  with thicknesses in the range of  $\approx 2.2$  to  $3 \text{ nm}$ . The thickness value is almost equal to the length of the 20 methylene groups sequence between the defects of the PEs. This confirms that using ADMET PE (precision PE), it is possible to get a crystalline Langmuir monolayer of PE. Finally, GI-WAXS revealed a rotator  $R_{II}$  crystal phase (pseudo-hexagonal unit cell) of the crystallites transferred after the plateau region of the isotherm.

Methyl-PPE-*co*-decadiene, where the methyl PPE defect is randomly created at 21 to 29 positions of the methylene backbone, however, showed a completely different crystal phase and film morphology, even though the  $\pi$ -*mmA* isotherm is very similar to the Ethoxy-PPE isotherm. Instead of single crystallites, film-like structures can be seen in the plateau region of the isotherm. AFM showed the film thickness in the range of  $\approx 3.2$  to  $3.5 \text{ nm}$ . A completely different crystal phase (i.e., orthorhombic rotator phase  $R_I$ ) was identified by GI-WAXS in LB films.

The variation in morphologies of PEs is due to the different crystal structures and stiffness of the polymers. For example, Phenoxy-PPE is stiffer as compared to Ethoxy-PPE, therefore, crystal growth in Phenoxy-PPE is highly restricted during compression, resulting in hexagonal/polygonal crystals. However, a similar crystal phase ( $R_I$ ) was found for both PEs since they have the same chain length between the phosphoester defects. On the other hand, the

Methyl-PPE-*co*-decadiene has randomly distributed defects in the main chain, which alter the chain packing and result in a different crystal structure. So, the film morphology of Methyl-PPE-*co*-decadiene is completely different compared to Ethoxy- and Phenoxy- PPE.

For PCL, butterfly-like domains were observed in the plateau region of the  $\pi$ -*mma* isotherm. These domains were the crystallites of PCL confirmed by IRRAS and GI-WAXS. The chain orientation (e.g., chain tilting) of PCL in the Langmuir films at different compression states of the  $\pi$ -*mma* isotherm was found in the range of 21° to 38° relative to the normal direction of the water surface. The crystallite orientations of PCL stayed similar even after transferring (at *mma*  $\approx 2 \text{ \AA}^2$ ) to the solid support confirmed by GI-WAXS.

In contrast to homopolymers, the scenario was found to be completely different for a series of PEG-*b*-P(MA-POSS) hybrid diblock copolymers. The copolymers comprised 113 ethylene glycol (EG) units and 4 to 21 units of MA-POSS. Instead of single crystallites that were observed in PEs and PCL, rigid films were seen. The  $\pi$ -*mma* isotherms of the copolymers showed typical isotherms with high surface pressure, confirming stable Langmuir film formation for all diblock copolymers. BAM and EFM revealed no film structure during the compression experiment. Among these diblock copolymers, only PEG<sub>113</sub>-*b*-P(MA-POSS)<sub>21</sub> showed two pseudo plateaus at  $\approx 18 \text{ mN/m}$  and  $\approx 42 \text{ mN/m}$  in the isotherm. They were related to the multilayer formation confirmed by AFM measurements and film collapse identified by BAM. More interestingly, these collapsed film fragments showed a unique sinusoidal periodic pattern called wrinkles when subjected to several compressions above  $\pi \approx 18 \text{ mN/m}$ . These structures disappeared when the film was expanded below  $\pi \approx 18 \text{ mN/m}$  or during transferring of the film by the LB technique. The collapsed film fragments were later extensively investigated by GI-WAXS measurements. Two different orientations of the MA-POSS block and a disordered state of the PEG block in the LB films of the diblock copolymer were identified. These orientations were found to be responsible for the unique wrinkle formation during the compression.

The overall conclusions from the experiments are that the air-water interface of a Langmuir trough can be used to study the crystallization in ultrathin films of different amphiphilic homopolymers and hybrid diblock copolymers. PE-like polymers can be successfully studied and crystallized at the air-water interface of a Langmuir trough by introducing polar defects in the main chain with ADMET polymerization. The crystallization process can be fully understood using BAM, EFM, IRRAS, AFM, and GI-WAXS measurements. Depending on the polymers (e.g., flexible to rigid), different crystal structures, morphologies from single

separated crystallites to film-like features, and chain tilting in the crystallites can be explored. Rigid Langmuir films instead of single-crystalline domains can be fabricated by introducing a hybrid block copolymer system. Furthermore, by taking advantage of the Langmuir trough, different periodic structures (wrinkles) can also be achieved.

This Thesis examined the possibility of crystallizing different polymers on the water surface of a Langmuir trough. There is also some work left for the future outlook. At the first point, it will be interesting to introduce new types of defects (e.g., instead of phosphoester groups) and to increase the methylene sequence between the defects greater than 30 units. The chain orientation at different compression states of the  $\pi$ -*mma* isotherm should be checked with angle-dependent IRRAS measurements and GI-WAXS. The kinetics of crystallization can also be studied. Instead of employing water as a subphase, the impact of an aqueous salt solution should be addressed. The melting behavior of the crystallites in the Langmuir film (e.g., either by film expansion or increasing subphase temperature) should be compared with the crystallites in bulk. High-resolution AFM can be employed to see more details of the crystallite morphologies. In the case of diblock PEG<sub>113</sub>-*b*-(MA-POSS)<sub>21</sub> copolymer, the wrinkle formation should be examined during the compression-expansion experiments on the Langmuir trough by GI-WAXS and IRRAS. The kinetics of the wrinkle formation is also interesting for future study. The amplitude of the wrinkles should be checked in order to calculate the elastic modulus of the system.

## References

- [1] U. W. Gedde, *Polymer Physics*, Chapman & Hall, London, UK, **1995**.
- [2] P. J. Flory, *J. Chem. Phys.* **1947**, *15*, 397–408.
- [3] E. W. Fischer, *Zeitschrift für Naturforsch. A* **1957**, *12*, 753–754.
- [4] H. Staudinger, *Naturwissenschaften* **1929**, *17*, 141–144.
- [5] V. Ratta, Crystallization, Morphology, Thermal Stability and Adhesive Properties of Novel High Performance Semicrystalline Polyimides, Virginia Polytechnic Institute and State University, USA, Ph.D. Thesis, **1999**.
- [6] G. B. Street, R. L. Greene, *IBM J. Res. Dev.* **1977**, *21*, 99–110.
- [7] E. Amado, N. Hasan, K. Busse, J. Kressler, *Macromol. Chem. Phys.* **2021**, *222*, 2100113.
- [8] K. Nitta, *Polymers* **2016**, *8*, 229.
- [9] A. Keller, *Philos. Mag.* **1957**, *2*, 1171–1175.
- [10] M. Zhang, B.-H. Guo, J. Xu, *Crystals* **2016**, *7*, 4.
- [11] J. D. Hoffman, G. T. Davis, J. I. Lauritzen, in *Treatise Solid State Chem.*, Springer US, Boston, MA, **1976**, pp. 497–614.
- [12] J. D. Hoffman, *Polymer* **1983**, *24*, 3–26.
- [13] A. Lustiger, R. L. Markham, *Polymer* **1983**, *24*, 1647–1654.
- [14] C. A. Kelly, M. J. Jenkins, *Polym. J.* **2022**, *54*, 249–257.
- [15] T. Albrecht, G. Strobl, *Macromolecules* **1996**, *29*, 783–785.
- [16] M. Schulz, A. Seidlitz, R. Kurz, R. Bärenwald, A. Petzold, K. Saalwächter, T. Thurn-Albrecht, *Macromolecules* **2018**, *51*, 8377–8385.
- [17] W. Banks, J. N. Hay, A. Sharples, G. Thomson, *Nature* **1962**, *194*, 542–544.
- [18] C. Liu, Q. Wang, H. Tian, Y. Geng, D. Yan, *Polymer* **2013**, *54*, 2459–2465.
- [19] X. Tang, W. Chen, L. Li, *Macromolecules* **2019**, *52*, 3575–3591.
- [20] Z. Yao, Y. Zheng, J. Dou, Y. Lu, Y. Ding, L. Ding, J. Wang, J. Pei, *Adv. Mater.* **2021**, *33*, 2006794.
- [21] D. J. Sikkema, *Adv. Ind. Eng. Polym. Res.* **2022**, *5*, 80–89.
- [22] M. M. Iovleva, S. I. Banduryan, *Polym. Sci. U.S.S.R.* **1980**, *22*, 2758–2767.
- [23] J. Kumaki, T. Kawauchi, E. Yashima, *J. Am. Chem. Soc.* **2005**, *127*, 5788–5789.
- [24] J. Liu, M. Arif, J. Zou, S. I. Khondaker, L. Zhai, *Macromolecules* **2009**, *42*, 9390–9393.
- [25] M. Ballauff, *Makromol. Chem., Rapid Commun.* **1986**, *7*, 407–414.
- [26] T. Babur, G. Gupta, M. Beiner, *Soft Matter* **2016**, *12*, 8093–8097.



- [27] G. C. Oppenlander, *Science* **1968**, *159*, 1311–1319.
- [28] F. R. Anderson, *J. Appl. Phys.* **1964**, *35*, 64–70.
- [29] G. W. Ehrenstein, R. P. Theriault, *Polymeric Materials: Structure, Properties, Applications*, Hanser Publishers, Munich, **2001**.
- [30] W. Rungswang, C. Jarumaneeroj, S. Patthamasang, P. Phiriyawirut, P. Jirasukho, S. Soontaranon, S. Rugmai, B. S. Hsiao, *Polymer* **2019**, *172*, 41–51.
- [31] M. Pulst, M. H. Samiullah, U. Baumeister, M. Prehm, J. Balko, T. Thurn-Albrecht, K. Busse, Y. Golitsyn, D. Reichert, J. Kressler, *Macromolecules* **2016**, *49*, 6609–6620.
- [32] J. Bojda, E. Piorkowska, G. Lapienis, A. Michalski, *Eur. Polym. J.* **2018**, *105*, 126–134.
- [33] N. A. Platé, V. P. Shibaev, *J. Polym. Sci. Macromol. Rev.* **1974**, *8*, 117–253.
- [34] W.-G. Hu, K. Schmidt-Rohr, *Acta Polym.* **1999**, *50*, 271–285.
- [35] G. Reiter, G. R. Strobl, Eds. , *Progress in Understanding of Polymer Crystallization*, Springer Berlin Heidelberg, Berlin, Heidelberg, **2007**.
- [36] B. Wunderlich, T. Arakawa, *J. Polym. Sci. Part A Gen. Pap.* **1964**, *2*, 3697–3706.
- [37] D. V. Rees, D. C. Bassett, *Nature* **1968**, *219*, 368–370.
- [38] M. Lemanowicz, A. Mielańczyk, T. Walica, M. Kotek, A. Gierczycki, *Polymers* **2021**, *13*, 2695.
- [39] G. Strobl, *The Physics of Polymers*, Springer, Berlin, **2007**.
- [40] J. Xu, G. Reiter, R. Alamo, *Crystals* **2021**, *11*, 304.
- [41] Y.-X. Liu, E.-Q. Chen, *Coord. Chem. Rev.* **2010**, *254*, 1011–1037.
- [42] J. M. Carr, D. S. Langhe, M. T. Ponting, A. Hiltner, E. Baer, *J. Mater. Res.* **2012**, *27*, 1326–1350.
- [43] C. Yu, Q. Xie, Y. Bao, G. Shan, P. Pan, *Crystals* **2017**, *7*, 147.
- [44] C. W. Frank, V. Rao, M. M. Despotopoulou, R. F. W. Pease, W. D. Hinsberg, R. D. Miller, J. F. Rabolt, *Science* **1996**, *273*, 912–915.
- [45] G. Reiter, *Phys. Rev. Lett.* **1992**, *68*, 75–78.
- [46] B. J. Factor, T. P. Russell, M. F. Toney, *Macromolecules* **1993**, *26*, 2847–2859.
- [47] Y. Wang, S. Ge, M. Rafailovich, J. Sokolov, Y. Zou, H. Ade, J. Lüning, A. Lustiger, G. Maron, *Macromolecules* **2004**, *37*, 3319–3327.
- [48] A.-K. Löhmann, T. Henze, T. Thurn-Albrecht, *Proc. Natl. Acad. Sci.* **2014**, *111*, 17368–17372.
- [49] W. Kossack, A. Seidlitz, T. Thurn-Albrecht, F. Kremer, *Macromolecules* **2016**, *49*, 3442–3451.
- [50] M. Tariq, Thermodynamics and Kinetics of Interface-Induced Crystallization, Martin-

- Luther-Universität Halle-Wittenberg, Germany, Ph.D. Thesis, **2021**.
- [51] S. Li, X. Sun, H. Li, S. Yan, *Eur. Polym. J.* **2018**, *102*, 238–253.
- [52] Khasanah, K. R. Reddy, S. Ogawa, H. Sato, I. Takahashi, Y. Ozaki, *Macromolecules* **2016**, *49*, 4202–4210.
- [53] V. H. Mareau, R. E. Prud'homme, *Macromolecules* **2005**, *38*, 398–408.
- [54] S. Ge, M. Rafailovich, J. Sokolov, Y. Zou, H. Ade, J. Lüning, A. Lustiger, G. Marom, *Macromolecules* **2005**, *38*, 2022–2022.
- [55] Y. Ma, W. Hu, G. Reiter, *Macromolecules* **2006**, *39*, 5159–5164.
- [56] H. Schönherr, R. M. Waymouth, C. W. Frank, *Macromolecules* **2003**, *36*, 2412–2418.
- [57] Y. Wang, C.-M. Chan, K.-M. Ng, L. Li, *Macromolecules* **2008**, *41*, 2548–2553.
- [58] P. Yang, Y. Han, *Langmuir* **2009**, *25*, 9960–9968.
- [59] N. N. Nikitenkov, Ed. , *Modern Technologies for Creating the Thin-Film Systems and Coatings*, InTech, **2017**.
- [60] C. Wenzel, K. Wetzig, J. Thomas, M. Hecker, W. Brückner, in *Met. Based Thin Film. Electron.*, Wiley-VCH Verlag GmbH & Co. KGaA, Weinheim, FRG, **2005**, pp. 121–203.
- [61] D. A. Jameel, *IJMPA* **2015**, *1*, 193–199.
- [62] S. J. Hitchcock, N. T. Carroll, M. G. Nicholas, *J. Mater. Sci.* **1981**, *16*, 714–732.
- [63] Z. Guo, S. Li, X. Liu, J. Zhang, H. Li, X. Sun, Z. Ren, S. Yan, *J. Phys. Chem. B* **2018**, *122*, 9425–9433.
- [64] M. C. Petty, *Langmuir-Blodgett Films: An Introduction*, Cambridge University Press, Cambridge, **1996**.
- [65] G. Roberts, Ed. , *Langmuir-Blodgett Films*, Springer, New York, **1990**.
- [66] K. Ariga, *Langmuir* **2020**, *36*, 7158–7180.
- [67] P. Cicutta, E. M. Terentjev, *Eur. Phys. J. E* **2005**, *16*, 147–158.
- [68] K. Yagi, M. Fujihira, *Appl. Surf. Sci.* **2000**, *157*, 405–411.
- [69] M. Jbeily, C. Schwieger, J. Kressler, *Colloids Surfaces A Physicochem. Eng. Asp.* **2017**, *529*, 274–285.
- [70] M. Lhor, S. C. Bernier, H. Horchani, S. Bussièrès, L. Cantin, B. Desbat, C. Salesse, *Adv. Colloid Interface Sci.* **2014**, *207*, 223–239.
- [71] N. F. Crawford, R. M. Leblanc, *Adv. Colloid Interface Sci.* **2014**, *207*, 131–138.
- [72] R. F. Lopez, T. M. Nobre, C. de M. Accardo, P. C. P. Filho, H. B. Nader, C. C. Lopes, L. Caseli, *Colloids Surfaces B Biointerfaces* **2013**, *111*, 530–535.
- [73] V. Tsukanova, O. Slyadneva, T. Inoue, A. Harata, T. Ogawa, *Chem. Phys.* **1999**, *250*,

- 207–215.
- [74] A.-C. Schöne, T. Roch, B. Schulz, A. Lendlein, *J. R. Soc. Interface* **2017**, *14*, 20161028.
- [75] O. N. Oliveira, L. Caseli, K. Ariga, *Chem. Rev.* **2022**, *122*, 6459–6513.
- [76] L. Rayleigh, *Proc. R. Soc. London* **1889**, *47*, 364–367.
- [77] I. Langmuir, *J. Am. Chem. Soc.* **1917**, *39*, 1848–1906.
- [78] K. B. Blodgett, *J. Am. Chem. Soc.* **1935**, *57*, 1007–1022.
- [79] S. Watson, M. Nie, L. Wang, K. Stokes, *RSC Adv.* **2015**, *5*, 89698–89730.
- [80] V. M. Kaganer, H. Möhwald, P. Dutta, *Rev. Mod. Phys.* **1999**, *71*, 779–819.
- [81] “Langmuir Films,” can be found under <https://www.nanoscience.com/techniques/langmuir-films/>, date accessed: **2022-06-04**.
- [82] M. D. Phan, J. Lee, K. Shin, *J. Oleo Sci.* **2016**, *65*, 385–397.
- [83] M. J. Campolongo, S. J. Tan, D.-M. Smilgies, M. Zhao, Y. Chen, I. Xhangolli, W. Cheng, D. Luo, *ACS Nano* **2011**, *5*, 7978–7985.
- [84] V. Lovis, C. Stefaniu, G. Brezesinski, *Colloids Surfaces A Physicochem. Eng. Asp.* **2019**, *576*, 29–35.
- [85] D. J. Crisp, *J. Colloid Sci.* **1946**, *1*, 49–70.
- [86] D. J. Crisp, *J. Colloid Sci.* **1946**, *1*, 161–184.
- [87] P. G. de Gennes, *Adv. Colloid Interface Sci.* **1987**, *27*, 189–209.
- [88] F. Monroy, L. R. Arriaga, D. Langevin, *Phys. Chem. Chem. Phys.* **2012**, *14*, 14450.
- [89] G. L. Gaines, *Langmuir* **1991**, *7*, 834–839.
- [90] C. Fuchs, Selbstorganisation von Homopolymeren Und Amphiphilen Triblockcopolymeren Auf Wässrigen Subphasen, Martin-Luther-Universität Halle-Wittenberg, Germany, Ph.D. Thesis, **2017**.
- [91] R. Vilanove, F. Rondelez, *Phys. Rev. Lett.* **1980**, *45*, 1502–1505.
- [92] B. Li, Surface Characterization of Poly ( $\epsilon$ -Caprolactone) at the Air/Water Interface, Virginia Polytechnic Institute and State University, USA, M.Sc Thesis, **2004**.
- [93] K. Watanabe, J. Kumaki, *Polym. J.* **2020**, *52*, 601–613.
- [94] C. Barentin, P. Muller, J. F. Joanny, *Macromolecules* **1998**, *31*, 2198–2211.
- [95] C. Peetla, K. Graf, J. Kressler, *Colloid Polym. Sci.* **2006**, *285*, 27–37.
- [96] K. Busse, C. Peetla, J. Kressler, *Langmuir* **2007**, *23*, 6975–6982.
- [97] R. Keller, Structure Formation of Amphiphilic Molecules at the Air/Water Interface and after Film Transfer, Johannes Gutenberg-Universität Mainz, Germany, Ph.D. Thesis, **2012**.
- [98] T. R. Baekmark, G. Elender, D. D. Lasic, E. Sackmann, *Langmuir* **1995**, *11*, 3975–3987.

- [99] W. Xu, G. Wen, T. Wu, N. Chen, *Langmuir* **2019**, *35*, 13435–13441.
- [100] N. Joshi, V. Saxena, A. Singh, S. P. Koiry, A. K. Debnath, M. M. Chehimi, D. K. Aswal, S. K. Gupta, *Sensors Actuators B Chem.* **2014**, *200*, 227–234.
- [101] B. Li, Y. Wu, M. Liu, A. R. Esker, *Langmuir* **2006**, *22*, 4902–4905.
- [102] B. Li, A. R. Esker, *Langmuir* **2007**, *23*, 2546–2554.
- [103] B. Li, A. R. Esker, *Langmuir* **2007**, *23*, 574–581.
- [104] B. Li, H. Marand, A. R. Esker, *J. Polym. Sci. Part B Polym. Phys.* **2007**, *45*, 3200–3318.
- [105] T. Naolou, K. Busse, B.-D. Lechner, J. Kressler, *Colloid Polym. Sci.* **2014**, *292*, 1199–1208.
- [106] C. Fuchs, H. Hussain, E. Amado, K. Busse, J. Kressler, *Macromol. Rapid Commun.* **2015**, *36*, 211–218.
- [107] K. Busse, C. Fuchs, N. Hasan, M. Pulst, J. Kressler, *Langmuir* **2018**, *34*, 12759–12763.
- [108] S. Ni, W. Lee, B. Li, A. R. Esker, *Langmuir* **2006**, *22*, 3672–3677.
- [109] J. M. Klass, R. B. Lennox, G. R. Brown, H. Bourque, M. Pérolet, *Langmuir* **2003**, *19*, 333–340.
- [110] C. Fuchs, K. Busse, A.-K. Flieger, J. Kressler, *Chem. Eng. Technol.* **2016**, *39*, 1333–1340.
- [111] V. Torrisi, A. Licciardello, G. Marletta, *Mater. Sci. Eng. B* **2010**, *169*, 49–54.
- [112] M. Pohjakallio, T. Aho, K. Kontturi, E. Kontturi, *Soft Matter* **2011**, *7*, 743–748.
- [113] J. Kumaki, T. Kawauchi, K. Okoshi, H. Kusanagi, E. Yashima, *Angew. Chemie Int. Ed.* **2007**, *46*, 5348–5351.
- [114] I. Hamley, *The Physics of Block Copolymers*, Oxford University Press, Oxford, **1998**.
- [115] I. I. Perepichka, Q. Lu, A. Badia, C. G. Bazuin, *Langmuir* **2013**, *29*, 4502–4519.
- [116] S. H. Mir, G. Rydzek, L. A. Nagahara, A. Khosla, P. Mokarian-Tabari, *J. Electrochem. Soc.* **2020**, *167*, 037502.
- [117] I. I. Perepichka, A. Badia, C. G. Bazuin, *ACS Nano* **2010**, *4*, 6825–6835.
- [118] J. Bowers, A. Zarbakhsh, J. R. P. Webster, L. R. Hutchings, R. W. Richards, *Langmuir* **2001**, *17*, 131–139.
- [119] T. J. Joncheray, K. M. Denoncourt, C. Mathieu, M. A. R. Meier, U. S. Schubert, R. S. Duran, *Langmuir* **2006**, *22*, 9264–9271.
- [120] T. J. Joncheray, S. A. Bernard, R. Matmour, B. Lepoittevin, R. J. El-Khoury, D. Taton, Y. Gnanou, R. S. Duran, *Langmuir* **2007**, *23*, 2531–2538.
- [121] C. Fuchs, H. Hussain, C. Schwieger, M. Schulz, W. H. Binder, J. Kressler, *J. Colloid Interface Sci.* **2015**, *437*, 80–89.

- [122] Z. Li, X. Ma, D. Zang, X. Guan, L. Zhu, J. Liu, F. Chen, *RSC Adv.* **2015**, *5*, 82869–82878.
- [123] P. Scheibe, M. Barz, M. Hemmelmann, R. Zentel, *Langmuir* **2010**, *26*, 5661–5669.
- [124] S. Alexander, *J. Phys.* **1977**, *38*, 983–987.
- [125] L. Deschênes, M. Bousmina, A. M. Ritcey, *Langmuir* **2008**, *24*, 3699–3708.
- [126] J. Zhu, R. B. Lennox, A. Eisenberg, *J. Phys. Chem.* **1992**, *96*, 4727–4730.
- [127] D. H. Kim, S. Y. Kim, *J. Phys. Chem. Lett.* **2017**, *8*, 1865–1871.
- [128] I. I. Perepichka, K. Borozenko, A. Badia, C. G. Bazuin, *J. Am. Chem. Soc.* **2011**, *133*, 19702–19705.
- [129] R. M. Van Horn, M. R. Steffen, D. O’Connor, *Polym. Cryst.* **2018**, *1*, e10039.
- [130] T. J. Joncheray, K. M. Denoncourt, M. A. R. Meier, U. S. Schubert, R. S. Duran, *Langmuir* **2007**, *23*, 2423–2429.
- [131] J. K. Palacios, J. Zhao, N. Hadjichristidis, A. J. Müller, *Macromolecules* **2017**, *50*, 9683–9695.
- [132] O. Suraeva, Polymer 2D Crystals via Crystallization Self-Assembly: Preparation, Properties and Features, Johannes Gutenberg-Universität Mainz, Germany, Ph.D. Thesis, **2020**.
- [133] J. K. Cox, K. Yu, A. Eisenberg, R. Bruce Lennox, *Phys. Chem. Chem. Phys.* **1999**, *1*, 4417–4421.
- [134] J. K. Cox, K. Yu, B. Constantine, A. Eisenberg, R. B. Lennox, *Langmuir* **1999**, *15*, 7714–7718.
- [135] J. L. Logan, P. Masse, Y. Gnanou, D. Taton, R. S. Duran, *Langmuir* **2005**, *21*, 7380–7389.
- [136] A. V. Sorokin, M. Bai, S. Ducharme, M. Poulsen, *J. Appl. Phys.* **2002**, *92*, 5977–5981.
- [137] T. C. Chung, H. L. Lu, C. L. Li, *Macromolecules* **1994**, *27*, 7533–7537.
- [138] Y. Zhang, C. Wang, S. Mecking, Z. Jian, *Angew. Chemie* **2020**, *132*, 14402–14408.
- [139] K. B. Wagener, J. M. Boncella, J. G. Nel, *Macromolecules* **1991**, *24*, 2649–2657.
- [140] K. N. Bauer, H. T. Tee, M. M. Velencoso, F. R. Wurm, *Prog. Polym. Sci.* **2017**, *73*, 61–122.
- [141] T. Haider, O. Suraeva, M. L. O’Duill, J. Mars, M. Mezger, I. Lieberwirth, F. R. Wurm, *Polym. Chem.* **2020**, *11*, 3404–3415.
- [142] N. Hasan, K. Busse, T. Haider, F. R. Wurm, J. Kressler, *Polymers* **2020**, *12*, 2408.
- [143] C. A. Devereaux, S. M. Baker, *Macromolecules* **2002**, *35*, 1921–1927.
- [144] A. M. G. da Silva, E. J. M. Filipe, J. M. R. D’Oliveira, J. M. G. Martinho, *Langmuir*



- 1999**, *12*, 6547–6553.
- [145] R. Gengler, A Modified Langmuir Schaefer Method For the Creation of Functional Thin Films, University of Groningen, the Netherlands, Ph.D. Thesis, **2010**.
- [146] A. Das, Controlling Phase Transitions in Langmuir Polymer Films, University of Freiburg, Germany, Ph.D. Thesis, **2020**.
- [147] I. Langmuir, V. J. Schaefer, *J. Am. Chem. Soc.* **1938**, *60*, 1351–1360.
- [148] S. Karaborni, J. I. Siepmann, *Mol. Phys.* **1994**, *83*, 345–350.
- [149] J. P. Bareman, M. L. Klein, *MRS Proc.* **1991**, *237*, 271.
- [150] C. Kong, H. Zhang, Z. Zhao, Q. Zheng, *Chem. Res. Chinese Univ.* **2013**, *29*, 545–550.
- [151] G. Watanabe, H. Eimura, N. L. Abbott, T. Kato, *Langmuir* **2020**, *36*, 12281–12287.
- [152] B. Desbat, S. Castano, in *Encycl. Biophys.*, Springer Berlin Heidelberg, Berlin, Heidelberg, **2013**, pp. 196–200.
- [153] S. Hénon, J. Meunier, *Rev. Sci. Instrum.* **1991**, *62*, 936–939.
- [154] D. Hoenig, D. Moebius, *J. Phys. Chem.* **1991**, *95*, 4590–4592.
- [155] J. C. Stockert, A. Blazquez-Castro, *Fluorescence Microscopy in Life Sciences*, Bentham Science Publishers, Sharjah, UAE, **2017**.
- [156] M. Lösche, H. Möhwald, *Rev. Sci. Instrum.* **1984**, *55*, 1968–1972.
- [157] S. Deike, M. Malke, B.-D. Lechner, W. H. Binder, *Polymers* **2017**, *9*, 369.
- [158] N. Hasan, K. Busse, A. Ullah, H. Hussain, J. Kressler, *Langmuir* **2021**, *37*, 13399–13408.
- [159] B. L. Stottrup, A. H. Nguyen, E. Tüzel, *Biochim. Biophys. Acta - Biomembr.* **2010**, *1798*, 1289–1300.
- [160] R. G. Nuzzo, D. L. Allara, *J. Am. Chem. Soc.* **1983**, *105*, 4481–4483.
- [161] R. G. Greenler, *J. Chem. Phys.* **1966**, *44*, 310–315.
- [162] R. A. Dluhy, D. G. Cornell, *J. Phys. Chem.* **1985**, *89*, 3195–3197.
- [163] R. Maoz, J. Sagiv, *J. Colloid Interface Sci.* **1984**, *100*, 465–496.
- [164] C. R. Flach, A. Gericke, R. Mendelsohn, *J. Phys. Chem. B* **1997**, *101*, 58–65.
- [165] R. Mendelsohn, G. Mao, C. R. Flach, *Biochim. Biophys. Acta - Biomembr.* **2010**, *1798*, 788–800.
- [166] N. Hasan, C. Fuchs, C. Schwieger, K. Busse, O. Dolynchuk, J. Kressler, *Polymer* **2020**, *196*, 122468.
- [167] W.-P. Ulrich, H. Vogel, *Biophys. J.* **1999**, *76*, 1639–1647.
- [168] C. Schwieger, B. Chen, C. Tschierske, J. Kressler, A. Blume, *J. Phys. Chem. B* **2012**, *116*, 12245–12256.

- [169] G. Binnig, C. F. Quate, C. Gerber, *Phys. Rev. Lett.* **1986**, *56*, 930–933.
- [170] F. J. Giessibl, *Rev. Mod. Phys.* **2003**, *75*, 949–983.
- [171] N. M. Peachey, C. J. Eckhardt, *Micron* **1994**, *25*, 271–292.
- [172] K. Xu, W. Sun, Y. Shao, F. Wei, X. Zhang, W. Wang, P. Li, *Nanotechnol. Rev.* **2018**, *7*, 605–621.
- [173] P. Müller-Buschbaum, *Adv. Mater.* **2014**, *26*, 7692–7709.
- [174] A. Naudon, D. Thiaudiere, *J. Appl. Crystallogr.* **1997**, *30*, 822–827.
- [175] J. Perlich, J. Rubeck, S. Botta, R. Gehrke, S. V. Roth, M. A. Ruderer, S. M. Prams, M. Rawolle, Q. Zhong, V. Körstgens, P. Müller-Buschbaum, *Rev. Sci. Instrum.* **2010**, *81*, 105105.

## Remarks on polymer naming

In paper (II), the investigated polymer is referred to in a simplified way as polyphosphoester (PPE). This can also be written as poly(ethylene) (PE) with regular phenoxy-phosphoester defects in the main backbone (Phenoxy-PPE). The latter naming style was used in the paper (I). The higher MA-POSS containing diblock copolymer is presented as PEG<sub>113</sub>-*b*-(MA-POSS)<sub>21</sub> in the paper (IV). This diblock copolymer is denoted as PEG<sub>5k</sub>-*b*-(MA-POSS)<sub>21</sub> in paper (V).

## Abbreviations

List of symbols and abbreviations:

2D	Two dimensional
3D	Three dimensional
Å	Angstrom
nm	Nanometer
µm	Micrometer
mN/m	Mili newton per meter
$A_{\text{lift-off}}$	Area when surface pressure starts to increase
$A_{\text{trough}}$	Trough area between the barriers
$A_o$	Limiting area
$A_S$	Substrate area dipped into the subphase
$\alpha_i$	Angle of incidence relative to the xy plane
$\alpha_f$	Scattering angle relative to the xy plane
$b$	Width of Wilhelmy plate
C	Collapse phase
$C$	Concentration of the polymer solution
$d$	Thickness of Wilhelmy plate
$\Delta A_L$	Area change of the trough during the film transfer process
$F_0$	Net downward force exerted by the pure water
$F$	Net downward force exerted by the adsorbed molecular film
G	Gas phase
$g$	Gravitational constant
$h$	Immersion depth of Wilhelmy plate
L <sub>1</sub>	Liquid expanded phase

$L_2$	Liquid condensed phase
$l$	Length of the Wilhelmy plate
$M_n$	Number average molar mass
$mmA$	Mean molecular area
$n$	Refractive index
$N_A$	Avogadro's constant
$k_B$	Boltzmann constant
$R$	Reflectivity
$S$	Solid phase
$\psi$	Scattering angle relative to the xz plane
$T$	Absolute temperature
$t$	Time
$V$	Volume of the polymer solution spread
$\rho_M$	Density of the Wilhelmy plate
$\varepsilon_S$	Elastic modulus
$\pi$	Surface pressure
$\Gamma$	Surface concentration
$\gamma_o$	Surface tension of water
$\gamma$	Surface tension of water with adsorbed molecules
$C^{-1}$	Compressibility constant
$\tau$	Transfer ratio
$\theta_B$	Brewster angle
$\theta$	Tilt angle
$\varphi_1$	Angle of incidence
$\varphi_2$	Angle of reflection



$\tilde{\varphi}_2$	Angle of refraction
$q_y$ and $q_z$	X-ray scattering vector in two components at y and z coordinates
$\vec{\mu}$	Transition dipole moment
ADMET PE	Acyclic diene metathesis poly(ethylene)
AFM	Atomic force microscopy
BAM	Brewster angle microscopy
Bis-ANS	Bis-anilinonaphthalene sulfonates
CCD	Charge-coupled device
DPPE	Dipalmitoylphosphatidylcholine
EFM	Epifluorescence microscopy
EG	Ethylene glycol
GI-WAXS	Grazing incidence wide-angle X-ray scattering
IR	Infrared
IRRAS	Infrared reflection absorption spectroscopy
i-PMMA	Isotactic poly(methyl methacrylate)
LB	Langmuir Blodgett
LBL	Layer by layer
LFP	Langmuir film of polymer
LS	Langmuir Schafer
MA-POSS	Methacrylate containing polyhedral oligomeric silsesquioxane (MA-POSS)
MCT	Mercury cadmium telluride
PCL	Poly( $\epsilon$ -caprolactone)
PE	Poly(ethylene)
PEs	Poly(ethylene)s
PEG	Poly(ethylene glycol)
PEO	Poly(ethylene oxide)

PDLA	Poly(D-lactide)
PLLA	Poly(L-lactide)
PMMA	Poly(methyl methacrylate)
PPE	Polyphosphoester
PS	Poly(styrene)
RA	Reflectance absorbance
s-PMMA	Syndiotactic poly(methyl methacrylate)
TDMs	Transition dipole moments

## **Erklärung**

Hiermit versichere ich, dass ich die vorliegende Arbeit selbständig und ohne fremde Hilfe verfasst und keine anderen als die von mir angegebenen Quellen und Hilfsmittel verwendet habe. Die den benutzten Werken wörtlich oder inhaltlich entnommenen Stellen, habe ich als solche kenntlich gemacht. Ich erkläre, keine anderweitigen Promotionsversuche unternommen und die vorliegende Dissertation weder in der jetzigen noch in einer anderen Fassung einer anderen wissenschaftlichen Einrichtung vorgelegt zu haben.

Halle (Saale), den

Nazmul Hasan

## **Acknowledgments**

I would like to thank and acknowledge all the people who supported me during my doctoral studies. First and foremost, I would like to thank my Thesis supervisor Prof. Dr. Joerg Kressler for giving me the opportunity to work in his group. I am grateful to him for his constant support during my Ph.D. I also thank him for his encouragement and guidance, which helped me to reach this point. My special thanks go to Prof. Dr. Dariush Hinderberger for his mentorship and continuous scientific guidance throughout my research. My thanks go to Dr. Karsten Busse, Dr. Oleksandr Dolynchuk, and Dr. Christian Schwieger for their support in GI-WAXS and IRRAS measurements as well as for the smooth cooperative work. I am especially thankful to Dr. Ann-Kristin Flieger and Dr. Mohamod Tareq for introducing AFM, WAXS, and spin coating techniques. I would also like to thank Dr. Martin Kordts and Jennica Träger for helping me to use the EFM instrument and for the valuable discussions about the instrumental setup. Many thanks to my colleagues in the physical chemistry group specially Razan Alaneed, Rana Hore, Julian Radicke, Dr. Muhammad Humayun Bilal, Haroon Rashid, and Muhammad Abu Bakar for the assistance and for providing a friendly atmosphere. Also thankful to my former colleague Dr. Martin Pulst. Thanks to Dr. Thomas Michael, and Beate Horn for organizing the SFB workshops, soft-skill courses, advanced training modules, and doctoral student seminars. Farhana Fatema Leon, my wife, and my brother Zahidul Hasan deserve huge thanks for their unwavering support and for making this possible.

## List of publications

- 1 N. Hasan, T. M. H. Nguyen, K. Busse, et al., Influence of tacticity on the structure formation of poly(methacrylic acid) in Langmuir/Langmuir–Blodgett and thin films, *Macromol. Chem. Phys.* 2023, 2200428.
- 2 N. Hasan, K. Busse, H. Husain, et al., Formation of surface wrinkles in collapsed Langmuir films of a polyhedral oligomeric silsesquioxane containing diblock copolymer, *Langmuir* 2021, 37, 13399.
- 3 E. Amado, N. Hasan, et al., Microscopic characterization of poly(sulfur nitride), *Macromol. Chem. Phys.* 2021, 2100113.
- 4 L. Chenming, P. Hilgeroth, N. Hasan, et al., Comparing C2=O and C2=S Barbiturates: different hydrogen bonding patterns of thiobarbiturates in solution and the solid-state, *Int. J. Mol. Sci.* 2021, 22, 12679.
- 5 N. Hasan, K. Busse, T. Haider, et al., Crystallization of poly(ethylene)s with regular phosphoester defects studied at the air-water interface, *Polymers* 2020, 12, 2408.
- 6 N. Hasan, C. Fuchs, K. Busse, et al., Crystallization of poly( $\epsilon$ -caprolactone) at the air-water interface studied by IRRAS and GI-WAXS, *Polymer* 2020, 196, 122468.
- 7 N. Hasan, et al., Comparison of Li<sup>+</sup> -ion conductivity in linear and crosslinked poly(ethylene oxide), *J. Polym. Sci., Part B: Polym. Phys.* 2019, 57, 21.
- 8 N. Hasan, A. Ullah, et al., Langmuir film formation of amphiphilic hybrid block copolymers based on poly(ethylene glycol) and poly(methacrylo polyhedral oligomeric silsesquioxane, *Colloid Polym. Sci.* 2019, 297, 1149.
- 9 K. Busse, C. Fuchs, N. Hasan, et al., Crystallization of poly(ethylene oxide) on the surface of aqueous salt solutions studied by GI-WAXS, *Langmuir* 2018, 34, 12759.
- 10 N. Hasan, C. Schwieger, et al., Crystallization of a polyphosphoester at the air-water interface, *Eur. Polym. J.* 2018, 101, 350.
- 11 C. Kirsch, M. Pulst, M. H. Samiullah, P. Ruda, N. Hasan, et al., 1,2,3-Triazole mediated Li<sup>+</sup> -ion conductivity in poly(ethylene oxide) based electrolytes, *Solid State Ionics*, 2017, 309, 163.

# Curriculum vitae

## Personal data

Name	Nazmul Hasan
Gender	Male
Date of birth/place	17.07.1989/Munshiganj, Bangladesh
Nationality	German

## Education

06/2018 – 02/2023	Doctoral studies Martin-Luther-Universität Halle-Wittenberg, Germany Institute of Chemistry Supervisor: Prof. Jörg Kressler
10/2013 – 08/2016	Master in Polymer Materials Science Martin-Luther-Universität Halle-Wittenberg, Germany Degree: Master of Science
10/2012 – 09/2013	Master in Applied Chemistry and Chemical Technology Islamic University Kushtia-Jhenidah, Bangladesh Degree: Master of Science
01/2007 – 08/2012	Bachelor in Applied Chemistry and Chemical Technology Islamic University Kushtia-Jhenidah, Bangladesh Degree: Bachelor of Science

Halle (Saale), den

Nazmul Hasan